University of Strathclyde

Department of Naval Architecture, Ocean and Marine Engineering

HYDRODYNAMIC INTERACTION BETWEEN SHIPS TRAVELLING OR STATIONARY IN SHALLOW WATERS

by

Zhi-Ming Yuan

A thesis submitted in fulfilment of the requirements for the degree of Doctor of Philosophy

May, 2014

This thesis is the result of the author's original research. It has been composed by the author and has not been previously submitted for examination which has led to the award of a degree.

Signed: Date:

失之东隅，收之桑榆. ---范晔

"What one loses on the swings, he gets back on the roundabouts."---Ye Fan

To my father

To my mother

Abstract

This thesis presents the development and application of a numerical method that associates the Rankine source method with double Doppler shift to predict the hydrodynamic interactions between two ships travelling or stationary in shallow waters.

Firstly, a 3-D Rankine source panel method was developed to predict the hydrodynamic properties of a single ship travelling with a wide range of forward speeds. Double Doppler shift was taken into consideration in the boundary condition of the control surface. A Wigley III hull travelling with different forward speeds was considered to validate this radiation condition. Comparing with the experimental data, both the hydrodynamic coefficients and motion responses were well predicted by the present method.

Then, the method for single ship was extended to ship-to-ship without forward speed problem. Comparing the present calculations of the hydrodynamic coefficients, wave excitation forces and motion responses with the experimental data, as well as with the numerical results from Green function method, a very good agreement was achieved which illustrated that the present program was a useful tool to predict the hydrodynamic behaviours of two ships arranged side by side without forward speed. The effects of mooring and fender system were also discussed based on the linear assumption.

Based on the same framework, the 3-D Rankine source panel method associated with double Doppler shift was applied to ship-to-ship interaction with forward speed problem. The validations were established through two pairs of models. The computed dynamic responses of both models in heave and pitch motions showed a good agreement with the published experimental results. However, the prediction of the roll motion was full of challenges due to the inviscid assumption in the potential flow theory. The comparison between the present and Sommerfeld radiation condition was

made at $\tau < 0.25$, while the comparison between the present and upstream radiation treatment was made at $\tau > 0.25$. It was shown that the present treatment could obtain a better wave pattern without reflections from the truncated control surface, which confirmed the effectiveness of the present radiation condition as a wave-pattern prediction tool for the ships travelling with a wide range of forward speed.

After the validations of the present method, the parametric study about the forward speed and configurations was carried out in order to develop recommendations for ship designers and operators for maximum speed and distance between two ships in given environmental conditions for safe operation. The analytical expression of the semi-wedge angle based on double Doppler shift theory was derived to obtain the wake and quiescent region of the free surface. Based on the semi-wedge angle, the analytical formulation was established to obtain the optimal transvers distance between two travelling ships.

Acknowledgements

I am deeply indebted to Professor Atilla Incecik for giving me the opportunity to do the research that I am enthusiastic about. It is my great honour to work with him and be supervised by him. Due to his generous academic support and guidance, I had an enjoyable and unforgettable time during the past three years in Glasgow.

I would like to express my gratitude to Dr. Shi He, Dr. Laibing Jia, Dr. Zhiliang Gao and Dr. Olgun Hizir for their advice and help. The numerous discussions are important to this work.

I am very grateful to Dr. Jianxin, Dr. Saishuai, Dr. Enhao, Dr. Ning, Dr. Zhengqiang, and other colleagues in the Research Centre of NAOME. They make my life in Glasgow full of unforgettable moments.

Many thanks are due to Mrs. Thelma Will for her support with the administrative details of the registration, preparation and submission of my thesis.

The financial support of Lloyd's Register is greatly acknowledged.

I also would like to express my gratitude to my girlfriend, Minglu, who makes my life more colourful and enjoyable during my study.

Finally, I want to dedicate this thesis to my father Shiqing Yuan and mother Jinxiu Wu for their unconditional love, support and encouragement throughout my life.

Table of Contents

List of Figures

List of Tables

Nomenclature

Roman Symbols

dt	transverse distance between two ships
dl	longitudinal distance between two ships
u_0	forward speed of the ship
$\mathbf{x}$	position vector
$\mathbf{n}$	unit normal vector
t	time
d	water depth
k	wave number
g	acceleration of gravity
m_j	*m*-term in *j-th* model
p_j	pressure in *j-th* model
F	wave excitation force
M_{ij}	mass matrix
K_{ij}	restoring force matrix
G	Green function
r	distance between the source point and field point
c	velocity of the scattered wave
k_s	local wave number
F_n	Froude number
L	length of the ship
B	breadth of the ship
D	draught of the ship

V	displacement of the ship
KR	centre of rotation above base line
KG	centre of gravity above base line
k_{yy}	radius of inertia for pitch
A_w	water-plane area
C_w	wave making resistance coefficient
C_B	block coefficient
C_p	water plane area coefficient
X_G	longitudinal centre of the gravity
Z_G	vertical centre of the gravity

Greek Symbols

η_j	motion amplitude in *j-th* model
β	incident wave angle
λ	incident wave length
ψ	velocity potential
φ_s	steady spatial potential
φ_j	unsteady spatial potential in *j-th* model
ω_0	incident wave frequency
ρ	fluid density
ω_e	encounter frequency
μ_{ij}	added mass
λ_{ij}	damping coefficient
ζ_j	wave elevation
θ	rotated angle
ω_s	local wave frequency

τ	Brard number
τ_0	incident Brard number
κ	non-dimensional roll damping coefficient
γ	semi-wedge angle

1. Introduction

1.1. Background

Hydrodynamic interaction between two or more ships occurs in harbour area and waterways with dense shipping traffic as the vessels have to pass each other in close proximity; between tugs and vessels during escorting or manoeuvring and berthing operations as well as during ship-to-ship operations for cargo. The behaviour of two ships in waves with speed effect is of special concern to the Navy, that is, for underway replenishment, and for other commercial purposes.

Lightering operations with forward speed are important for the transfer of fuel in naval operations. Nowadays, lighting operations without forward speed is important for the LNG offloading from LNG FPSOs or FSRUs (Floating Storage and Regassification Units). The loads in the mooring lines between the two vessels, the loads in the floating fenders and the relative motions at the manifold location are the most critical issues during this operation. These are determined by the wave, wind and current loads on the two vessels in close proximity, as well as by the strong hydrodynamic interaction between the vessels. Even in head seas, the two vessels could be subjected to a very large separating force as the waves run between the two hulls. The resulting motions and mooring loads determine the operability of the operation in certain environmental conditions.

1.2. Objectives and scope of research

The primary objective of the work presented in this thesis is to study the hydrodynamic interactions between two ships travelling or stationary in shallow waters. This entails the following specific tasks:

- Develop a numerical program to predict the behaviour of single ships travelling in waves.
- Develop a numerical program to predict the coupled behaviour of stationary ships moored side-by-side in waves.

- Develop a numerical program to predict the coupled behaviour of two travelling ships arranged side-by-side in shallow water.
- Validate the numerical programs described above through the commerce software as well as the experimental measurements.
- Carry out parametric studies in order to develop recommendations for ship designers and operators for maximum speed and distance between two ships in given environmental conditions for safe operation.

1.3. Challenges

The seakeeping characteristics between two ships are a complicated issue due to the strong hydrodynamic interactions. Besides, the forward speed and shallow water effects involved in the present study also add the difficulties to ship-to-ship problem. The challenges which will arise in this thesis are summarized as follows:

1) Hydrodynamic interactions. The hydrodynamic properties of one ship will be greatly influenced by the presence of the other ship. The influence will be reflected on the radiation problem as well as the diffraction problem. Specially, if the dimension of the two ships differs a lot, even relatively small wave can induce large motions of the smaller ship due to the nearness of the larger ship. Besides, compared with the single ship problem, there are 12 independent degrees of freedom, which are coupled in the motion equation.
2) Shallow water effects. Ship motions are directly affected in two ways by the restricted water depth: (1) the incident waves are changed and as a result, the wave exciting forces exerted on ship differ from those in deep water; (2) the hydrodynamic coefficients of the ship are changed by the nearness of the sea bottom. Therefore, the coupled motion responses of both ships will be influenced accordingly.
3) Forward speed effects. Even for a single vessel travelling with forward speed, the hydrodynamic responses are difficult to predict due to the additional items involved in the boundary value problem induced by the forward speed. When it refers to the ship-to-ship problem, the radiated and diffracted waves of one ship will bring a significant influence to the motion of the other ship. Special

attention should be paid on the very low forward speed problem, since the traditional radiation condition is not valid and a new radiation condition must be proposed in this study to investigate the ship-to-ship interaction with very low forward speed problem.

4) Parametric study. The hydrodynamic interactions between two ships are mainly determined by the forward speed of the ships and the transverse and longitudinal distance between the ships. A systematic study should be carried out to find the regularities of these parameters in order to develop recommendations for ship designers and operators for maximum speed and distance between two ships in given environmental conditions for safe operation.

1.4. Organization of the thesis

The primary objective of the present thesis is to carry out the parametric studies in order to develop recommendations for ship designers and operators for maximum speed and distance between two ships in given environmental conditions for safe operation. Before we achieve this objective, the basic solution should be established on single ship with zero speed. The forward speed effect should then be imposed on the boundary conditions of single ship. After that, we can extend the approach of single ship to two ships without forward speed problem. Two ships advancing in shallow water with any configurations will be the last step of our numerical program. This thesis is structured in the follow chapters and a brief outline of the content of each chapter is given bellow:

- Chapter 1 (Introduction) introduces the background and objectives of the research. The challenges, which will arise in the study, are also presented in this chapter.
- Chapter 2 (Critical review) gives a report of literature review on ship-to-ship interactions, forward speed and shallow water effects. The methodology adopted is also presented in this chapter.

- Chapter 3 (Formulation of 3-D flow) summaries the fundamental formulations of 3-D potential flow. The boundary value problem will be discussed in this chapter.
- Chapter 4 (3-D Rankine source panel method) describes the numerical solution of the boundary value problem. The desingularied method, as well as difference scheme, will be introduced in this chapter.
- Chapter 5 (Implementation of radiation condition) complements a new radiation condition which takes into account the Doppler shift of the scattered waves. This new radiation condition is applicative to a wide range of forward speeds, including very low forward speed problem where the Brard number is smaller than 0.25.
- Chapter 6 (Validations and discussion of single ship travelling or stationary in waves) validates the present method through a single Wigley hull with or without forward speed. The comparisons between the computed results and experimental data are given.
- Chapter 7 (Validations and discussion of two identical ships stationary in waves) validates the present method through two pairs of models stationary in waves. The comparisons are established between the present results and the experimental data. The calculations from the commercial software are also included. Discussions are highlighted on the effects from the fender and mooring system.
- Chapter 8 (Validations and discussion of two ships advancing in waves) validates the present program through two pairs of models advancing in head seas. The corresponding model test results are presented and compared. Discussions are highlighted on the scattered wave patterns obtained by the present radiation condition and upstream treatment.
- Chapter 9 (Parametric study and optimal design) carries out a systematic parametric study to investigate the regularities of multi-parameters in order to develop recommendations for ship designers and operators for maximum speed and distance between two ships in given environmental conditions for safe operation.

- Chapter 10 (Conclusions and recommendations) summaries the main contributions of the present work and suggestions of the future work.

2. Critical review

2.1. Introduction

The present study involves in ship-to-ship interactions associated with the forward speed and shallow water problem. In this chapter, the first comprehensive review is undertaken concerning the state-of-the-art of the approaches about investigating the hydrodynamic interactions between two ships. The discussions then will be made about different problems, which includes the forward speed problem and shallow water problem. The particular discussion about the numerical treatment of the radiation condition will be highlighted. At last, the comparison study is performed and the approaches adopted in the present study can be elaborated.

2.2. Ship-to-ship interactions

Early studies on the hydrodynamic interactions focused on 2-D strip theory. Ohkusu (1974) used the multipoles method and theory to calculate the response of parallel, slender, ship like bodies in beam waves. His results clearly illustrated the effect of position of a smaller body on the weather and lee side against a large body. Kodan (1984) extended Ohkusu's theory (Ohkusu, 1974) to hydrodynamic interaction between two parallel structures in oblique waves by strip method. Fang and Kim (1986) analyzed the hydrodynamic coupled motions of two longitudinally parallel barges advancing in oblique waves by strip method. His analysis showed that the coupling motions of two advancing ships depend on the speed, wave heading and distance. The 2-D method was a simple and effective tool in predicting the hydrodynamic interaction between two adjacent ships. Ronæss (2002) applied a unified slender body theory to investigate the ship-to-ship with forward speed problem. Her results showed good agreement with her model tests at the Marine Technology Centre in Trondheim, Norway. However, the limitations of applying 2-D methods in ship-to-ship interaction problem in waves have been confirmed by Fang and Kim (1986). The two ships were assumed to be in each other's near-field. The 2-D method overestimates the interaction effects due to the wave energy trapped between the two hulls in the frequency range

which is important for ship motions, which also leads to the overestimation of the mean second order wave loads on each ship. Besides, the strip theory can only predict the motion responses of conventional monohull ships in waves at low to moderate Froude numbers. However at high Froude numbers, three-dimensional (3-D) effects become dominant and strip theory fails to predict the hydrodynamic performance of vessel travelling with high forward speed. Under these circumstances, an advanced computational technique which accounts for the 3D flow interactions is necessary for motion and loading predictions.

Chen and Fang (2001) extended Fang's method (Fang and Kim, 1986) to 3-D. They used a 3-D Green function method to investigate the hydrodynamic problems between two moving ships in waves. It was found that the hydrodynamic interactions calculated by 3-D method were more reasonable in the resonance region, where the responses were overestimated by 2-D method. However, their method was only validated by model tests with zero speed. More rigorous validation should be made by further experiments. Kim and Ha (2002) used 3-D pulsating source distribution techniques to calculate twelve coupled linear motion responses and relative motions of the barge and the ship in oblique waves. Their computational results gave a good correlation with the experimental results and also with other numerical results. Taggart et al. (2003) and Li (2007) developed a frequency domain code based on 3-D Green function method. They validated their numerical predictions by model tests conducted at the Institute for Marine Dynamics (IMD) in St. John's, Newfoundland. It was showed that the presence of a larger ship could significantly influence the motions of a smaller ship in close proximity. But the numerical prediction of roll motion was not accurate. Inoue and Kamruzzaman (2008) developed a computer code YNU-SEA based on the 3-D Green function method to predict the relative wave elevations under the bridging structures for multihull ships traveling with forward speed in waves. They compared the calculations with those of their previous calculations as well as with experimental results to validate the efficiency of the code. Xiang and Faltinsen (2011) used a 3-D Rankine source method to solve the linear initial-boundary value problem of two ships advancing in waves. The time domain analysis was validated through the frequency solution via Fourier transform, and also the model test results. Recently, within the frame work of Green function, Xu and Dong (2013) developed a 3-D translating-pulsating (3DTP)

source method to calculate wave loads and free motions of two ships advancing in waves. Model tests were carried out to measure the wave loads and the heave, roll and pitch motions for a pair of side-by-side arranged ship models advancing with an identical speed in head regular waves. Both the experiment and the numerical prediction showed that hydrodynamic interaction effects on wave loads and motions were significant. They also pointed out that the prediction accuracy of the 3DTP method was much better than that of 3DP, especially for peak values of the motion responses.

It is found that most of the publications on two ships with forward speed problem are based on Green function that satisfies the Kelvin free surface conditions, as well as the radiation condition, and it is so-called Green function method. In terms of the Green function used in the boundary value problem (BVP), the Green function method can be classified into two categories: pulsating source Green function method (PSM) and translating-pulsating source Green function method (TPSM). As reported by many investigators (Chen and Fang, 2001; Li, 2001; McTaggart et al., 2003), the Green function used in PSM satisfies the zero speed and linear free surface condition, and the correction of the speed effects on the free surface neglects the interactions between the ship oscillation and translation. The diffraction-radiation waves obtained in this formulation are pure cylindrical waves which are not true, because the convective effects of the forward speed in the free surface wave field make the free surface disturbances produced at the bow region convecting downstream. Since hydrodynamic interactions between two hulls are caused by radiation and diffraction waves produced by these two ships, the prediction accuracy of this method is limited. In this case, the 3D translating-pulsating source Green function, which satisfies the classical linear free surface condition with forward speed and can accommodate the 3D convective effects on the free surface (Chan, 1992), may be more genuine and rigorous than PSM. This Green function has been successfully adopted by many researchers to predict seakeeping characteristics of a single ship (including multihull ship) advancing in waves (Inoue and Kamruzzaman, 2008; Maury et al., 2003). However, the expression of the Green function, which satisfies the free surface condition with forward speed, is very complicated. In the case of forward speed, many numerical and theoretical difficulties appear. Firstly, it is difficult to account for the near-field flow condition.

Although some researchers (Lee and Sclavounos, 1989; Nossen et al., 1991) extended it to include the near-field free surface condition, the so-called irregular frequency still cannot be avoided. And it will bring singularity to the coefficient matrix equation. Secondly, it is impossible for the Green function to account for the effects of the unsteady flow on the steady potential.

An alternative method, which can avoid the limitation of Green function method, is called Rankine source method. It uses a very simple Green function in the boundary integral formulation and requires the sources distributed not only on the body surface, but also on the free surface and control surface. Therefore, a flexible choice of free-surface boundary conditions can be realized in these methods. The coupled behavior between steady and unsteady wave potential could be expressed in a direct formula. Meanwhile, the nonlinearity on the free surface could also be added in the boundary condition. The Rankine source approach has been used by many investigators since it has been first proposed by Hess and Smith (Hess and Smith, 1964). Investigators from MIT (Kring, 1994; Nakos and Sclavounos, 1990; Scalvounos and Nakos, 1988) applied the Rankine source approach to model steady and unsteady waves as a ship moves in waves. An analysis technique developed by Sclavounos and Nakos (Scalvounos and Nakos, 1988) for the propagation of gravity waves on a panelized free surface showed that the Rankine source method could adequately predict the ship wave patterns and forces. Their work led to the development of a frequency-domain formulation for ship motions with a consistent linearization based upon the double body steady flow model which assumeed small and moderate Froude numbers. Applications were reported by Nakos et al. (1990). This model was extended to the time domain by Kring (1994) who also proposed a physically rational set of Kutta conditions at a ship's transom stern. Recently, Gao et al. (Gao and Zou, 2008) developed a high-order Rankine panel method based on Non-Uniform Rational B-Spline (NURBS) to solve the 3-D radiation and diffraction problems with forward speed. Their results had very good agreement with the experimental data.

In terms of ship-to-ship with forward speed problem, the only available publication about using Rankine source method can be found in Xiang and Faltinsen (2011). They used a 3-D Rankine source method to solve the initial boundary value problem of two

ships advancing in waves. An artificial beach is applied to satisfy the radiation condition and good agreement had been achieved between their results and experimental data.

In the present study, the Rankine source approach proposed by Hess and Smith (Hess and Smith, 1964) will be applied, which will be discussed latter in Section 2.6.

2.3. Forward speed problem

Because of the hydrodynamic interactions, even relatively small wave can induce large motions of the smaller ship due to the nearness of the larger ship. When the ships are travelling with forward speed, the hydrodynamic interactions become more complicated. Fang and Kim (1986) firstly took forward speed into consideration in ship-to-ship problem. They utilized a 2-D procedure, including the hydrodynamic interaction and an integral equation method, to predict the coupled motions between two ships advancing in oblique seas. They found that the roll motion was reduced while the ships were advancing. However, due to the 2-D assumptions, some deficiencies including the special treatment of the convective term still exist. Kashiwagi (1993) used an unified theory to investigate the heave and pitch motions of a catamaran advancing in waves. Iwashita and Kataoka (1996) used the 3D translating and pulsating Green-function method to analyse the hydrodynamic interaction between steady and unsteady flows for a catamaran. Chen and Fang (2001) extended Fang's method (Fang and Kim, 1986) to 3-D. They used a 3-D Green function method to investigate the hydrodynamic problems between two moving ships in waves. It was found that the hydrodynamic interactions calculated by 3-D method were more reasonable in the resonance region, where the responses were not so significant predicted by 2-D method. However, their method was only validated by model tests with zero speed. More rigorous validation should be made by further experiments. The first model test of two ships advancing in waves was conducted by Li (2001). Both ships were restrained in surge, sway and yaw, as well as the free motions in heave, roll and pitch. Taggart et al. (2003) and Li (2007) used that model test data to verify their numerical programs, which was based on 3-D Green function method. The numerical predictions and experiments showed that the presence of a larger ship could

significantly influence the motions of a smaller ship in close proximity. But the numerical prediction of roll motion was not accurate. Another model test of two ships advancing in waves was conducted by Ronæss (2002) at MARINTEK. The experiments were performed at different speeds and with different longitudinal distances between the ships. The numerical program based on unified theory was verified. It was found that the heave and pitch motions could be predicted well while the roll motion was hard to be predicted due to the viscous effect. Ronæss's model test data was used by Xiang and Faltinsen (2011) to verify their numerical program based on 3-D Rankine source method. They applied an artificial numerical beach to satisfy the radiation condition. They found that the hydrodynamic peaks and spikes were related to the resonance modes in the water gap between the hulls. However, they also failed to predict the roll motion precisely. Recently, within the frame work of Green function, Xu and Dong (2013b) developed a 3-D translating-pulsating (3DTP) source method to calculate wave loads and free motions of two ships advancing in waves. Model tests were carried out to measure the wave loads and the free motions for a pair of side-by-side arranged ship models advancing with an identical speed in head regular waves. Both the experiment and the numerical prediction showed that hydrodynamic interaction effects on wave loads and free motions were significant. They also pointed out that the prediction accuracy of the 3DTP method was much better than that of 3DP, especially for peak values of the free motion responses.

2.4. Shallow water problem

Most work on ship-to-ship interaction problem assumes that the water is infinitely deep. In deep water, the major stimulus for systematic study of the phenomenon arose from the needs of the warship replenishing while underway at sea. It has already been pointed out that merchant ships are most likely to be in close quarters situation in shallow water where the interaction effects may be larger. Meanwhile, the increasing demands for LNG and the associated safety requirements have resulted in a large number of offshore LNG terminal developments and most of these are located near-shore, in relatively shallow water. In addition to shallow water effects on the waves, the clearance to the bottom might become an issue when the water depth to draft ratio becomes small. Ship motions are directly affected in two ways by the restricted water

depth: (1) the incident waves are changed and as a result, the wave exciting forces exerted on ship differ from those in deep water; (2) the hydrodynamic coefficients of the ship (i.e. radiation forces) are changed by the nearness of the sea bottom. The influence of limited water depth on the ship motions becomes obvious when the water depth is less than 4 times of the draft of the vessel. When the ratio of water depth to draft is less than 2, the effect of the bottom becomes significant (Van Oortmerssen, 1976). Published work on the effect of water depth can be found in Kim (1969), Tuck (1970) and Andersen (1979). Most of them were based on the slender body assumption and no consideration of free-surface was involved by solving a two-dimensional problem. Endo (1987) produced a more accurate seakeeping prediction in shallow water, but parts of his method still needed to be improved.

Very few studies can be found on the ship motions in shallow water recently. In terms of ship-to-ship interaction with forward speed problem, the only available publication is reported by Zou and Larsson (2013). They used a steady state Reynolds averaged Navier–Stokes solver to simulate the ship-to-ship interactions during a lightering operation in shallow water. However, the difference between the measured forces and moments and results from computations by the two CFD methods was relatively large in many cases.

2.5. Radiation condition

The limitations for the extensive use of the Rankine source approach lies on the computational time and the requirement of a radiation condition. It requires much more panels on the wet body surface, free surface and control surface, which will considerably increase the computation time, especially when the matrix equation is full range matrix. However, the computation time will strongly depend on the numerical method and computer language. As the performance of computers increase rapidly, it is possiblem to solve the large full range matrix within an acceptable time scale in engineering applications. Besides, the Rankine source method requires a suitable radiation boundary condition to account for the scattered waves in current. A very popular radiation condition for the forward speed problem, which is so-called upstream radiation condition, was proposed by Nakos (Nakos, 1990). The free surface

was truncated at some upstream points, and a quiescent boundary condition was imposed at these points to ensure the consistency of the upstream truncation of the free surface. Another method to deal with the radiation condition is to move the source points on the free surface at some distance downstream (Jensen et al., 1986). The results from these two methods show very good agreement with published experimental data when the Brard number τ ($\tau = u\omega/g$) is greater than 0.25, since they are both based on the assumption that there is no scattered wave travelling ahead of the vessel. However, when the forward speed of the vessel is very low, the Brard number will be smaller than 0.25. When this case occurs, the scattered waves could travel ahead of the vessel, and these traditional radiation conditions could no longer be valid. For ship-to-ship problem, the forward speed is usually limited to a low level for the safe operation. Therefore, a new extensive radiation condition should be proposed to deal with the very low forward speed problem. Das and Cheung (2012a, b) provided an alternate solution to the boundary-value problem for forward speeds above and below the group velocity of the scattered waves. They corrected the Sommerfeld radiation condition by taking into account the Doppler shift of the scattered waves at the control surface that truncates the infinite fluid domain. They compared their results with the experimental data, and good agreement was achieved. They also computed the wave elevation on the free surface, and a reasonable wave pattern was obtained at $\tau < 0.25$ by using their new radiation condition.

2.6. Approach adopted

In the present study, the Rankine source approach proposed by Hess and Smith (Hess and Smith, 1964) will be applied, which uses a very simple Green function in the boundary integral formulation. This method requires the sources distributed not only on the body surface, but also on the free surface, control surface and sea bottom surface. Therefore, a flexible choice of free-surface condition and sea bottom condition can be realized in these methods. The forward speed and shallow water effects can be directly taken into the consideration in the boundary value problem. Besides, the near field wave elevations can be directly obtained by boundary integration on the free surface.

In order to complete the boundary value problem, a radiation condition should be imposed on the control surface. For ship-to-ship problem, the forward speed is usually limited to a low level for the safe operation. Therefore, a new extensive radiation proposed by Das and Cheung (2012a, b) will be adopted in the present study to provide an alternate solution to the boundary-value problem for forward speeds above and below the group velocity of the scattered waves.

A 3-D boundary element program based on Rankine source method will be developed to investigate the hydrodynamic interaction between two vessels arranged side by side with forward speed in shallow water. The motion responses of both ships will be calculated and compared to the commercial program and experimental results. After the validation, this program will be used for the parametric study to investigate the regularities of multi-parameters in order to develop recommendations for ship designers and operators for maximum speed and distance between two ships in given environmental conditions for safe operation.

3. Formulations of 3-D flow

3.1. Introduction

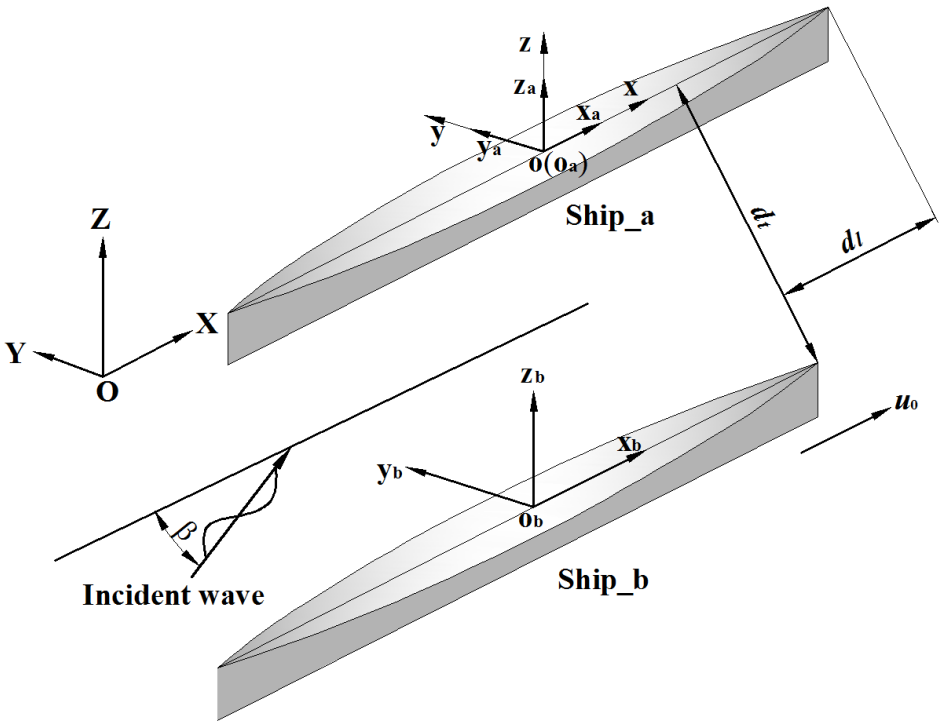

Figure 3.1: An example vessels and coordinate system.

The corresponding right-handed coordinate systems are shown in Figure 3.1. The body coordinate systems o_a-$x_a y_a z_a$ and o_b-$x_b y_b z_b$ are fixed on ship_a and ship_b respectively with their origins on the mean free surface, coinciding with the corresponding centre of gravity (CoG) in respect to *x* and *y* coordinates when both of the ships are at their static equilibrium positions. o_a-z_a and o_b-z_b are both positive upward. The inertia coordinate system *o-xyz* with origin located on the calm free surface coincides with o_a-$x_a y_a z_a$ when the ship has no unsteady motions. *O-XYZ* is the earth-fixed coordinate system with its origin located on the calm free surface and *OZ* axis positive upward. Three components of translation motions include surge (η_1^a and η_1^b, which are parallel to *x*-axis), sway (η_2^a and η_2^b, which are parallel to *y*-axis) and heave (η_3^a and η_3^b, which are parallel to *z*-axis). Another three rotational motion components are roll (η_4^a

and η_4^b, which rotates around *x*-axis), pitch (η_5^a and η_5^b, which rotates around *y*-axis) and yaw (η_6^a and η_6^b, which rotates around *z*-axis). The incident wave direction is defined as the angle β between the wave propagation direction and *X*-axis and $\beta = 180°$ corresponds to head sea; $\beta = 90°$ corresponds to beam sea. *dt* denotes the transverse distance between two ships while *dl* is the longitudinal distance. u_0 is the forward speed.

In the computation, the motions and forces of each ship are concerted to the local coordinate system in which the origins are at the canter of gravity of each ship.

3.2. Fundamental equations

It is assumed that the surrounding fluid is inviscid and incompressible, and that the motion is irrotational, the total velocity potential exists which satisfies the Laplace equation in the whole fluid domain. Let *t* denote time and $\vec{\mathbf{x}} = (x, y, z)$ denote the position vector. The velocity potential provides a description of the flow as

$$\begin{aligned}\psi(\vec{\mathbf{x}},t) &= u_0\left[\varphi_s(\vec{\mathbf{x}}) - x\right] + \mathrm{Re}\sum_{j=1}^{6}[\eta_j^a\varphi_j^a(\vec{\mathbf{x}})e^{-i\omega_e t} + \eta_j^b\varphi_j^b(\vec{\mathbf{x}})e^{-i\omega_e t}] \\ &+ \mathrm{Re}[\eta_0\varphi_0(\vec{\mathbf{x}})e^{-i\omega_e t}] + \mathrm{Re}[\eta_7\varphi_7(\vec{\mathbf{x}})e^{-i\omega_e t}],\ j = 1,2,...,6\end{aligned} \tag{3.1}$$

where φ_s is the steady potential; φ_j^a and φ_j^b (j = 1,2,…,6) are the spatial radiation potential in six degrees of freedom corresponding to the oscillations of Ship_a and Ship_b respectively and $\eta_j(j = 1,2,...,6)$ is the corresponding motion amplitude (η_1, surge; η_2 ,sway; η_3 ,heave; η_4 ,roll; η_5 ,pitch; η_6 ,yaw); $\eta_7 = \eta_0$ is the incident wave amplitude; φ_7 is the spatial diffraction potential; φ_0 is the spatial incident wave potential and ω_e is the encounter frequency, which can be given by

$$\varphi_0 = -\frac{ig\eta_0}{\omega_0}\frac{\cosh k(z+d)}{\cosh kd}e^{i[k(x\cos\beta + y\sin\beta)]} \tag{3.2}$$

$$\omega_e = \omega_0 - u_0 k\cos\beta \tag{3.3}$$

where *d* denotes the water depth and *k* is the wave number. If the incident wave frequency ω_0 and water depth are given, the wave number *k* can be determined by the dispersion relation as

$$k \cdot \tanh kd = \omega_0^2 / g \tag{3.4}$$

3.3. Steady flow

When a ship advances at constant speed in water, it will generate steady waves and produce the so-called wave making resistance. In the present study, the wave making resistance will not be considered, since it can be balanced by the propulsion force. However, the steady wave will still influence the radiated and diffracted waves. It can interact with the unsteady wave field generated by the ship's motion. The interaction between the steady flow and unsteady wave field appears in so-called *m*-term. Generally, there are three different steady flow models, that is, free stream, double body flow and steady wave flow (Kim and Shin, 2007). In this thesis, we will use steady wave flow model to treat the steady potential problem. The steady potential φ_s satisfies the following boundary conditions:

$$\nabla^2 \varphi_s = 0 \quad \text{in the fluid domain} \tag{3.5}$$

$$u_0^2 \frac{\partial^2 \varphi_s}{\partial x^2} + g \frac{\partial \varphi_s}{\partial z} = 0 \quad \text{on the undisturbed free surface} \tag{3.6}$$

$$\frac{\partial \varphi_s}{\partial n} = u_0 n_1 \quad \text{on the mean wetted part of body surface} \tag{3.7}$$

$$\frac{\partial \varphi_s}{\partial z} = 0 \quad \text{on the sea bottom} \tag{3.8}$$

where $\vec{\mathbf{n}} = (n_1, n_2, n_3)$ is the unit normal vector inward on the wet body surface. Moreover, a radiation condition which states that the waves propagate away from the ship, is required and it will be discussed later in Chapter 5.

3.4. Incident wave

The spatial incident wave potential was given in Eq. (3.2) and the real part and imaginary part of φ_0 can be expressed respectively by

$$\varphi_{0R} = \frac{g\eta_0}{\omega_0} \cdot \frac{\cosh(k(z+d))}{\cosh(kd)} \cdot \sin(k(x\cos\beta + y\sin\beta)) \tag{3.9}$$

$$\varphi_{0I} = -\frac{g\eta_0}{\omega_0} \cdot \frac{\cosh(k(z+d))}{\cosh(kd)} \cdot \cos(k(x\cos\beta + y\sin\beta)) \tag{3.10}$$

In the body boundary condition of radiation problem, the normal induced velocity of incident wave is required. It can be obtained from the partial derivative of the real part and imaginary part of the incident wave potential, which are given by

$$\frac{\partial\varphi_{0R}}{\partial x} = \eta_0\omega_0 \cos\beta \cdot \frac{\cosh(k(z+d))}{\sinh(kd)} \cdot \cos\left[k(x\cos\beta + y\sin\beta)\right] \tag{3.11}$$

$$\frac{\partial\varphi_{0R}}{\partial y} = \eta_0\omega_0 \sin\beta \cdot \frac{\cosh(k(z+d))}{\sinh(kd)} \cdot \cos\left[k(x\cos\beta + y\sin\beta)\right] \tag{3.12}$$

$$\frac{\partial\varphi_{0R}}{\partial z} = \eta_0\omega_0 \cdot \frac{\sinh(k(z+d))}{\sinh(kd)} \cdot \sin\left[k(x\cos\beta + y\sin\beta)\right] \tag{3.13}$$

$$\frac{\partial\varphi_{0I}}{\partial x} = \eta_0\omega_0 \cos\beta \cdot \frac{\cosh(k(z+d))}{\sinh(kd)} \cdot \sin\left[k(x\cos\beta + y\sin\beta)\right] \tag{3.14}$$

$$\frac{\partial\varphi_{0I}}{\partial y} = \eta_0\omega_0 \sin\beta \cdot \frac{\cosh(k(z+d))}{\sinh(kd)} \cdot \sin\left[k(x\cos\beta + y\sin\beta)\right] \tag{3.15}$$

$$\frac{\partial\varphi_{0I}}{\partial z} = -\eta_0\omega_0 \cdot \frac{\sinh(k(z+d))}{\sinh(kd)} \cdot \cos\left[k(x\cos\beta + y\sin\beta)\right] \tag{3.16}$$

3.5. Diffraction wave

The diffraction potential can be solved by the following boundary value problem:

$$\nabla^2\varphi_7 = 0 \quad \text{in the fluid domain} \tag{3.17}$$

$$g\frac{\partial\varphi_7}{\partial z} - \omega_e^2\varphi_7 + 2i\omega_e u_0 \frac{\partial\varphi_7}{\partial x} + u_0^2 \frac{\partial^2\varphi_7}{\partial x^2} = 0 \quad \text{on the undisturbed free surface } S_f \tag{3.18}$$

$$\frac{\partial\varphi_7}{\partial n} = -\frac{\partial\varphi_0}{\partial n}\Big|_{S_a} \quad \text{on the mean wetted part of Ship\_a} \tag{3.19}$$

$$\frac{\partial\varphi_7}{\partial n} = -\frac{\partial\varphi_0}{\partial n}\Big|_{S_b} \quad \text{on the mean wetted part of Ship\_b} \tag{3.20}$$

$$\frac{\partial\varphi_7}{\partial z} = 0 \quad \text{on the sea bottom} \tag{3.21}$$

Moreover, a radiation condition must be implemented to the boundary value problem, which will be discussed later in Chapter 5.

3.6. Radiation wave

Radiation waves are generated by the oscillation of both ships. The main difference between single ship motion and two ship motion can be reflected on the radiation wave. The radiation wave force of a ship is not only due to its own oscillation, but also due to the oscillation of the other ship. For linearization, the radiation potential can be written as:

$$\Psi_R(\vec{\mathbf{x}},t) = \mathrm{Re}\sum_{j=1}^{6}[\eta_j^a\varphi_j^a(\vec{\mathbf{x}})e^{-i\omega_e t} + \eta_j^b\varphi_j^b(\vec{\mathbf{x}})e^{-i\omega_e t}] \tag{3.22}$$

The corresponding radiation potential of Ship_a and Ship_b can be obtained by solving the following boundary value problem:

1) Ship_a is oscillating while Ship_b is fixed

$$\nabla^2\varphi_j^a = 0 \quad \text{in the fluid domain} \tag{3.23}$$

$$g\frac{\partial\varphi_j^a}{\partial z} - \omega_e^2\varphi_j^a + 2i\omega_e u_0\frac{\partial\varphi_j^a}{\partial x} + u_0^2\frac{\partial^2\varphi_j^a}{\partial x^2} = 0 \quad \text{on the undisturbed free surface } S_f \tag{3.24}$$

$$\frac{\partial\varphi_j^a}{\partial n} = -i\omega_e n_j^a + u_0 m_j^a\Big|_{S_a} \quad \text{on the mean wetted part of Ship\_a} \tag{3.25}$$

$$\frac{\partial\varphi_j^a}{\partial n} = 0\Big|_{S_b} \quad \text{on the mean wetted part of Ship\_a} \tag{3.26}$$

$$\frac{\partial\varphi_j^a}{\partial z} = 0 \quad \text{on the sea bottom} \tag{3.27}$$

2) Ship_b is oscillating while Ship_a is fixed

$$\nabla^2\varphi_j^b = 0 \quad \text{in the fluid domain} \tag{3.28}$$

$$g\frac{\partial\varphi_j^b}{\partial z} - \omega_e^2\varphi_j^b + 2i\omega_e u_0\frac{\partial\varphi_j^b}{\partial x} + u_0^2\frac{\partial^2\varphi_j^b}{\partial x^2} = 0 \quad \text{on the undisturbed free surface } S_f \tag{3.29}$$

$$\frac{\partial \varphi_j^b}{\partial n} = -i\omega_e n_j^b + u_0 m_j^b \Big|_{S_b} \quad \text{on the mean wetted part of Ship\_b} \tag{3.30}$$

$$\frac{\partial \varphi_j^b}{\partial n} = 0 \Big|_{S_a} \quad \text{on the mean wetted part of Ship\_a} \tag{3.31}$$

$$\frac{\partial \varphi_j^b}{\partial z} = 0 \quad \text{on the sea bottom} \tag{3.32}$$

Besides, a radiation condition must be imposed on the control surface to complete the boundary value problem. The generalized normal vectors are defined as

$$n_j = \begin{cases} \vec{\mathbf{n}}, \; j = 1,2,3 \\ \vec{\mathbf{x}} \times \vec{\mathbf{n}}, \; j = 4,5,6 \end{cases} \tag{3.33}$$

and $\vec{\mathbf{n}} = (n_1, n_2, n_3)$ is the unit normal vector directed inward on body surface, $\vec{\mathbf{x}} = (x, y, z)$ is the position vector on body surface. The m_j denotes the *j*-th component of the so-called *m*-term, which can be expressed as

$$m_j = \begin{cases} -\left(\vec{\mathbf{n}} \cdot \nabla\right) \nabla \varphi_s, \; j = 1,2,3 \\ -\left(\vec{\mathbf{n}} \cdot \nabla\right) \left(\vec{\mathbf{x}} \times \nabla \varphi_s\right), \; j = 4,5,6 \end{cases} \tag{3.34}$$

where φ_s is the steady wave potential. The *m*-terms provide coupling effects between the steady and unsteady flows and involve the second derivatives of the steady potential. However, in the present study, we are interested in low forward speed problem of the slender vessels. Therefore, the Neumann-Kelvin linearization can be used to simplify the *m*-terms,

$$\begin{aligned} (m_1, m_2, m_3) &= (0,0,0) \\ (m_4, m_5, m_6) &= (0, n_3, -n_2) \end{aligned} \tag{3.35}$$

3.7. Motion equation

Once the unknown diffraction potential φ_7 and radiation potential φ_j are solved, the time-harmonic pressure can be obtained from Bernoulli's equation:

$$p_j = -\rho \left[i\omega_e \eta_j \varphi_j + \nabla(\varphi_s - u_0 x) \cdot \nabla \eta_j \varphi_j \right], \quad \text{j = 0, 1,..., 7} \tag{3.36}$$

where ρ is the fluid density. The hydrodynamic force produced by the oscillatory motions of the vessel in the six degrees of freedom can be derived from the radiation potentials as

$$\begin{aligned} F_i^{Ra} &= \sum_{j=1}^{6} \iint_{S_a} p_j^a n_i dS \cdot (\eta_j^a + \eta_j^b) \\ &= \sum_{j=1}^{6} \left[\omega_e^2 \mu_{ij}^{aa} + i\omega \lambda_{ij}^{aa} \right] \eta_j^a + \sum_{j=1}^{6} \left[\omega_e^2 \mu_{ij}^{ab} + i\omega \lambda_{ij}^{ab} \right] \eta_j^b \end{aligned} \quad , \quad i = 1, 2, ..., 6 \qquad (3.37)$$

$$\begin{aligned} F_i^{Rb} &= \sum_{j=1}^{6} \iint_{S_b} p_j^b n_i dS \cdot (\eta_j^a + \eta_j^b) \\ &= \sum_{j=1}^{6} \left[\omega_e^2 \mu_{ij}^{ba} + i\omega_e \lambda_{ij}^{ba} \right] \eta_j^a + \sum_{j=1}^{6} \left[\omega_e^2 \mu_{ij}^{bb} + i\omega_e \lambda_{ij}^{bb} \right] \eta_j^b \end{aligned} \quad , \quad i = 1, 2, ..., 6 \qquad (3.38)$$

The added mass and damping can be expressed respectively as:

$$\begin{aligned} \mu_{ij}^{aa} &= -\frac{\rho}{\omega_e} \iint_{S_a} (\varphi_{Ij}^a - \frac{u_0}{\omega_e} \frac{\partial \varphi_{Rj}^a}{\partial x}) n_i ds \\ \mu_{ij}^{ab} &= -\frac{\rho}{\omega_e} \iint_{S_a} (\varphi_{Ij}^b - \frac{u_0}{\omega_e} \frac{\partial \varphi_{Rj}^b}{\partial x}) n_i ds \\ \mu_{ij}^{bb} &= -\frac{\rho}{\omega_e} \iint_{S_b} (\varphi_{Ij}^b - \frac{u_0}{\omega_e} \frac{\partial \varphi_{Rj}^b}{\partial x}) n_i ds \\ \mu_{ij}^{ba} &= -\frac{\rho}{\omega_e} \iint_{S_b} (\varphi_{Ij}^a - \frac{u_0}{\omega_e} \frac{\partial \varphi_{Rj}^a}{\partial x}) n_i ds \end{aligned} \quad , \quad (i = 1, 2, ..., 6; j = 1, 2, ..., 6) \qquad (3.39)$$

$$\begin{aligned} \lambda_{ij}^{aa} &= -\rho \iint_{S_a} (\varphi_{Rj}^a + \frac{u_0}{\omega_e} \frac{\partial \varphi_{Ij}^a}{\partial x}) n_i ds \\ \lambda_{ij}^{ab} &= -\rho \iint_{S_a} (\varphi_{Rj}^b + \frac{u_0}{\omega_e} \frac{\partial \varphi_{Ij}^b}{\partial x}) n_i ds \\ \lambda_{ij}^{bb} &= -\rho \iint_{S_b} (\varphi_{Rj}^b + \frac{u_0}{\omega_e} \frac{\partial \varphi_{Ij}^b}{\partial x}) n_i ds \\ \lambda_{ij}^{ba} &= -\rho \iint_{S_b} (\varphi_{Rj}^a + \frac{u_0}{\omega_e} \frac{\partial \varphi_{Ij}^a}{\partial x}) n_i ds \end{aligned} \quad , \quad (i = 1, 2, ..., 6; j = 1, 2, ..., 6) \qquad (3.40)$$

where μ_{ij}^{aa} is the added mass of Ship_a in *i-th* mode which is induced by the motion of Ship_a in *j-th* mode; μ_{ij}^{ab} is the added mass of Ship_a in *i-th* mode which is induced by the motion of Ship_b in *j-th* mode; μ_{ij}^{ba} is the added mass of Ship_b in *i-th* mode which is induced by the motion of Ship_a in j-th mode; μ_{ij}^{bb} is the added mass of Ship_b in i-th mode which is induced by the motion of Ship_b in *j-th* mode; λ is the damping coefficient and the definition the subscript is the same as that of added mass; φ_{Rj} is the real part of *j-th* potential, and φ_{Ij} is the imaginary part. The wave excitation force can be obtained by the integration of incident and diffraction pressure as

$$F_i^{Wa} = \iint_{S_a} (p_0 + p_7) n_i dS \tag{3.41}$$

$$F_i^{Wb} = \iint_{S_b} (p_0 + p_7) n_i dS \tag{3.42}$$

Applying Newton's second law, the 12 components of ship motions in the frequency domain can be obtained by solving the following equation system:

$$\sum_{j=1}^{6} \left\{ \left[-\omega_e^2 \left(M_{ij}^a + \mu_{ij}^{aa} \right) + i\omega_e \lambda_{ij}^{aa} + K_{ij}^a \right] \eta_j^a + \left[-\omega_e^2 \mu_{ij}^{ab} + i\omega_e \lambda_{ij}^{ab} \right] \eta_j^b \right\} = F_i^{Wa}, i = 1, 2, ..., 6 \tag{3.43}$$

$$\sum_{j=1}^{6} \left\{ \left[-\omega_e^2 \mu_{ij}^{ba} + i\omega_e \lambda_{ij}^{ba} \right] \eta_j^a + \left[-\omega_e^2 \left(M_{ij}^b + \mu_{ij}^{bb} \right) + i\omega_e \lambda_{ij}^{bb} + K_{ij}^b \right] \eta_j^b \right\} = F_i^{Wb}, i = 1, 2, ..., 6 \tag{3.44}$$

where M_{ij}^a and M_{ij}^b represent the generalized mass matrix for Ship_a and Ship_b; K_{ij}^a and K_{ij}^b represent the restoring matrix for Ship_a and Ship_b. The mass and restoring force matrix can be given by

$$M_{ij}=\begin{bmatrix} m & 0 & 0 & 0 & mz_G & 0 \\ 0 & m & 0 & -mz_G & 0 & mx_G \\ 0 & 0 & m & 0 & -mx_G & 0 \\ 0 & -mz_G & 0 & I_{44} & 0 & I_{46} \\ mz_G & 0 & -mx_G & 0 & I_{55} & 0 \\ 0 & mx_G & 0 & I_{64} & 0 & I_{66} \end{bmatrix} \tag{3.45}$$

$$K_{ij}=\begin{bmatrix} 0 & 0 & 0 & 0 & 0 & 0 \\ 0 & 0 & 0 & 0 & 0 & 0 \\ 0 & 0 & \rho g A_w & 0 & -\rho g M_w & 0 \\ 0 & 0 & 0 & \rho g(I_{w1}+Vz_B) & 0 & 0 \\ 0 & 0 & -\rho g M_w & 0 & \rho g(I_{w2}+Vz_B) & 0 \\ 0 & 0 & 0 & 0 & 0 & 0 \end{bmatrix} \tag{3.46}$$

where m is the body mass; (x_G, y_G, z_G) is the center of gravity; I_{44}, I_{55} and I_{66} are the roll, pitch and yaw moments of inertia; the roll-yaw moment of inertia holds the symmetry relation $I_{46} = I_{64}$; A_w is the water plane area; M_w is the first moment of the water plane about the y-axis; I_{w1} and I_{w2} are the second moments of the water plane about the x-axis and y-axis respectively; V is the underwater volume; z_B is the vertical center of buoyancy. The standard matrix solution routine provides the complex amplitude of the oscillatory motions from Eqs. (3.43)-(3.44). The wave elevation on the free surface then can be obtained from the dynamic free surface boundary condition in the form

$$\zeta_j=\frac{i\omega_e}{g}(\eta_j^a\varphi_j^a+\eta_j^b\varphi_j^b)+\frac{1}{g}\nabla(\varphi_s-u_0x)\cdot\nabla(\eta_j^a\varphi_j^a+\eta_j^b\varphi_j^b)=\zeta_{Rj}+i\zeta_{Ij},\ j=0,1,...,7 \tag{3.47}$$

where ζ_{Rj} is the the real part of *j-th* model, and ζ_{Ij} is the imaginary part.

3.8. Summary

In this chapter, the basic formulations of the 3-D potential flow as well as the motion equations are presented. The boundary value problem for each special potential are given to solve all of the components of the potential. These formulations constitute the basic frame work of the boundary element method. The corresponding numerical solution for these boundary value problems will be described in the following chapters.

4.3-D Rankine source panel method

4.1. Introduction

In the design of ship and other marine structure, the potential flow method is practical and efficient to predict the body's motions and wave loads. As a numerical tool for computation of potential flow, the panel method is widely used. The original panel method proposed by Hess and Smith (1964) uses large numbers of plane quadrilateral panels to discretize the body surface, and on each panel a constant source density distribution is assumed.

The discretization of the boundary integral consists of two categories. First, we have to divide the body-, free- and control-surface into panels. Second, we have to choose a certain shape for the source function. This can be done in many ways, ranging from a very simple first-order approximation of flat panels and constant sources on each panel, to a high-order approximation that, for example, uses NURBS-based panels to describe the geometry of a panel and the shape of the source function. The first-order approximation leads to a relatively easy evaluation of the influence coefficients, and the number of the unknown of source density equals to the panel number. A high-order approximation leads to a more difficult evaluation of the influence coefficients, and to a large number of unknowns of each panel. Although the panels can be taken larger due to the higher accuracy, it mostly increases the size of the leading matrix (Bunnik, 1999).

In the present study, we use a constant panel method to discretize the boundary integral. The exact formulas for the velocity components induced at points in space by a plane quadrilateral source element with a unit value of source density are derived. The desingularied method and difference scheme are also discussed in this chapter.

4.2. Constant panel method

Before we discretize the boundary integral, a Green function should be chosen. Rankine source method uses a very simple Green function $G = 1/r$ in the boundary

integral formulation and requires the sources distributed not only on the body surface, but also on the free surface and control surface. Considering the sea bottom boundary condition in Eq. (3.8), (3.21), (3.27) and (3.32), the Green function can be modified through the method of image as

$$G(\vec{\mathbf{x}},\vec{\boldsymbol{\xi}}) = \frac{1}{r} + \frac{1}{r'} \tag{4.1}$$

where $r = \sqrt{(x-\xi)^2 + (y-\eta)^2 + (z-\varsigma)^2}$ is the distance between the source point $\vec{\mathbf{x}} = (x, y, z)$ and field point $\vec{\boldsymbol{\xi}} = (\xi, \eta, \varsigma)$, $r' = \sqrt{(x-\xi)^2 + (y-\eta)^2 + (z+2d+\varsigma)^2}$ is the distance between the image source point and field point. Therefore, the Green function in Eq.(4.1) can satisfy the sea bottom boundary condition.

There are generally two categories of coordinate systems in the discretization of the boundaries: the reference coordinate system and element coordinate system. The input data and the influence coefficients should be based on the reference coordinate system, while the element coordinate system is used for calculating the exact induced velocity component. The transformation matrix can be obtained easily to transform the coordinate (Hess and Smith, 1964). Consider a plane quadrilateral source element lying in the $\xi\eta$-plane (element coordinate system) as shown in Figure 4.1. The source density of panel Q is written as $\sigma(Q)$. Denote the number of panels on body, free and control surface as N_B, N_F and N_C respectively. Apart from the reference coordinate system O-XYZ, an element system O'-$\xi\eta\zeta$ is established with O' on the geometry centroid and ζ axis on its normal vector, as shown in Figure 4.1.

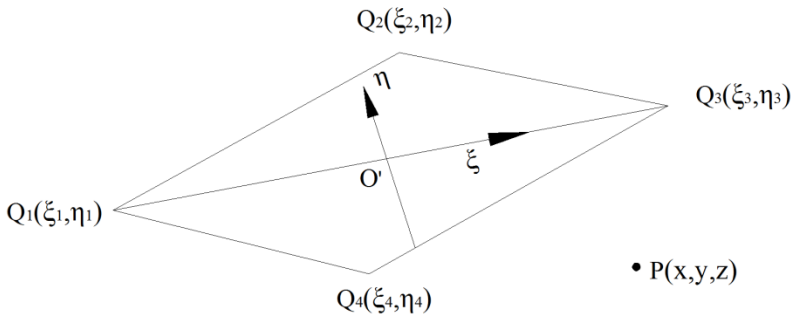

Figure 4.1: Quadrilateral element coordinate system.

It is desired to determine the velocity components induced by this source element at a general point *P* in space with its coordinate *(x, y, z).* The potential at point *P* is

$$\varphi_{Q,P} = \sigma(Q)\iint_{Q} G_{Q,P}\, d\xi d\eta \tag{4.2}$$

Since the source density on panel *Q* is constant. The velocity components at point *P* could be expressed as

$$\frac{\partial \varphi_{Q,P}}{\partial \xi} = \sigma(Q)\iint_{Q} \frac{\partial G_{Q,P}}{\partial \xi} d\xi d\eta \tag{4.3}$$

$$\frac{\partial \varphi_{Q,P}}{\partial \eta} = \sigma(Q)\iint_{Q} \frac{\partial G_{Q,P}}{\partial \eta} d\xi d\eta \tag{4.4}$$

$$\frac{\partial \varphi_{Q,P}}{\partial \zeta} = \sigma(Q)\iint_{Q} \frac{\partial G_{Q,P}}{\partial \zeta} d\xi d\eta \tag{4.5}$$

Hess and Smith (1964) provided the accurate solution for the integrals of Eqs. (4.2)-(4.5) as

$$\frac{\partial \varphi_{Q,P}}{\partial \xi} = -\sigma(Q)\cdot \sum_{i=1}^{4} \frac{\eta_{i+1}-\eta_i}{l_{i,i+1}} \ln \frac{r_i + r_{i+1} + l_{i,i+1}}{r_i + r_{i+1} - l_{i,i+1}} \tag{4.6}$$

$$\frac{\partial \varphi_{Q,P}}{\partial \eta} = \sigma(Q)\cdot \sum_{i=1}^{4} \frac{\xi_{i+1}-\xi_i}{l_{i,i+1}} \ln \frac{r_i + r_{i+1} + l_{i,i+1}}{r_i + r_{i+1} - l_{i,i+1}} \tag{4.7}$$

$$\frac{\partial \varphi_{Q,P}}{\partial \zeta} = \sigma(Q)\cdot \sum_{i=1}^{4} \left(\arctan \frac{m_{i,i+1} e_i - h_i}{z r_i} - \arctan \frac{m_{i,i+1} e_{i+1} - h_{i+1}}{z r_{i+1}} \right) \tag{4.8}$$

$$\varphi_{Q,P} = \sigma(Q)\cdot \sum_{i=1}^{4} \frac{(\xi_{i+1}-\xi_i)(y-\eta_i) - (\eta_{i+1}-\eta_i)(x-\xi_i)}{l_{i,i+1}} \times \ln \frac{r_i + r_{i+1} + l_{i,i+1}}{r_i + r_{i+1} - l_{i,i+1}} + z\cdot \frac{\partial \varphi_{Q,P}}{\partial \zeta} \tag{4.9}$$

where

$$r_i = \sqrt{(x-\xi_i)^2 + (y-\eta_i)^2 + z^2} \tag{4.10}$$

$$l_{i,i+1} = \sqrt{(\xi_{i+1}-\xi_i)^2 + (\eta_{i+1}-\eta_i)^2} \tag{4.11}$$

$$m_{i,i+1} = \frac{\eta_{i+1}-\eta_i}{\xi_{i+1}-\xi_i} \tag{4.12}$$

$$e_i = z^2 + (x - \xi_i)^2 \tag{4.13}$$

$$h_i = (y - \eta_i)(x - \xi_i) \tag{4.14}$$

We notice that the second partial derivative of φ is also required in the free surface boundary condition in Eqs. (3.6), (3.18), (3.24) and (3.29). Therefore, the accurate form of the second partial derivative of φ is provided here as

$$\frac{\partial^2 \varphi_{Q,P}}{\partial \xi^2} = -2z\sigma(Q) \cdot \sum_{i=1}^{4} \frac{(\eta_{i+1} - \eta_i)(r_i + r_{i+1})}{r_i r_{i+1}\left[(r_i + r_{i+1})^2 - l_{i,i+1}^2\right]} \tag{4.15}$$

$$\frac{\partial^2 \varphi_{Q,P}}{\partial \eta^2} = 2z\sigma(Q) \cdot \sum_{i=1}^{4} \frac{(\xi_{i+1} - \xi_i)(r_i + r_{i+1})}{r_i r_{i+1}\left[(r_i + r_{i+1})^2 - l_{i,i+1}^2\right]} \tag{4.16}$$

$$\frac{\partial^2 \varphi_{Q,P}}{\partial \zeta^2} = -2\sigma(Q) \cdot \sum_{i=1}^{4} \frac{[(\xi_{i+1} - \xi_i)(y - \eta_i) - (\eta_{i+1} - \eta_i)(x - \xi_i)](r_i + r_{i+1})}{r_i r_{i+1}\left[(r_i + r_{i+1})^2 - l_{i,i+1}^2\right]} \tag{4.17}$$

Special attention should be paid on Eq. (4.8) when the field point *P* approaches a point at the same *O'*-$\xi\eta$ plane as panel *Q*. In such case, if *P* is within the quadrilateral, $\frac{\partial \varphi_{Q,P}}{\partial \zeta} = 2\pi$; otherwise, $\frac{\partial \varphi_{Q,P}}{\partial \zeta} = 0$ (Hess and Smith, 1964). It should also be drawn to our attention that Eqs. (4.2)-(4.17) are based on the element coordinate system and a transformation matrix is required to make all the physical quantities to the reference coordinate system.

The entire boundaries are discretized into a number of quadrilateral panels as

$$S = \sum_{1}^{N_b} \Delta s_j + \sum_{1}^{N_f} \Delta s_j + \sum_{1}^{N_c} \Delta s_j \tag{4.18}$$

where N_b, N_f and N_c are the panel number on the body-, free- and control surface respectively. Let *N* denotes the total number of the panels, the potential at point $\vec{\mathbf{x}}$ (here $\vec{\mathbf{x}}$ denotes the point on the boundary of the computational domain) becomes

$$\varphi(\vec{\mathbf{x}}_i) = \sum_{j=1}^{N} \sigma_j \iint_{S_b + S_f + S_c} G(\vec{\mathbf{x}}_i, \vec{\boldsymbol{\xi}}) dS_{\xi} = \sum_{j=1}^{N} \sigma_j G_{i,j}, i = 1, 2, ..., N \tag{4.19}$$

The influence coefficients $G_{i,j}$ can be calculated with analytical formulas derived from Eq. (4.9). Similarly, the other components in the boundary integral formulations for the velocity and acceleration can be given by

$$\frac{\partial \varphi}{\partial n}(\vec{\mathbf{x}}_i) = 2\pi\sigma_i + \sum_{\substack{j=1 \\ j\neq i}}^{N} \sigma_j \iint_{S_b+S_f+S_c} \frac{\partial}{\partial n_i} G(\vec{\mathbf{x}}_i, \vec{\boldsymbol{\xi}}) dS_\xi = 2\pi\sigma_i + \sum_{\substack{j=1 \\ j\neq i}}^{N} \sigma_j G^n_{i,j}, i = 1,2,...,N \quad (4.20)$$

$$\frac{\partial \varphi}{\partial x}(\vec{\mathbf{x}}_i) = 2\pi\sigma_i + \sum_{\substack{j=1 \\ j\neq i}}^{N} \sigma_j \iint_{S_b+S_f+S_c} \frac{\partial}{\partial x_i} G(\vec{\mathbf{x}}_i, \vec{\boldsymbol{\xi}}) dS_\xi = 2\pi\sigma_i + \sum_{\substack{j=1 \\ j\neq i}}^{N} \sigma_j G^x_{i,j}, i = 1,2,...,N \quad (4.21)$$

$$\frac{\partial \varphi}{\partial z}(\vec{\mathbf{x}}_i) = 2\pi\sigma_i + \sum_{\substack{j=1 \\ j\neq i}}^{N} \sigma_j \iint_{S_b+S_f+S_c} \frac{\partial}{\partial z_i} G(\vec{\mathbf{x}}_i, \vec{\boldsymbol{\xi}}) dS_\xi = 2\pi\sigma_i + \sum_{\substack{j=1 \\ j\neq i}}^{N} \sigma_j G^z_{i,j}, i = 1,2,...,N \quad (4.22)$$

$$\frac{\partial^2 \varphi}{\partial x^2}(\vec{\mathbf{x}}_i) = \sum_{j=1}^{N} \sigma_j \iint_{S_b+S_f+S_c} \frac{\partial G(\vec{\mathbf{x}}_i, \vec{\boldsymbol{\xi}})}{\partial x_i^2} dS_\xi = \sum_{j=1}^{N} \sigma_j G^{xx}_{i,j}, i = 1,2,...,N \quad (4.23)$$

The influence coefficients $G^n_{i,j}$, $G^x_{i,j}$ and $G^z_{i,j}$ can be derived from Eqs. (4.6)-(4.8), and $G^{xx}_{i,j}$ can be derived from Eqs. (4.15)-(4.17). Substituting Eqs. (4.19)-(4.23) into the body-, free- and control-surface boundary conditions, we can obtain an equation system for the solution of source density σ as

$$\left[\mathbf{P}_{i,j}\right]\left\{\boldsymbol{\sigma}_j\right\} = \left[\mathbf{Q}_i\right], i = 1,2,...,N; j = 1,2,...,N \quad (4.24)$$

$\mathbf{P}_{i,j}$ is so-called coefficient matrix. Once $\boldsymbol{\sigma}_j$ is determined, the potential, velocity and acceleration at any points in the computational domain can be obtained accordingly from Eqs. (4.19)-(4.23). Typically, the coefficient matrix $\mathbf{P}_{i,j}$ is a full rank matrix. A standard matrix solution, such as Gaussian Elimination, can provide the source density of each panel.

4.3. Desingularied method

We find from the present study that the denominator in Eq. (4.17) is not always non-zero. From Figure 4.1 we can observed that if any angle of Q_iPQ_{i+1} (i=1, 2, 3) is $\pi/2$,

$(r_i + r_{i+1})^2 - l_{i,i+1}^2$ in Eq. (4.17) is zero. At this case, the second derivative of the potential in the free surface boundary condition would be infinite. As a consequence, the coefficient matrix in Eq. (4.24) is singular. In practice, the source distribution does not have to be located on the free surface itself, it can also be located at a short distance above the free surface, as long as the collocation points, where the boundary condition has to be satisfied, stay on the free surface. This raised-panel method has becomes very popular, especially in non-linear method. Cao et al. (1991) desingularized the boundary integral equation by moving the singular points away from the boundary and outside the problem domain and showed that the desingularization presented better solutions to several problems. As a result of desingularization, the surface integrals can be evaluated by simpler techniques, speeding up the computation. They also discussed the effects of the desingularization distance on the solution and the condition of the resulting system of algebraic equations. Computations show that a broad range of desingularization distances gives accurate solutions with significant savings in the computation time. The raised-panel method is also examined by Bunnik (1999), Kim et al. (2005) and Gao and Zou (2008) and it provides good results for different problems. The first advantage of this is the velocity field induced in the fluid domain is much smoother than with a free surface singularity method. Second, the integrals of Green functions over panels are desingularized because the collocation points are not located inside the panels, which is easier to evaluate. Third, it is easier to extend our program to a non-linear on in the future.

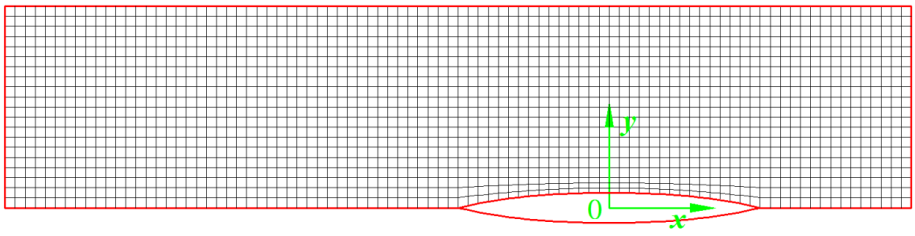

Figure 4.2: A typical vessel and its free surface mesh.

Figure 4.2 shows a typical free surface panel model. Das and Cheung (2014b) indicated that the panel number per ship length N_L should not be less than 18. In the present study, N_L is fixed at 30. We also use the raised-free surface approach with the raised distance $\Delta z_i = \gamma \cdot \sqrt{S_i}$, where S_i is the area of the *i-th* panel on the free surface

and γ is the raising coefficient. Figure 4.3 presents the definition sketch for raised-panel approach with $\gamma = 1$. We examine the convergence of the raising distance by the wave field, since the free surface wave elevation can be easily influenced by the treatment of the free surface boundary integral. Figure 4.4 compares the wave patterns at different raising coefficients. The upper half of each figure represents the wave pattern at $\gamma = 1$, while the lower half represents the wave pattern at $\gamma = 0.25$. Very good agreement has been achieved, which indicates that both of the coefficients can provide a convergence results. However, as the raising coefficient increases to 4, the solution is diverged and it cannot provide a satisfied wave pattern, as shown in Figure 4.5. This coincides with the conclusions made by Cao et al. (1991) and Bunnik (1999). It is suggested that the optimal raising distance should be at the same order of the mesh size ($\gamma = 1$), since the larger distance could cause the problem of ill-conditioned coefficient matrix. In the present study, we fix the raising coefficient at $\gamma = 1$, which can provide a stable and converged results.

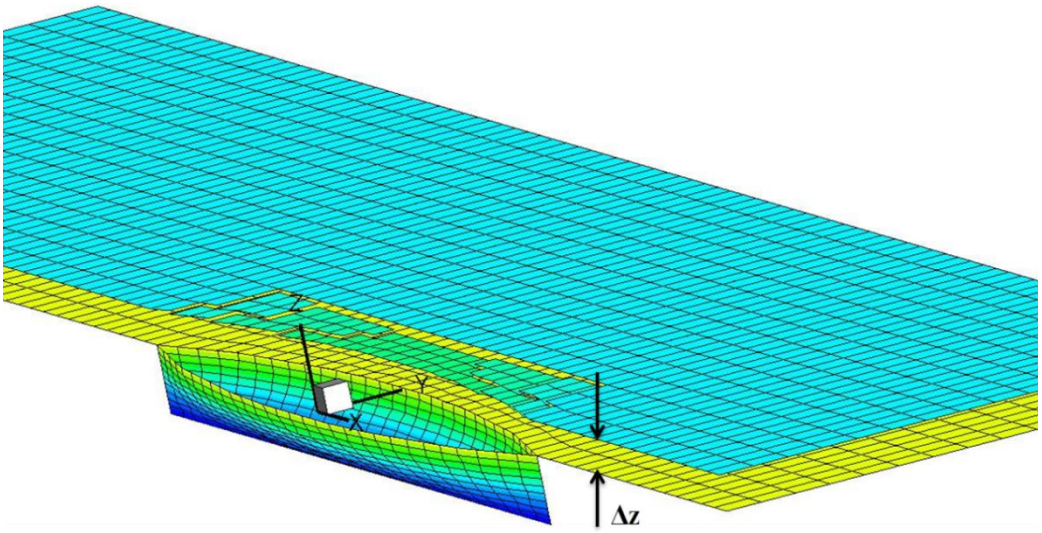

Figure 4.3: An example vessel and definition sketch for raised-panel approach.

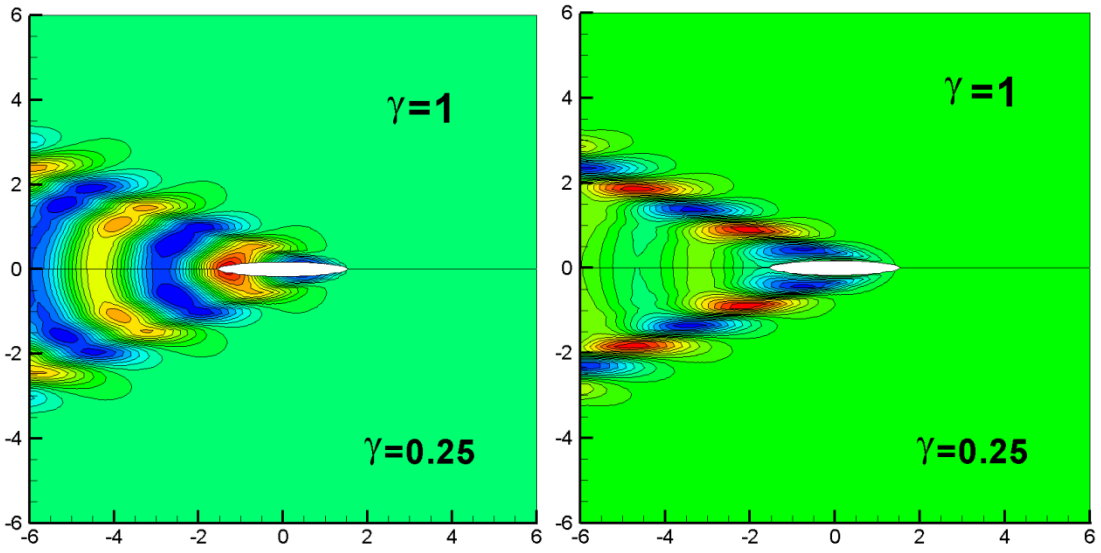

(a) (b)

Figure 4.4: Wave patterns at different raising coefficients, *Fn* = 0.3, *λ/L* = *1*. (a) Diffracted waves; (b) Radiated waves.

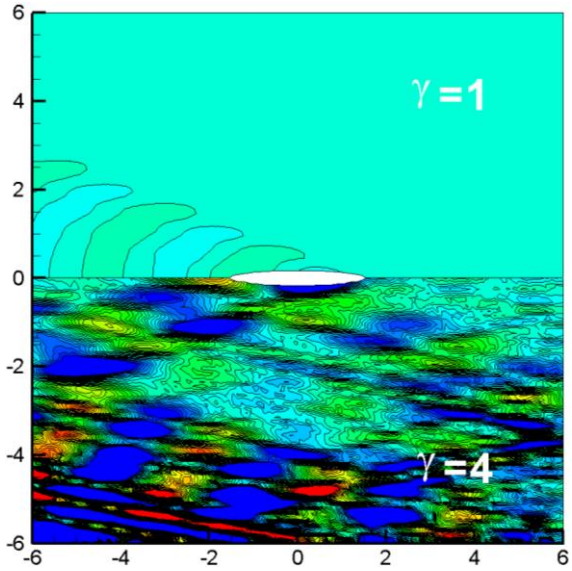

Figure 4.5: Diffracted waves at different raising coefficients, *Fn* = 0.3, *λ/L* = *1*.

4.4. Effect of difference scheme

The choice of the difference scheme is very important to obtain an accurate prediction of the wave pattern near an advancing ship. In the numerical experiments, we find even we use the accurate derivatives provided in Eqs. (4.6)-(4.17), the wave pattern solution is not stable. Even though the singularities on the free surface can be treated by the raising-panel approach, the condition number of the coefficient matrix is extremely

large, which could also bring the so-called ill-conditioning problem. As a consequence, the accuracy of solution for the source density should be challenged.

The reliability of the difference schemes can be investigated by many ways, for example, Bunnik (1999) investigated the schemes through the damping and dispersion parameters. A more effective method of examining the efficiency of the difference schemes is to calculate the wave pattern on the free surface. We find that the hydrodynamic coefficients and diffraction forces are hardly influenced by the difference scheme, but the wave elevation is very sensitive to the difference scheme of the first and second derivative on the free surface boundary condition. Therefore, we examine the stability of the difference schemes by the solution of the wave patterns.

Firstly, we need a difference schemes for the first derivatives of the potential in all of the boundary conditions. Two of the most commonly used approaches are upwind difference scheme and central difference scheme. The upwind difference scheme uses the points that are on the upstream side, while the central difference scheme uses the points on both sides where the derivative is required. The first derivative of φ to x can be written as follows

$$\frac{\partial \varphi}{\partial x}(\vec{\mathbf{x}}_i) = \frac{\varphi_{(\vec{\mathbf{x}}_i)} - \varphi_{(\vec{\mathbf{x}}_{i-1})}}{\Delta x} \quad \text{(First-order upwind scheme)} \qquad (4.25)$$

$$\frac{\partial \varphi}{\partial x}(\vec{\mathbf{x}}_i) = \frac{\varphi_{(\vec{\mathbf{x}}_{i+1})} - \varphi_{(\vec{\mathbf{x}}_{i-1})}}{2\Delta x} \quad \text{(Second-order central scheme)} \qquad (4.26)$$

A similar formula holds for the second derivative of φ to x can be written as

$$\frac{\partial^2 \varphi}{\partial x^2}(\vec{\mathbf{x}}_i) = \frac{\varphi_{(\vec{\mathbf{x}}_i)} - 2\varphi_{(\vec{\mathbf{x}}_{i-1})} + \varphi_{(\vec{\mathbf{x}}_{i-2})}}{\Delta x^2} \quad \text{(First-order upwind scheme)} \qquad (4.27)$$

$$\frac{\partial^2 \varphi}{\partial x^2}(\vec{\mathbf{x}}_i) = \frac{\varphi_{(\vec{\mathbf{x}}_{i+1})} + \varphi_{(\vec{\mathbf{x}}_i)} - 2\varphi_{(\vec{\mathbf{x}}_{i-1})}}{\Delta x^2} \quad \text{(Second-order central scheme)} \qquad (4.28)$$

Figure 4.6 shows the wave field with difference schemes. The upper half of each figure represents the wave pattern with upwind scheme, while the lower half shows the wave pattern with central scheme. These two schemes generally provide the reasonable wave field for the diffraction and radiation problem. However, the upwind scheme is observed to provide a better solution. Although the central difference schemes are

more accurate than the upwind schemes, they have the disadvantage that they often lead to instabilities. One of the explanation for the spikes in the lower half of each figure can be found by Bunnik (1999). At the high frequency range, the discrete dispersion relation has no longer a root near the solution of the continuous dispersion relation, but only so-called spurious root, which has a large real part (short wave) and a positive imaginary part. These short waves will amplify rapidly and cause numerical instabilities. Upwind difference schemes, however, are well known for their stabilizing properties. The physical explanation is that the new information on the wave pattern mainly comes from the upstream side, especially at high speeds, whereas the downstream side only contains old information.

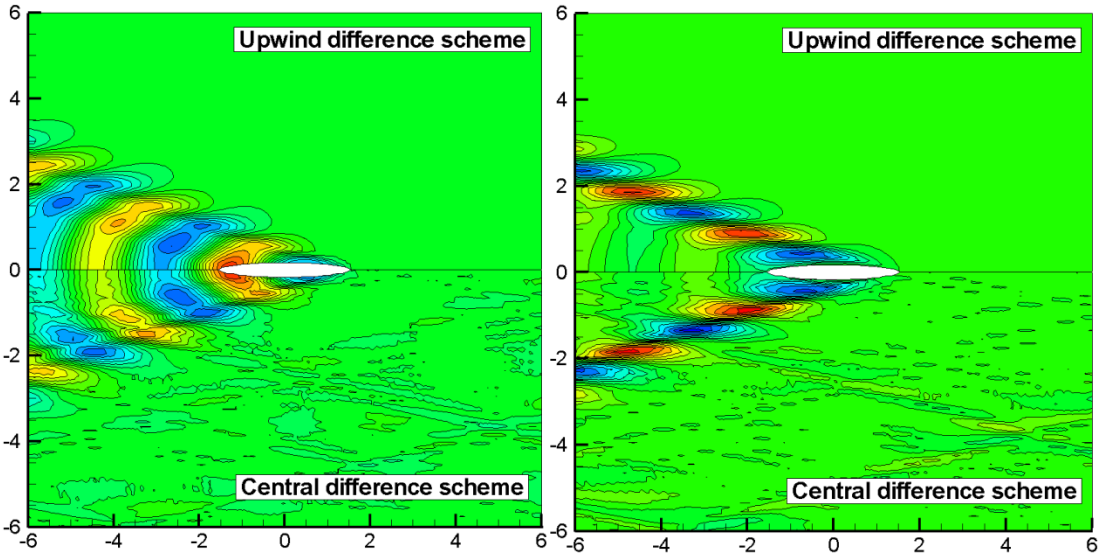

(a) **(b)**

Figure 4.6: Wave patterns with upwind and central difference schemes, Fn = 0.3, λ/L = 1. (a) Diffracted waves; (b) Radiated waves.

We also compare the upwind difference scheme to the accurate scheme provided in Eqs. (4.6)-(4.17). It can be observed clearly from Figure 4.7 that the upwind scheme provides a better wave pattern. For the accurate scheme, except the diffracted and radiated wave modes, some spurious wave modes can also be observed, which could interfere with the physical waves and eventually destroy the credibility of the solution completely. This is a purely numerical phenomenon that firstly discussed by Longuet-Higgins and Cokelet (1976). They found that the saw-tooth like waves were superimposed on the physical waves such that the waves were zigzag alike if no preventive measure is taken. The general consensus on the cause of the problem is that

there is high concentration of fluid particles with high speed in certain regions especially near the wave crests, as shown in the lower half of each figure in Figure 4.7. The same phenomenon was also encountered by Xu and Yue (1995) in their 3-D solution.

A typical treatment to remove the saw-tooth instability is by introducing a low-pass numerical filter (Huang, 1997; Longuet-Higgins and Cokelet, 1976; Xu and Yue, 1995). Although it can provide a smooth wave pattern, it is believed that this numerical filter can bring some influence to the real wave elevation. Through the comparison from Figure 4.7, we find the difference scheme on the free surface boundary condition is the main reason for the spurious wave modes. Even without numerical filtering, the upstream difference scheme can obtain a smooth wave pattern. It is found that when the accurate scheme provided in Eqs. (4.6)-(4.17) is used, the condition number of the coefficient matrix in Eq. (4.24) is extremely large and the coefficient matrix tends to be an ill-conditioned matrix. The diagonal elements $\mathbf{P}_{i,j}\,(i = j)$ is very large due to the factor that the field point is within the source panel. When the upwind difference scheme is used, the diagonal elements of the coefficient matrix can be restrained and as a result, the condition number decreases and the solution tends to be stable, which can be observed in the upper half of each figure in Figure 4.7.

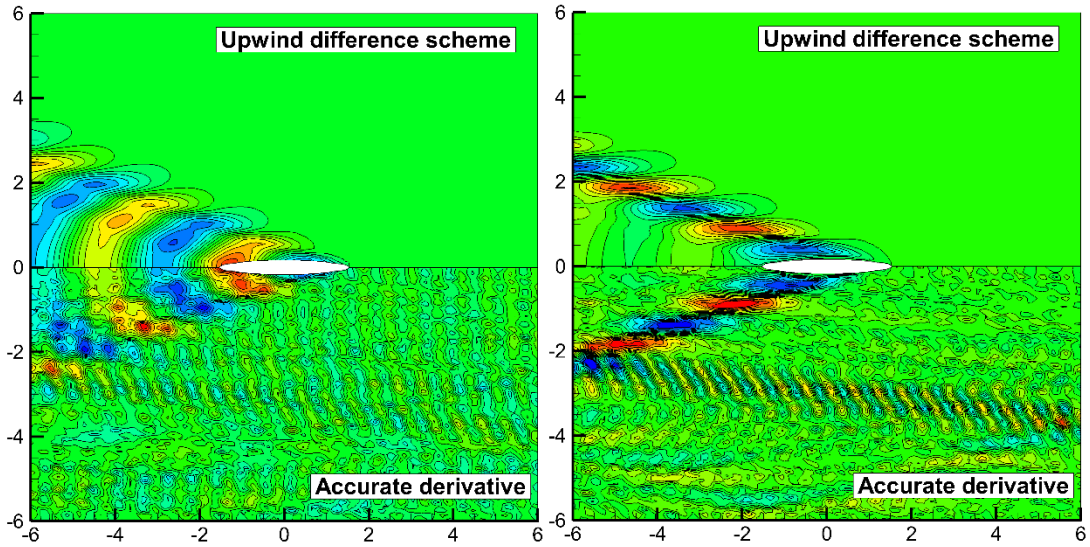

Figure 4.7: Wave patterns with upwind and accurate difference schemes, *Fn* = 0.3, *λ/L* = *1.* (a) Diffracted waves; (b) Radiated waves.

4.5. Summary

In this chapter, we introduced a numerical solution for the boundary value problem. The Rankine source method can provide a satisfied solution for the present problem of two ships travelling or stationary in the shallow waters. It gives a flexible choice of free-surface and sea bottom condition, which can take the forward speed and shallow water directly into the boundary value problem. We also introduced a desingularization method by raising the free surface at some distance above the undisturbed water line. A wide range of raising coefficients was investigated and the optimal value had been suggested. Besides, the difference schemes were discussed. Through the comparisons, it was found that the upwind difference scheme can provide a stable solution for the wave elevation and thus, it will be included in our numerical program to investigate the seakeeping problems of single or multi-ships advancing or stationary in waves.

5. Implementation of radiation condition

5.1. Introduction

In order to complete the boundary value problem by Rankine source method, a radiation condition should be imposed on the control surface. A common used treatment was proposed by Nakos (1990). The free surface was truncated at some upstream points, and a quiescent boundary condition was imposed at these points to ensure the consistency of the upstream truncation of the free surface. Another method to deal with the radiation condition is to move the source points on the free surface at some distance downstream (Jensen et al., 1986). The results from these two methods show very good agreement with published experimental data when the Brard number τ ($\tau = u\omega/g$) is greater than 0.25, since they are both based on the assumption that there is no scattered wave travelling ahead of the vessel. However, when the forward speed of the vessel is very low, the Brard number will be smaller than 0.25 and the scattered waves could travel ahead of the vessel. These traditional radiation conditions could no longer be valid at this case. For ship-to-ship problem, the forward speed is usually limited to a low level for the safe operation. Therefore, a new extensive radiation condition is required to deal with the very low forward speed problem. Das and Cheung (2012a, b) provided an alternate solution to the boundary-value problem for forward speeds above and below the group velocity of the scattered waves. They corrected the Sommerfeld radiation condition by taking into account the Doppler shift of the scattered waves at the control surface that truncates the infinite fluid domain. They compared their results with the experimental data, and good agreement was achieved. They also computed the wave elevation on the free surface, and a reasonable wave pattern was obtained at $\tau < 0.25$ by using their new radiation condition. In this chapter, we will extend Das and Cheung's radiation condition to the ship-to-ship interaction with forward speed problem.

5.2. Formulation of radiation condition

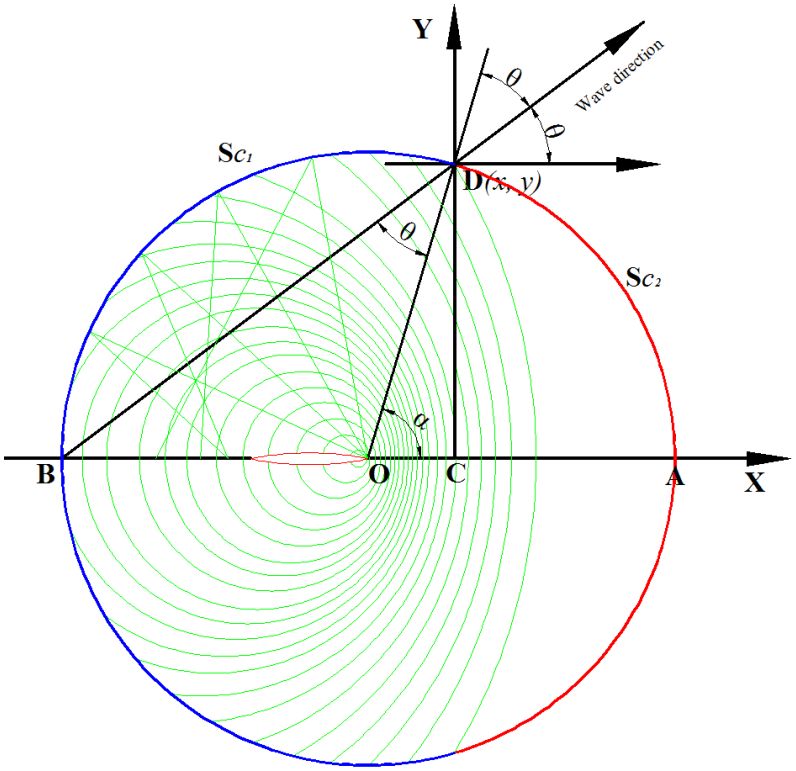

Figure 5.1: Sketch of Doppler shift and radiation condition of single ship.

Figure 5.1 shows the Doppler Shift of the scattered wave field by a vessel travelling with constant forward speed u_0 in the positive x direction. When a vessel is moving from point *B* to point *O*, the traveling time should be $t = BO/u_0$. During this period of time, the vessel produces scattered waves all along *BO* (the first scattered wave should arise at point *B*). The control surface here is defined as a circle with its centroid on point *O* and its radius as *BO*. The velocity of the scattered wave is defined as *c*, $BO/u_0 = BD/c$. According to the sine theorem, it can be easily transferred to

$$\frac{u_0}{c} = \frac{\sin\theta}{\sin\alpha} \tag{5.1}$$

The scattered wave velocity at *D* can be expressed as

$$c^2 = \frac{g}{k_s}\tanh k_s d \tag{5.2}$$

where ω_s is the angular frequency of the scattered waves from a fixed reference point given as

$$\omega_s = \omega_e + u_0 k_s \cos(\alpha - \theta) \tag{5.3}$$

$$\omega_s^2 = g k_s \tanh k_s d \tag{5.4}$$

in which k_s is the local wave number at any point on the free or control surface, and d is the water depth.

Combining Eqs. (5.1)-(5.3), we can obtain the following governing equation

$$\begin{aligned} &\cos^2\left[\alpha - \sin^{-1}\left(\sqrt{\kappa}\sin\alpha / \sqrt{\tanh\left(\kappa / F_h^2\right)}\right)\right]\kappa^2 \\ &+\left\{2\tau\cos\left[\alpha - \sin^{-1}\left(\sqrt{\kappa}\sin\alpha / \sqrt{\tanh\left(\kappa / F_h^2\right)}\right)\right] - \tanh\left(\kappa / F_h^2\right)\right\}\kappa + \tau^2 = 0 \end{aligned} \tag{5.5}$$

At infinite water depth, $d \to \infty$, Eq. (5.5) can be reduced to

$$\cos^2\left[\alpha - \sin^{-1}\left(\sqrt{\kappa}\sin\alpha\right)\right]\kappa^2 + \left\{2\tau\cos\left[\alpha - \sin^{-1}\left(\sqrt{\kappa}\sin\alpha\right)\right] - 1\right\}\kappa + \tau^2 = 0 \tag{5.6}$$

where $\lambda_s = 2\pi / k_s$ is the local wave length, $\gamma = \lambda_s g / u_0^2$ is the dimensionless local wave length, $F_h = u_0 / \sqrt{gd}$ is the depth Froude number, $\kappa = 2\pi / \gamma$ is the dimensionless local wave number, and parameter $\tau = u_0 \omega_e / g$.

Let's discuss the dimensionless local wave length on x-axis. At $\alpha \to 0$ or π, $\sin^{-1}\left(\kappa \sin\alpha\right) = 0$ Eq. (5.6) becomes

$$\cos^2(\alpha)\kappa^2 + \left[2\tau\cos(\alpha) - 1\right]\kappa + \tau^2 = 0 \tag{5.7}$$

The solutions for Eq. (5.7) can be written as

$$\kappa = \frac{1 - 2\tau\cos\alpha \pm \sqrt{1 - 4\tau\cos\alpha}}{2\cos^2\alpha} \tag{5.8}$$

At $\alpha = 0$ and $\tau < 0.25$, two solutions can be obtained from Eq.(5.8)

$$\gamma_1 = \frac{4\pi}{1 - 2\tau - \sqrt{1 - 4\tau}} \tag{5.9}$$

$$\gamma_2 = \frac{4\pi}{1 - 2\tau + \sqrt{1 - 4\tau}} \tag{5.10}$$

At $\alpha = \pi$, another group of two solutions can be obtained from Eq.(5.8)

$$\gamma_3 = \frac{4\pi}{1+2\tau-\sqrt{1+4\tau}} \tag{5.11}$$

$$\gamma_4 = \frac{4\pi}{1+2\tau+\sqrt{1+4\tau}} \tag{5.12}$$

These four solutions are shown in Figure 5.2, which are identical to Becker's (1958) results. It has been found by using the Green function method that at $\tau < 0.25$, there are three wave systems: one ring wave system and two Kelvin fan wave systems with different wedge angle (Becker, 1958; Miao et al., 1995). At $\tau > 0.25$, there are only two wave systems, one of which is the wave system formed by the outer fan waves. From Figure 5.2, we find that at $\tau < 0.25$, there are four wave lengths in x-axis: γ_1 and γ_3 corresponds to the ring wave system, γ_2 and γ_4 corresponds to the inner and outer Kelvin fan wave systems respectively. It can also be found that at $\tau > 0.25$, there are only two wave lengths in x-axis: γ_3 corresponds to the ring wave system and γ_4 corresponds to outer Kelvin fan wave system. We notice that the wave length of the ring wave system is much larger than that of Kelvin fan wave systems. In the numerical study, the free surface is usually truncated at $2L$ - $3L$ upstream and downstream. This truncation length is in the same order as the length of the ring wave system. But for the Kelvin fan wave systems, this truncation length is much larger, and it can be regarded as infinity. In Rankine source method, if the truncation length is very large ($R\rightarrow\infty$), the radiation condition is not necessary. Therefore, in the present study, there is no radiation condition imposed to Kelvin fan wave systems. The radiation condition proposed in this paper is only applicable to solve the radiation and diffraction problem of the ring wave system. Therefore, the parameter k_s only refers to the local wave number of the ring wave system.

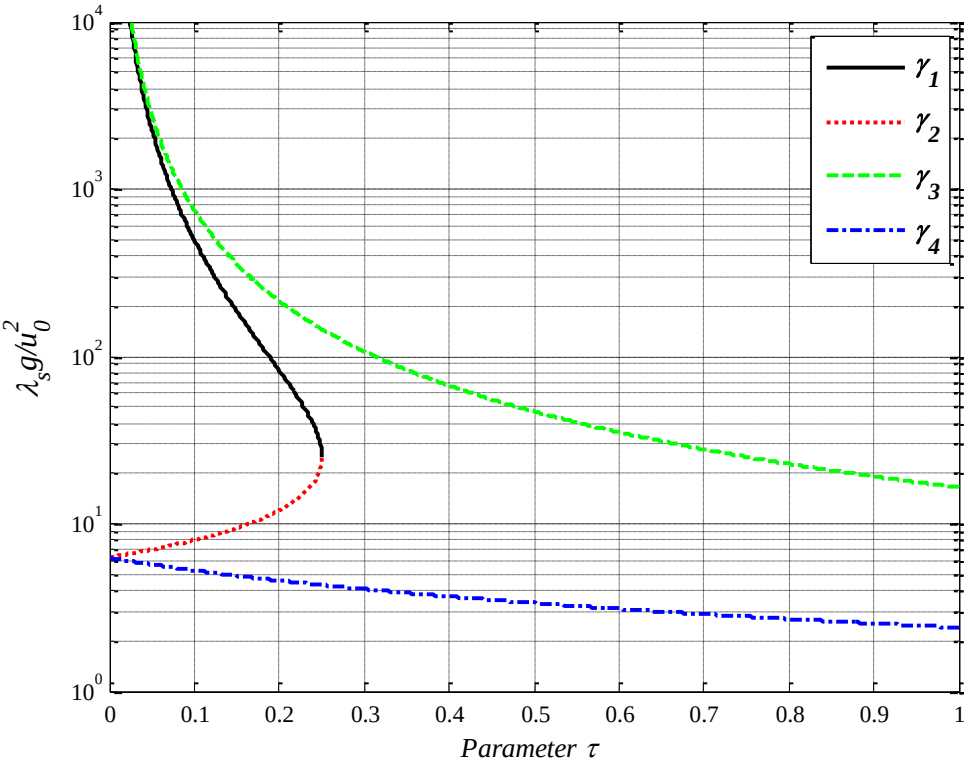

Figure 5.2: The dimensionless local wave length on *x*-axis

Let's define a point *D(x, y)*, which is used to divide the control surface into two parts, S_{C1} and S_{C2}. If we cannot find the solutions for Eq. (5.5), these points must be on the control surface S_{c2}. Otherwise, they are on S_{C1}. The critical θ at point *D* can be derived analytically. The scattered wave reaching point *D* is produced by the vessel at point *B*. Notice that $\alpha = 2\theta$, Eq. (5.1) can be written as

$$\frac{u_0}{c} = \frac{1}{2\cos\theta} \tag{5.13}$$

Substituting Eqs. (5.2) and (5.13) into Eq. (5.3), we can obtain the following equation at infinite water depth

$$\frac{u_0\omega_e}{g} = \frac{1}{4\cos\theta} \tag{5.14}$$

Notice that the Brard number is defined as $\tau = \frac{u_0\omega_e}{g}$, Eq. (5.14) becomes

$$\cos\theta = \frac{1}{4\tau} \tag{5.15}$$

From Eq. (5.15), we find that

I. $\tau < 0.25$, no solution can be found for the critical θ since the scattered waves can reach any points on the whole control surface. At this case, the scattered wave produced at point *B* should reach somewhere ahead of point *A*. Correspondingly, the wave group will travel ahead of the vessel.

II. $\tau = 0.25$, the critical rotated angle θ = 0. At this case, the scattered wave produced at point *B* is propagating to point *A*. Correspondingly, the wave group is reaching point *O*.

III. $\tau > 0.25$, the critical θ can be found at point *D*. At this case, the control surface could divide into arc *DB* (S_{C1}) and arc *DA* (S_{C2}).

In the numerical calculation, the coordinates of any arbitrary point on the control surface are given, and then the unknowns θ and k_s could be obtained by solving Eq. (5.5). The double Doppler shift radiation condition is defined as two different equations on S_{c1} and S_{c2} independently,

$$\frac{\partial \varphi_j}{\partial n} - ik_s \varphi_j \cos\theta = 0 \quad \text{(j = 1, 2, ... , 7) on } S_{C1} \tag{5.16}$$

$$\nabla \varphi_j = 0 \quad \text{(j = 1, 2, ... , 7) on } S_{C2} \tag{5.17}$$

Eq. (5.16) is an updated Sommerfeld radiation condition with forward speed correction. If the forward speed is zero, $k_s = k$, θ = 0 and Eq. (5.16) could reduce to the Sommerfeld radiation condition as

$$\frac{\partial \varphi_j}{\partial n} - ik\varphi_j = 0 \quad \text{(j = 1, 2, ... , 6) on } S_C \tag{5.18}$$

5.3. Validation of single vessel

Figure 5.3 and Figure 5.5 show a Wigley hull traveling with different Froude number in the positive *x* direction and the free surface is truncated by a rectangle and circular control surface respectively. The control surface is dispersed into a number of panels (20 panels in the present model). Figure 5.4 and Figure 5.6 are the results of the local

wave number k_s on different control surfaces and different Froude numbers. k_s = 0 illustrates that no solution is found at these panels and these panels are on S_{C2}. It can be found from Figure 5.4 that as the Froude number increases, the range of S_{C1} shrinks. At Fn = 0, θ = 0 and k_s = k, which is a constant independent of the location. At Fn = 0.1, the scattered wave at B can only reach No.1-12 panels, and for No.13-20 panels, no solutions can be found there. When the Froude number increases to Fn = 0.3, only No.1-5 panels on the downstream side can be influenced by the scattered waves. Figure 5.6 transmits the same information as Figure 5.4, which indicates that the truncation of free surface could be arbitrary and k_s and θ are only determined by the coordinates of the points on the control surface.

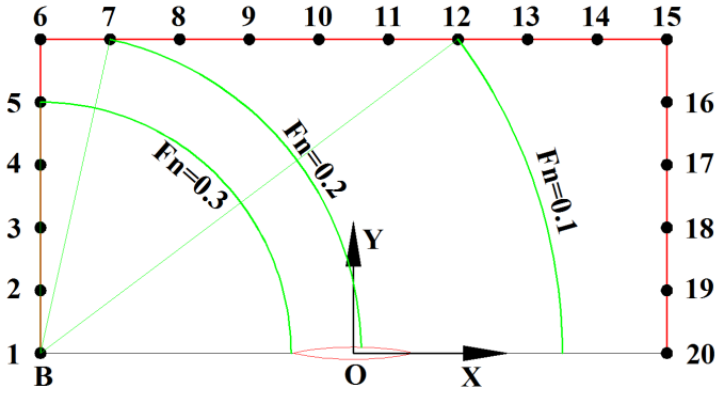

Figure 5.3: Rectangle control surface for single ship.

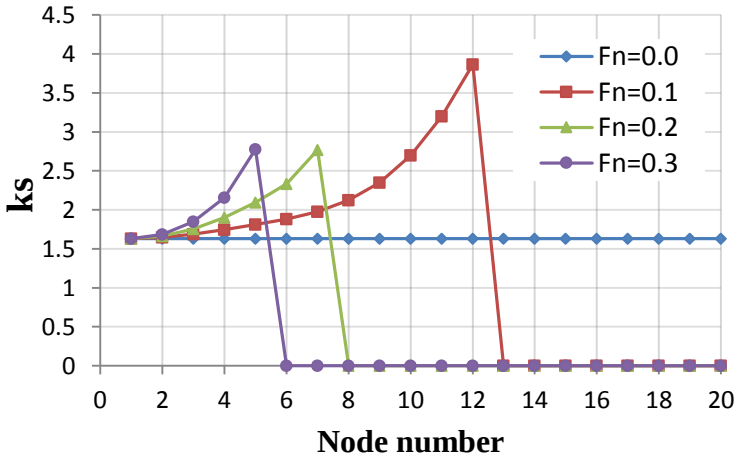

Figure 5.4: Local wave number on rectangle control surface.

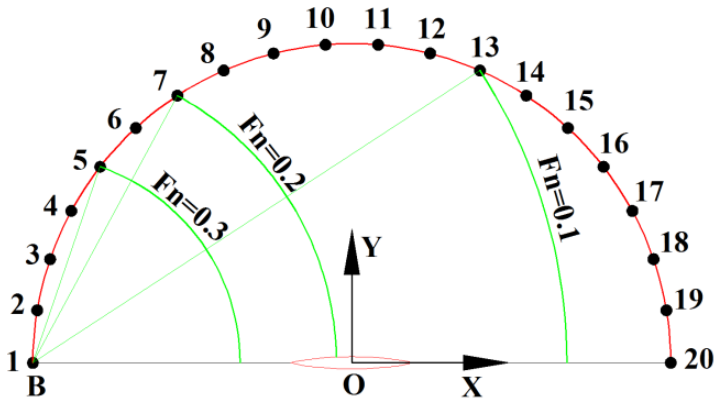

Figure 5.5: Circular control surface for single ship

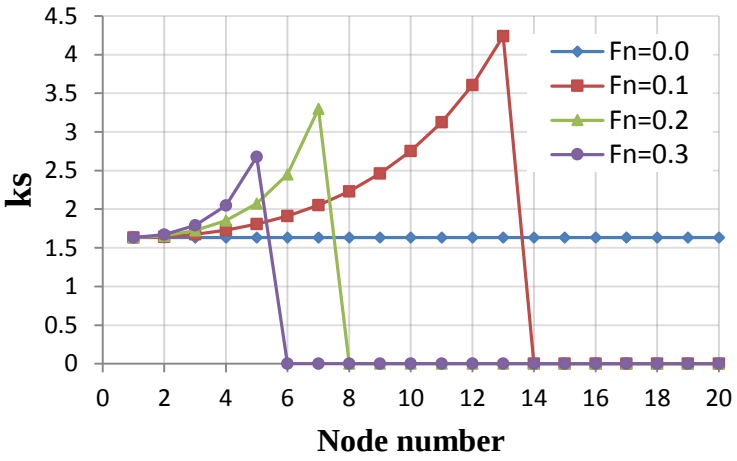

Figure 5.6: Local wave number on circular control surface.

5.4. Validation of two vessels

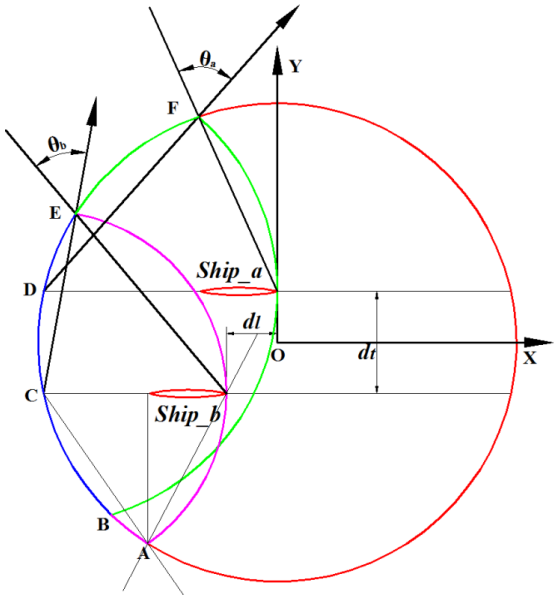

Figure 5.7: Sketch of Doppler shift and radiation condition of two ships advancing in waves.

The radiation condition in Eq. (5.16) and Eq. (5.17) can also be applicable to ship-to-ship problem, as shown in Figure 5.7. It is assumed that two ships are advancing in waves with the same forward speed. The transverse and longitudinal distances between two ships are *dt* and *dl* respectively. The inertia coordinate system is shown in Figure 5.7 with its origin located on the central line between two ships. Figure 5.8 is a numerical case of two oscillating sources advancing in the positive *x* direction. The free surface is truncated by a circular. To simplify the problem, only 40 nodes are distributed on the control surface (20 nodes on the upper half circle and 20 nodes on the lower half circle). Figure 5.9 and Figure 5.10 are the calculated local wave number and rotated angle respectively at $\tau = 0.2$. The solutions of k_s and θ can be found at any nodes on the control surface, which illustrates that the scattered waves could reach any points on the truncated surface. Due to the Doppler Effect, the scattered waves upstream have shorter wavelengths. As a result, the local wave number upstream is greater than that downstream, which is shown in Figure 5.9. But the maximum values of rotated angle appear around $y = 0$, and it decreases upstream and downstream gradually. It is very interesting to find that on the upper half circle, the rotated angle θ_a is close to zero at Node 1 and Node 19 while on the lower half circle, θ_b turns to be zero at Node 1 and Node 19. This is because these two nodes are almost on the trajectory of source ***a*** and source ***b,*** which can be shown in Figure 5.8. At these points, the scattered wave direction is parallel to *x* axis and it will not be rotated at all. Since the origin of the control surface is located on the central line between two sources, the symmetry cannot be achieved about the trajectory of source ***a*** and source ***b***. Therefore, the results on upper and lower half circle are different. The results of source ***a*** and source ***b*** are also not identical to each other.

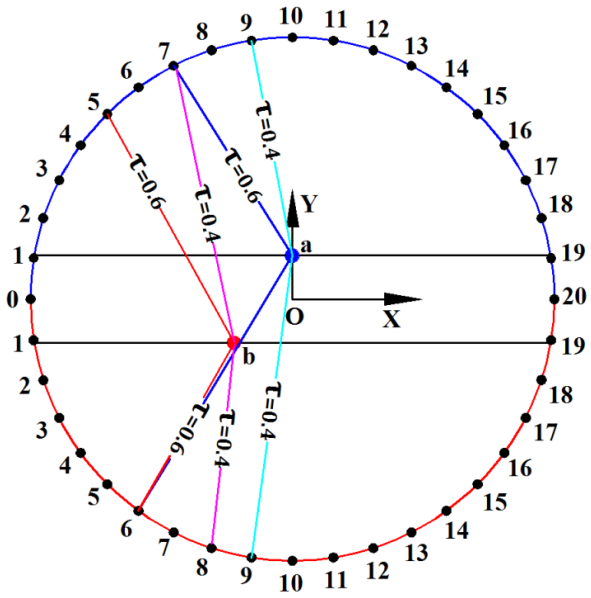

Figure 5.8: Doppler shift of two oscillating sources with forward speed.

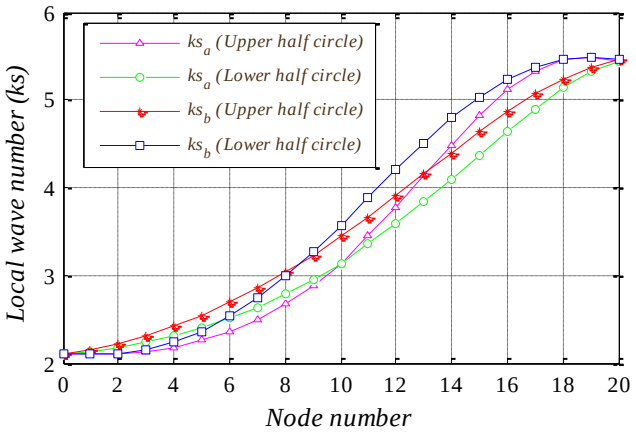

Figure 5.9: Local wave number at τ = 0.2.

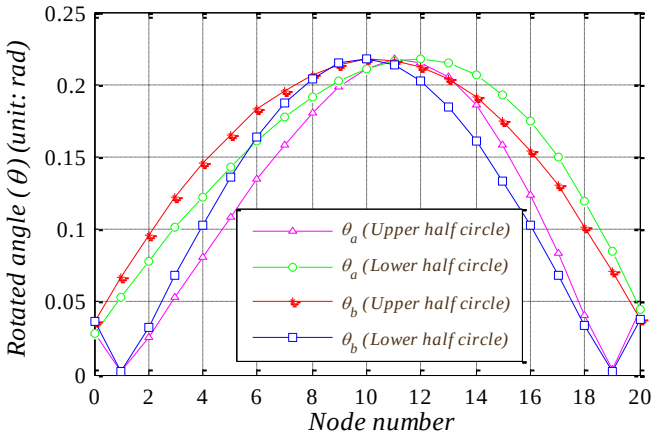

Figure 5.10: Rotated angle at τ = 0.2.

Figure 5.11 and Figure 5.12 are the calculated local wave number and rotated angle respectively at τ = 0.6. In numerical calculation, if there is no solution for Eq. (5.5), the k_s and θ are labelled as 0. With regard to source ***a***, the scattered waves can only propagate to Node 7 on the upper half circle, while Node 6 is the furthest point on the lower half circle. Ahead of these two nodes, there is no scatter wave and k_s and θ are labelled as 0. Since source ***b*** is located at some distance afterward, its scattered waves can only reach Node 5 on the upper half circle while Node 6 is the furthest point on the lower half circle. We also calculate k_s and θ at τ = 0.4. The critical nodes are shown inFigure 5.8. It can be concluded that the quiescent region expands with increasing Brard number as the scattered waves are convected behind the sources. It can also be easily demonstrated that the truncation of free surface could be arbitrary (circular, rectangular or ellipse) and k_s and θ are only determined by the coordinates of the points on the control surface.

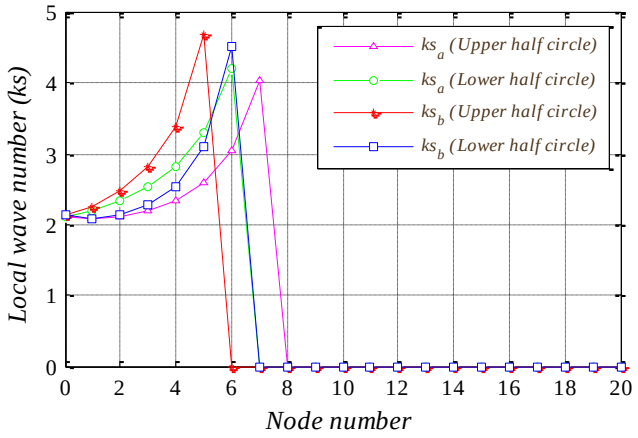

Figure 5.11: Local wave number at τ = 0.6.

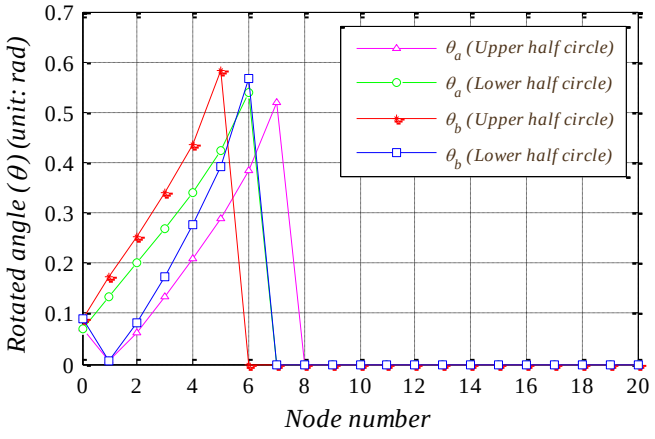

Figure 5.12: Rotated angle at τ = 0.6.

5.5. Summary

In this chapter, we introduced a new modified Sommerfeld radiation condition which takes into account the Doppler shift of the scattered waves. This new radiation condition is applicative to a wide range of forward speeds, including very low forward speed problem where the Brard number is smaller than 0.25. We examined this new radiation condition through a two models: a single ship model and two ships model. The results indicated that the present radiation condition can give a reasonable explanation of the physical scattered waves.

6. Validations and discussion of single ship travelling or stationary in waves

6.1. Introduction

Before we get down to the multi-body problem, the program for single vessel should be validated firstly. Compare to ship-to-ship problem, the coordinate system and boundary conditions of single ship is different. Figure 6.1 shows a vessel travelling with a constant forward speed in a Cartesian coordinate system which is moving together with the body. The origin is located on the still water and axis *Z* points upward. *X* and *Y* axis is on the geometric centroid of the water-plane.

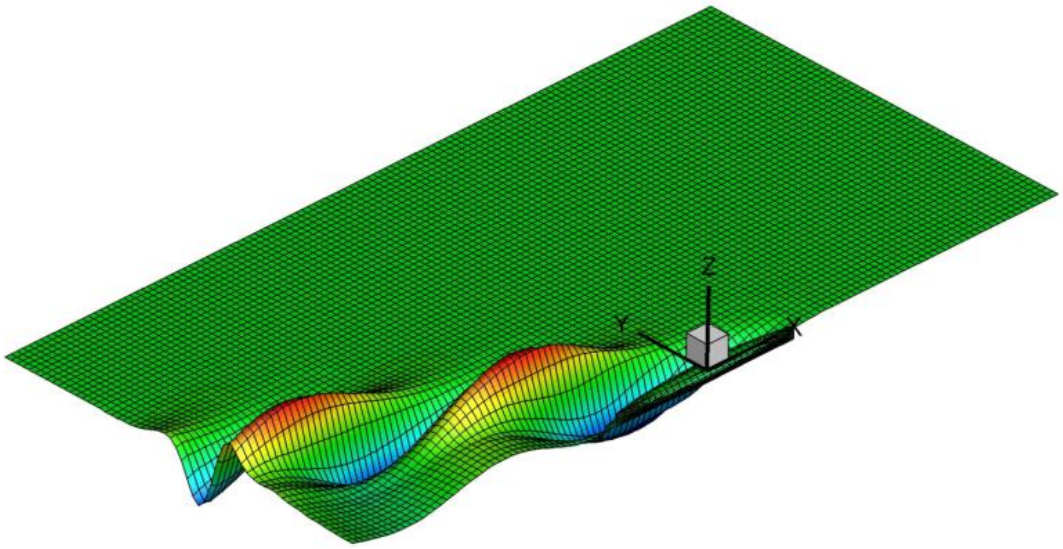

Figure 6.1: An example vessel and coordinate system.

The total potential can be decomposed into

$$\Psi(\vec{\mathbf{x}},t) = -u_0 x + \varphi_s(\vec{\mathbf{x}}) + \mathrm{Re}\sum_{j=0}^{7}\eta_j\varphi_j(\vec{\mathbf{x}})e^{-i\omega_e t}, \quad j = 0,1,\ldots,7 \tag{6.1}$$

The boundary value problem of the steady wave is the same as defined in Eq. (3.5)-(3.8), while the diffraction and radiation boundary condition is different and can be given by

$$\nabla^2 \varphi_j = 0 \qquad \text{in the fluid domain} \tag{6.2}$$

$$-\omega_e^2 \varphi_j - 2i\omega_e u_0 \frac{\partial \varphi_j}{\partial x} + u_0^2 \frac{\partial^2 \varphi_j}{\partial x^2} + g \frac{\partial \varphi_j}{\partial z} = 0 \quad \text{on the undisturbed free surface } S_f \tag{6.3}$$

$$\frac{\partial \varphi_j}{\partial z} = 0 \qquad \text{on the sea bottom} \tag{6.4}$$

$$\frac{\partial \varphi_j}{\partial n} = \begin{cases} -i\omega_e n_j + m_j, \; j = 1,2,...,6 \\ -\dfrac{\partial \varphi_0}{\partial n}, \; j = 7 \end{cases} \quad \text{on the mean wetted part of the body surface } S_b \tag{6.5}$$

The same numerical method illustrated in Chapter 4 and Chapter 5 can provide a solution for the boundary value problem of single ship.

6.2. Single Wigley hull stationary in waves

6.2.1. Description of the model

In realistic conditions, a ship cannot be considered as a point source and different parts of its hull usually produce several wave systems. Generally, only stern waves have magnitude comparable with that of bow waves. The diverging bow and stern waves may travel independently if the ship is long enough (Tarmo, 2007). The longer waves and the shift of the origin downstream of the vessel require the replacement of the control surface further away to satisfy the point source assumption. However, Das and Cheung (2012b) carried out the convergence study and found that the present model apparently handled those phenomena well with constant panels and provided accurate results with a domain of reasonable dimensions and solution commonly used in ship and offshore platform design. In the present numerical study, a Wigley III hull advancing or stationary in head sea is modelled by using the present method. Journee's (1992) experimental results are quoted to verify the efficiency of the present model. The model can be defined as

$$y = \frac{B}{2}\left[1-\left(\frac{z}{T}\right)^s\right]\left[1-\left(\frac{2x}{L}\right)^2\right]\left[1+0.2\left(\frac{2x}{L}\right)^2\right] \tag{6.6}$$

where B is the breadth, L is the length and T is the draft of the ship. The main dimensions of Wigley III model are shown in Table 6.1.

Table 6.1: Main dimensions of Wigley III hull

Length, L *(m)*	3
Breadth, B *(m)*	0.3
Draught, T *(m)*	0.1875
Displacement, V *(m^3)*	0.078
Centre of rotation above base, *KR (m)*	0.1875
Centre of gravity above base, *KG (m)*	0.17
Radius of inertia for pitch, k_{yy} *(m)*	0.75

The computational range on the free surface is extended to 2L upstream, 2L downstream and 2L sideways, where L = 3 m is the length of the vessel. Since the flow around a symmetric body is symmetric about x-z plane, only half computational domain is modelled. There are 300 panels on the body surface, 7200 on free surface and 1200 on the control surface, which is shown in Figure 6.2. But the free surface is extended to 1L upstream, 3L downstream and 1L sideways in the steady wave problem in order to simulate the full Kelvin wave.

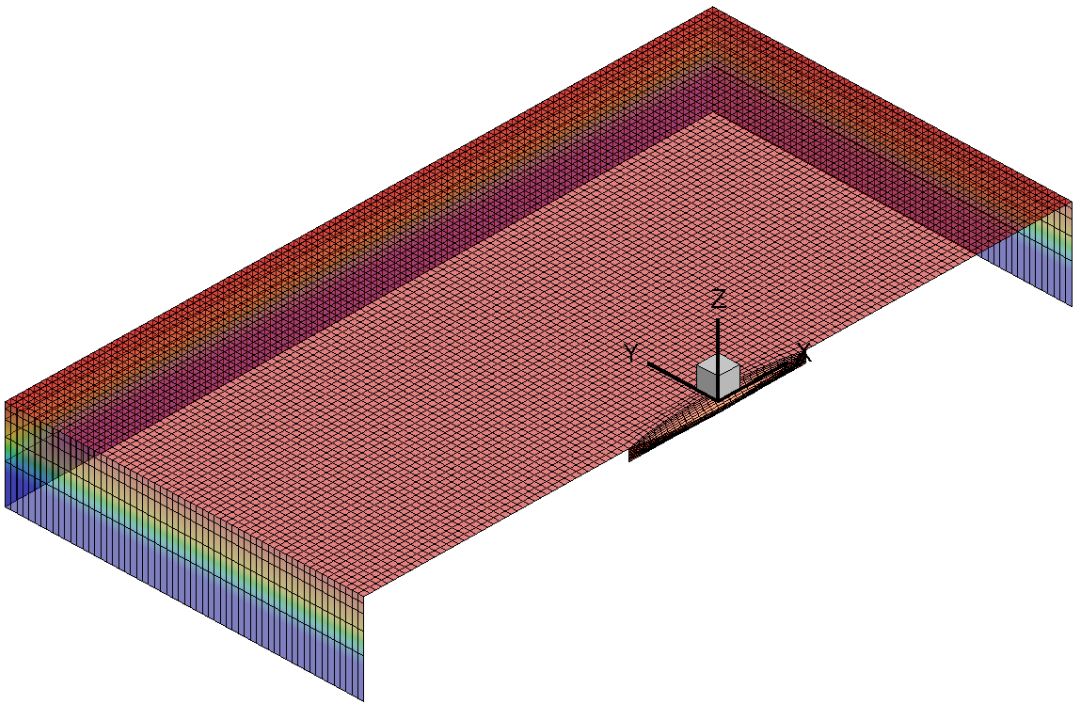

Figure 6.2: Computational domain and panel distribution of single Wigley hull.

6.2.2. Results and discussion

Figure 6.3 and Figure 6.4 show the comparison of the hydrodynamic coefficient between the present and Wadam (2010) results. Good agreement is achieved between the present method and Wadam solution. For the present 3-D Rankine source method, 8700 panels are distributed on the body-, free- and control-surface, while only 2000 panels on the body surface are required for the Wadam program which is based on the frame work of 3-D Green function. Therefore, more CPU time is consumed by the present program on modelling as well as solving a very large full rank matrix. It can be concluded that both Rankine source method and Green function method can provide a stable solution for the ship-to-ship with zero speed problem. The advantage of the present method should lie on the two ships travelling with forward speed in the restricted waters, which will be discussed in the next chapter. Besides, it can be observed from Figure 6.4 (b) that there is an unrealistic spike arising at high frequency area. This is so-called irregular frequency problem introduced by Green function method. However, the irregular frequency problem can be avoided by using the present 3-D Rankine source method.

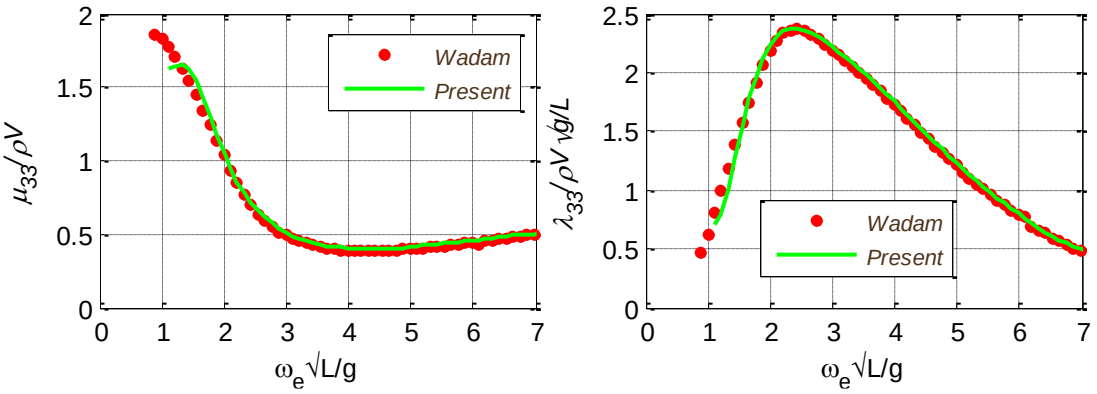

(a) **(b)**

Figure 6.3: Heave hydrodynamic coefficients. (a) Added mass; (b) Damping.

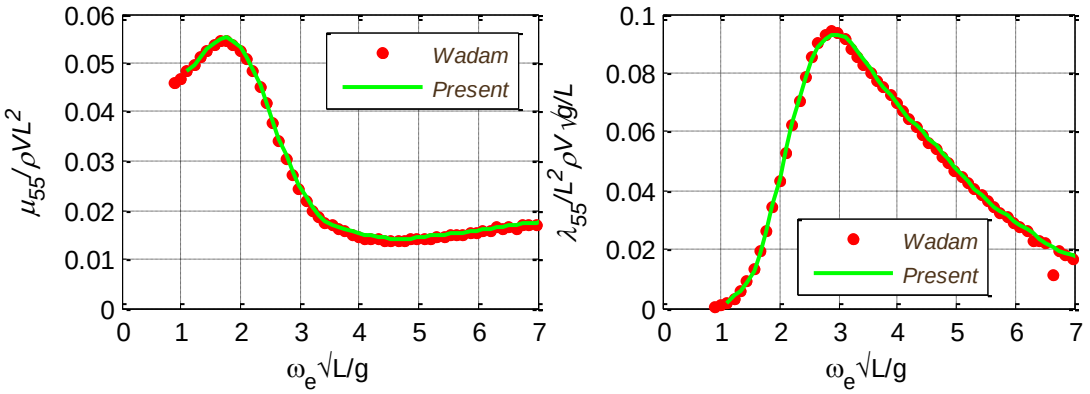

(a) **(b)**

Figure 6.4: Pitch hydrodynamic coefficients. (a) Added mass; (b) Damping.

Figure 6.5 and Figure 6.6 show the comparison of the hydrodynamic coefficients between the present results and Wadam solution. Very satisfied agreement has been obtained, which indicates that the present 3-D Rankine source panel program can predict the hydrodynamic properties of single ship stationary in the waves.

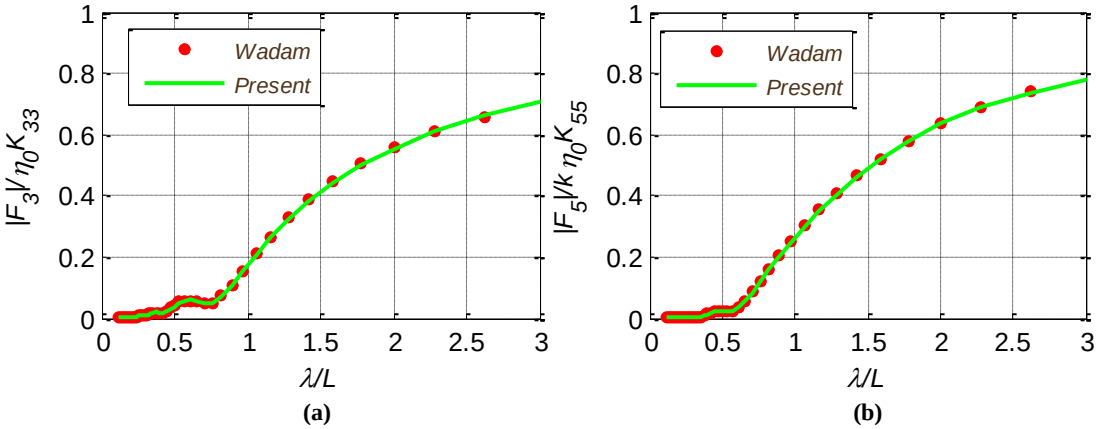

(a) **(b)**

Figure 6.5: Wave excitation forces. (a) Heave; (b) Pitch.

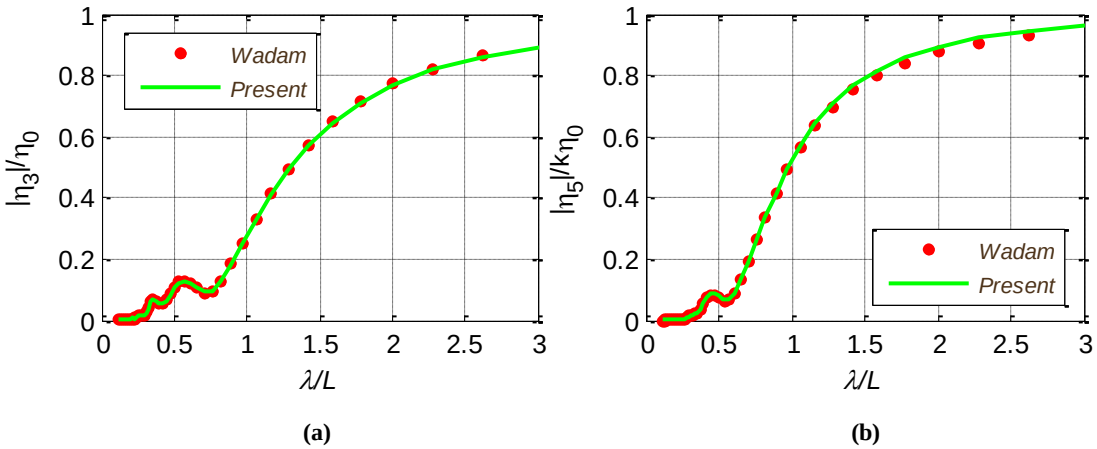

(a) **(b)**

Figure 6.6: Response amplitude operators. (a) Heave; (b) Pitch.

6.3. Single Wigley hull advancing in waves

The same Wigley III model in Section 6.2.1 will be used to investigate the hydrodynamic properties of single ship travelling in waves.

6.3.1. Steady wave problem

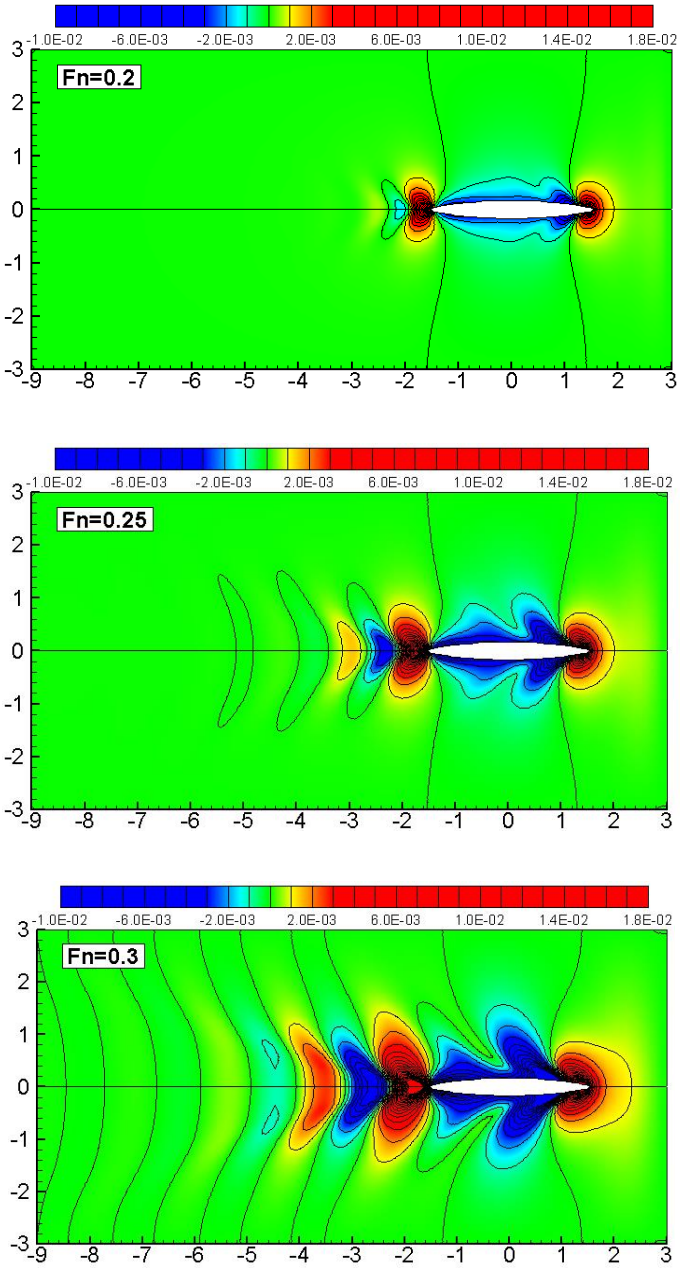

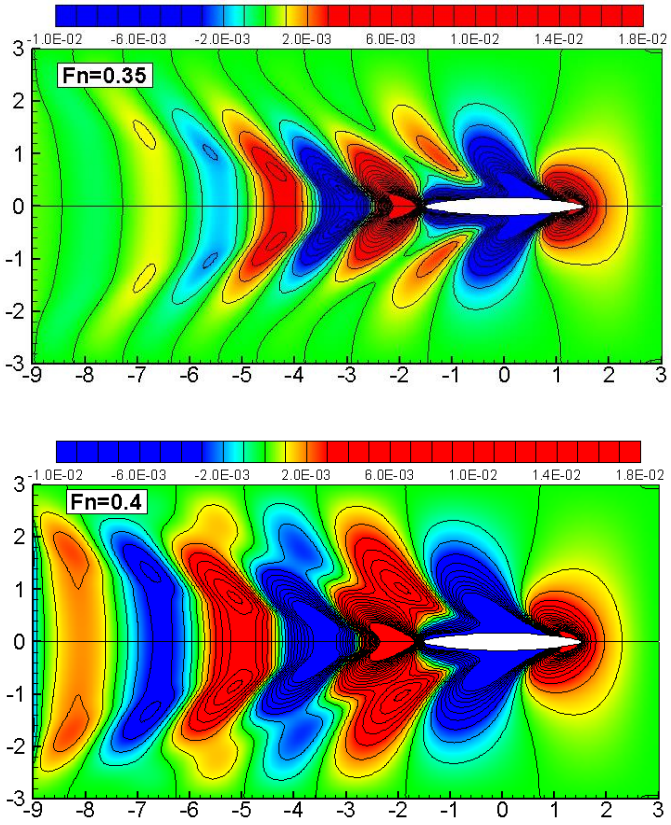

Figure 6.7: Steady wave patterns at various forward speeds.

Figure 6.7 shows the comparison of the wave pattern around the Wigley hull at different Froude number ($F_n = u_0 / \sqrt{gL}$) ranging from 0.2 to 0.4. As can be seen in these figures, the steady wave elevation attenuates rapidly behind the ship. The diverging waves are radiating from the bow together with the transverse waves following behind the stern. The Kelvin angle increases as the forward speed of the ship increases. If the Froude number is smaller than 0.2, the steady wave elevation is very small, which means the energy dissipation is relatively small at low forward speed. This can also be observed from the wave making resistance in Figure 6.8. The wave making resistance can be defined as

$$C_w = \frac{F_1^s}{\frac{1}{2}\rho u_0^2 S} \tag{6.7}$$

where S is the area of the wetted body surface and F_1^s is the steady hydrodynamic forces, which can be obtained by the pressure integrals on the wet body surface as follows:

$$F_i^S = \iint_{S_b} p_s n_i dS\,, \quad i = 1, 2, ..., 6 \tag{6.8}$$

$$p_s = \rho\left(u_0 \frac{\partial \varphi_s}{\partial x} - \frac{1}{2}\nabla\varphi_s \cdot \nabla\varphi_s \right) \tag{6.9}$$

Compared with the ITTC experimental results (SRI: Ship Research Institute, Tokyo; TOKYO: University of Tokyo), the present results based on the steady flow is satisfactory. The result from Xiang and Faltinsen (2011) is also included in the comparison, which is based on the unified flow model. It can be found that in the very low forward speed region, the wave making resistance is negligible. For the ship-to-ship problem, the forward speed is usually limited to a low level for the safe operation. Therefore, we will ignore the coupled behavior between the steady waves and unsteady waves in the following chapters.

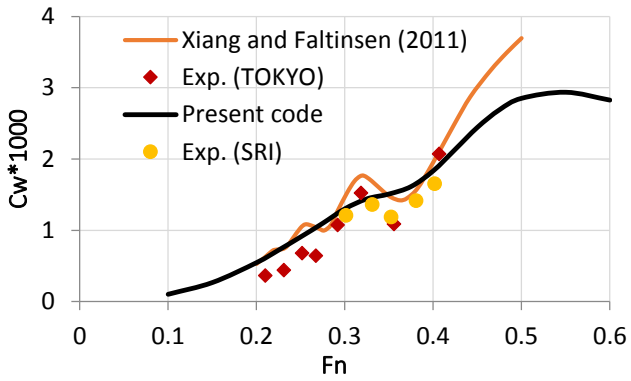

Figure 6.8: Wave making resistance of the Wigley hull.

6.3.2. Radiation problem

Figure 6.12 shows the radiated waves of single ship with different forward speeds in head seas. It can be found that the present method can provide a satisfied wave pattern, even when the Brard number is smaller than the critical value 0.25. From Figure 6.12 (a), we find there are some scattered waves travelling ahead of the vessel. And in this case, the traditional upstream radiation condition is invalid since it cannot satisfy the assumption that there is no wave propagating ahead of the vessel. A V-shape region is clearly convected downstream as the Brard number increases. No reflections can be found on the boundary, which indicates physically that the present radiation condition can ensure that the waves propagate away from the ship.

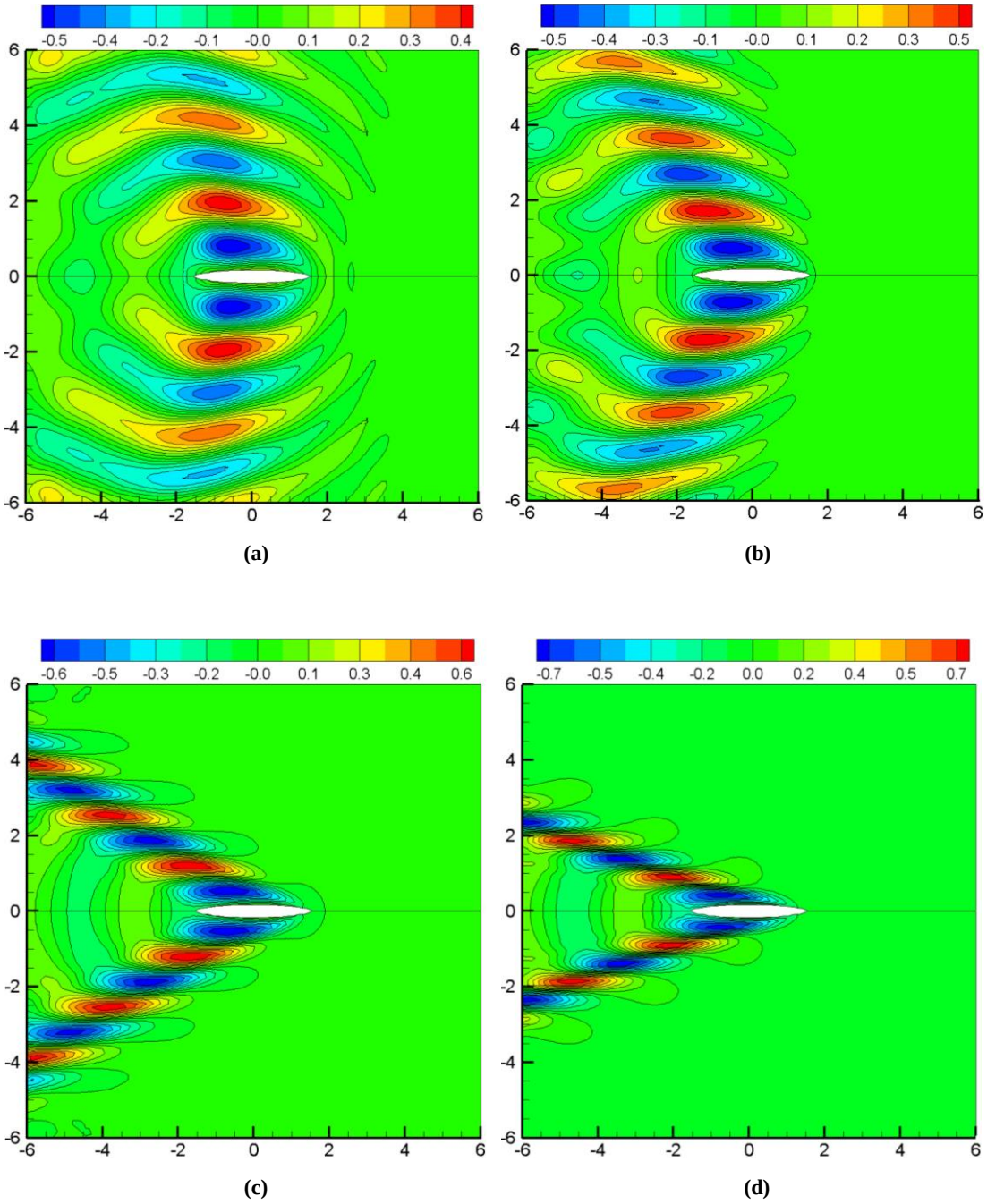

Figure 6.9: Radiation wave pattern for unit heave motion at λ/L = 1. (a) *Fn* = 0.07, τ = 0.2; (b) *Fn* = 0.1, τ = 0.31; (c) *Fn* = 0.2, τ = 0.75; (d) *Fn* = 0.3, τ = 1.32.

Figure 6.10 and Figure 6.11 are the comparison of hydrodynamic coefficients between present calculations and experimental results. Overall, the agreement is quite good in added mass and damping coefficients of heave and pitch motion. Discrepancy arises near $\tau = 0.25$ ($\omega_e\sqrt{L/g} = 1.26$). This phenomenon has also been observed by Kim and Shin (2007) by using Green function method. The main reason for the difference lies on the steady wave m_j terms given by Eq. (3.34). In the present code, the free-stream

assumption of Eq. (3.35) is used and the coupling effects between the steady and unsteady flows have been neglected. However, this *m*-term appeared in the body boundary condition will bring some influences to the radiation problem, which is reflected in the hydrodynamic coefficients. In order to get better hydrodynamic coefficients, the double-body or steady-wave flow should be taken as the basic flow. Experimental data for very low forward speed is unfortunately not available.

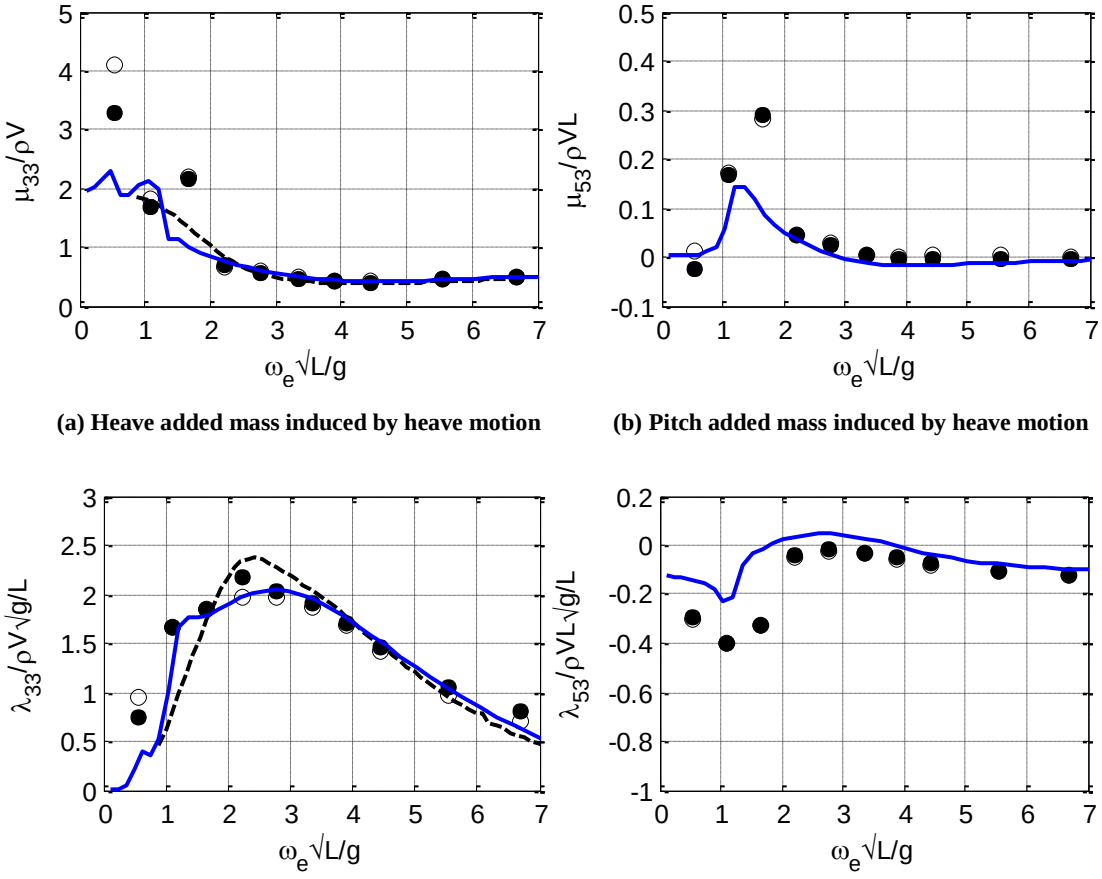

(a) Heave added mass induced by heave motion

(b) Pitch added mass induced by heave motion

(c) Heave damping induced by heave motion

(d) Pitch damping induced by heave motion

Figure 6.10: Hydrodynamic coefficients of heave motion at Fn = 0.2. (- -, Fn = 0; −, Present calculation; ○, Experiment, η_3 = 2.5cm; •, Experiment, η_3 = 5cm).

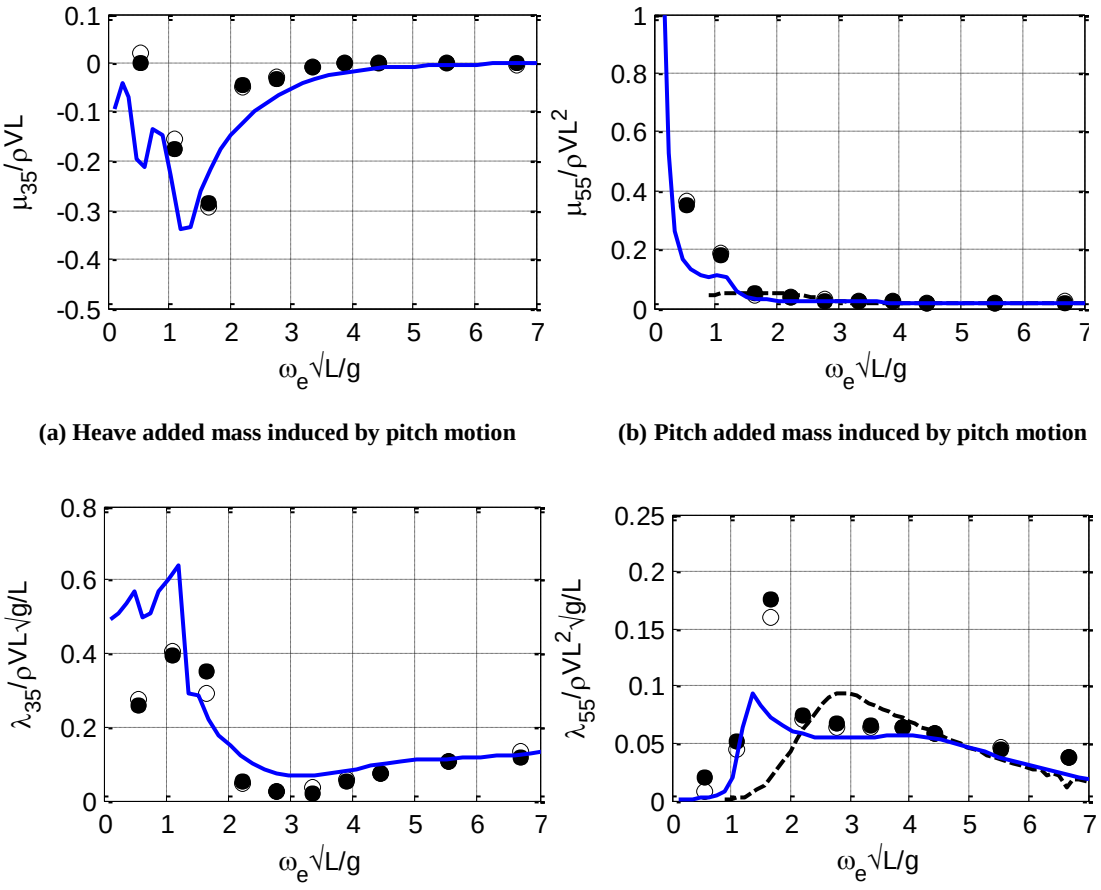

(a) Heave added mass induced by pitch motion

(b) Pitch added mass induced by pitch motion

(c) Heave damping induced by pitch motion

(d) Pitch damping induced by pitch motion

Figure 6.11: Hydrodynamic coefficients of pitch motion at *Fn* = 0.2. (- -, Fn = 0; −, Present calculation; ○, Experiment, η_5 = 1.5°; •, Experiment, η_5 = 3°).

6.3.3. Diffraction problem

Figure 6.12 shows the diffracted waves induced by unit heave motion of a single ship with different forward speeds in head seas. It can be found that the present method can provide a satisfied diffracted wave pattern, even when the Brard number is smaller than the critical value 0.25. From Figure 6.12 (a), we find there are some scattered waves travelling ahead of the vessel. And in this case, the traditional upstream radiation condition is invalid since it cannot satisfy the assumption that there is no wave propagating ahead of the vessel. A V-shape region is clearly convected downstream as the Brard number increases. No reflections can be found on the boundary, which indicates physically that the present radiation condition can ensure that the waves propagate away from the ship.

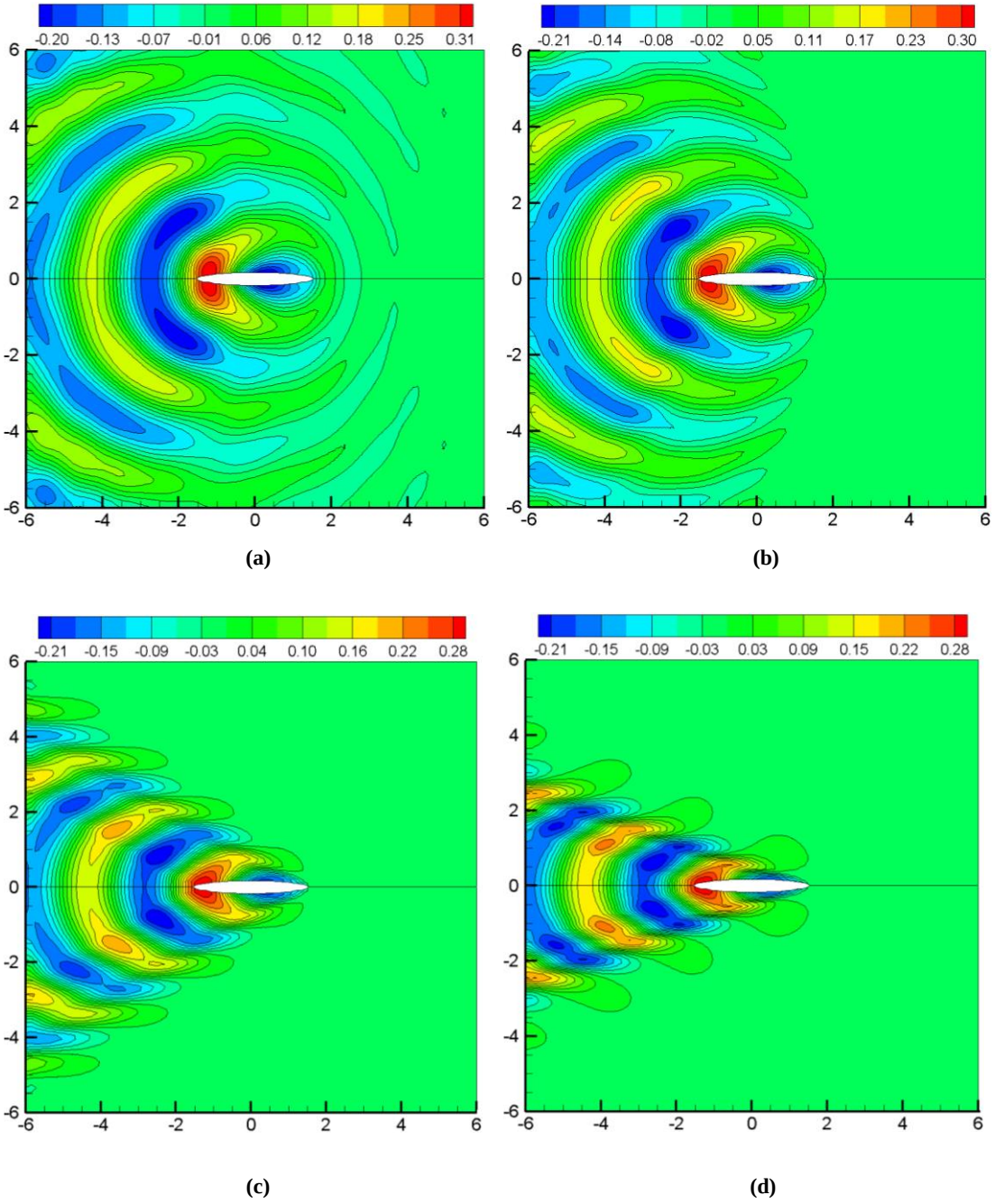

Figure 6.12: Diffraction wave pattern at λ/L = 1. (a) *Fn* = 0.07, τ = 0.2; (b) *Fn* = 0.1, τ = 0.31; (c) *Fn* = 0.2, τ = 0.75; (d) *Fn* = 0.3, τ = 1.32.

Good agreement of wave exciting forces between the present calculation and experimental results can be observed in Figure 6.13 and Figure 6.14. The forward speed effect on the wave exciting forces is not significant. And it is different to the radiation problem that the diffraction potential does not strongly depend on the steady flow solution since m_j terms appear only in the body boundary condition for the radiation problem.

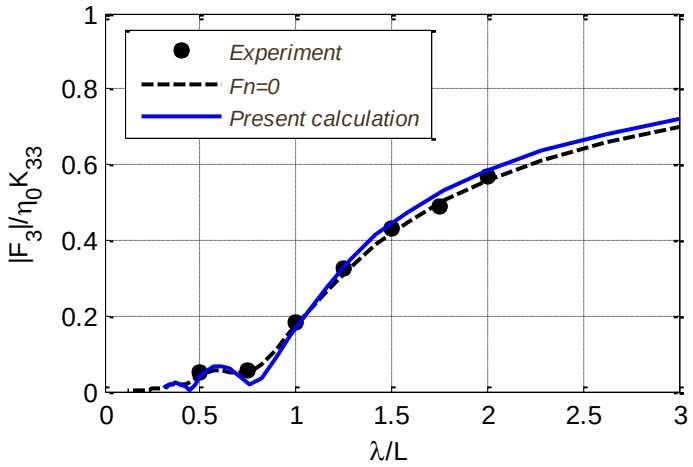

Figure 6.13: Wave excitation force in heave at *Fn* = 0.2.

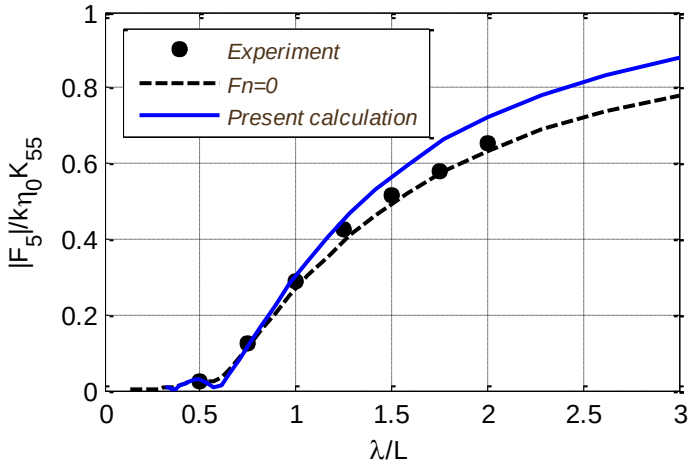

Figure 6.14: Wave excitation moment in pitch at *Fn* = 0.2.

6.3.4. Motion responses

It can be seen from Figure 6.15 and Figure 6.16 that the heave and pitch RAO calculated by the present method agrees well with the model test results of Journee (1992). Peak values in the heave and pitch RAOs can be observed at λ/L = 1 and 1.2 corresponding to resonance of the Wigley hull in the respective motions. But at zero forward speed, there is no peak and the RAO curve differs considerably from the forward speed curve. It requires special attention in the design and operation of marine vessels with forward speed.

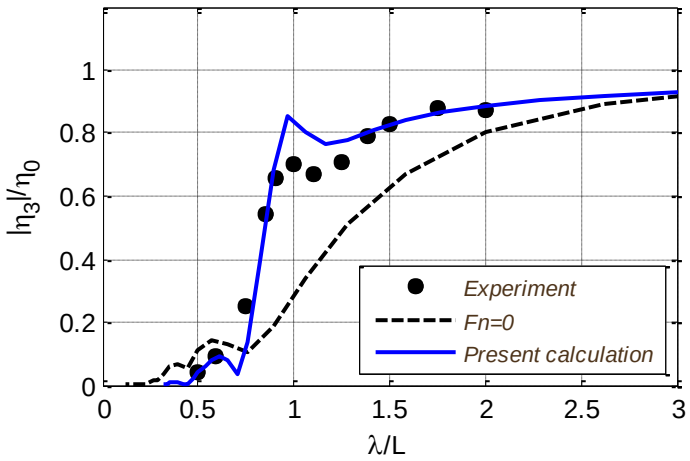

Figure 6.15: Heave response amplitude operators at *Fn* = 0.2.

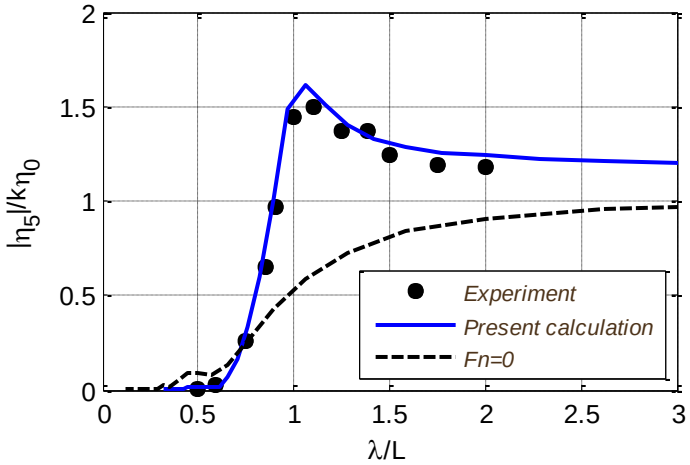

Figure 6.16: Pitch response amplitude operators at *Fn* = 0.2.

6.3.5. Effect of radiation condition

(1) Sommerfeld radiation condition

Figure 6.17 is the diffraction wave pattern with different radiation conditions, while the radiation wave patterns induced by unit heave motion are presented in Figure 6.18. The wave length to ship length ratio of $\lambda/L = 1$ in head sea corresponds to the critical conditions in ship design. In order to investigate how the new double Doppler shift radiation condition changes the wave field in very low forward speed, we make the comparison between the present model and Sommerfeld radiation condition over a wide range of Brard number from 0 to 0.26. The lower half of each sub-figure of Figure 6.17 and Figure 6.18 shows the wave pattern obtained from Sommerfeld radiation condition, while the radiation condition in the upper half account for the new double

Doppler shift radiation condition defined by Eqs. (5.16)-(5.17). At zero forward speed, the wave elevation calculated from present radiation condition is exactly the same as that from Sommerfeld radiation condition. The waves propagate as a circle pattern beyond one wavelength from the center with the main radiation energy on either side of the vessel. From Figure 6.18 (b) we can find that even at very low forward speed, the Doppler shift becomes evident and it modifies the wave length. The wave length downstream is larger than the upstream wave length. It can also be found that if the new radiation condition associated with Doppler shift correction is used, the waves appear smooth and stable. While for the Sommerfeld radiation condition, there are some distortions and reflections from the control surface. As the Brard number increases to 0.25, or just a little greater than 0.25, the forward speed of the vessel is equal to or greater than the wave group velocity. There should be no waves propagating ahead of the vessel. This phenomenon could be illustrated well from Figure 6.17 (c)-(d) and Figure 6.18 (c)-(d). And also, the wave pattern is smooth and stable by using the new model.

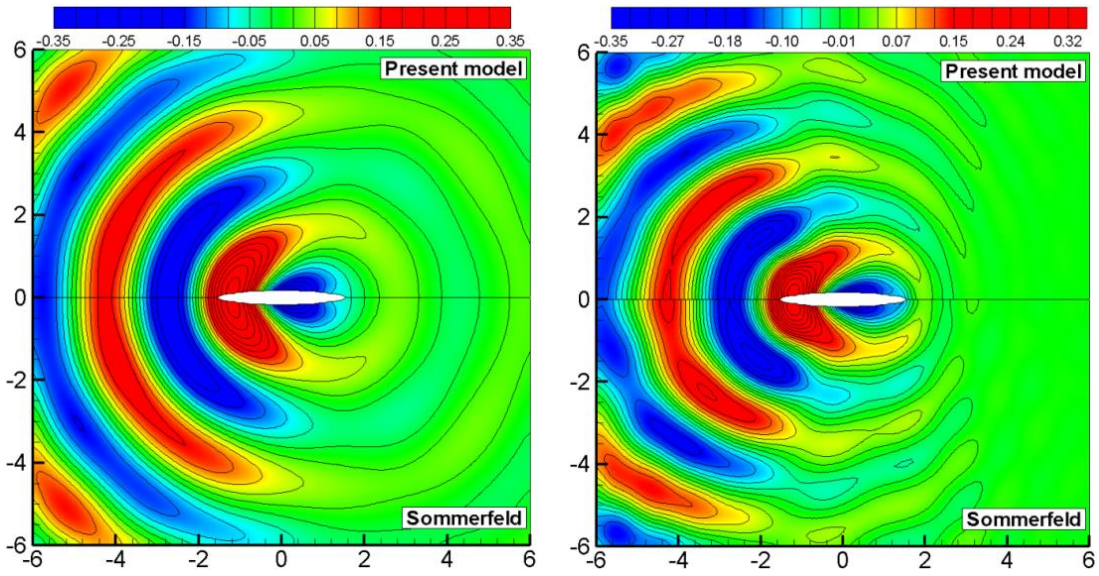

(a) **(b)**

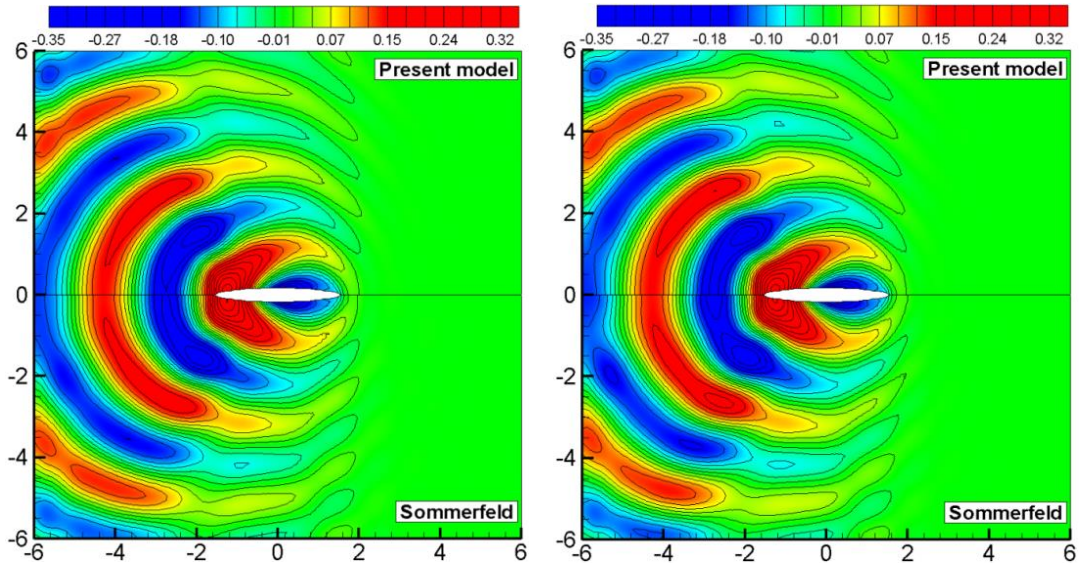

(c) **(d)**

Figure 6.17: Diffraction wave patterns by using Sommerfeld and present radiation conditions at λ/L = 1. (a) Fn = 0, τ = 0; (b) Fn = 0.068, τ = 0.2; (c) Fn = 0.083, τ = 0.25; (d) Fn = 0.09, τ = 0.26.

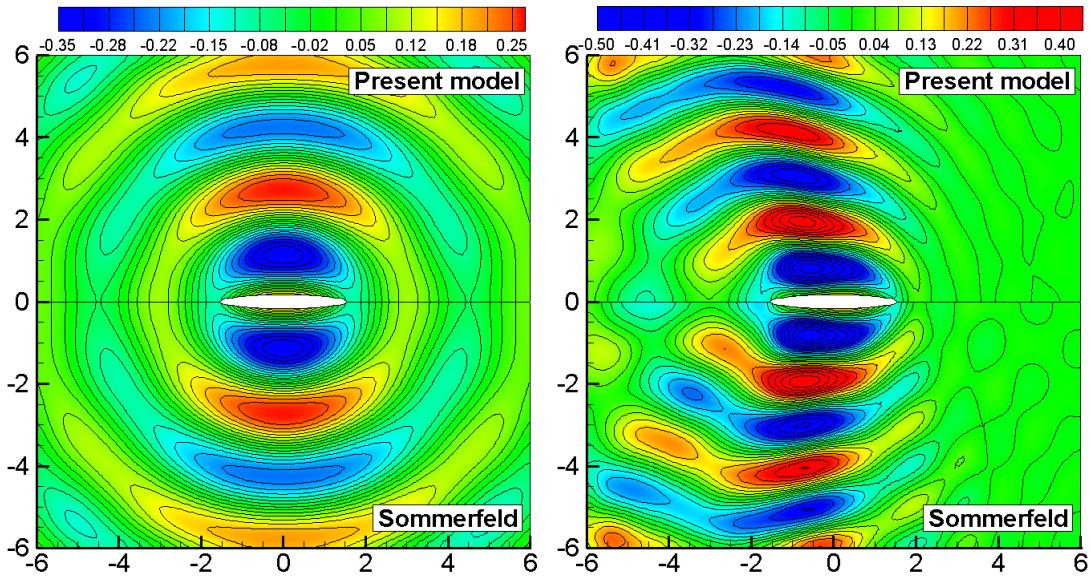

(a) **(b)**

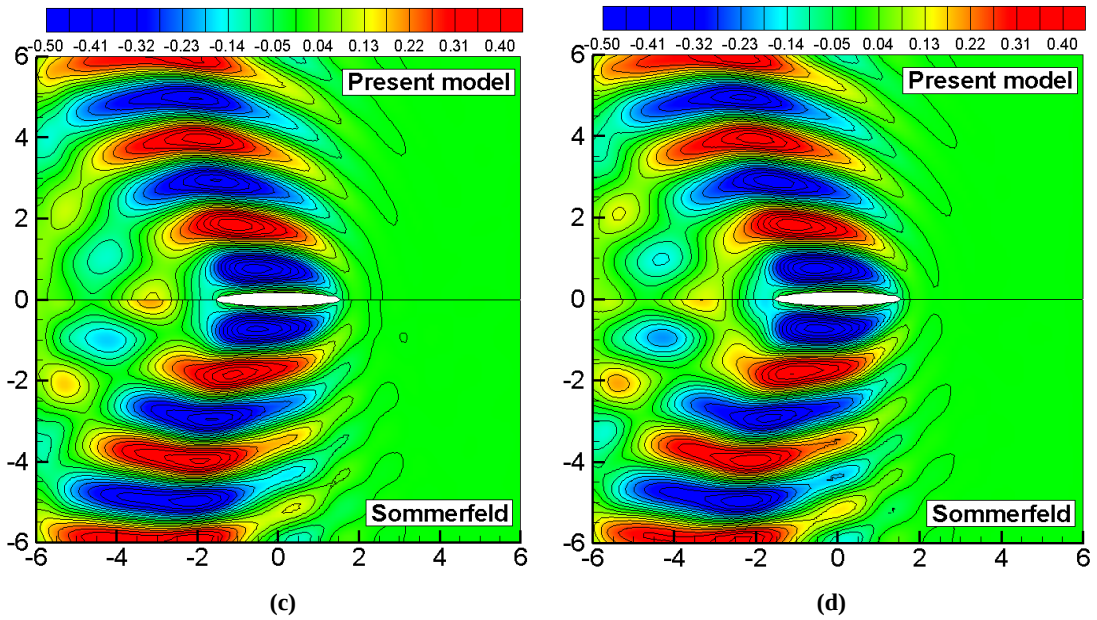

Figure 6.18: Radiation wave patterns by using Sommerfeld and present radiation conditions at λ/L = 1. (a) Fn = 0, τ = 0; (b) Fn = 0.068, τ = 0.2; (c) Fn = 0.083, τ = 0.25; (d) Fn = 0.09, τ = 0.26.

(2) Upstream radiation condition

In order to validate the wave patterns calculated by the present radiation condition at $\tau > 0.25$, we implement an upstream boundary condition of Nakos (1990) for comparison. The upstream boundary condition assumes that there is no scattered wave travelling ahead of the vessel and a quiescent condition is imposed at the upstream boundary as

$$(i\omega_e - u_0 \frac{\partial}{\partial x})\varphi_j = 0 \tag{6.10}$$

$$(i\omega_e - u_0 \frac{\partial}{\partial x})^2 \varphi_j = 0 \tag{6.11}$$

Besides, no control surface is required in Nakos's (1990) model. Figure 6.19 is the diffracted waves with different radiation conditions, while the radiated waves induced by unit heave motion are presented in Figure 6.20. The wave length to ship length ratio of λ/L = 1 in head sea corresponds to the critical conditions in ship design. In order to investigate how the new radiation condition changes the wave patterns at different forward speeds, we make the comparison between the present model and traditional upstream radiation condition over a wide range of Brard number from 0.26 to 1.32. The lower half of each sub-figure of Figure 6.19 and Figure 6.20 shows the wave

pattern obtained from the upstream radiation condition, while the radiation condition in the upper half account for the new treatment of the radiation condition defined by Eqs. (5.16)-(5.17). From the comparison in Figure 6.19 and Figure 6.20, we find that an upstream quiescent region is achieved by both methods. A very good agreement of the wave fields can be observed around the ship hulls, especially at high forward speed. The discrepancies increase as the waves propagate to the truncated control surface. For the upstream treatment, the reflections can be clearly observed form Figure 6.19 (a) and Figure 6.20 (a) when the waves approach the control surface. As the forward speed increases, the reflections from the control surface become not evident and very satisfied agreement has been achieved between these two radiation conditions. It can be supposed that at low forward speed, if the truncated free surface domain is not sufficient, the reflected waves could inevitably influence the ship motions. But for the present radiation condition, the rotated angle θ has been calculated before we solve the boundary value problem. The corrected Sommerfeld radiation condition can ensure the out-going property of the scattered waves. Therefore, no reflections can be found for the present model at $\tau > 0.25$. The results in Figure 6.19 and Figure 6.20 confirm the effectiveness of the present radiation condition as a wave-pattern prediction tool for the ships travelling with a wide range of forward speed. However, the traditional upstream radiation condition is limited to the high forward speed problem. For the low forward speed range, a reasonable control surface is required downstream to ensure the out-going property of the scattered waves.

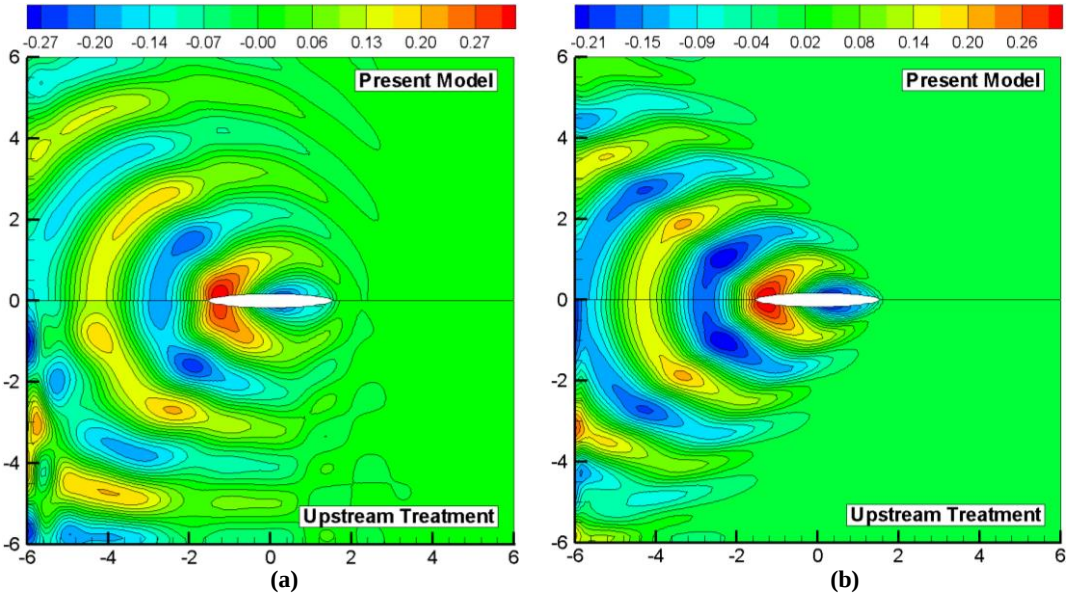

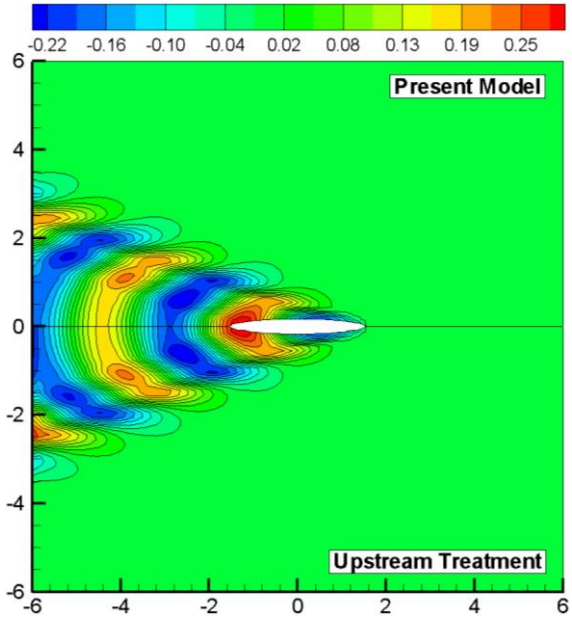

(c)

Figure 6.19: Diffracted waves of single ship in head seas by using upstream and present radiation condition: λ/L = 1. (a) Fn = 0.09, τ = 0.26; (b) Fn = 0.15, τ = 0.5; (c) Fn = 0.3, τ = 1.32.

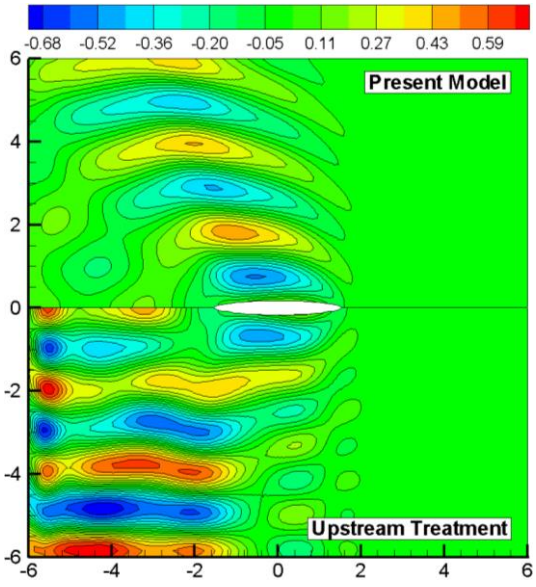

(a)

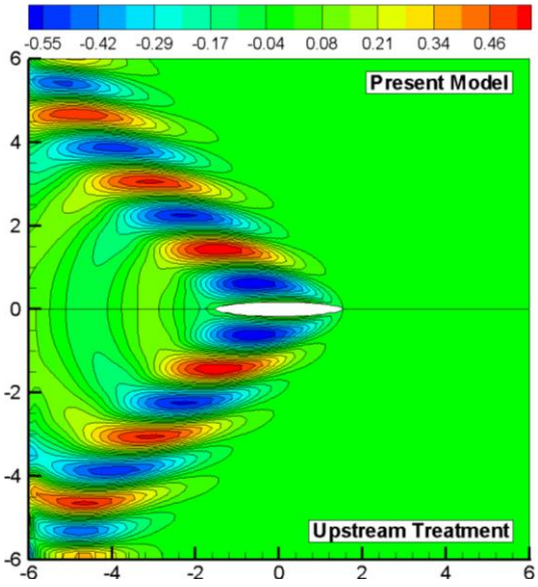

(b)

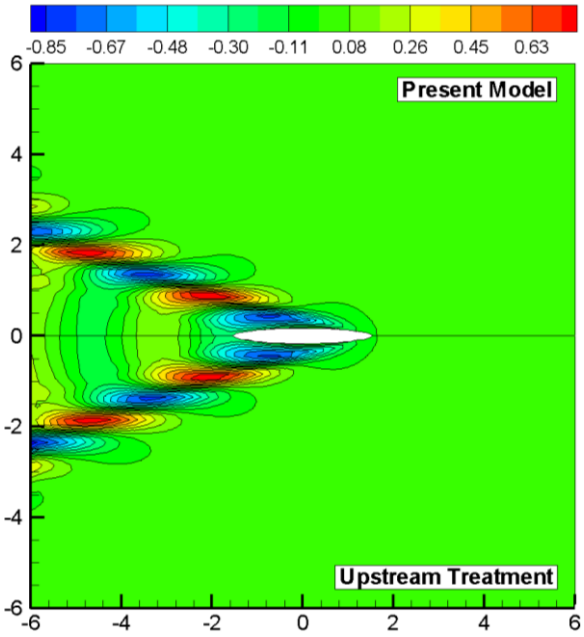

(c)

Figure 6.20: Radiated waves of single ship in head seas by using upstream and present radiation condition: λ/L = 1. (a) *Fn* = 0.09, τ = 0.26; (b) *Fn* = 0.15, τ = 0.5; (c) *Fn* = 0.3, τ = 1.32.

We also examine the effect of the radiation condition through the comparison study about the hydrodynamic coefficients. Figure 6.21 shows the hydrodynamic coefficients with the upstream and present radiation condition at F_n = 0.09. It can be clearly seen that at $\omega_e\sqrt{L/g} < 3$ ($\omega_e\sqrt{L/g} = 3$ corresponds to $\tau = 0.25$), the results from the upstream treatment are diverged and cannot provide a stable solutions. At the range of $3 < \omega_e\sqrt{L/g} < 3.5$ (corresponds to $0.25 < \tau < 0.29$), the results from the upstream radiation treatment tends to be stable. When the non-dimensional frequency is greater than 3.5 (corresponds to $\tau > 0.29$), these two radiation conditions can provide the identical results. This coincides with the assumption of the upstream treatment that the scattered waves could not propagate ahead of the vessel ($\tau < 0.25$). Even though the Brard number is slightly greater than critical value 0.25, there are still some waves upstream, which can be observed from Figure 6.19 (a) and Figure 6.20 (a). At this case, the reflected waves from the control surface can bring some influences to the vessel's motion, which can explain the discrepancies between these two radiation conditions at $0.25 < \tau < 0.29$. As the Brard number keeps increasing, there is no wave ahead of the vessel, as shown in Figure 6.19 (b)-(c) and Figure 6.20 (b)-(c), and it fully satisfies the upstream assumption. Therefore, both of the radiations can give a stable result. We

also investigate the hydrodynamic coefficients at Fn = 0.3, as shown in Figure 6.21. It can be found that the added mass and damping with the present radiation condition are almost the same as these with the upstream treatment. It can be concluded that the present radiation condition can predict the hydrodynamic properties of vessels with forward speed above and below the group velocity of the scattered waves while the upstream treatment is only valid for the case of $\tau > 0.25$.

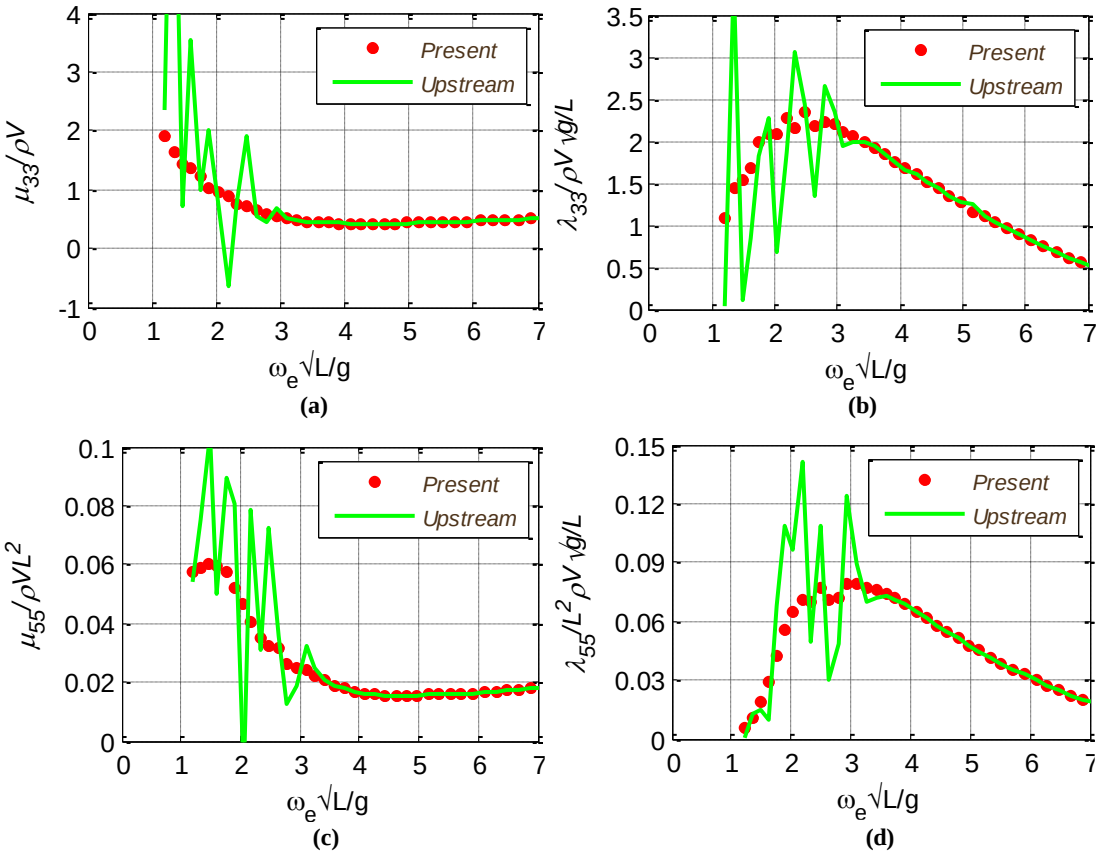

Figure 6.21: Hydrodynamic coefficients of single ship by using upstream and present radiation condition at *Fn* = 0.09. (a) Heave added mass; (b) Heave damping; (c) Pitch added mass; (d) Pitch damping.

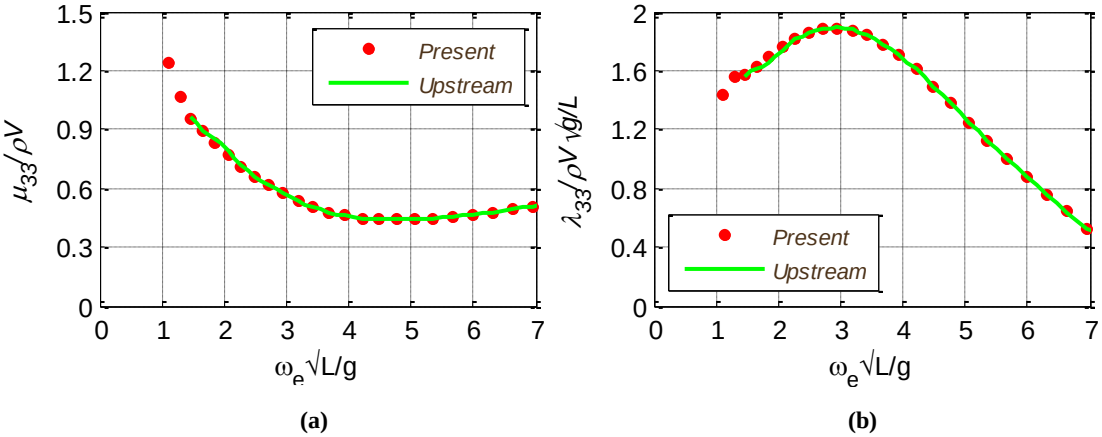

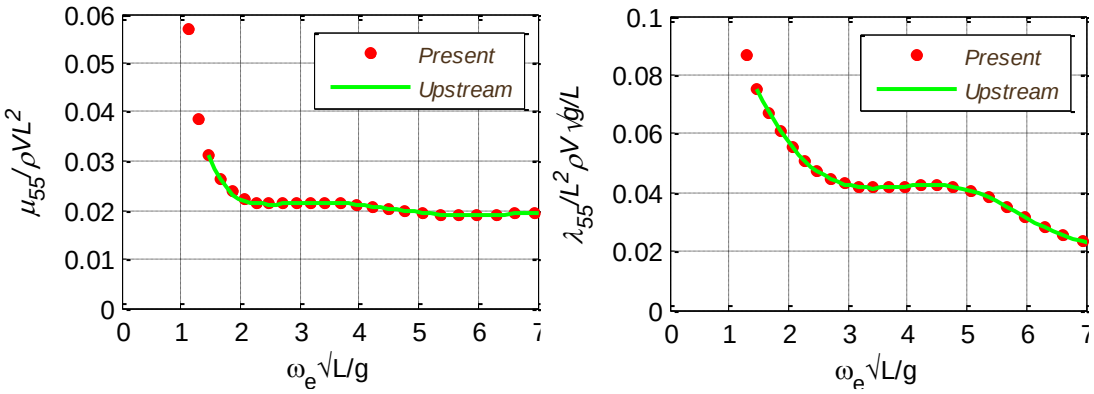

(c) **(d)**

Figure 6.22: Hydrodynamic coefficients of single ship by using upstream and present radiation condition at *Fn* = 0.3. (a) Heave added mass; (b) Heave damping; (c) Pitch added mass; (d) Pitch damping.

6.4. Summary

In this chapter, we validated the present 3-D Rankine source panel method associated with a new radiation condition by solving the hydrodynamic problem of single ship travelling or stationary in waves. We examined the hydrodynamic coefficients, wave excitation forces and motion responses and established the comparisons between the present calculations and the commercial software as well as the experimental data. Very good agreement had been achieved which illustrates that the present program is a useful tool to predict the hydrodynamic behaviours of single ship with a wide range of forward speed in waves. We also examined the present radiation condition and effect of forward speed through a series of numerical experiments involving single Wigley hull with different forward speeds in head seas. The forward speed introduces the Doppler shift which modifies the length of the scattered waves. The comparison between the present and Sommerfeld radiation condition was made at $\tau < 0.25$, while the comparison between the present and upstream radiation treatment was made at $\tau < 0.25$. Our solution shows a better wave pattern without reflections from the truncated control surface, which confirms the effectiveness of the present radiation condition as a wave-pattern prediction tool for the ships travelling with a wide range of forward speed.

7. Validations and discussion of two ships stationary in waves

7.1. Introduction

Moored side-by-side operations are important options for the offloading of oil offshore. Nowadays, they are also considered seriously for the LNG offloading from LNG FPSOs or FSRUs (Floating Storage and Regasification Units). The loads in the mooring lines between the two vessels, the loads in the floating fenders and the relative motions at the manifold location are the most critical issues during this operation. These are determined by the wave, wind and current loads on the two vessels in close proximity, as well as by the strong hydrodynamic interaction between the vessels. Even in head waves the two vessels are jack-kniving (relative yaw motion of the vessel out of phase) as the waves run between the two hulls. The resulting motions and mooring loads determine the operability of the operation in certain environmental conditions.

In this chapter, we will validate our program through a numerical study about two ships stationary in waves. The validation is established through two pairs of models. Model 1 is about a modified Wigley hull and a box model at beam sea case and the experimental results as well as some published numerical results will be used for the validation. Model 2 is about two identical Wigley III hulls at head sea condition and the results from the commercial software will be used for the comparison. The discussions on shallow water effects and the distance between two ships are also included in this chapter. But these discussions are based on zero speed case. The systematic discussions about the water depth variation, the transverse and longitudinal distance between the ships and the forward speed effects will be presented latter in Chapter 8 and Chapter 9.

7.2. Validations of Model 1 (Beam sea)

Model 1 is about a modified Wigley hull (Ship_a) and a rectangular box (Ship_b) model at beam sea condition. The modified model can be defined as (Kashiwagi et al., 2005)

$$\frac{2y}{B}=\left[1-\left(\frac{2x}{L}\right)^2\right]\left[1-\left(\frac{z}{T}\right)^2\right]\left[1+0.2\left(\frac{2x}{L}\right)^2\right]+\left(\frac{z}{T}\right)^2\left[1-\left(\frac{z}{T}\right)^8\right]\left[1-\left(\frac{2x}{L}\right)^2\right]^4 \quad (7.1)$$

where B is the breadth, L is the length and T is the draft of the ship. The main dimensions of the modified Wigley and the rectangular box are shown in Table 7.1.

Table 7.1: Main dimensions of the modified Wigley hull and the box (Kashiwagi et al., 2005).

	Modified Wigley hull	Rectangular box
Length between perpendicular	$L_a = 2\ m$	$L_b = 2\ m$
Breadth	$B_a = 0.3\ m$	$B_b = 0.3\ m$
Draught	$T_a = 0.125\ m$	$T_b = 0.125\ m$
Displacement	$V_a = 0.04205\ t$	$V_b = 0.075\ t$
Water-plane area	$A_{wa} = 0.416\ m^2$	$A_{wb} = 0.60\ m^2$

Two typical cases are simulated here:

1) Ship_a is situated in the weather side and Ship_b is in the lee side. The transverse (*dt*) and longitudinal distance (*dl*) between the two ships is 1.097 *m* and 0 *m* respectively.
2) Ship_a is situated in the lee side and Ship_b is in the weather side. The transverse (*dt*) and longitudinal distance (*dl*) between the two ships is 1.797 *m* and 0 *m* respectively.

The computational range on the free surface is extended to 2*L* upstream, 2*L* downstream and 2*L* sideways, where $L = 2\ m$ is the length of the vessel. For the case of $dt = 1.079$, there are 320 panels on the body surface of Wigley hull, 480 on the body surface of the rectangular box, 7800 on free surface and 2052 on the control surface, which is shown in Figure 7.1. For the case of $dt = 1.797$, there are 320 panels on the body surface of Wigley hull, 480 on the body surface of the rectangular box, 8360 on free surface and 1780 on the control surface.

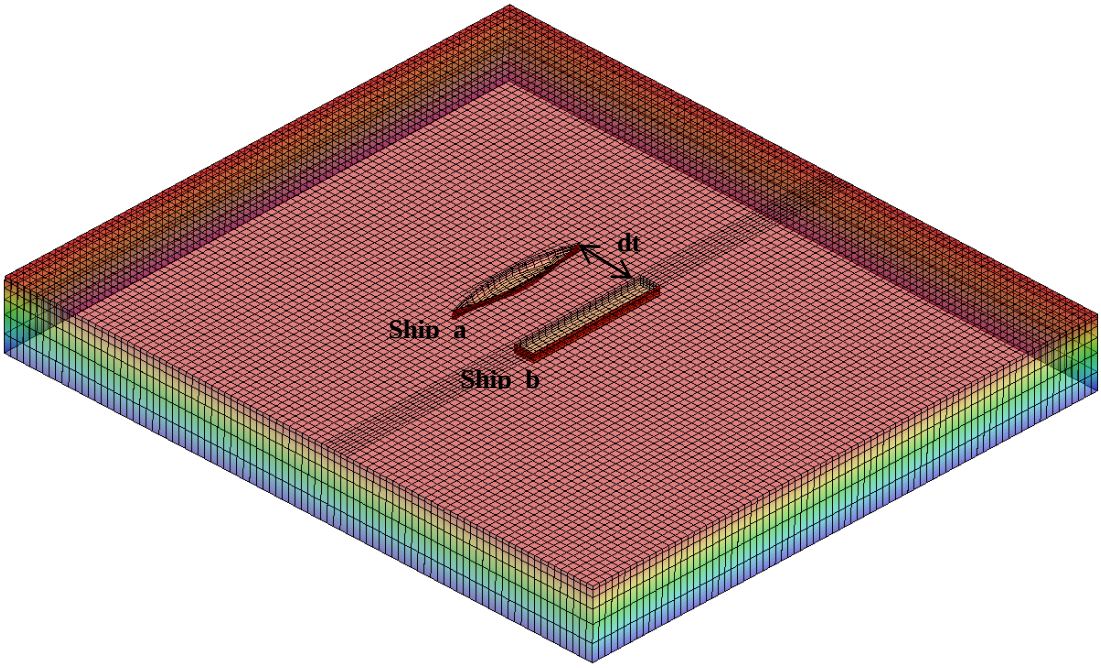

Figure 7.1: Computational domain and panel distribution of a modified Wigley hull and a rectangular box model stationary in waves at *dt* = 1.079.

Figure 7.2 shows the hydrodynamic coefficients of a modified Wigley hull due to the heave motion of the Wigley hull itself when the rectangular box is fixed with the separation distance of dt = 1.797 m, where $K = \frac{\omega_0^2 L_c}{g}$ and L_c is the characteristic length scale for nondimension (which is taken as $L_c = L_a/2$). The comparisons with experimental data and Green function method (Kashiwagi et al., 2005) are also included. The numerical results calculated by the present 3-D Rankine source method generally agree well with the experimental data. The hydrodynamic interactions are properly accounted for, especially in the sway added mass and damping (μ_{23}^{aa} and λ_{23}^{aa}) which are exerted only by wave interactions between Ship_a and Ship_b. Some discrepancies can be observed in the heave added mass and damping (μ_{33}^{aa} and λ_{33}^{aa}) at low frequency range, which could be attributed to the effect of the reflection waves from the parallel side walls of the tank, as explained by Kashiwagi et al. (2005).

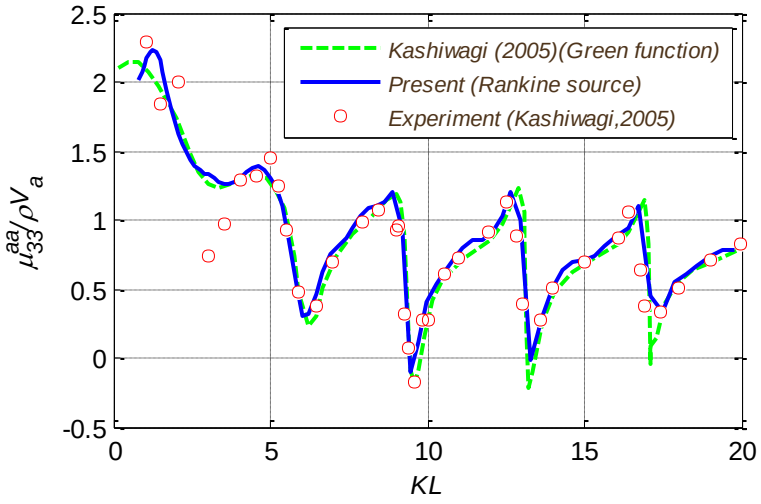
Kashiwagi (2005)(Green function)
Present (Rankine source)
Experiment (Kashiwagi,2005)
$\mu_{33}^{aa}/\rho V_a$
KL

(a)

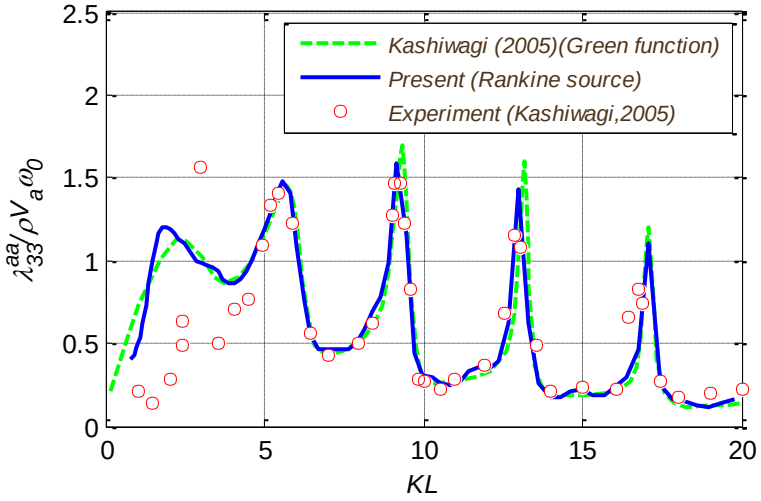
Kashiwagi (2005)(Green function)
Present (Rankine source)
Experiment (Kashiwagi,2005)
$\lambda_{33}^{aa}/\rho V_a \omega_0$
KL

(b)

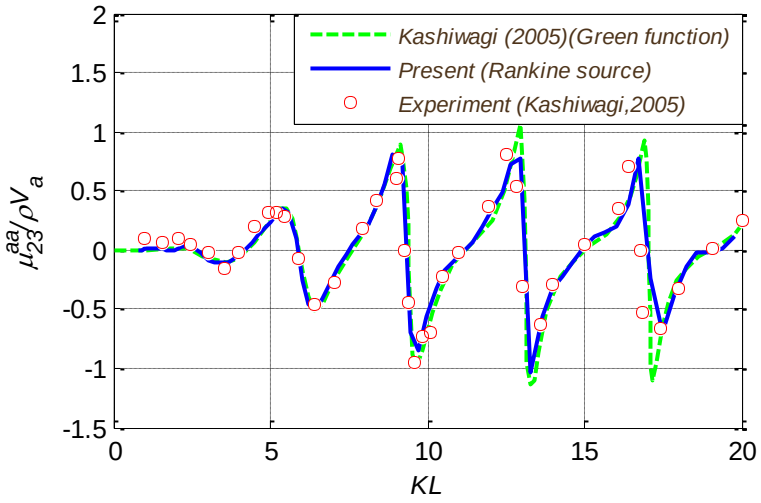
Kashiwagi (2005)(Green function)
Present (Rankine source)
Experiment (Kashiwagi,2005)
$\mu_{23}^{aa}/\rho V_a$
KL

(c)

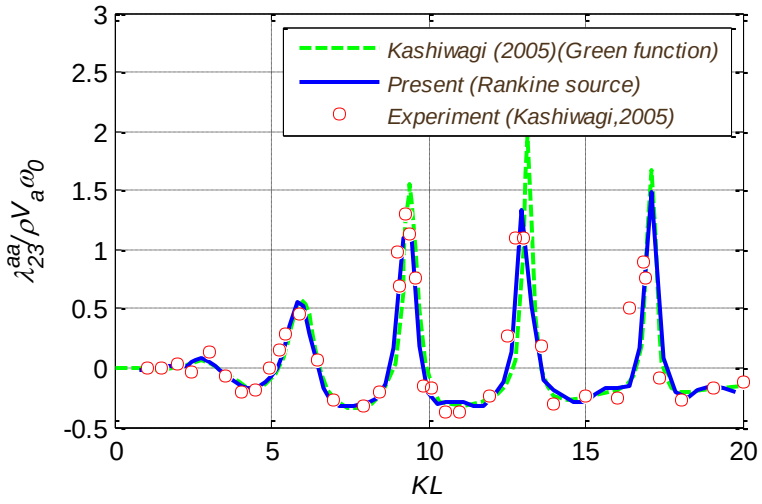

(d)

Figure 7.2: Hydrodynamic coefficients of a modified Wigley hull due to the heave motion of the Wigley hull itself when the rectangular box is fixed with the separation distance of *dt* = 1.797 *m*. (a) Heave added mass; (b) Heave damping; (c) Sway added mass; (d) Sway damping.

Figure 7.3 shows the wave excitation forces on the modified Wigley hull (Ship_a, in the weather side) and rectangular box (Ship_b, in the lee side) with the separation distance of *dt* = 1.097 *m*. The overall agreement between measured and computed results is good, although slight discrepancies can be seen in a range of long wavelengths, which is due to the reflection wave effects from the side walls of the towing tanker. Very good agreement has been obtained between the present Rankine source method and Green function method. It can be concluded that both Green function method and Rankine source method can predict the hydrodynamic forces of two ships arranged side by side with zero speed in beam waves.

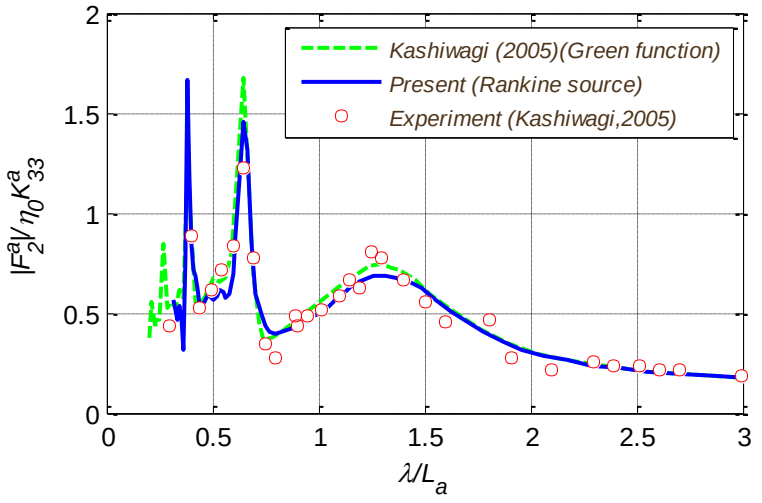

(a)

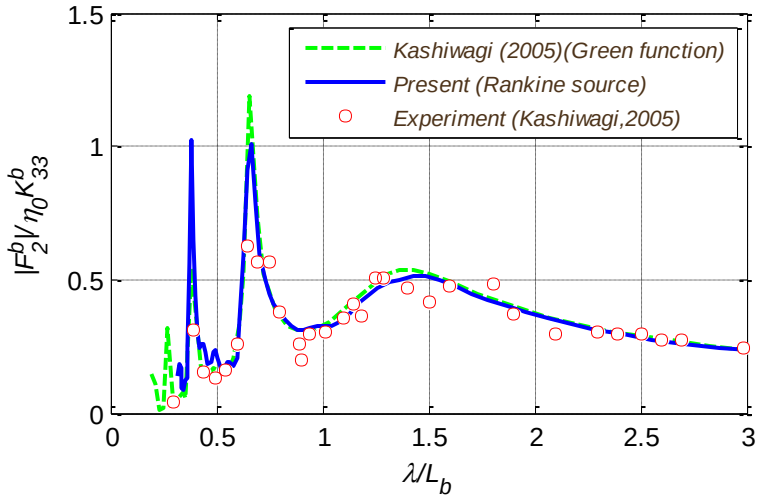

(b)

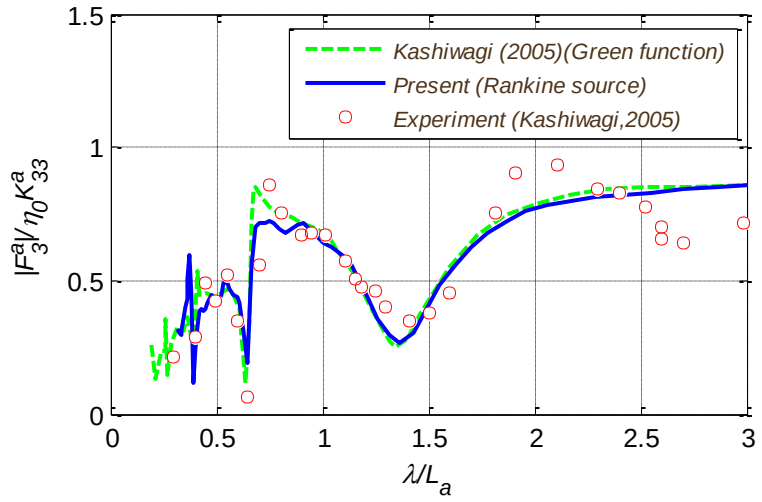

(c)

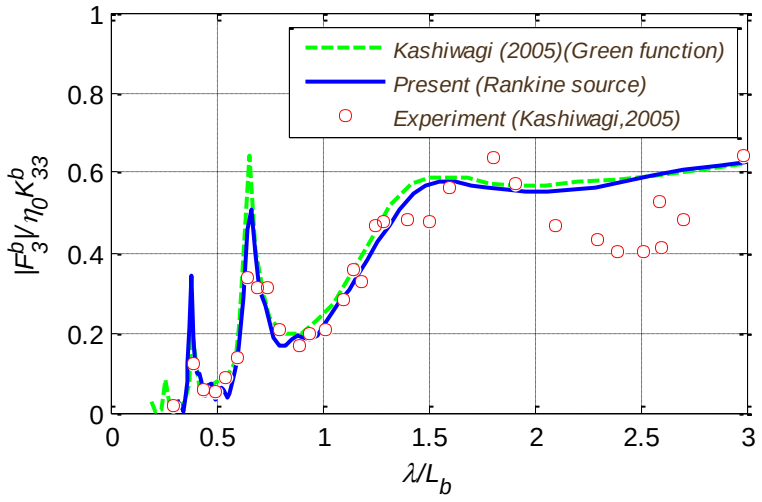

(d)

Figure 7.3: Wave excitation forces in beam waves with the transverse distance between two ships of *dt* = 1.097 *m*. (a) Sway forces on Ship_a; (b) Sway forces on Ship_b; (c) Heave forces on Ship_a; (d) Heave forces on Ship_b.

7.3. Validations of Model 2 (Head sea)

Model 2 is about two identical Wigley III hulls at head sea condition. The Wigley models used here is the same as defined in Eq. (6.6), and the main dimensions of the hull are given in Table 6.1. The transverse and longitudinal distance between these two vessels is 1 m and 0 m respectively. The computational range on the free surface is extended to 1.33L upstream, 1.33L downstream and 2L sideward, where $L = 3m$ is the length of the vessel. There are 600 panels on the each body surface, 10400 on free surface and 2100 on the control surface, which is shown in Figure 7.4.

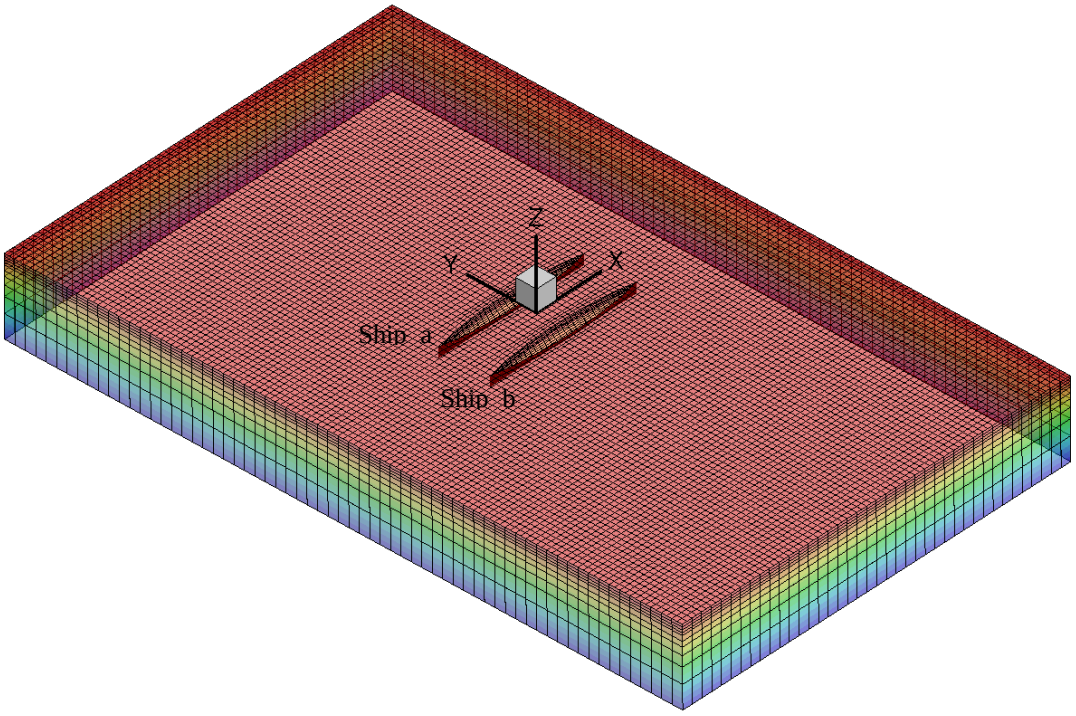

Figure 7.4: Computational domain and panel distribution of two Wigley hulls stationary in waves.

Figure 7.5 and Figure 7.6 show the wave excitation forces and response amplitudes of both ships in 6 degree of freedom. Good agreement is achieved between the present method and Wadam solution. For the present 3-D Rankine source method, 13700 panels are distributed on the body-, free- and control-surface, while only 2000 panels on the body surface are required for the Wadam program which is based on the frame work of 3-D Green function. Therefore, more CPU time is consumed by the present program on modelling as well as solving a very large full rank matrix. It can be concluded that both Rankine source method and Green function method can provide a stable solution for the ship-to-ship with zero speed problem. The advantage of the

present method should be concentrated on the two ships travelling with forward speed in the restricted waters, which will be discussed in next chapter. Peak value of roll motion in Figure 7.6 (d) can be found around λ/L = 0.65, which corresponds to the nature frequency of roll motion. We also find that there are some spikes in sway force and roll moment in Figure 7.5 (b) and Figure 7.5 (d). The first spike appears at λ/L = 0.33, which corresponds to the wave length that equals to the transverse distance dt (L = 3 m, dt = 1m). Similarly, the second and third spikes arise at λ/L = 0.66 and λ/L = 1, which correspond to the wave length that equals to 2dt and 3dt respectively. Special attention should be paid on the force and motion of sway. As we can see from Figure 7.5 (b) and Figure 7.6 (b), there is a significant leap at high frequency around λ/L = 0.25. The reason for these spikes will be discussed later in next chapter. However, there are no obvious spikes observed at these λ/L values for surge, heave and pitch, which indicates that in head sea condition, the transverse distance between two ships will bring more influence on the dynamic responses in sway, roll and yaw. The numerical results of single ship are also included in the comparison. In head sea case, the motions in sway, roll and yaw should be zero due to the symmetrical characteristic of the vessel. But even in surge, heave and pitch, the influence from the hydrodynamic interaction is not significant.

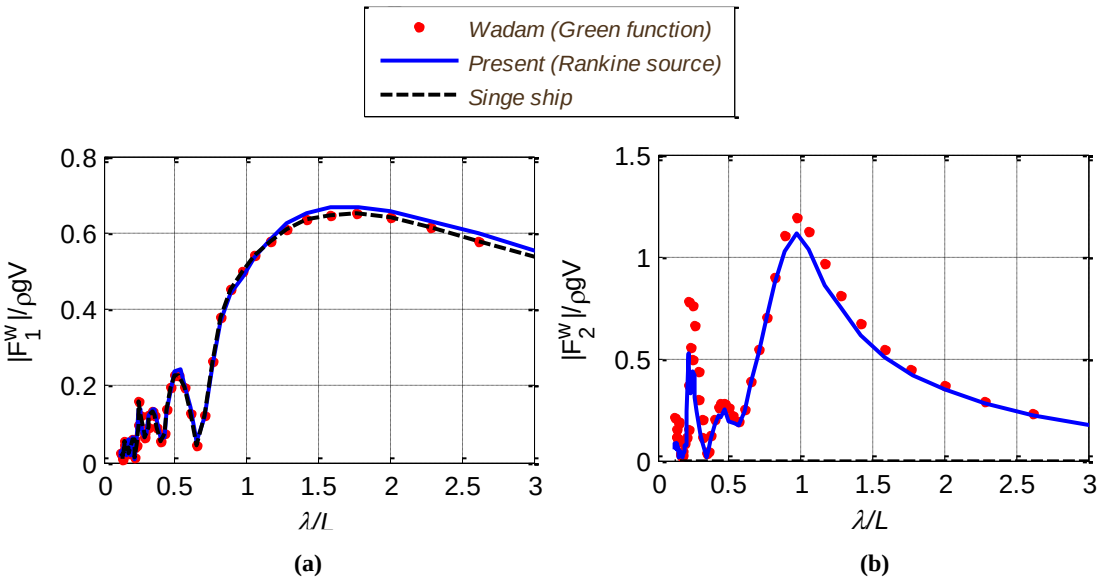

(a) **(b)**

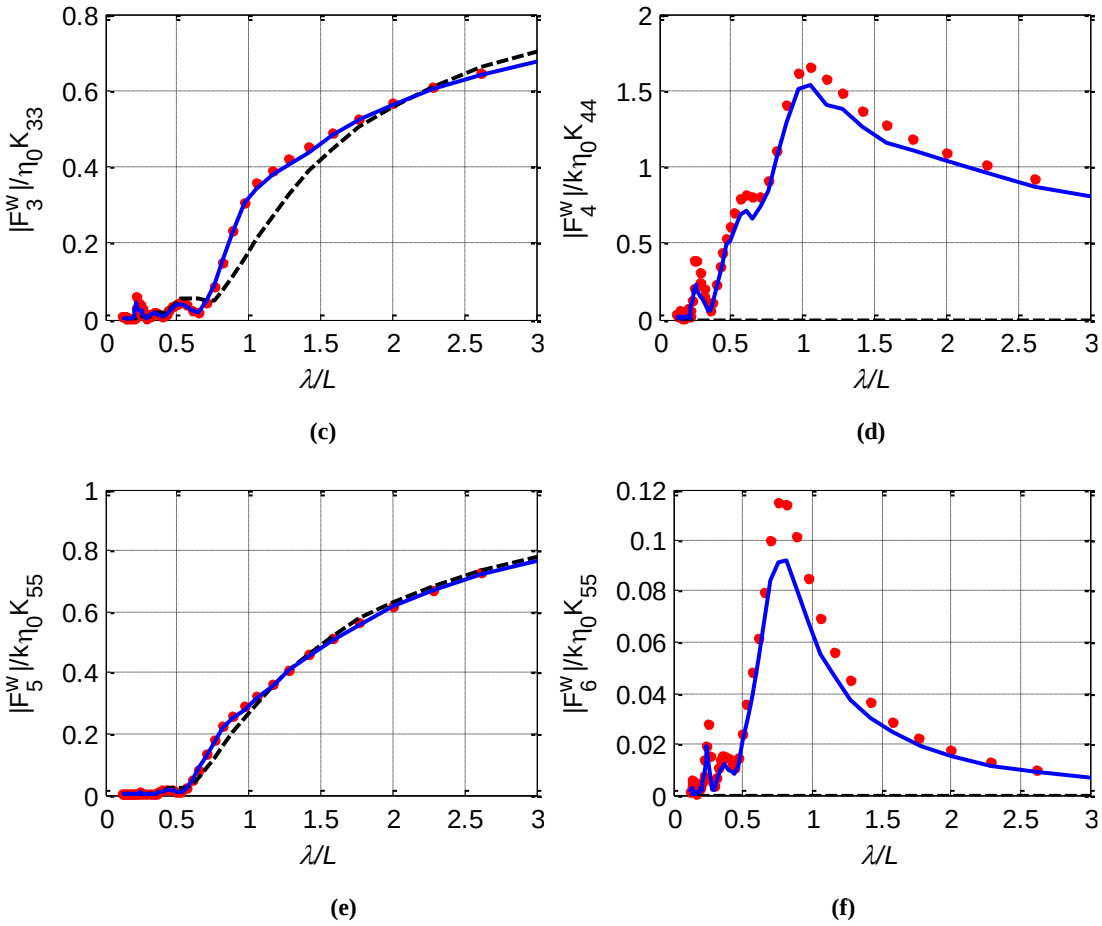

Figure 7.5: Wave excitation forces of both Wigley hulls with zero speed in head waves. (a) Surge; (b) Sway; (c) Heave; (d) Roll; (e) Pitch; (f) Yaw.

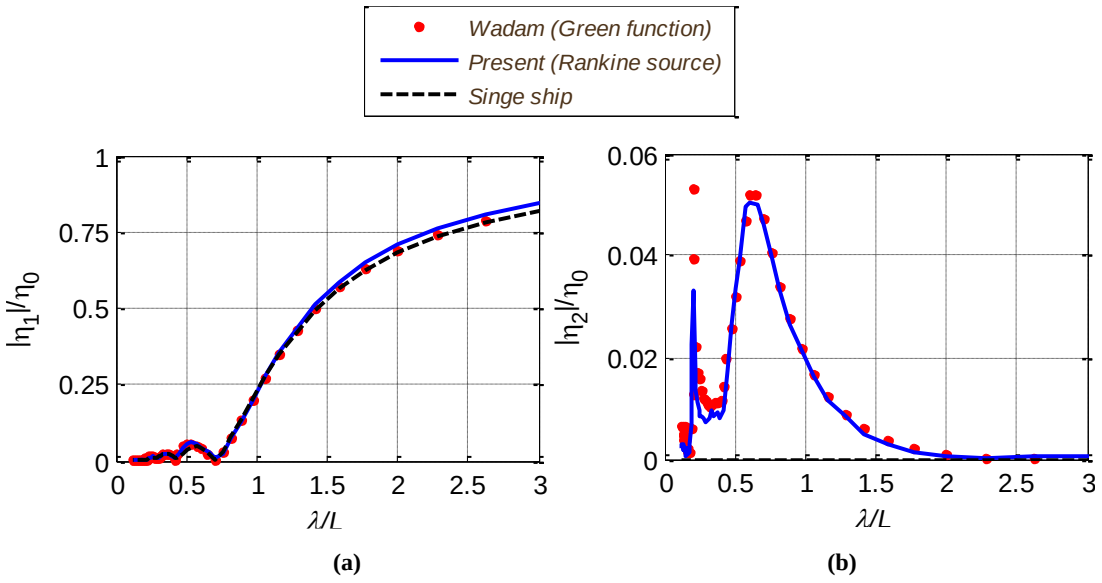

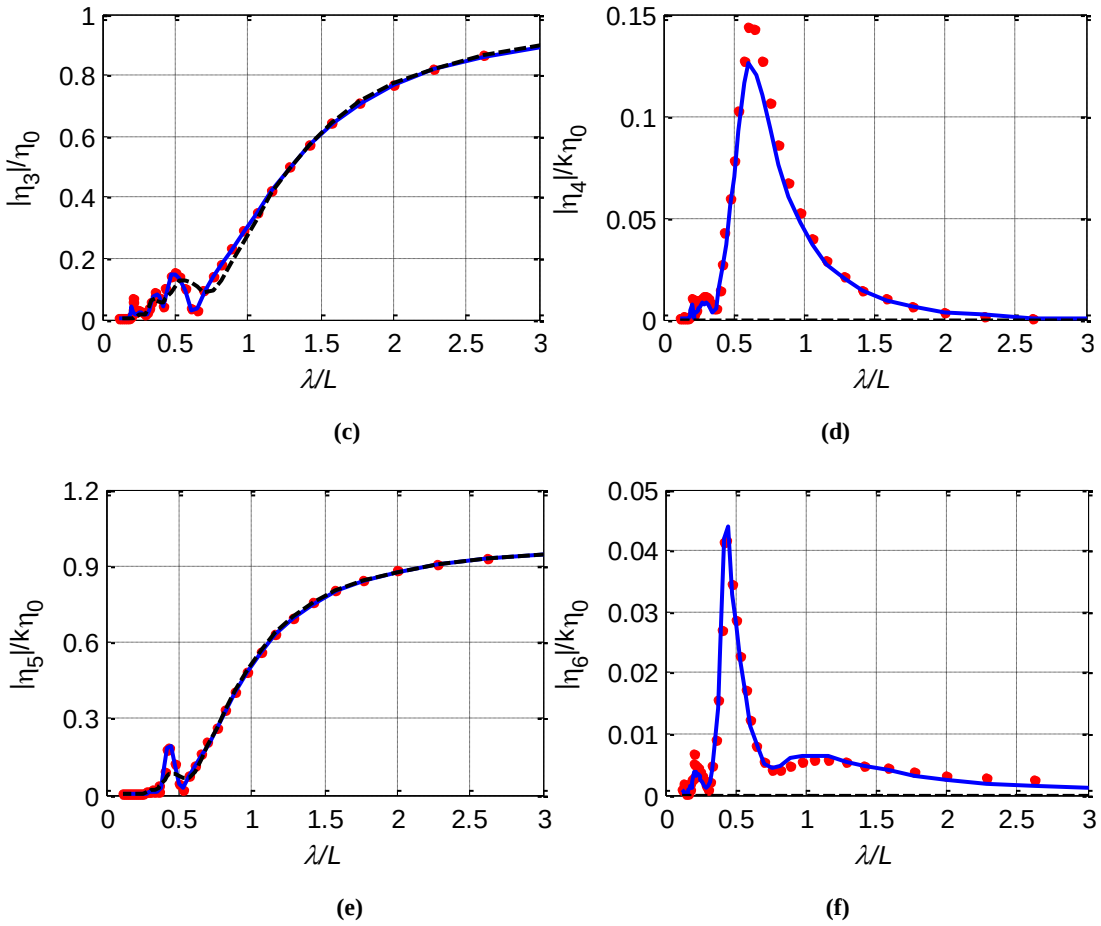

Figure 7.6: Response amplitude operators of both Wigley hulls with zero speed in head waves. (a) Surge; (b) Sway; (c) Heave; (d) Roll; (e) Pitch; (f) Yaw.

As we can see from Figure 7.5 (b) and (d) that the peak values of sway force and roll moment appear at $\lambda/L = 1$. In order to investigate the mechanism, we calculate the wave elevation at $\lambda/L = 1$, as shown in Figure 7.7. For a single Wigley hull, the sway force and roll moment should be zero due to the symmetrical characteristic of the vessel and the wave profiles in the portside and starboard are exactly the same. However, for the ship-to-ship problem, the wave elevation in the portside and starboard is different. For the zero speed case, the diffracted waves are trapped in the gap between the hulls and they are not able to propagate sideward. Consequently, the wave elevation in the portside of Ship_a is smaller than that in the starboard, which is shown in Figure 7.8. As a result, the symmetrical characteristic of the pressure distribution around the ship hull is violated, which could result in a significant sway force and roll moment. We can also observe from Figure 7.8 that the wave profile is non-symmetrical not only about y-axis, but also about x-axis. This can account for the yaw moment in Figure 7.5 (f).

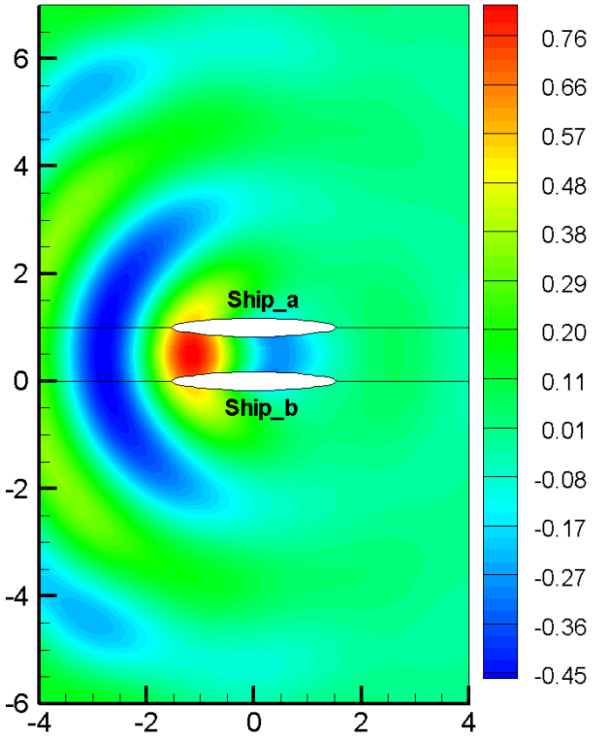

Figure 7.7: Diffraction wave pattern of two Wigley hulls stationary in head seas: λ/L = 1.

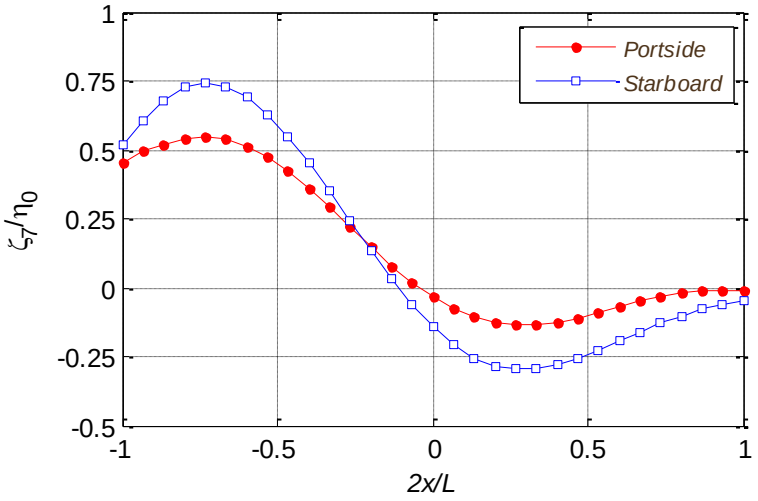

Figure 7.8: Wave profiles at portside and starboard of Ship_a: λ/L = 1.

7.4. Effects of water depth

In order to investigate the effects of water depth, the model of two identical Wigley III hulls in Section 7.3 are used. The computational domain and panel distribution is shown in Figure 7.4. These two ships are stationary in beam waves (Ship_a is in the

lee side and Ship_b is in the weather side) with the separation distance fixed at $dt = 1$ *m*. The water depth to draught ratio (*d/T*) is fixed at 2, 4 and infinity.

Figure 7.9 and Figure 7.10 show the motion responses of Ship_a (Lee side) and Ship_b (Weather side) at different water depths in beam waves. From the figures it can be seen that the water depth has a significant influence on the responses of both ships. Both of the amplitudes and resonance frequencies are changed by the water depth. There are mainly two reasons for these discrepancies. The first reason is that the shallow water dispersion relation in Eq. (3.4) changes the incident wave length and as a result, the wave exciting forces and the resonance frequencies differ from those in deep water. The results in Figure 7.11 can explain this phenomenon. The *x*-axis of Figure 7.11 is the non-dimensional incident wave length, where λ_0 is the wave length in infinite water depth. We find at small λ/L, the wave length at different water depths differs a little. The difference keeps an increased trend as the wave length increases. The second reason is the hydrodynamic coefficients and diffraction forces of the ship are changed by the nearness of the sea bottom. As can be seen from Figure 7.9 and Figure 7.10, the water depth can significantly influence the motion amplitudes of sway and roll at full range of wave length. But for the heave motion, the water depth will only shift the resonance frequency. As a result, a very large discrepancy can be observed at low wave length range, while the motion responses at high wave length range are hardly influenced by the water depth. We also include the results of single ship for comparison. It can be found that the hydrodynamic interactions are important at the low wave length range. As the wave length increases, the discrepancies become not evident.

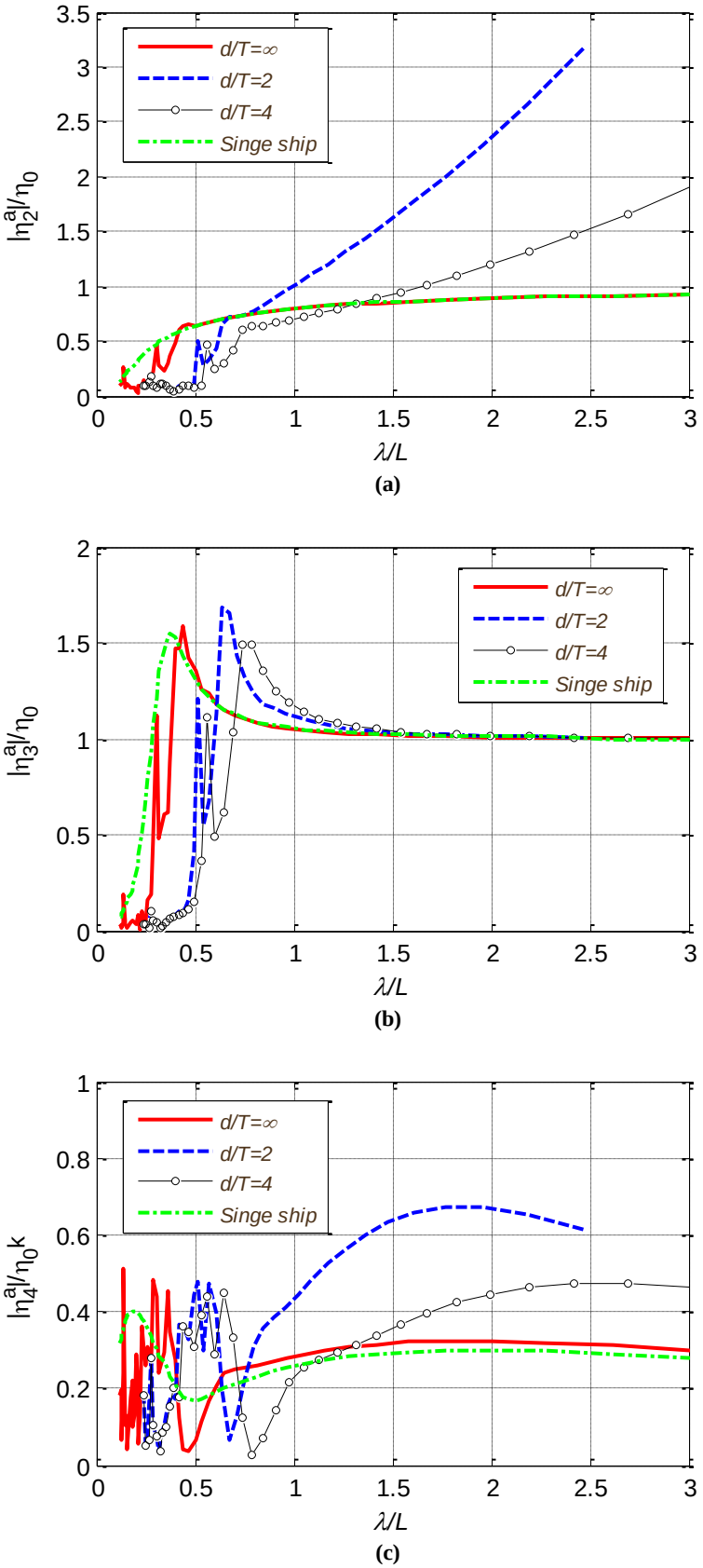

Figure 7.9: Response amplitude operators of Ship_a (Lee side) at different water depths in beam waves. (a) Sway; (b) Heave; (c) Roll.

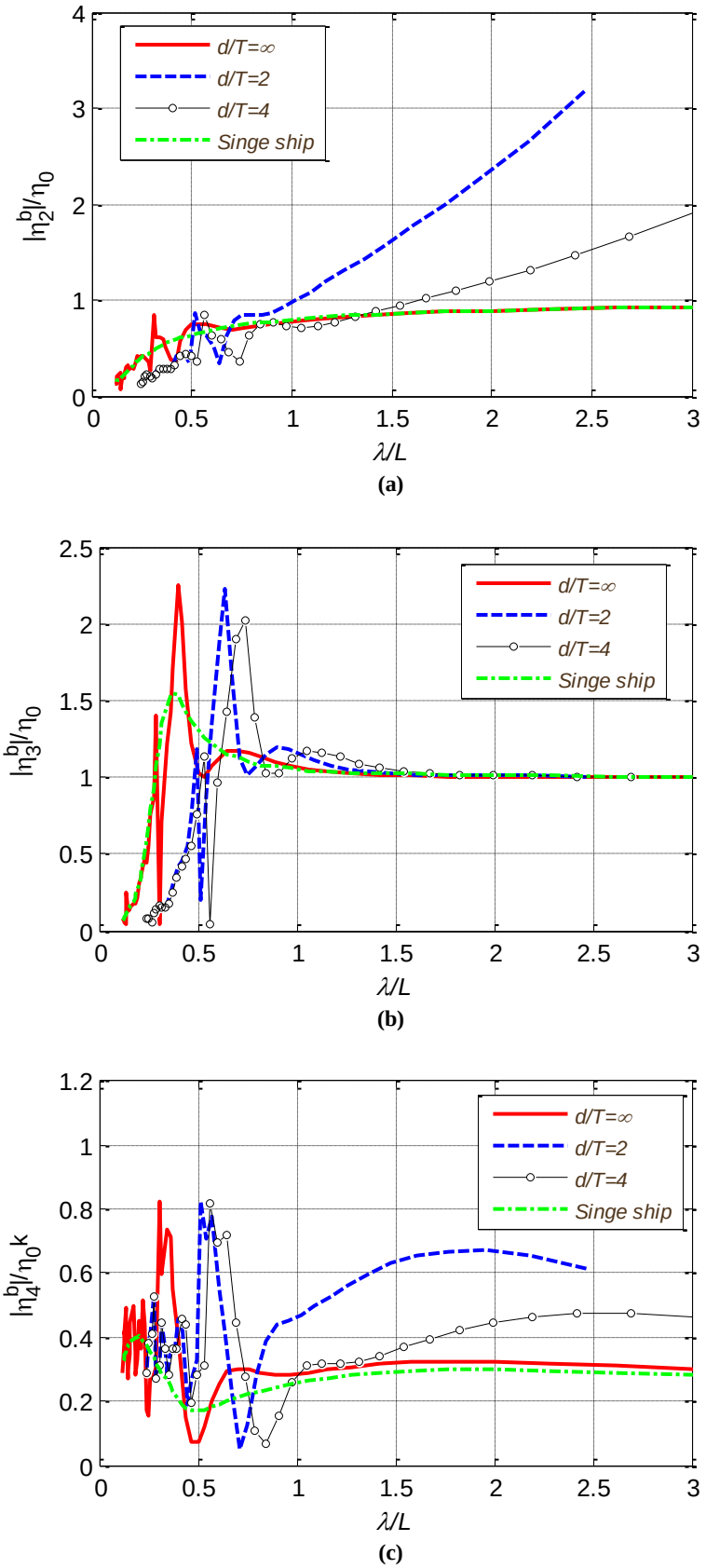

Figure 7.10: Response amplitude operators of Ship_b (Weather side) at different water depths in beam waves. (a) Sway; (b) Heave; (c) Roll.

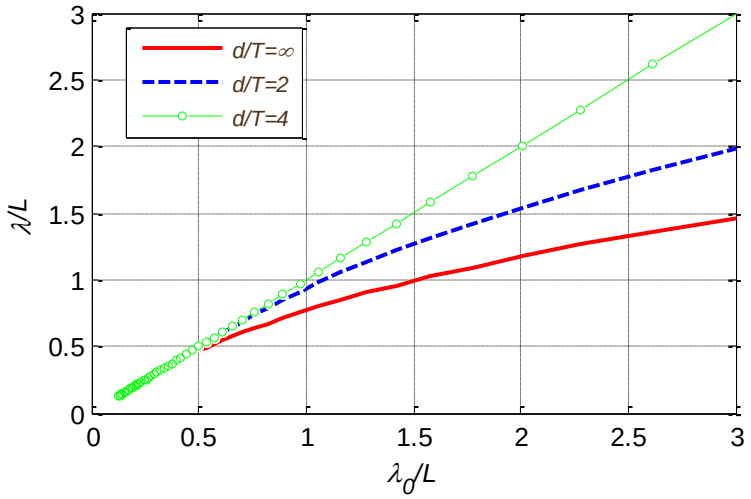

Figure 7.11: Wave length at different water depths.

7.5. Effects of transverse distance between two ships

In order to investigate the effects of the transverse distance between two ships, the model of two identical Wigley III hulls in Section 7.3 are used. The computational domain and panel distribution is shown in Figure 7.4. These two ships are stationary in beam waves (Ship_a is in the lee side and Ship_b is in the weather side) with infinite water depth. The transverse distance to ship length ratio (dt / L) is fixed at 1/3, 2/3 and 1. The results of single ship represent $dt / L = \infty$.

Figure 7.12 and Figure 7.13 show the motion responses of Ship_a (Lee side) and Ship_b (Weather side) at different separation distance in beam waves. It can be observed that the transverse distance between two ships could influence the motion responses at low wave length range. At $\lambda / L > 0.5$, the hydrodynamic interactions between two ships in beam waves are quite small. There are a large number of spikes at low λ / L. The main reason for these spikes can be attributed to the radiation problem. Since the distance between the two ships is small, the radiated waves of Ship_a will significantly influence the motion responses of Ship_b, and vice versa. It can also be observed that the values of these spikes increase as the transverse separation distance increases, which indicates that the larger distance can bring more risks to the ship-to-ship operation in beam waves while the responses of the ships are supposed to be more stable with a smaller separation distance.

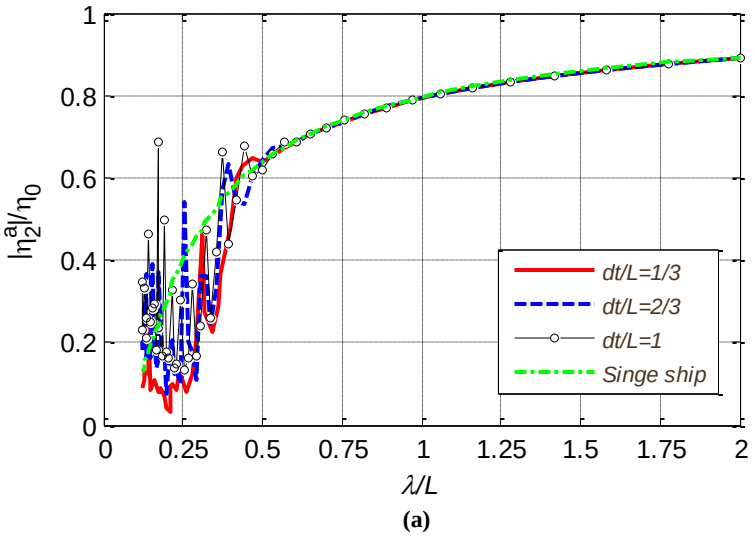

(a)

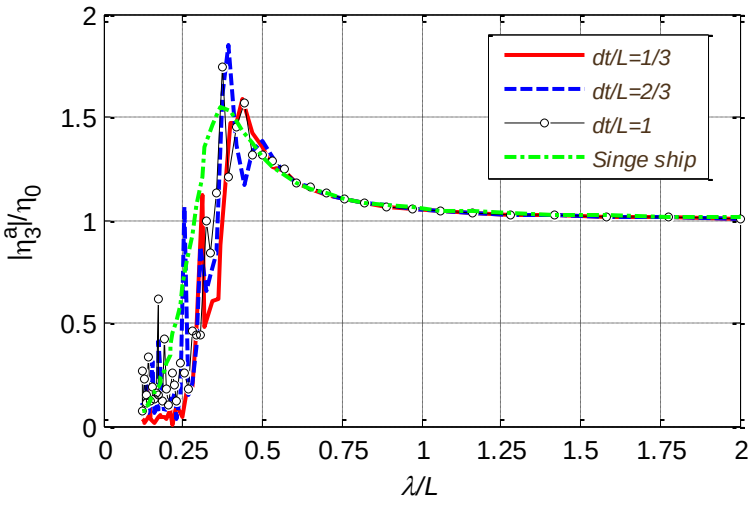

(b)

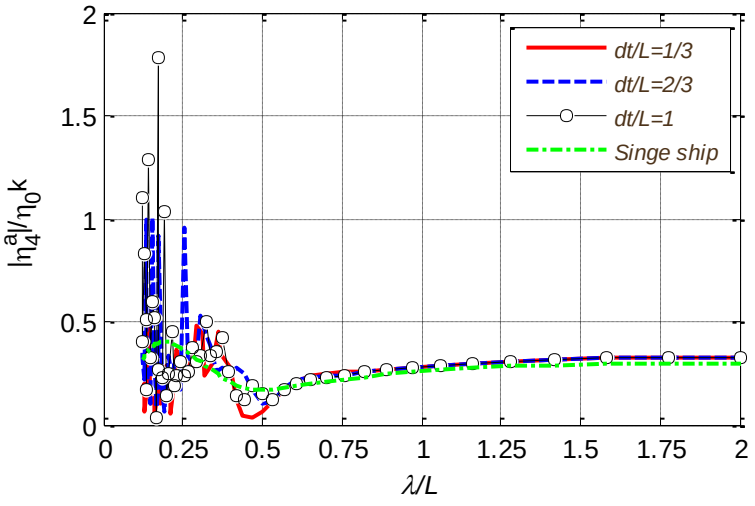

(c)

Figure 7.12: Response amplitude operators of Ship_a (Lee side) with different separation distance in beam waves. (a) Sway; (b) Heave; (c) Roll.

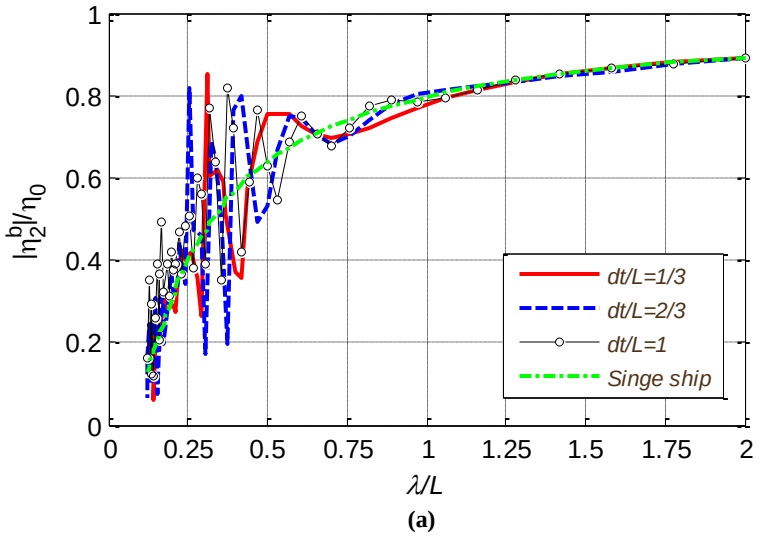

(a)

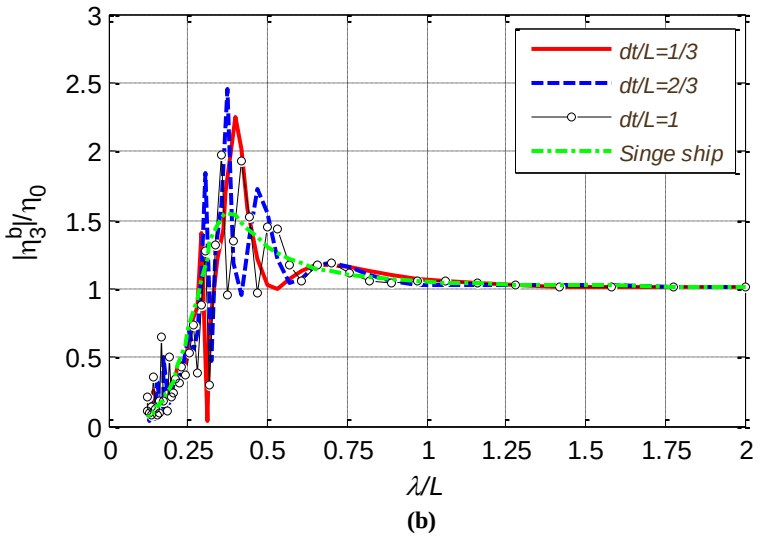

(b)

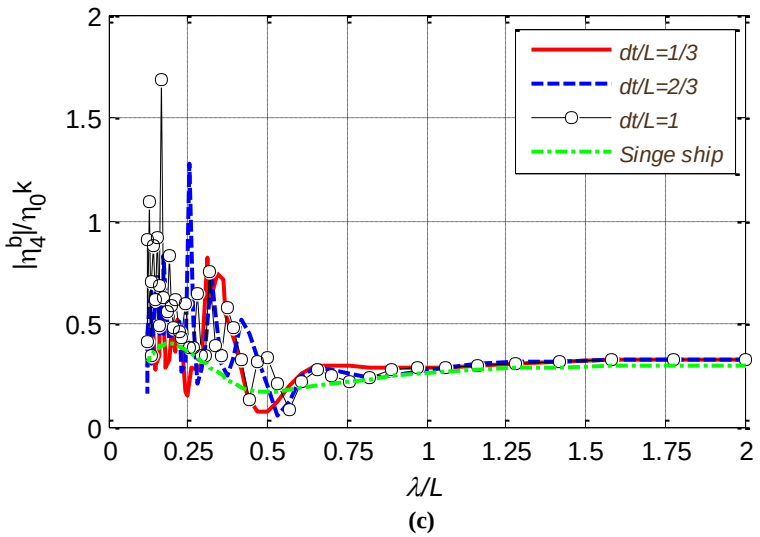

(c)

Figure 7.13: Response amplitude operators of Ship_b (Weather side) with different separation distance in beam waves. (a) Sway; (b) Heave; (c) Roll.

7.6. Effects of mooring lines, hawsers and fenders

In order to investigate the effects of the mooring lines and fenders, the model of a modified Wigley hull (Ship_a) and a rectangular box (Ship_b) model in Section 7.3 is used. The main dimensions of the modified Wigley and the rectangular box are shown in Table 7.1. The computational domain and panel distribution is shown in Figure 7.1. The rectangular box represents a floating platform or FPSO, while the modified Wigley hull represents the shuttle tanker. These two floating objects are stationary in beam waves (Ship_a is in the weather side and Ship_b is in the lee side) with the water depth of $d = 0.5\ m$. The transverse distance dt is fixed at 0.5 m. The rectangular box is moored by a spread catenary mooring system composed of four symmetrical arranged mooring lines, as shown in Figure 7.14. The physical property of each mooring line is given in

Table 7.2. To simplify the solution, the inelastic catenary equations (Faltinsen, 1993) will be used here to analyse the effects of the mooring lines.

The effects of hawsers and fenders are also taken into account in the present study. The arrangement of the hawsers and fenders is shown in Figure 7.14. Within the frame work of linear assumption, the effects of the hawsers and fenders can be simplified as a series of springs with constant stiffness. In the present study, the stiffness of the fender is given by: $k_1 = k_2 = k_3 = 26\ N/m$; the stiffness of the hawser is given by: $k_4 = k_5 = 34\ N/m$. The fender $\boldsymbol{k_2}$ is placed at the mid-ship. The distance between $\boldsymbol{k_1}$ ($\boldsymbol{k_4}$) and $\boldsymbol{k_2}$ is the same as the distance between $\boldsymbol{k_3}$ ($\boldsymbol{k_5}$) and $\boldsymbol{k_2}$, which is given by: $d_s = 0.75\ m$.

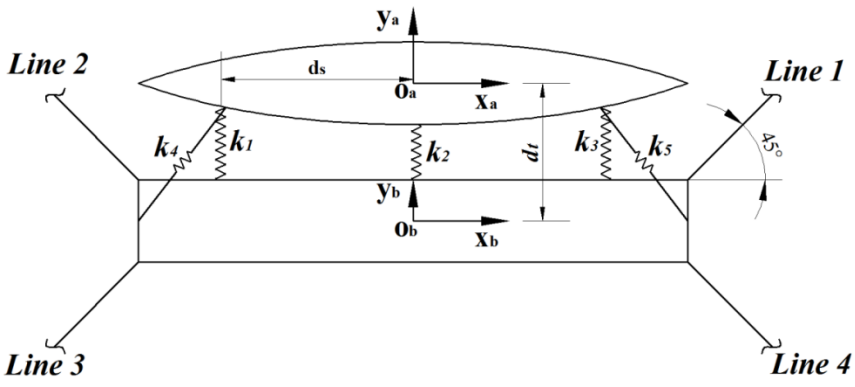

Figure 7.14: The sketch of mooring and fender system of a coupled model of a modified Wigley hull and a rectangular box.

Table 7.2: Physical properties of the mooring lines.

Length (*m*)	3.33
Diameter (*mm*)	6
Axial stiffness (*N*)	430
Wet Weight (*N/m*)	1.76
Horizontal pretension (*N*)	5
Water depth (*m*)	0.5
Coordinate of fairlead 1 (*m*)	(1, 0.15, 0)
Coordinate of fairlead 2 (*m*)	(-1, 0.15, 0)
Coordinate of fairlead 3 (*m*)	(-1, -0.15, 0)
Coordinate of fairlead 4 (*m*)	(1, -0.15, 0)

Due to the effects of the mooring and fender system, the coupled motion equations in Eqs. (3.37)-(3.38) become

$$\sum_{j=1}^{6}\left\{\left[-\omega_e^2\left(M_{ij}^{a}+\mu_{ij}^{aa}\right)+i\omega_e\lambda_{ij}^{aa}+K_{ij}^{a}+K_{ij}^{Fa}\right]\eta_j^{a}+\left[-\omega_e^2\mu_{ij}^{ab}+i\omega_e\lambda_{ij}^{ab}-K_{ij}^{Fb}\right]\eta_j^{b}\right\}=F_i^{Wa},\ i=1,2,...,6 \tag{7.2}$$

$$\sum_{j=1}^{6}\left\{\left[-\omega_e^2\mu_{ij}^{ba}+i\omega_e\lambda_{ij}^{ba}-K_{ij}^{Fa}\right]\eta_j^{a}+\left[-\omega_e^2\left(M_{ij}^{b}+\mu_{ij}^{bb}\right)+i\omega_e\lambda_{ij}^{bb}+K_{ij}^{b}+K_{ij}^{Mb}+K_{ij}^{Fb}\right]\eta_j^{b}\right\}=F_i^{Wb},\ i=1,2,...,6 \tag{7.3}$$

in which K_{ij}^{Fa} denotes the restoring matrix of Ship_a produced by the fender and hawser system, K_{ij}^{Fb} is the restoring matrix of Ship_b produced by the fender and hawser system, K_{ij}^{Mb} represents the restoring matrix of Ship_b produced by the mooring system.

Figure 7.15 shows the results of the response amplitude operators of both ships with or without the mooring and fender system. As illustrated by Ji and Yuan (2014), the mooring lines can significantly influence the low frequency responses of the vessels. However, in the wave frequency range, the influence on RAO from the mooring system is not evident. Since the heave motion is dominated by the wave frequency response, the discrepancies of the RAOs with or without mooring system are quite small, as shown in Figure 7.15 (b). For the sway and roll motions, both low frequency

and wave frequency responses are important. It can be seen from Figure 7.15 (a) and (c) that at low range of λ / L (high frequency), the difference between the RAOs with or without mooring and fender system is very small. As λ / L increases, the corresponding frequency decreases and the discrepancies tend to increase.

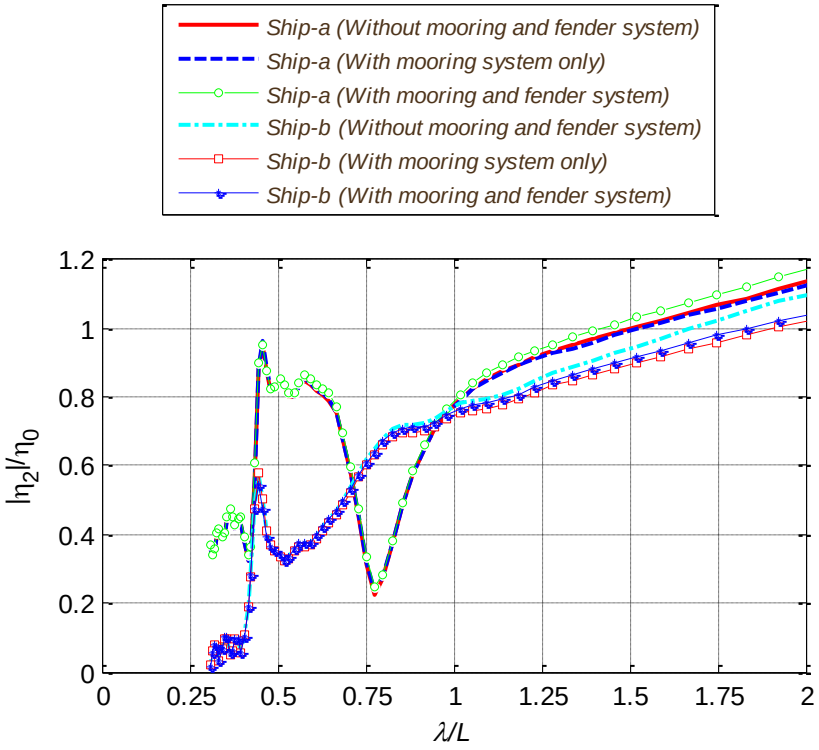

(a)

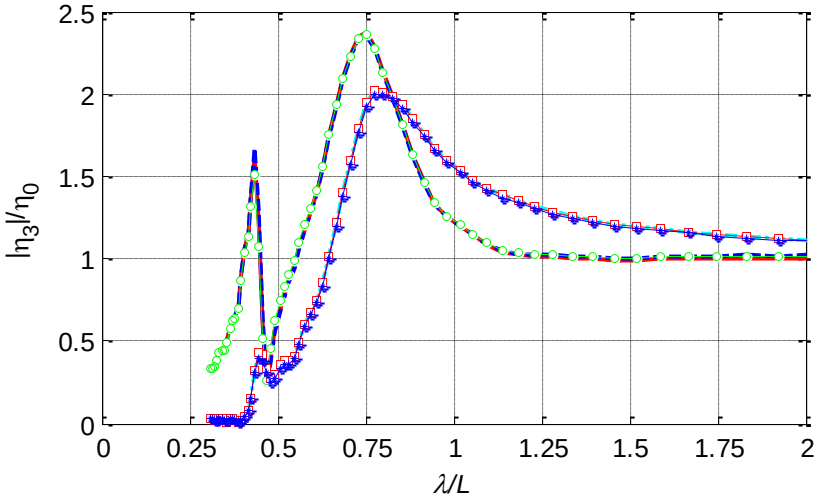

(b)

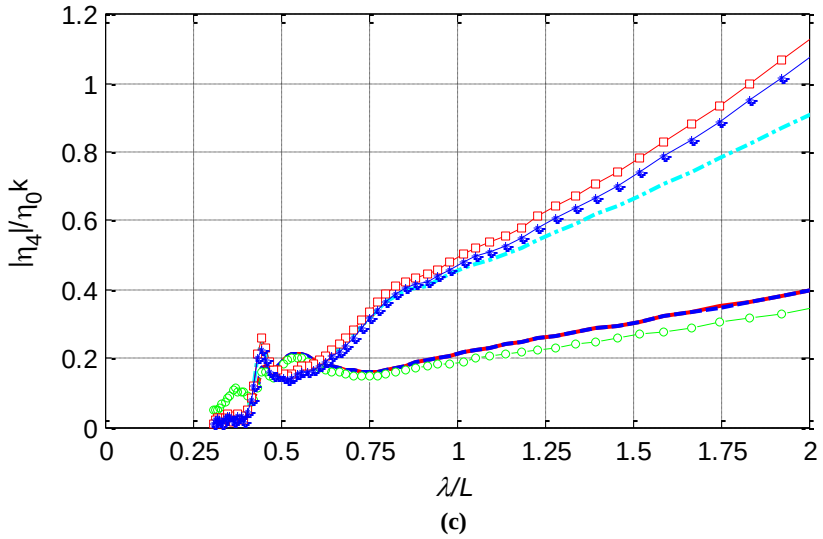

(c)

Figure 7.15: Response amplitude operators of Ship_a (Weather side) and Ship_b (Lee side) with or without mooring and fender system in beam waves. (a) Sway; (b) Heave; (c) Roll.

We notice that the motion RAOs with fender system could be even higher than these without fenders and hawsers, as shown in Figure 7.15 (a). In order to investigate the effects of the fenders and hawsers, 4 cases with different spring stiffness are studied here. The stiffness of the fenders and hawsers for these 4 cases are given in Table 7.3. Figure 7.16 shows the sway RAO of Ship_a (Weather side) and Ship_b (Lee side) for different cases. It can be found that as the stiffness of the fenders increases from 0 *N/m* to 78 *N/m* (from 0 *N/m* to 102 *N/m* for the hawsers), the motion responses of both ships keep an increase trend. However, as the stiffness of the fenders and the hawsers increases to a very large value (the infinity stiffness represents the rigid connection), the motion responses become smaller and the sway motion of Ship_a is identical to that of Ship_b due to the rigid connection.

Table 7.3: The stiffness of the fenders and hawsers for different cases.

No.	Case 1	Case 2	Case 3	Case 4
k_1 *(N/m)*	0	26	78	Infinity
k_2 *(N/m)*	0	26	78	Infinity
k_3 *(N/m)*	0	26	78	Infinity
k_4 *(N/m)*	0	34	102	Infinity
k_5 *(N/m)*	0	34	102	Infinity

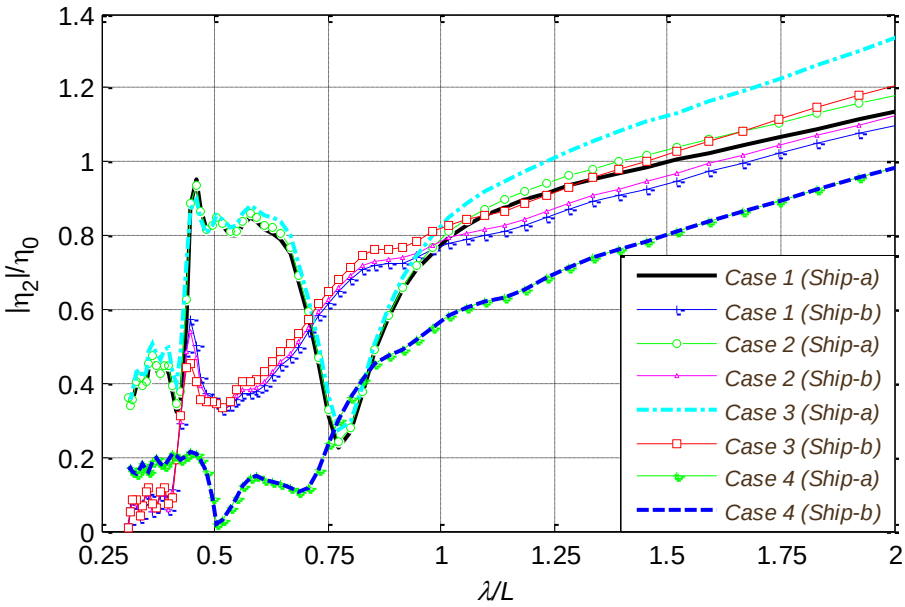

Figure 7.16: Sway response amplitude operator of Ship_a (Weather side) and Ship_b (Lee side) for different cases in beam waves.

7.7. Summary

In this chapter, we validated the present 3-D Rankine source panel method by solving the hydrodynamic interaction problem of two ships stationary in head and beam waves. We examined the hydrodynamic coefficients, wave excitation forces and motion responses and established the comparisons between the present calculations and the commercial software as well as the experimental data. Very good agreement has been achieved which illustrates that the present program is a useful tool to predict the hydrodynamic behaviours of two ships arranged side by side without forward speed. We also calculated the motion responses of both ships at different water depths and separation distances. It was found that the effect of the water depth and separation distance is very important. The discussion in this chapter was highlighted on the effects of mooring and fender system. We found that the influence of the mooring lines, fenders and hawsers on the motion responses of both ships is not evident.

8. Validations and discussion of two ships advancing in waves

8.1. Introduction

Ship-to-ship with forward speed problem occurs in harbor area and waterways with dense shipping traffic as the vessels have to pass each other in close proximity; between tugs and vessels during escorting or maneuvering and berthing operations as well as during ship-to-ship operations for cargo transfers during oil and gas offloading operations. The behavior of two ships in waves with speed effect is of special concern to the Navy, that is, for underway replenishment, and for other commercial purposes. Because of the hydrodynamic interactions, even relatively small wave can induce large motions of the smaller ship due to the nearness of the larger ship. When the ships are travelling with forward speed, the hydrodynamic interactions become more complicated.

In this chapter, the 3-D Rankine source method will be extended to investigate the hydrodynamic interactions between two ships arranged side by side with forward speed. The radiation condition is satisfied by using a modified Sommerfeld radiation condition which takes into account the Doppler shift of the scattered waves. This new radiation condition is applicable to a wide range of forward speeds, including very low forward speed problem where the Brard number is smaller than 0.25. The numerical solution is evaluated by applying the present method to two pairs of models in head seas. Model 1 is about a full scale supply ship and frigate model, and Li's model test results (Li, 2007) will be used to validate the present numerical calculation. Model 2 is a tanker and LNG ship model in model scale, and Ronæss' experiments (Ronæss, 2002) will provide the motion responses for validation. The hydrodynamic coefficients and wave excitation forces are investigated and a very large sway force is predicted when the transverse distance between two ships equalled to the wave length. The wave elevations in the gap will be also calculated. Discussions are highlighted on the effect of the radiation conditions.

8.2. Validation of Model 1

8.2.1. Description of the model

The main particulars of the supply ship (Ship_a) and frigate (Ship_b) are shown in Table 8.1. The transverse and longitudinal distances between two ships are 52.702 *m* and 0 *m* respectively. A typical case is simulated here: head sea with forward speed of 6.18 *m/s*. To be consistent with the model tests condition, both ships are restrained in surge, sway and yaw while the motions in heave, roll and pitch are free. In order to make comparison, we also present the numerical results of two ships at zero forward speed. The computational domain is shown in Figure 8.1. The free surface is truncated at L_a upstream, $2L_a$ downstream, L_a in the supply ship sideward and L_b in the frigate sideward. There are 378 panels on the body surface of supply ship, 5400 on free surface, 2432 on the control surface and 414 on the body surface of frigate.

Table 8.1: Main particulars of supply ship and frigate (Li, 2001).

	Supply ship	Frigate
Length between perpendicular	L_a = 180 *m*	L_b = 122 *m*
Breadth	B_a = 30.633 *m*	B_b = 14.78 *m*
Draught	T_a = 8.5 *m*	T_b = 4.5 *m*
Displacement	V_a = 28223.3 *t*	V_b = 4023.7 *t*
Block coefficient	C_B^a = 0.588	C_B^b = 0.484
Longitudinal CoG (rel. midship)	X_G^a = -1.688 *m*	X_G^b = 3.284 *m*
Vertical CoG (rel. calm waterline)	Z_G^a = 3.925 *m*	Z_G^b = 2.049 *m*
Radius of inertia for roll	r_{44}^a = 8.047 *m*	r_{44}^b = 4.921 *m*
Radius of inertia for pitch	r_{55}^a = 45 *m*	r_{55}^b = 30.5 *m*
Radius of inertia for yaw	r_{66}^a = 45 *m*	r_{66}^b = 30.5 *m*

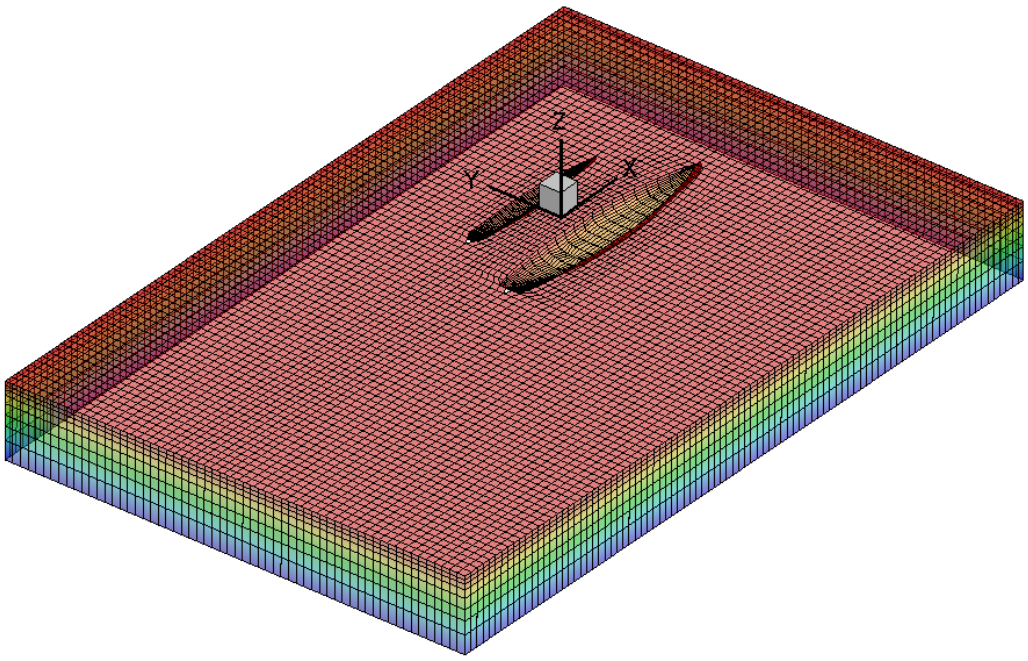

Figure 8.1: Computational domain and panel distribution of Ship_a and Ship_b in head waves.

8.2.2. Results and discussions

Figure 8.2 shows the response amplitudes of two ships in heave, roll and pitch motions. The comparisons with experimental data and Green function method (Li, 2007) are also included. The numerical results calculated by the present 3-D Rankine source method generally agree with the experimental data. In order to investigate the speed effect, we also present the results of two ships without forward speed. It can be observed that the increase of the response amplitude operators with forward speed is considerable, especially for the smaller ship (Ship_b). Roll motion of Ship_a is obviously reduced due to the forward speed. But for Ship_b, the roll motion increases dramatically at $\lambda/L > 1$ due to the forward speed. In heave and pitch motions, there are also some discrepancies between the predictions and measurements, especially in the long wave case. There are two aspects to explain these discrepancies. The first reason should be the model test set-up. From the published work, only three model tests can be found on ship-to-ship with forward speed problem (Li, 2001; Ronæss, 2002; Xu and Dong, 2013). It was found that the model test set-up was very challenging, especially for the measurement of roll motion. The second reason is the numerical program. The present potential flow program is based on the linear assumption. It can be found in Figure 8.2 that the greatest discrepancies between

measured and predicted motions generally occur at long wave length. In these conditions, the motions of Ship_b are very large, especially in roll motion. It violates the linear assumption. Even for the model test, as demonstrated by Li (2003), the experiments could not be completed for the highest two wavelengths due to excessive motions of the Ship_b (roll amplitude exceeds 30 degrees). Furthermore, the hydrodynamic interactions between these two ships are also very important. The motions of the larger ship (Ship_a) could influence the motions of smaller ship (Ship_b) significantly. The large amplitude roll motion is coupled with the heave and pitch motions, which is different from the single ship problem. The unpredictable roll motion in long wave length could also influence the predictions of heave and pitch motions.

We also find the roll motions of both ships are significantly influenced by the roll damping coefficient. It is found that the damping in roll cannot be predicted well by the radiation component only (Chakrabarti, 2001). The difficulty in predicting the roll motion arises from the nonlinear characteristics of roll due to the effect of fluid viscosity. In ship-to-ship problem, the roll motion is always remarkable due to the hydrodynamic interaction between two ships. The present potential flow theory is based on the assumption that the surrounding fluid is inviscid and it cannot predict the roll damping precisely. To complement the viscid component, an equivalent linear damping coefficient is applied in the present study. The non-dimensional roll damping coefficient, κ, is given by

$$\kappa = \frac{\lambda_{44} + \lambda_{44v}}{2 \cdot \sqrt{(I_{44} + \mu_{44}) \cdot K_{44}}} \tag{8.1}$$

where λ_{44v} is the viscous damping. This damping coefficient is written as a fraction between the actual damping coefficient, $\lambda_{44} + \lambda_{44v}$, and the critical damping coefficient, $2 \cdot \sqrt{(I_{44} + \mu_{44}) \cdot K_{44}}$. Figure 8.3 is the numerical results of roll motion amplitudes of two ships at different damping coefficients. We find that $\kappa_a = 0.2$ and $\kappa_b = 0.6$ agree with the experimental results better than other values. This is because the roll motion of Ship_a is relatively small, while the roll motion of Ship_b is extremely large. Correspondingly, the nonlinear viscous characteristics of roll motion of Ship_b are

more obvious. A larger equivalent linear damping coefficient should be used in the numerical simulations.

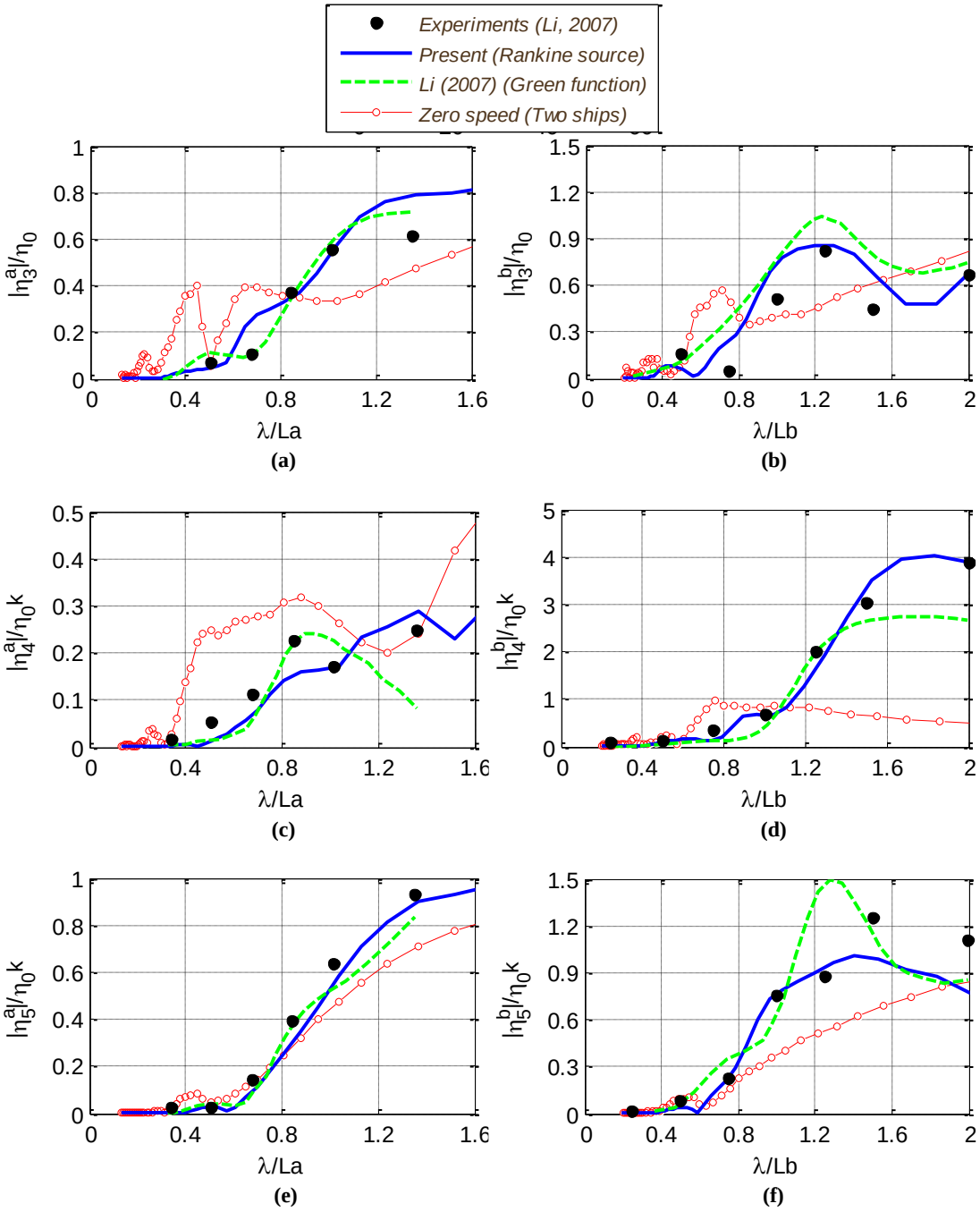

Figure 8.2: Response amplitude operators. (a) Heave of Ship_a; (b) Heave of Ship_b; (c) Roll of Ship_a; (d) Roll of Ship_b; (e) Pitch of Ship_a; (f) Pitch of Ship_b.

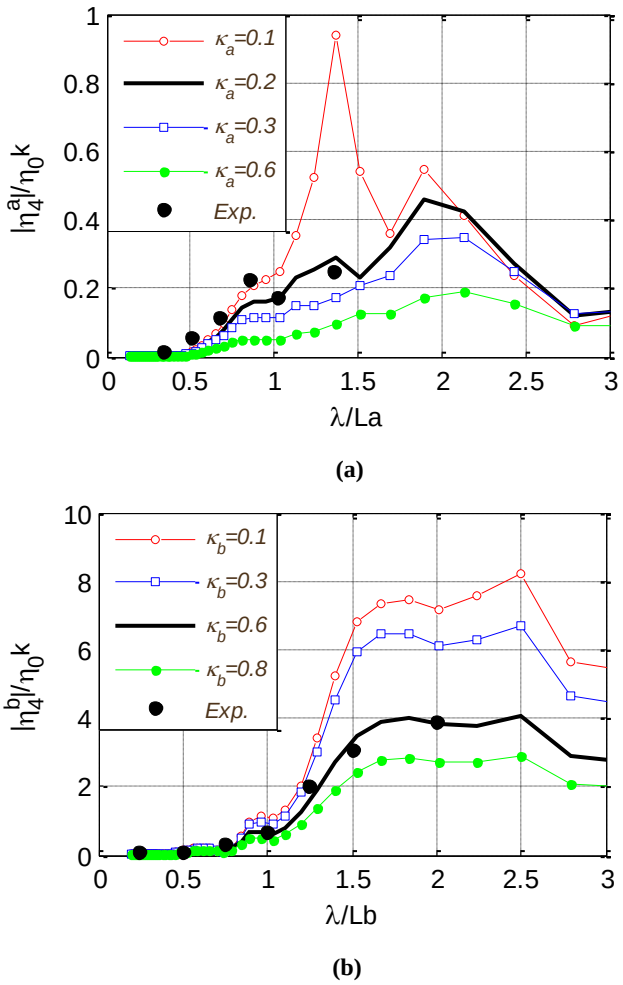

Figure 8.3: Roll motion amplitudes at different damping coefficients. (a) Ship_a; (b) Ship_b.

8.3. Validation of Model 2

8.3.1. Description of the model

The main particulars of the tanker (Ship_a) and LNG (Ship_b) are shown in Table 8.2. The details of model test set-up is elaborated by Ronæss (2002). She analysed the bias sources and carried out comparative study. She found that the experimental setup corrections were necessary and in the present calculation, such corrections will be used, as shown in Table 8.3. The forced roll centre is taken to be 0.032 *m* below the mean water level for Ship_a and 0.104 *m* above the mean water level for Ship_b. To be consistent with the model tests condition, Ship_a is restrained in surge and sway while the motions in heave, roll, pitch and yaw are free; Ship_b is restrained in surge, sway and yaw while the other degrees of freedom are set free. Two typical cases are studied here to simulate the different configurations of ship-to-ship problem. In Case 1, the

transverse and longitudinal distances between two ships are 1.25 *m* and 0.09 *m* respectively, which indicates that the longitudinal centre of these two ships are approximately the same. In Case 2, the longitudinal centre of two ships is staggered and the transverse and longitudinal distances between two ships are 1.25 *m* and 0.59 *m* respectively. Both cases are in head sea condition with forward speed of 0.608 *m/s* ($Fn = u_0 / \sqrt{gL_a} = 0.1$). In order to make comparison, we also present the results of single ship with the same forward speed and two ships at zero forward speed. The computational domain of Case 1 is shown in Figure 8.4. The free surface is truncated at 1.05L_a upstream, 1.84L_a downstream, 1.05 L_a in the tanker sideward and 1.3 L_b in the LNG ship sideward. There are 420 panels on the body surface of tanker, 9020 on free surface, 2464 on the control surface and 420 on the body surface of LNG ship.

Table 8.2: Main particulars of tanker and LNG ship (Ronæss, 2002)

	Tanker	LNG ship
Length between perpendicular	L_a = 3.76 *m*	L_b = 2.28 *m*
Breadth	B_a = 0.625 *m*	B_b = 0.387 *m*
Draught	T_a = 0.232*m*	T_b = 0.124 *m*
Displacement	V_a = 0.4355 *t*	V_b = 0.074 *t*
Block coefficient	C_B^a = 0.83	C_B^b = 0.68
Water plane area coefficient	C_p^a = 0.90	C_p^b = 0.79
Longitudinal CoG (rel. midship)	X_G^a = 0.086 *m*	X_G^b = -0.01 *m*
Vertical CoG (rel. calm waterline)	Z_G^a = -0.052 *m*	Z_G^b = 0.012 *m*
Radius of inertia for roll	r_{44}^a = 0.175 *m*	r_{44}^b = 0.103 *m*
Radius of inertia for pitch	r_{55}^a = 1.008 *m*	r_{55}^b = 0.604 *m*
Radius of inertia for yaw	r_{66}^a = 1.008 *m*	r_{66}^b = 0.604 *m*

Table 8.3: Corrections for model set-up of Ship_b, non-dimensionalized using ρ, V_b, L_b, g and A_{wb}. (Ronæss, 2002)

Component, *i j*	33	55	35, 53
Additional inertia, I_{ij}	1.6E-01	5.5E-02	-7.2E-04
Additional damping, B_{ij}	5.2E-03	1.6E-03	-2.6E-03
Additional restoring, C_{ij}	4.8E-04	1.5E-04	-2.1E-06

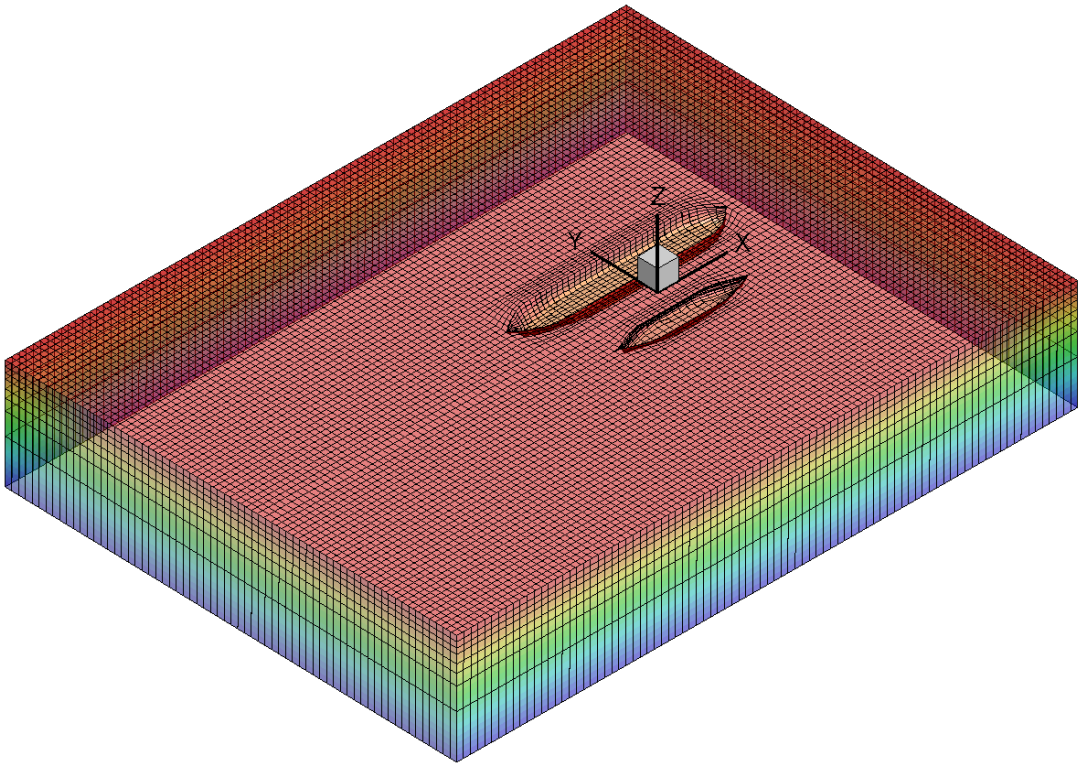

Figure 8.4: Computational domain and panel distribution of Ship_a and Ship_b model in head waves.

8.3.2. Motion responses

Figure 8.5 and Figure 8.6 are the response amplitudes of Case 1 and Case 2 respectively. The comparisons with experimental data and unified theory are also included. The present results in heave and pitch motion of both ships generally have a satisfied agreement with those of experimental data. A noticeable discrepancy in Case 1 can be observed in Figure 8.5 (a) and Figure 8.5 (e) at $\lambda/L_a = 1.2$ and $\lambda/L_a = 1.3$, which corresponds to the resonant frequency of heave and pitch of Ship_a respectively. Such discrepancy can also be observed in Case 2 from Figure 8.6 (a) and Figure 8.6 (e). But the resonant frequency in the numerical calculation is around $\lambda/L_a = 1$ for both heave and pitch of Ship_a. This difference is attributed to the trim suspensions in the model test set-up (Ronæss, 2002). When it comes to roll, the present prediction, as well as Ronæss' (2002) calculation, is not satisfactory. The main reason for the discrepancies is about the damping coefficient. According to Ronæss (2002), the roll viscous damping of Ship_a is taken as $\lambda_{44v} = 2\lambda_{44}$ for the forward speed case and $\lambda_{44v} = \lambda_{44}$ for the zero speed case. For Ship_b, it is taken as $\lambda_{44v} = 6\lambda_{44}$ for the forward speed case and $\lambda_{44v} = 4\lambda_{44}$ for the zero speed case. The lift damping is another factor, which will

increase when the roll centre is above the mean water level (Himeno, 1981). Besides, the measurement of roll motions from the model test is full of challenges. The devices used to measure the roll motion could bring additional friction and upward forces, as demonstrated by Ronæss (2002). In order to investigate the speed effect, the results of two ships without forward speed are presented. It is found that the increase of the response amplitude operators with forward speed is considerable for both Case 1 and Case 2. We also include the results of single ship with forward speed. From the comparison, we find that the hydrodynamic interaction has much greater influence on the motions of the smaller ship. For heave and pitch motion of the larger ship (Ship_a), the influence from the smaller ship (Ship_b) is not noticeable. But the hydrodynamic interaction is the essential reason that induces the roll motion for both ships. There is no roll motion in head sea condition for a single ship due to the symmetrical characteristics.

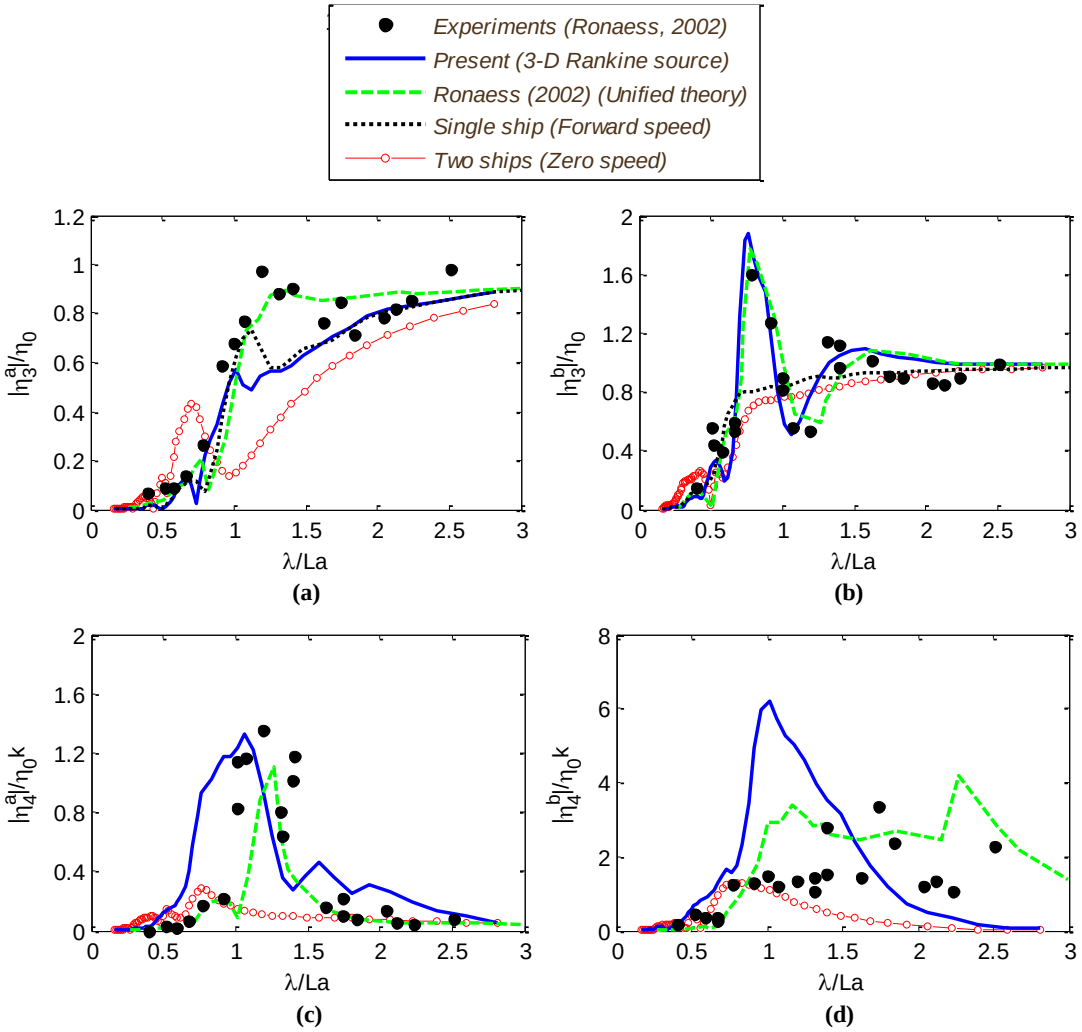

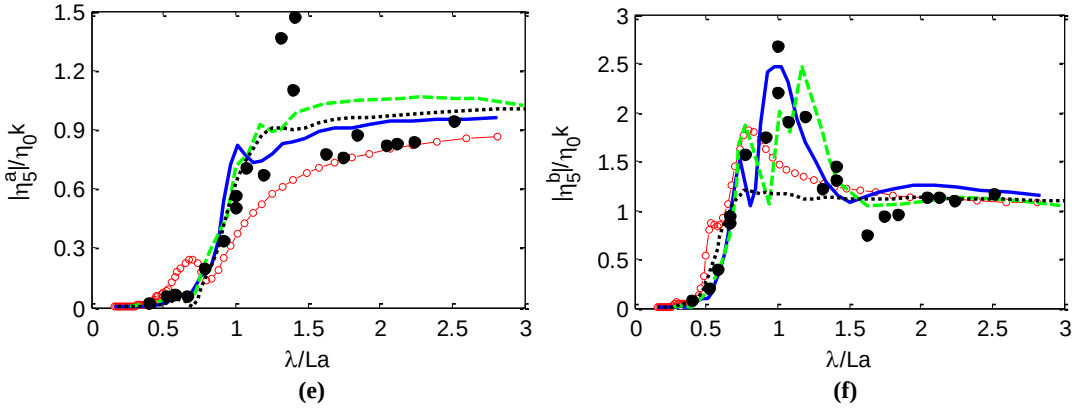

Figure 8.5: Response amplitude operators of Case 1. (a) Heave of Ship_a; (b) Heave of Ship_b; (c) Roll of Ship_a; (d) Roll of Ship_b; (e) Pitch of Ship_a; (f) Pitch of Ship_b.

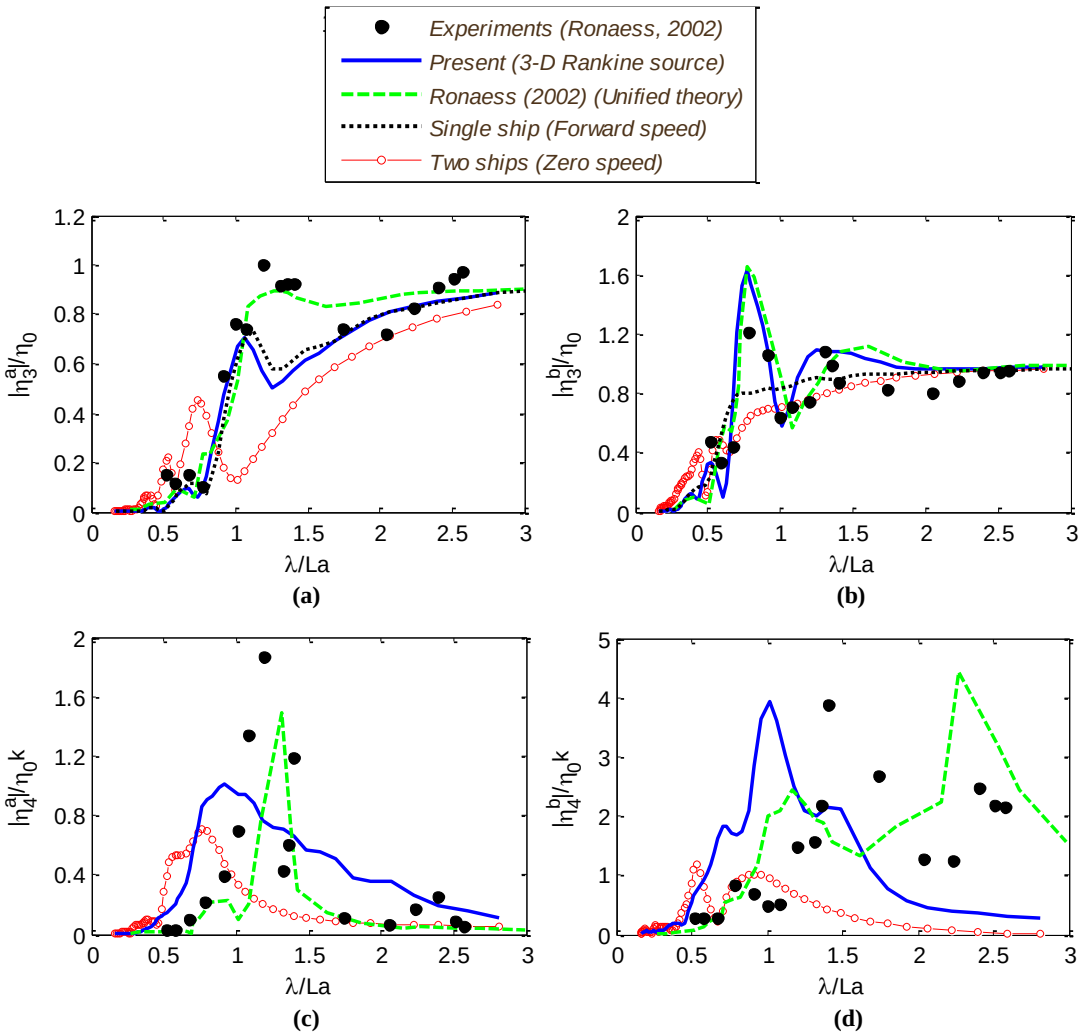

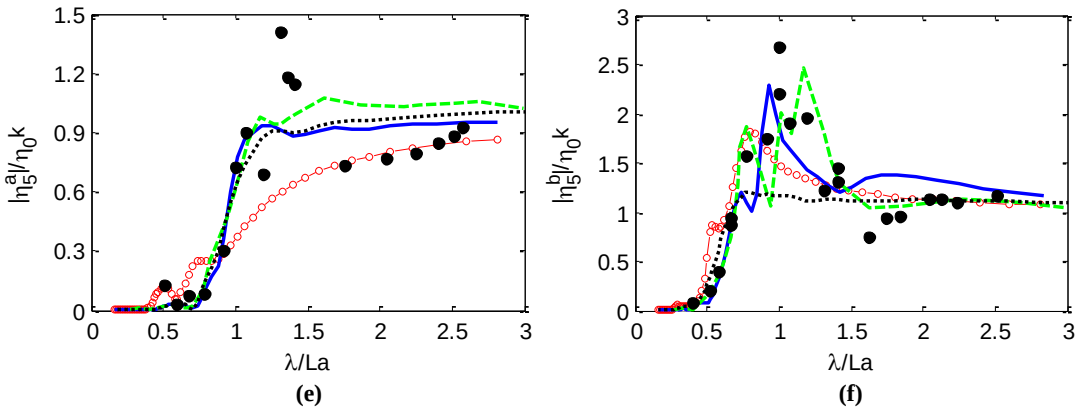

Figure 8.6: Response amplitude operators of Case 2. (a) Heave of Ship_a; (b) Heave of Ship_b; (c) Roll of Ship_a; (d) Roll of Ship_b; (e) Pitch of Ship_a; (f) Pitch of Ship_b.

8.3.3. Hydrodynamic coefficients

Figure 8.7 and Figure 8.8 are the non-dimensional added mass and damping coefficients respectively. The first comparison should be made from the added mass and damping of Ship_a. The hydrodynamic coefficients of Ship_a are composed of two components, self-induced component (labelled by *aa* as its superscript, e.g. μ_{ij}^{aa}) and external-induced component (labelled by *ab* as its superscript, e.g. μ_{ij}^{ab}). From Figure 8.7 (a)-(d) and Figure 8.8 (a)-(d), we find the self-induced hydrodynamic coefficients of Ship_a are much greater than the external-induced ones, which indicates that the hydrodynamic coefficients of Ship_a are mainly determined by the oscillation of Ship_a itself. The hydrodynamic coefficients of Ship_a induced by the oscillation of Ship_b are not significant compared to the self-induced component. This can explain why the hydrodynamic interaction has less influence on the motions of the larger ship in Figure 8.5 (a), (e) and Figure 8.6 (a), (e). But when it comes to the hydrodynamic coefficients of Ship_b, the self-induced and external-induced components are at the same level. This can explain why the hydrodynamic interaction has much greater influence on the motions of the smaller ship in Figure 8.5 (b), (f) and Figure 8.6 (b), (f). Particular attention should be paid on the roll added mass and damping. Since the models are restrained in surge and sway (Ship_b is also restrained in yaw), the roll added mass is mainly composed of roll-induced, heave-induced and pitch-induced components, which are shown in Figure 8.7 (d), (e) and (f) respectively. It is very interesting to find that the main contribution to the roll added mass comes from the heave-induced component, while the roll-induced component takes the

smallest part. It is not the case for heave added mass. As can be seen from Figure 8.7 (a) and (b) that the heave-induced heave added mass is much greater than the pitch-induced heave added mass. It can also be observed from Figure 8.7 (d)-(f) that the non-dimensional added mass of Ship_b is much greater than that of Ship_a, especially in heave-induced and pitch-induced components. Similar findings are also found in damping curves shown in Figure 8.8 (d)-(f). This explains why the hydrodynamic interaction brings a greater influence on the roll motion of the smaller ship, as shown in Figure 8.5 (c)-(d) and Figure 8.6 (c)-(d).

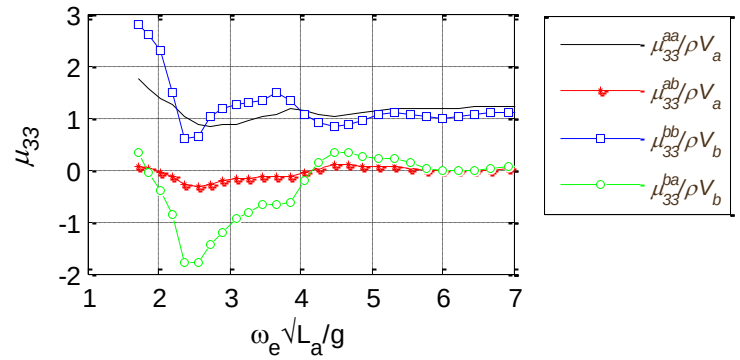

(a)

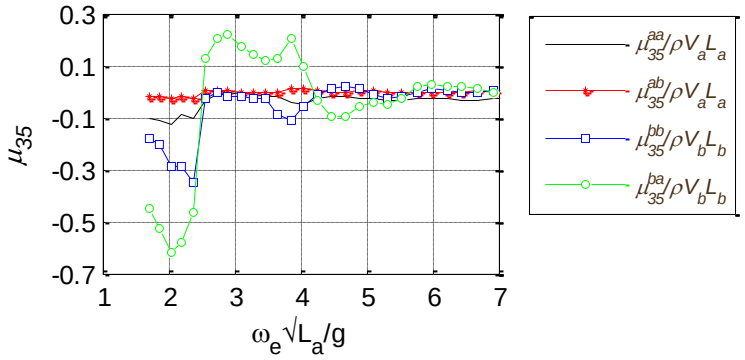

(b)

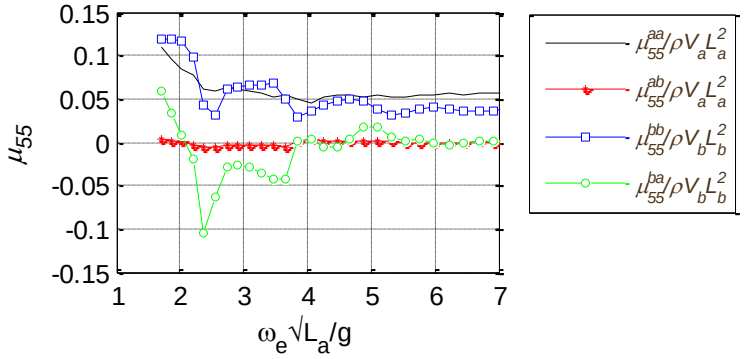

(c)

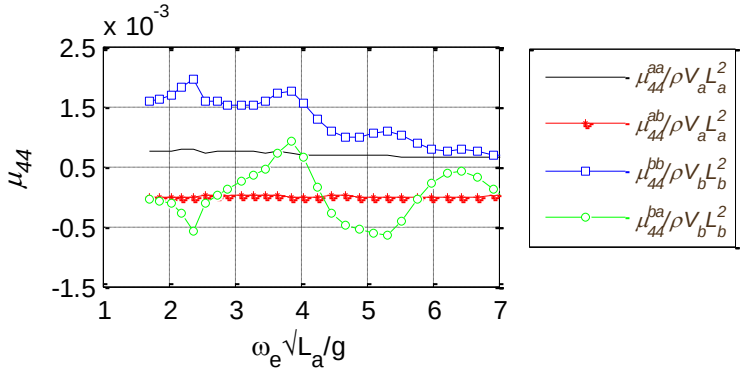

(d)

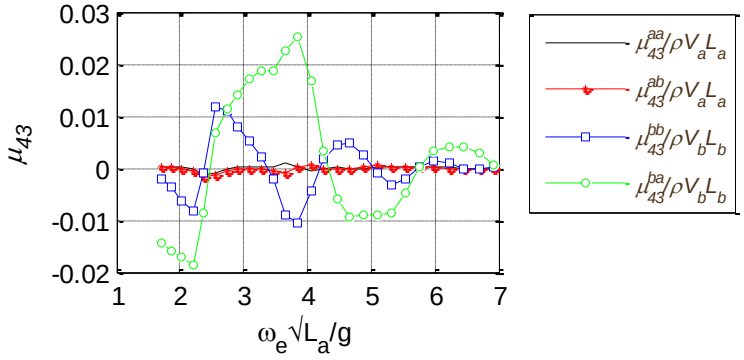

(e)

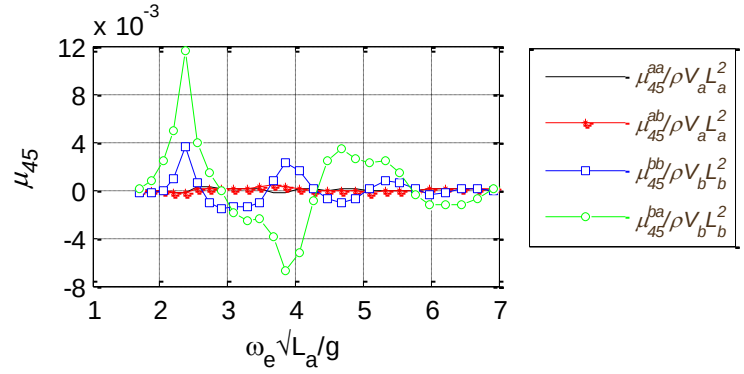

(f)

Figure 8.7: Added mass. (a) Heave added mass induced by heave motion; (b) Heave added mass induced by pitch motion; (c) Pitch added mass induced by pitch motion; (d) Roll added mass induced by roll motion; (e) Roll added mass induced by heave motion; (f) Roll added mass induced by pitch motion.

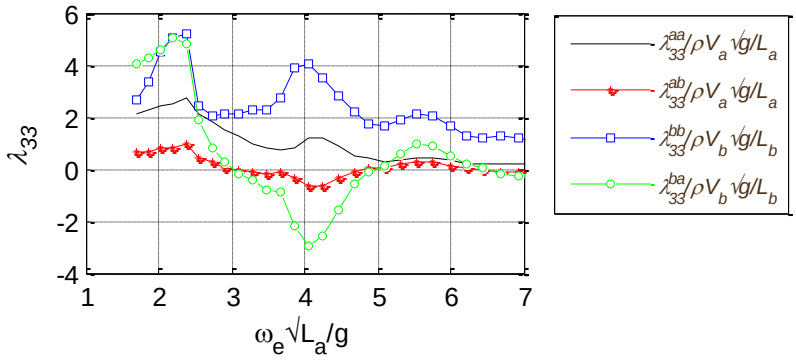

(a)

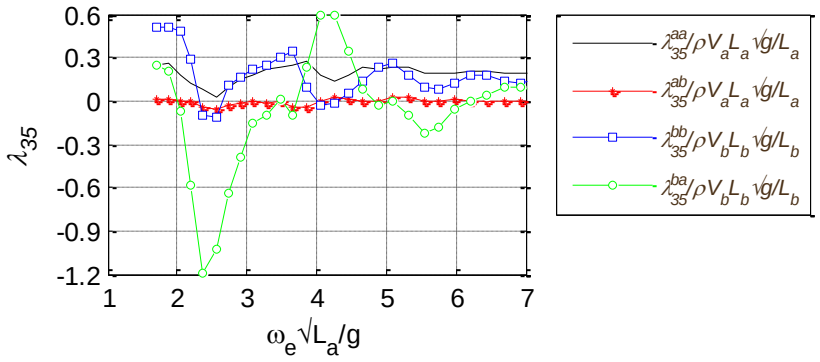
λ35
ωe√La/g
λ35aa/ρVaLa√g/La
λ35ab/ρVaLa√g/La
λ35bb/ρVbLb√g/Lb
λ35ba/ρVbLb√g/Lb

(b)

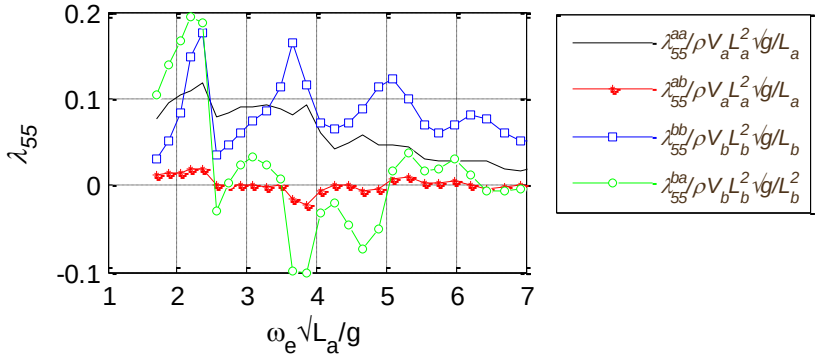
λ55
ωe√La/g
λ55aa/ρVaLa2√g/La
λ55ab/ρVaLa2√g/La
λ55bb/ρVbLb2√g/Lb
λ55ba/ρVbLb2√g/Lb2

(c)

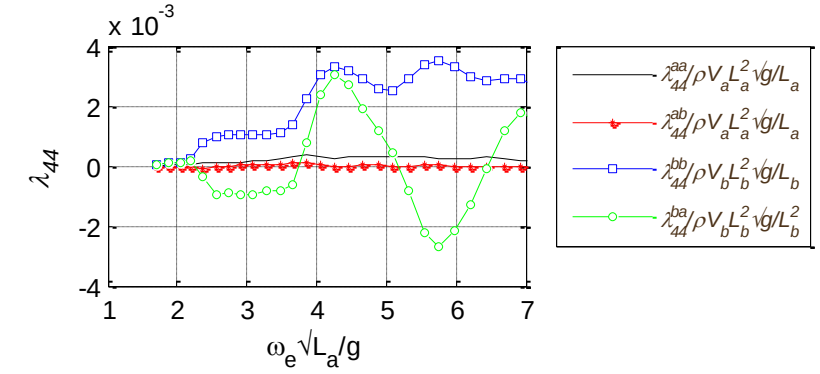
x 10-3
λ44
ωe√La/g
λ44aa/ρVaLa2√g/La
λ44ab/ρVaLa2√g/La
λ44bb/ρVbLb2√g/Lb
λ44ba/ρVbLb2√g/Lb2

(d)

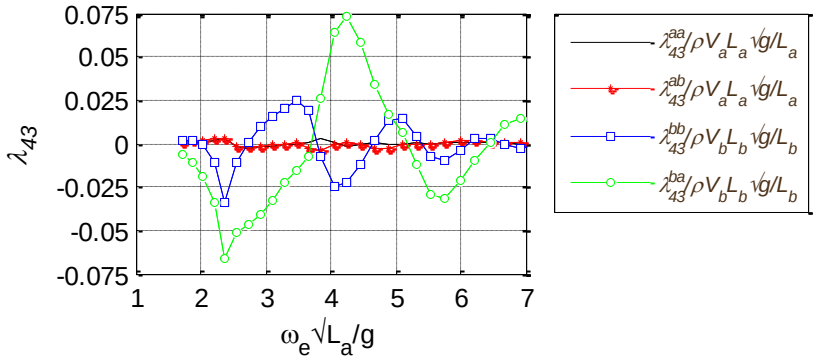
λ43
ωe√La/g
λ43aa/ρVaLa√g/La
λ43ab/ρVaLa√g/La
λ43bb/ρVbLb√g/Lb
λ43ba/ρVbLb√g/Lb

(e)

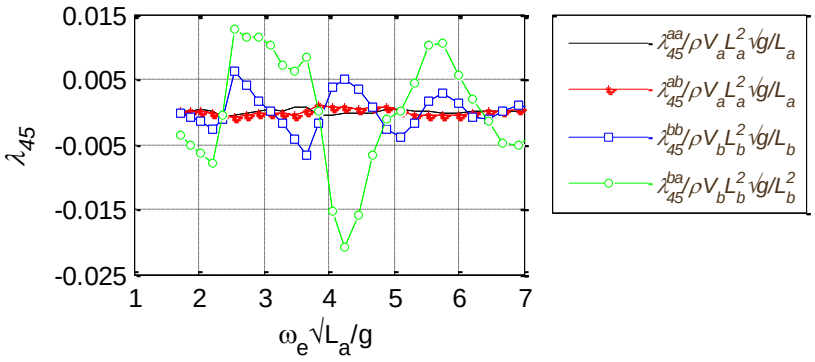

(f)

Figure 8.8: Damping. (a) Heave damping induced by heave motion; (b) Heave damping induced by pitch motion; (c) Pitch damping induced by pitch motion; (d) Roll damping induced by roll motion; (e) Roll damping induced by heave motion; (f) Roll damping induced by pitch motion.

8.3.4. Wave excitation forces

Figure 8.9 gives the non-dimensional wave excitation forces on both ships. Two large spikes can be observed in Figure 8.9 (a) - (b) for the zero speed cases of both ships at $\lambda/L_a = 0.33$, which corresponds to the wave length that equals to the transverse distance between two ships. At this wave length, the sway force can reach an extreme value, which could be twice as large as that at $\lambda/L_a = 1$. We also investigate the wave elevation at $\lambda/L_a = 0.33$, which is shown in Figure 8.10. The wave elevation in the gap between two ships can also achieve a considerable value. In this case, the ship-to-ship offloading operation will be at great risks. On the one hand, the large sway force will bring a huge separating load on the mooring lines between the two vessels; on the other hand, the large wave elevation in the gap will cause the green water problem, especially for the smaller ship with small freeboard. But in the forward speed cases, there is no large spike at $\lambda/L_a = 0.33$. This is because the Doppler shift modifies the wave length according to the propagation direction. It can also be observed in Figure 8.9 (b) that the non-dimensional roll moment on Ship_b is much greater than that on Ship_a. This can explain why the roll motion amplitude of Ship_b is much greater than that of Ship_a, which is shown in Figure 8.5 (c)-(d) and Figure 8.6 (c)-(d). Comparing the results of a single ship and two ships with forward speed in Figure 8.9 (c) and (e), we find the difference is not significant, which can explain why the motion responses of a single ship with forward speed are quite close to that of two ships' case, as shown in Figure 8.5 (a), (e) and Figure 8.6 (a), (e). From Figure 8.9 (d) and (f), we find the curves of the forces on Ship_b without interference are smoother. Some fluctuations

can be observed when Ship_a is in presence. A sudden increase of heave force on Ship_b at λ/L_a = 1.5 can be found in Figure 8.9 (e) for two ships with speed case, which results in an increase in heave motion as shown in Figure 8.5 (b), while a drop of pitch moment at λ/L_a = 1.5 in Figure 8.9 (f) can give an explain why the pitch motion experience a decrease at λ/L_a = 1.5 in Figure 8.5 (f).

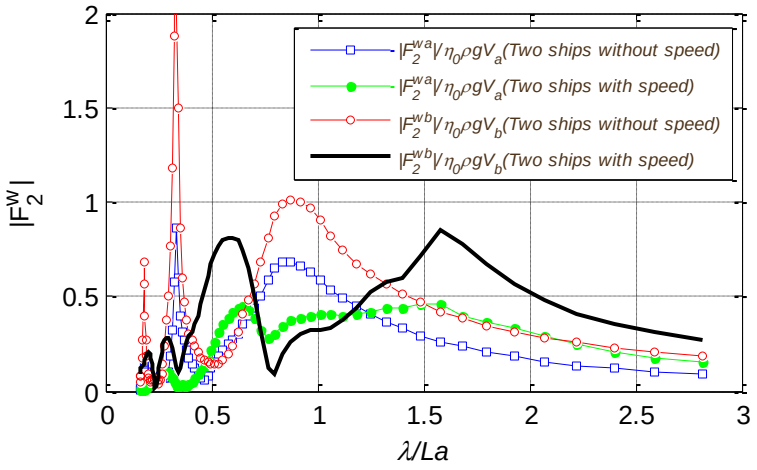

(a)

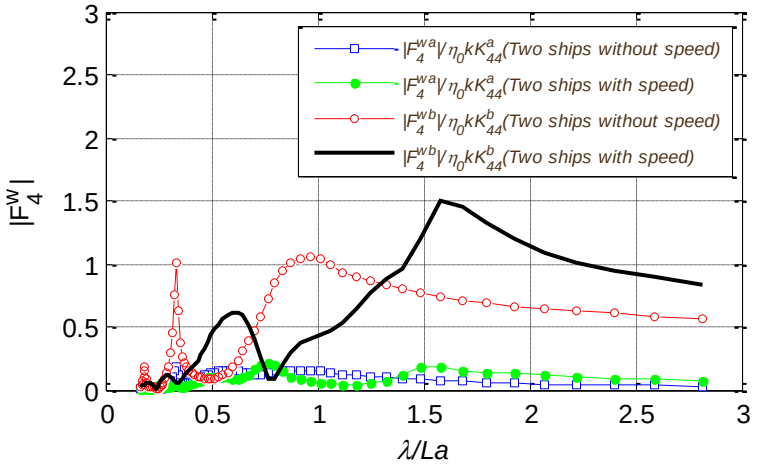

(b)

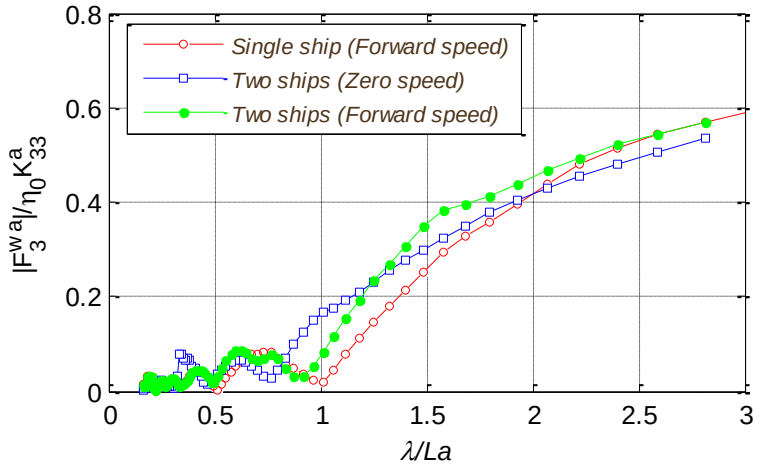
Single ship (Forward speed)
Two ships (Zero speed)
Two ships (Forward speed)
$|F_3^{wa}|/\eta_0 K_{33}^a$
λ/La

(c)

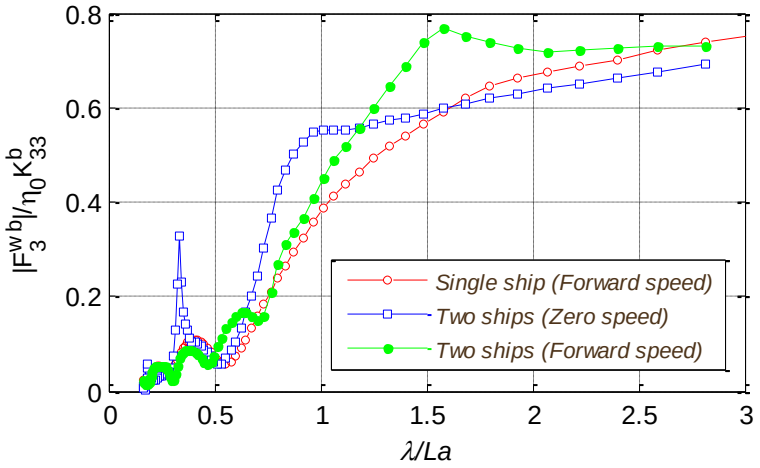
Single ship (Forward speed)
Two ships (Zero speed)
Two ships (Forward speed)
$|F_3^{wb}|/\eta_0 K_{33}^b$
λ/La

(d)

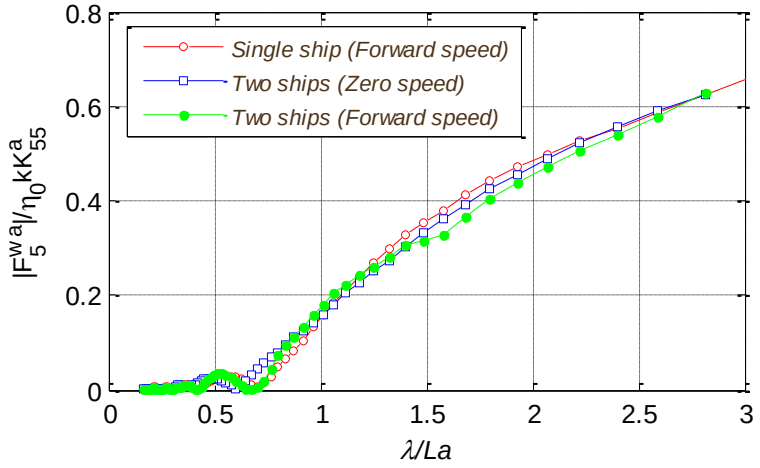
Single ship (Forward speed)
Two ships (Zero speed)
Two ships (Forward speed)
$|F_5^{wa}|/\eta_0 k K_{55}^a$
λ/La

(e)

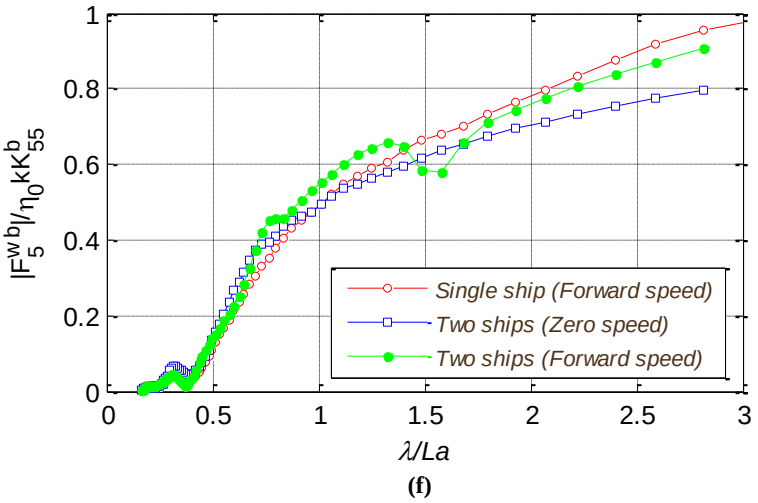

(f)

Figure 8.9: Wave excitation forces. (a) Sway forces on Ship_a and Ship_b; (b) Roll moments on Ship_a and Ship_b; (c) Heave force on Ship_a; (d) Heave force on Ship_b; (e) Pitch moment on Ship_a; (f) Pitch moment on Ship_b.

Figure 8.10 shows the wave elevation of two ships without forward speed at $\lambda = 1.25$ *m*, which corresponds to $\lambda/L_a = 0.33$. The wave elevation is non-dimensionalized by the incident wave amplitude η_0. The contour lines of the wave elevation in the gap between the two ships are presented on the top of each figure. The total wave elevation is composed of incident, diffraction and radiation components. Since the models are restrained in surge and sway (Ship_b is also restrained in yaw), the radiation component is mainly from the oscillation of heave, roll and pitch. From Figure 8.5 we can find the motion amplitudes at $\lambda/L_a = 0.33$ are very small and the corresponding radiated wave amplitude should also be at a small level. Therefore, the incident and diffraction components contribute for the major parts. In can be observed in Figure 8.10 (a) that the diffracted wave elevation in the gap is much higher than that outside the gap, which indicates that most of the diffracted wave energy is trapped in the gap. These trapped waves will inevitably induce an extremely inhomogeneous wave loads on both ships, which explains the enormous sway force and roll moment in Figure 8.9 (a) and (b). Meanwhile, from Figure 8.10 (b) we can also find that the longitudinal distribution of the wave elevation along Ship_b is not balanced. As a consequence, a yaw moment will be induced, which could produce a very large yaw motion.

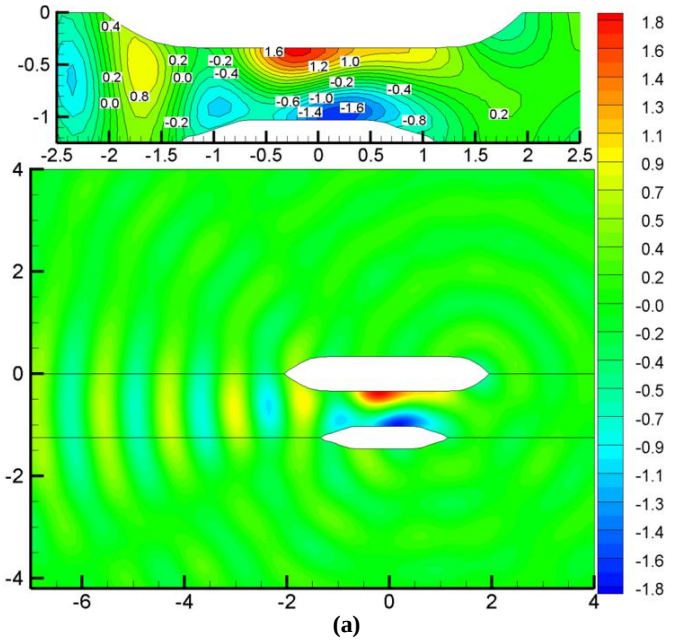

(a)

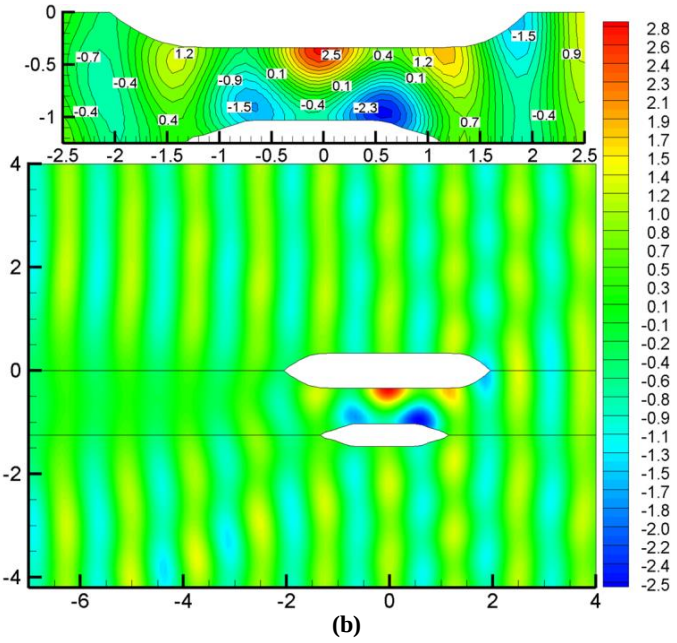

(b)

Figure 8.10: Wave elevation of two ships without speed at $\lambda = 0.33$, $L_a = dt$. (a) Real part of diffracted waves; (b) Real part of total wave elevation.

8.3.5. Wave pattern

Figure 8.11 shows the real part of diffracted and radiated waves of two ships with high forward speed. Figure 8.12 shows the total wave elevation, which is non-dimensionalized by the incident wave amplitude η_0. It is observed that the symmetrical characteristic of wave pattern produced by single ship has been modified in the presence of the other one. A V-shape region is clearly convected downstream. The diffracted waves from the two sides interact with those from the gap through a system

of transverse waves and approach the downstream boundary at an oblique angle. The radiated waves propagate sideward independently and approach the downstream boundary parallel. No reflections can be found on the boundary, which indicates physically that the present radiation condition can ensure that the waves propagate away from the ship.

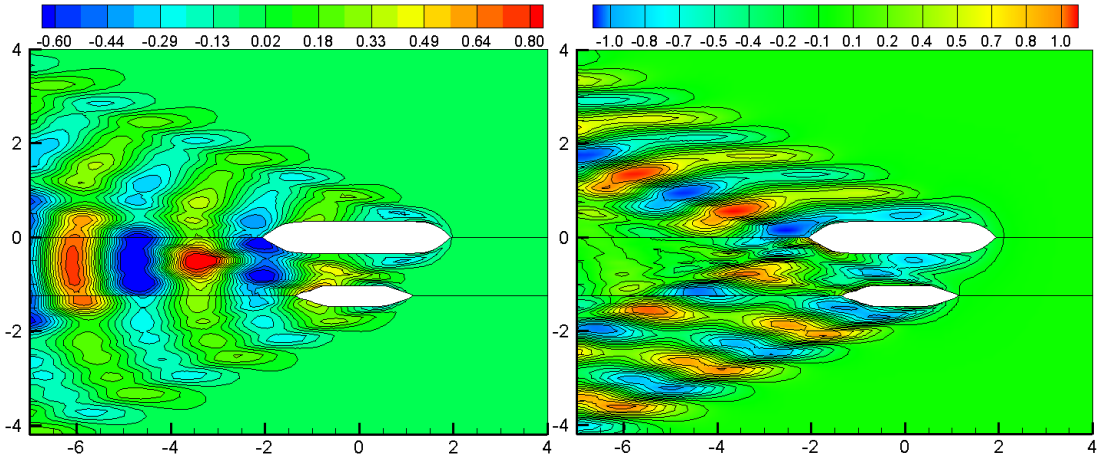

(a) **(b)**

Figure 8.11: Wave patterns of two ships in head seas: $\lambda/L_b = 1.08$, $F_n = 0.25$, $\tau = 1.35$. (a) Real part of diffracted waves; (b) Real part of radiated waves for unit heave motion of both ships.

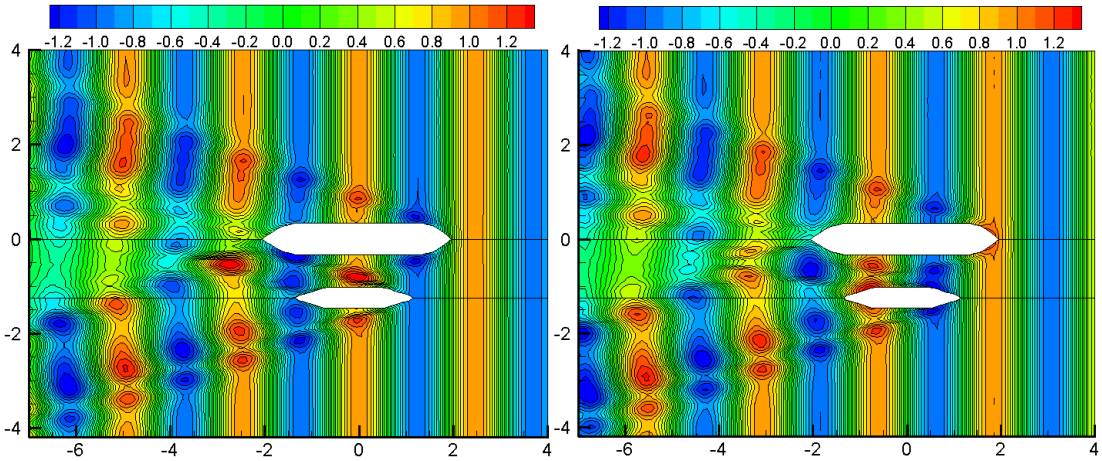

(a) **(b)**

Figure 8.12: Total wave elevation on the free surface of two ships in head seas: $\lambda/L_b = 1.08$, $F_n = 0.25$, $\tau = 1.35$. (a) Real part; (b) Imaginary part.

8.3.6. Effects of the radiation condition

Figure 8.13 and Figure 8.14 compare the wave patterns with and without Doppler shift correction in the radiation condition. In order to make an intuitive comparison, we divide the whole free surface into two parts through the centre line of Ship_a: portside part and starboard part. The lower half of each figure shows the wave pattern with

Sommerfeld radiation condition in Eq. (5.18), while the radiation condition in the upper half accounts for the Doppler shift correction as given by Eq. Eq. (5.16) and Eq. (5.17). Since the Brard number τ is smaller than 0.25, the scattered waves will propagate ahead of the vessel. It can be observed that if the new radiation condition associated with Doppler shift correction is used, the waves appear smooth and stable. But for the Sommerfeld radiation condition, there are some distortions and reflections from the control surface. Theoretically, all scattered waves normal to the control surface must be out-going to avoid reflection. Since the Doppler shift results in rotation of the scattered waves relative to the radial axis by an angle θ, the Sommerfeld radiation condition in Eq. (5.18) should be modified accordingly to ensure the out-going property of the scattered waves and lack of it will result in distortions and reflections. The results in Figure 8.13 and Figure 8.14 confirm the effectiveness of the present radiation condition as a wave-pattern prediction tool for the ships travelling with very low forward speed.

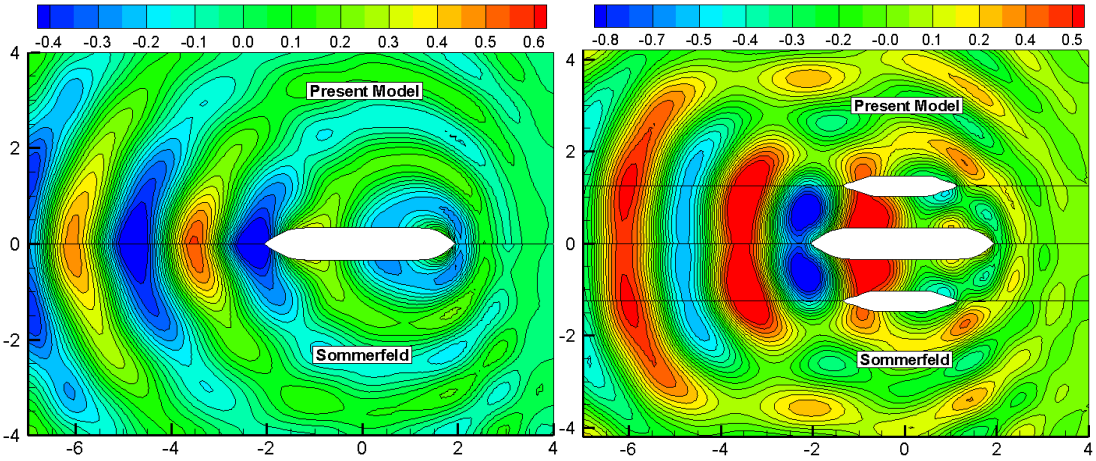

(a) **(b)**

Figure 8.13: Real part of diffracted waves of two ships in head seas by using Sommerfeld and present radiation condition: $\lambda/L_b = 1.08$, $F_n = 0.05$, $\tau = 0.2$. (a) Wave pattern in the portside of Ship_a; (b) Wave pattern in the starboard of Ship_a.

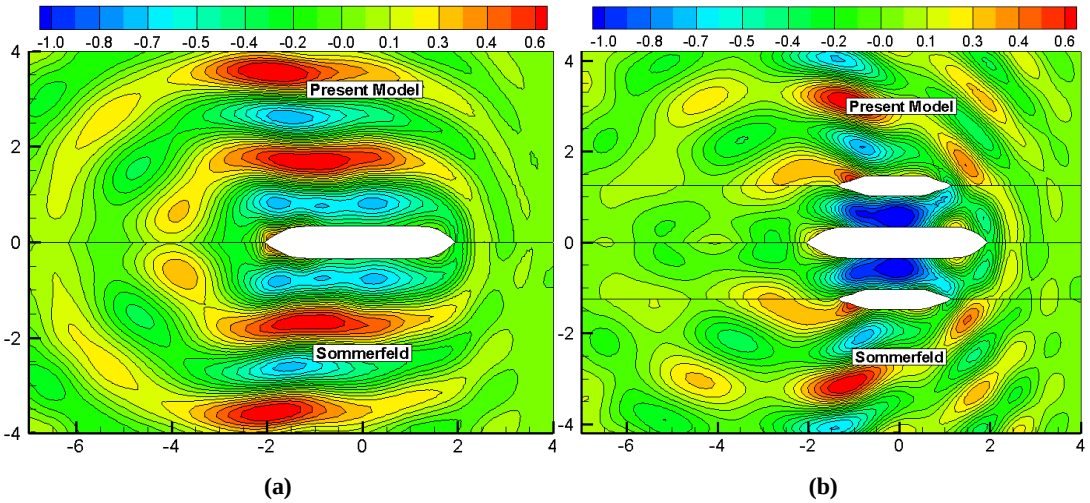

Figure 8.14: Real part of radiated waves of two ships in head seas by using Sommerfeld and present radiation condition: $\lambda/L_b = 1.08$, $F_n = 0.05$, $\tau = 0.2$. (a) Wave pattern in the portside of Ship_a; (b) Wave pattern in the starboard of Ship_a.

In order to validate the wave patterns calculated by the present radiation condition at $\tau > 0.25$, we implement an upstream boundary condition of Nakos (1990) for comparison. Figure 8.15 and Figure 8.16 show the diffracted and radiated wave patterns of both ship at $\tau = 0.27$. The upper half of each figure represents the wave pattern obtained from the present radiation condition, while the radiation condition in the lower half accounts for the upstream treatment given in Eq. (6.10)-(6.11). An evident difference of the wave patterns can be observed between these two radiation conditions, especially at far field close to the control surface. The satisfactory radiation condition must ensure that the normal component of the scattered waves is outgoing. The upstream treatment can only ensure that there is no wave travelling ahead of the vessel. However, due to the forward speed effect, most of the wave energy is transferred downstream. The outgoing property at downstream control surface cannot be guaranteed since that no radiation condition is imposed there. As a result, the reflected waves become very large at downstream control surface, as shown in Figure 8.15 and Figure 8.16. If the control surface is placed far enough away from the centre ($dc/\lambda > 3$, as suggested by Das and Cheung (2012b), where dc is the distance between the control surface and the center, λ is the wave length), the reflected waves will not influence the near field wave patterns. But for the case of $\tau = 0.27$, the wave length is very large and $dc/\lambda = 1.4$ downstream, $dc/\lambda = 0.8$ sideward. Therefore, the near field wave patterns are also modified by the reflected wave form the control surface. As the Brard number increases, the wave length becomes smaller. For the case of $\tau = 0.51$ in

Figure 8.17 and Figure 8.18, dc/λ = 4.1 downstream, dc/λ = 2.4 sideward. Although there are some reflections from the control surface, they will not influence the near field wave patterns, as shown in Figure 8.17 and Figure 8.18. In the near field of the ship hulls, a very good agreement of the wave fields is obtained between these two radiation conditions. For the present radiation condition, the rotated angle θ has been calculated before we solve the boundary value problem. The corrected Sommerfeld radiation condition can ensure the outgoing property of the scattered waves. Therefore, no reflections can be found for the present model at $\tau > 0.25$. The results in Figure 8.11-Figure 8.18 confirm the effectiveness of the present radiation condition as a wave-pattern prediction tool for the ships travelling with a wide range of forward speed.

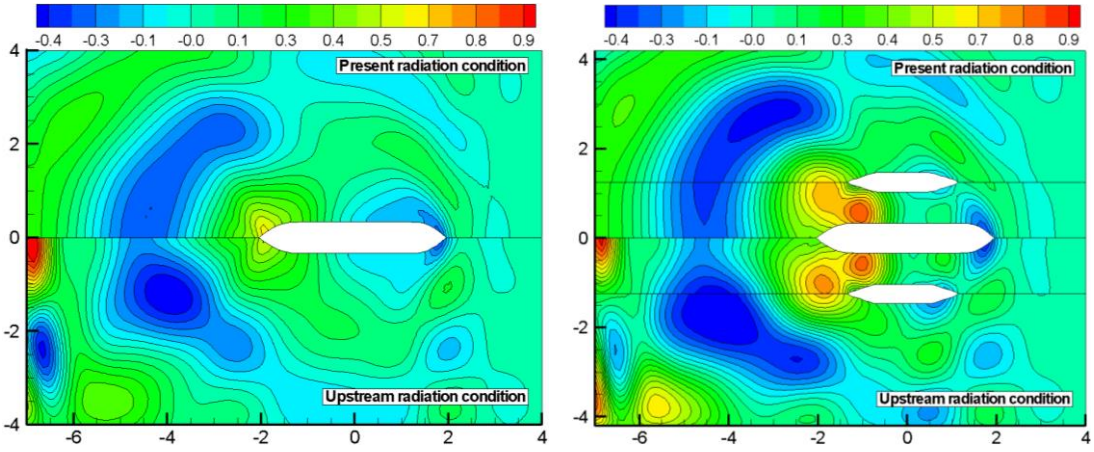

(a) **(b)**

Figure 8.15: Real part of diffracted waves of two ships in head seas by using upstream boundary condition of Nakos (1990) and present radiation condition: λ/L_b = 2.15, F_n = 0.1, τ = 0.27. (a) Wave pattern in the portside of Ship_a; (b) Wave pattern in the starboard of Ship_a.

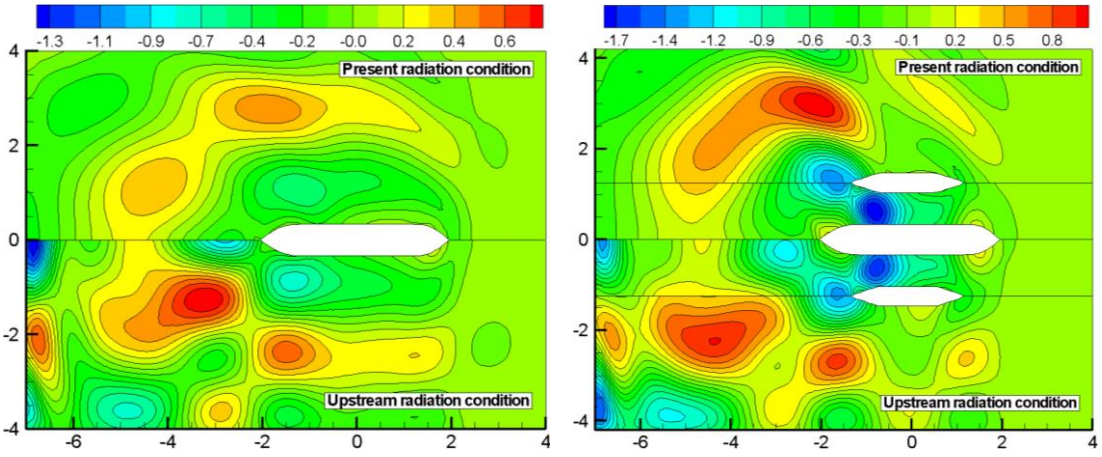

(a) **(b)**

Figure 8.16: Real part of radiated waves of two ships in head seas by using upstream boundary condition of Nakos (1990) and present radiation condition: λ/L_b = 2.15, F_n = 0.1, τ = 0.27. (a) Wave pattern in the portside of Ship_a; (b) Wave pattern in the starboard of Ship_a.

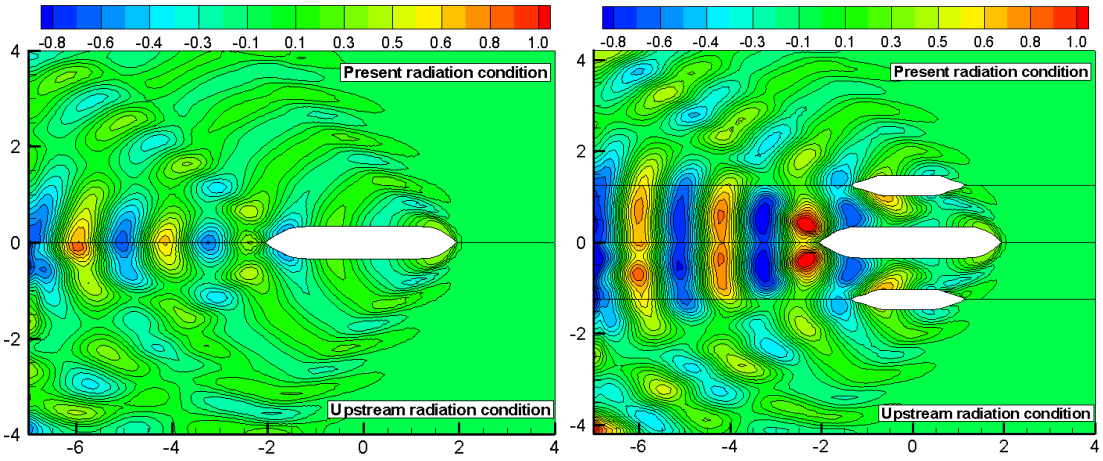

(a) **(b)**

Figure 8.17: Real part of diffracted waves of two ships in head seas by using upstream boundary condition of Nakos (1990) and present radiation condition: λ/L_b = 0.75, F_n = 0.1, τ = 0.51. (a) Wave pattern in the portside of Ship_a; (b) Wave pattern in the starboard of Ship_a.

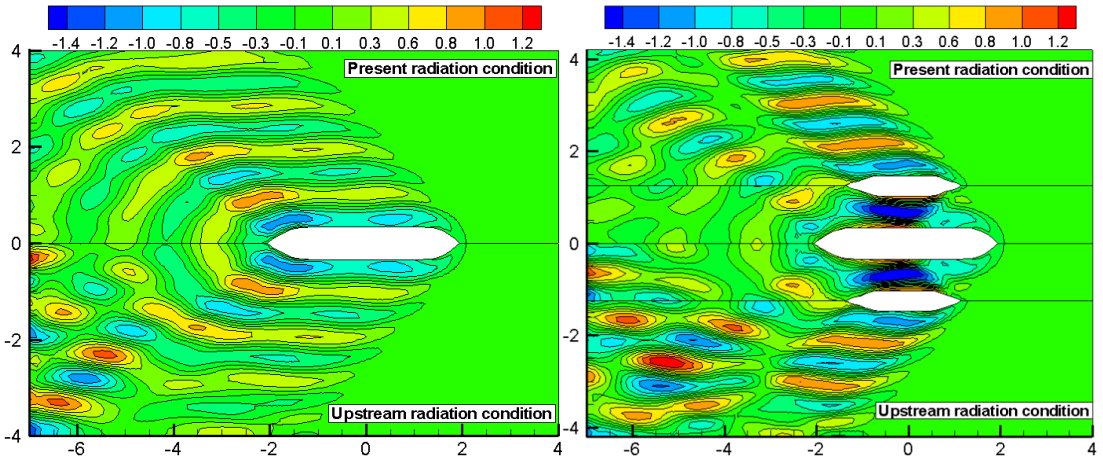

(a) **(b)**

Figure 8.18: Real part of radiated waves of two ships in head seas by using upstream boundary condition of Nakos (1990) and present radiation condition: λ/L_b = 0.75, F_n = 0.1, τ = 0.51. (a) Wave pattern in the portside of Ship_a; (b) Wave pattern in the starboard of Ship_a.

We also examine the effect of the radiation condition through the comparison study based on the wave excitation forces and the hydrodynamic coefficients at F_n = 0.1, as shown in Figure 8.19 and Figure 8.20 respectively. It can be clearly seen that at $\tau <$ *0.25*, the results from the upstream treatment are diverged and cannot provide a stable solutions. Even though the Brard number is slightly greater than critical value 0.25, the near field wave pattern obtained by upstream treatment can still be influenced by the reflected waves from the control surface, which is analysed previously. This explains the discrepancies between the results obtained by two different radiation conditions at the range of $0.25 < \tau < 0.35$. When the Brard number is greater than 0.35,

these two radiation conditions can provide the identical results. For the present method, the solutions of the wave excitation forces and the hydrodynamic coefficients are quite stable in the full range of Brard number. It can be concluded that the present radiation condition can predict the hydrodynamic properties of vessels with forward speed above and below the group velocity of the scattered waves while the upstream treatment is only valid for the case of $\tau > 0.25$.

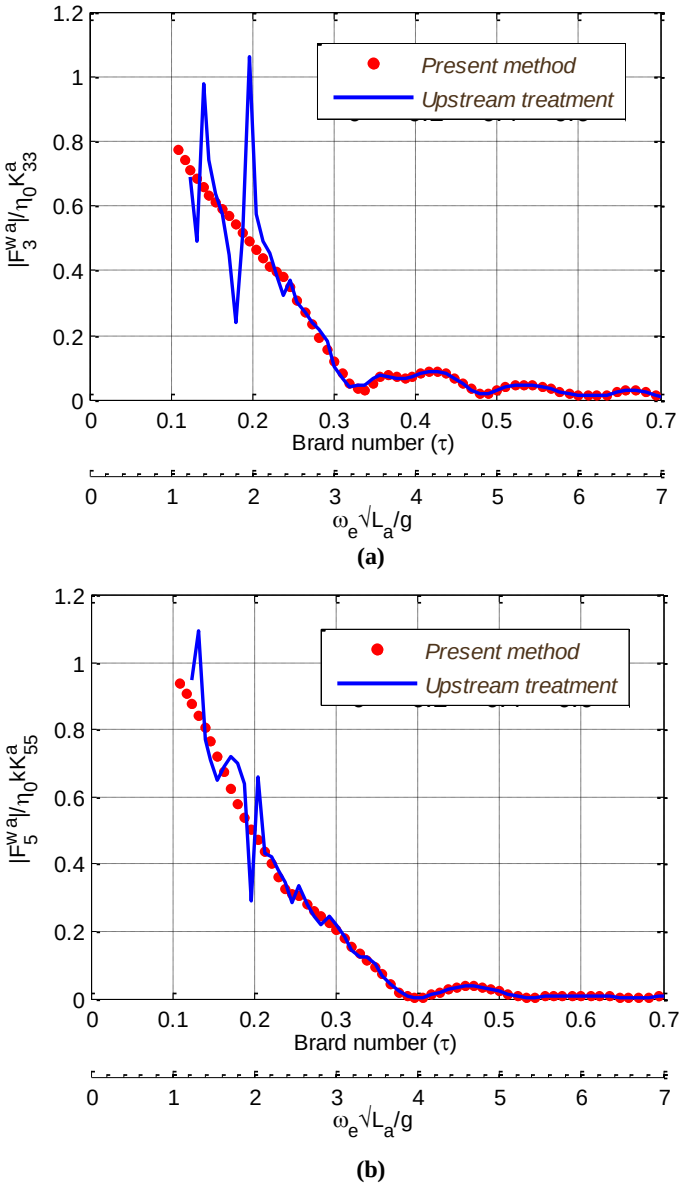

Figure 8.19: Wave excitation forces on Ship_a by using upstream boundary condition of Nakos (1990) and present radiation condition at F_n = 0.1. (a) Heave; (b) Pitch.

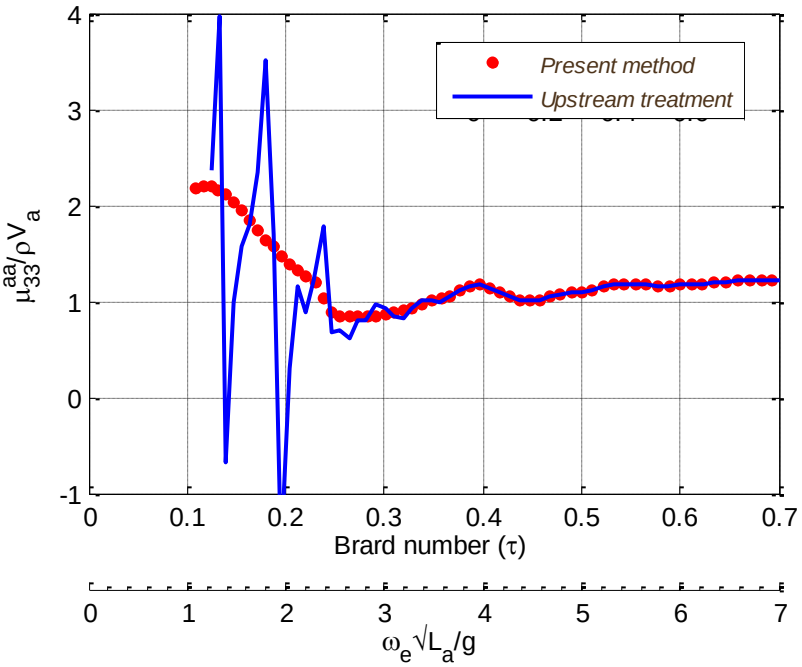

(a)

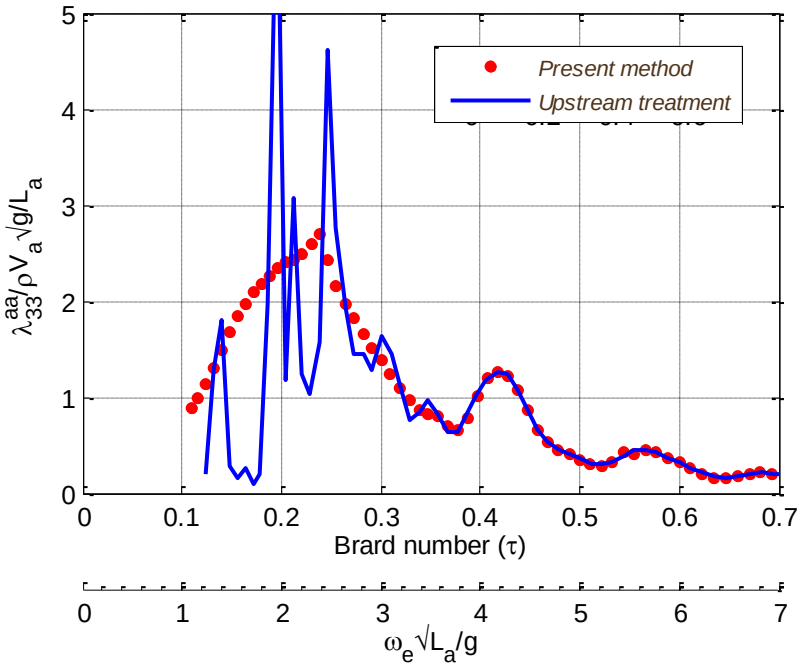

(b)

Figure 8.20: Hydrodynamic coefficients by using upstream boundary condition of Nakos (1990) and present radiation condition at F_n = 0.1. (a) Heave added mass of Ship_a induced by heave motion of Ship_a itself; (b) Heave damping of Ship_a induced by heave motion of Ship_a itself.

8.3.7. Effects of water depth

The Green function method is regarded as an effective solution for the marine vessels without speed in deep waters. When it refers to the shallow water associated with the forward speed problem, the Green function becomes very complicated. However, the

present Rankine source method can provide an intuitive solution for this issue. It takes account of the forward speed into the boundary value problem and the Rankine-type Green function can satisfy the seabed boundary condition through the method of image in Eq. (4.1). Figure 8.21 shows the motion responses of both ships at different water depths. The parameters of Case 1 are used here with Fn = 0.1 and dl = 0.09 m. From the figures it can be seen that the water depth has a significant influence on the responses of both ships. Both of the amplitudes and resonance frequencies are changed by the water depth. There are mainly two reasons for these discrepancies. The first reason is that the shallow water dispersion relation in Eq. (3.4) changes the incident wave length and as a result, the wave exciting forces and the resonance frequencies differ from those in deep water. It can be observed that at small λ/L_a, the difference is very small. As λ/L_a increases, the discrepancies tend to be very large. The results in Figure 7.11 can explain this phenomenon. The x-axis of Figure 7.11 is the non-dimensional incident wave length, where λ_0 is the wave length in infinite water depth. We find at small λ/L_a, the wave length at different water depths differs a little. The difference keeps a similar increase trend with that of motion responses in Figure 8.21 as λ/L_a increases. The second reason is the hydrodynamic coefficients and diffraction forces of the ship are changed by the nearness of the sea bottom. As can be seen from Figure 8.22, the diffracted wave pattern in shallow water differs a lot from that in infinite water. Since λ/L_a is fixed at 1, the wave trough arises around bow area, while the wave crest arises around the stern. This is the most unfavourable load case, since both the heave force and pitch moment achieves a maximum value. As a consequence, the motion responses in heave and pitch reach their peaks around $\lambda/L_a = 1$, which can be observed in Figure 8.21 (a) and (e). At $\lambda/L_a = 1$, the heave force on Ship_a is mainly determined by the wave elevation. It can be seen from Figure 8.22 that the diffracted wave elevation in deep water is much larger than that in shallow water, which explains why heave motion of Ship_a in deep water is greater than that in shallow as shown in Figure 8.21 (a). The roll moment mainly comes from the pressure difference at portside and starboard of the ships. We find in deep water, the wave crest around the stern is asymmetric. As a consequence, the roll motion should be significant. But in shallow water, a better symmetrical wave pattern presents at portside and starboard of Ship_a.

This can explain why the roll motion at $\lambda/L_a = 1$ in deep water is much greater than that in shallow water.

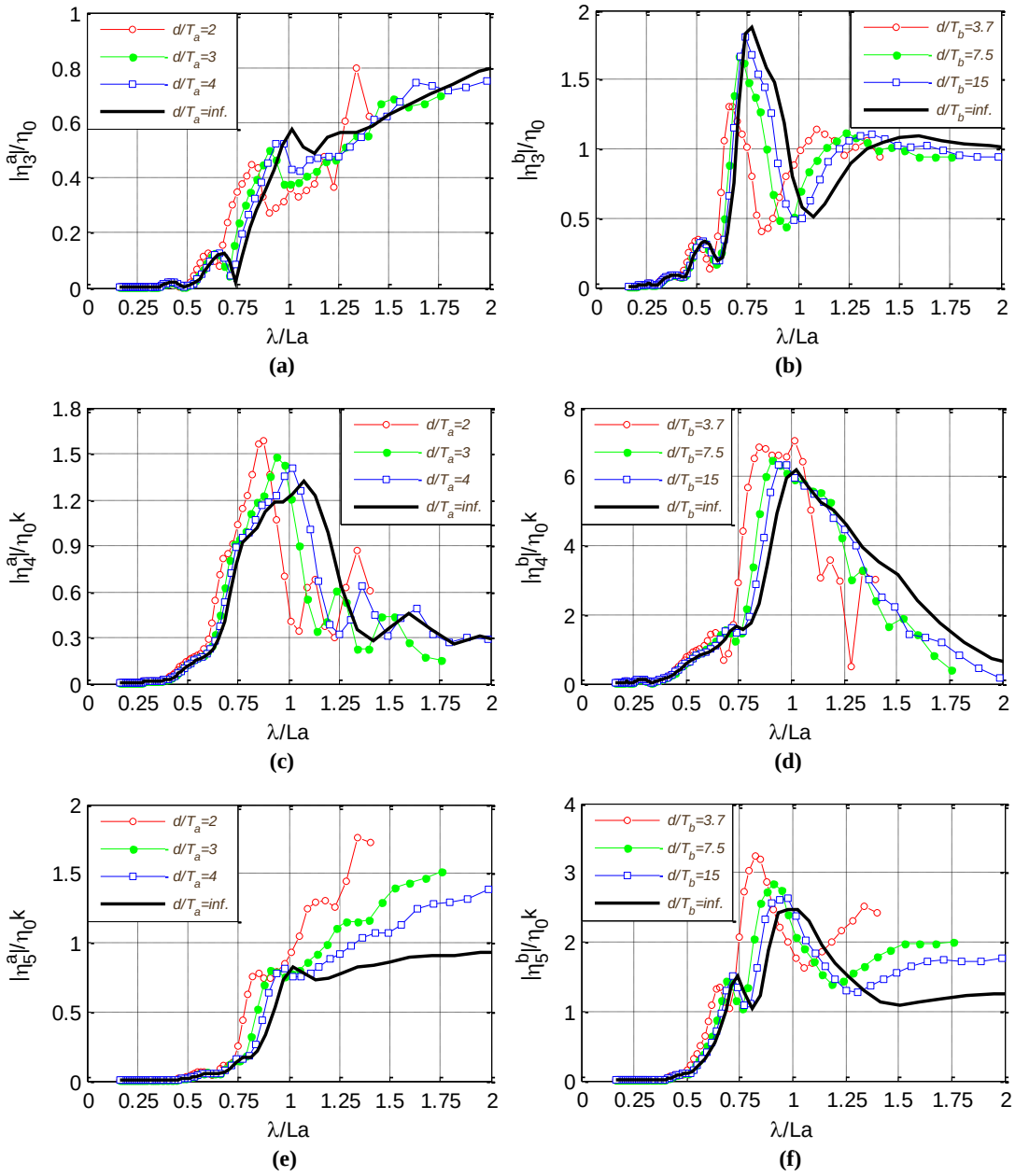

Figure 8.21: Response amplitude operators of different depths at *Fn* = 0.1. (a) Heave of ship_a; (b) Heave of Ship_b; (c) Roll of ship_a; (d) Roll of Ship_b; (e) Pitch of ship_a; (f) Pitch of Ship_b.

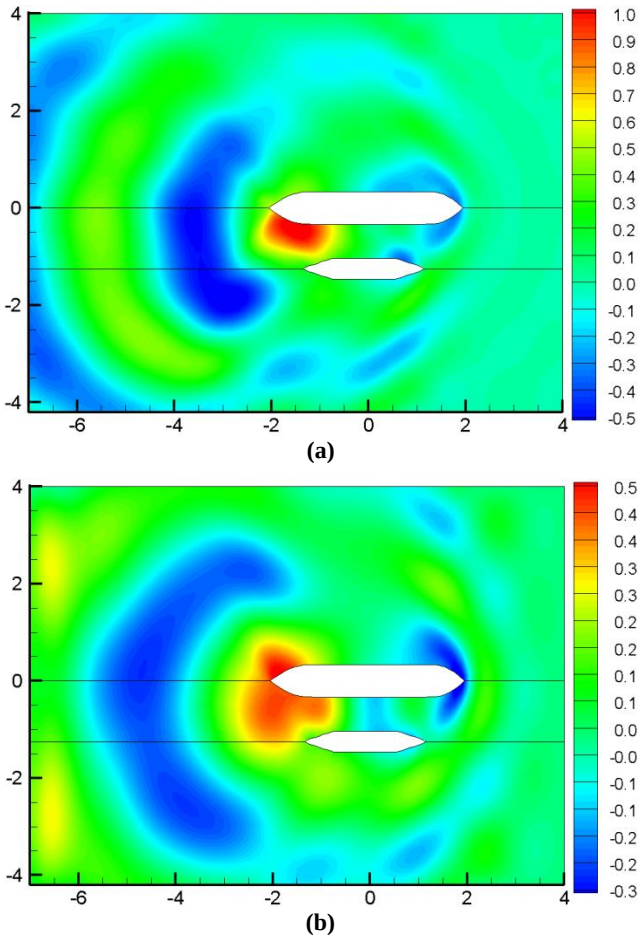

Figure 8.22: Wave elevation of two ships at $\lambda/L_a = 1$, $Fn=0.1$. (a) Infinite water; (b) Shallow water at $d/T_a=2$.

8.4. Summary

In this chapter, we developed a boundary element program based on 3-D Rankine source method to investigate the ship-to-ship with forward speed problem. A new radiation condition, which takes Doppler shift into account, was imposed on the control surface to complete the boundary value problem. This new method is applicable to forward speeds above and below the critical Brard number $\tau = 0.25$.

The present method was validated through two pairs of models. The computed dynamic responses of both models in heave and pitch motions show a good agreement with the published experimental results. However, the prediction of roll motion is full of challenges due to the inviscid assumption in the potential flow theory. The contribution of the radiation conponent is small, especially for the smaller ship with large amplitude of roll motion which violates the present linear assumption. In order to improve the accuracy of the prediction, a roll damping coefficient should be applied

in the motion equation to avoid the unrealistic roll motions. Unfortunately, this damping coefficient could not be determined without model test results. A future study based on CFD solutions should be carried out. We also find that the hydrodynamic interaction has much greater influence on the motions of the smaller ship.

We investigated the hydrodynamic interactions through the hydrodynamic coefficients and wave excitation forces. It is found that the hydrodynamic coefficients of the larger ship are mainly determined by the oscillation of the larger ship itself, while the self-induced and external-induced components of the hydrodynamic coefficients are at the same level for the smaller ship. This can explain why the hydrodynamic interaction has much greater influence on the motions of the smaller ship. We also observed a very large sway force for zero speed case when the transverse distance between two ships equals to the wave length. This extreme force is due to the diffracted wave energy that trapped in the gap and it will bring a great risk to the ship-to-ship offloading operation.

We also examined the present radiation condition and the effect of forward speed through a series of numerical experiments involving two ships with a wide range of forward speed in head seas. The forward speed introduces the Doppler shift which modifies the length of the scattered waves. The symmetrical characteristic of wave pattern produced by single ship has been modified in the presence of the other one. The comparison between the present and Sommerfeld radiation condition was made at $\tau < 0.25$, while the comparison between the present and upstream radiation treatment was made at $\tau > 0.25$. Our solution shows a better wave pattern without reflections from the truncated control surface, which confirms the effectiveness of the present radiation condition as a wave-pattern prediction tool for the ships travelling with a wide range of forward speed.

9. Parametric study and optimal design

9.1. Introduction

Chapters 6-8 have illustrated the details of the validations of the present method. It was concluded that the present method could provide a satisfactory prediction of the hydrodynamic properties of single ship or two ships with or without forward speed. Based on these validations, a systematic parametric study will be carried out in this chapter. For the ship-to-ship interaction with forward speed problem, there are mainly three parameters which can influence the hydrodynamic responses significantly. The first parameter is the forward speed (u_0). It was found by Fang and Kim (1986) that the forward speed effects were very important and the roll motion could be reduced as the forward speed increased. The second and third parameters are the transverse and longitudinal distances (*dt* and *dl*) between two ships. Li (2001) studied the effects of transverse distance of two ships travelling in shallow water and found that the motion responses and wave exciting forces were greatly influenced by the transverse distance. However, no published study can be found on the effects of the longitudinal distance between two travelling ships. But in the engineering practice, this case could occur in the harbour area and waterways with dense shipping traffic. In this chapter, we take the longitudinal distance as an important parameter in ship-to-ship interaction with forward speed problem and carry out the corresponding comparison study.

The parameter study on a specified parameter (e.g. different transverse distances *dt* while *dl* and u_0 are fixed) can be useful for us to understand the effects of this parameter. But a more practical objective of the parametric study is to provide the recommendations for the ship designers and operators with an optimal result in given environmental conditions for safe operation. To achieve this goal, a systematic optimal study about all the relevant parameters should be carried out. The hydrodynamic interactions can be divided into two categories: the radiation problem (radiation forces or so-called hydrodynamic coefficients) and diffraction problem (diffraction forces). We find that the coupled term (the extra force components due to the existence of the other ship) of these forces on a specified ship (e.g. Ship_a) are determined by the waves

produced by the other ship (e.g. Ship_b). If the scattered waves produced by Ship_a can propagate to the body surface of Ship_b, the hydrodynamic interaction must be taken into consideration. Otherwise, the hydrodynamic interaction can be neglected. In the previous chapters, we found that as the forward speed increases, the quiescent region in front of the ship would be enlarged, as shown in Figure 8.12. It can be supposed that if Ship_b is located in the quiescent region of Ship_a, while Ship_b is located in the quiescent region of Ship_a, there should be no hydrodynamic interactions between these two ships. In this chapter, we will connect each parameter through the scattered waves to find a reasonable and optimal speed and configuration to avoid the hydrodynamic interactions between two ships.

The tanker (Ship_a) and LNG (Ship_b) model used in this chapter are the same as the models described in Section 8.3.1. The main particulars are shown in Table 8.2. In the previous validation, both ships are restrained in surge, sway and yaw while the motions in heave, roll and pitch are free in order to keep consistent with the model tests condition. But in this chapter, only the numerical results will be presented and the motions in surge, sway and yaw are also of significance. Therefore, all the 6 degrees of freedom are set free.

9.2. Forward speed effects

In order to investigate the forward speed effects, we keep the configuration of the models constant with the transverse dt = 1.25 m and longitudinal distance dl = 0 m. These two ships travel with the same forward speed in head waves at infinite water depth. We compare the motion responses and wave excitation forces over a wide range of Froude number from 0 to 0.3 (F_n = 0, 0.05, 0.1, 0.2, 0.3). Figure 9.1 and Figure 9.2 show the motion responses of Ship_a and Ship_b respectively with different forward speeds in head waves. In general, the forward speed has a significant influence on the motion responses of both ships. From Figure 9.1 (a), we can see that the surge motion of Ship_a becomes smaller as the forward speed increases. The sway and roll motions in head sea condition are caused by the hydrodynamic interactions between two ships and they are quite sensitive to the forward speed, as shown in Figure 9.1 (b) and (d). At zero forward speed, the sway and roll motions are very small. They increase

gradually as the Froude number increases from 0 to 0.1. As the Froude number becomes larger then 0.1, the sway and roll motions tend to be very large. This finding is different from Fang and Kim's (1986) conclusion. One reason is that Fang and Kim (1986) only discussed the speed effects at very low forward speed (F_n < 0.071), while in this thesis we discuss the speed effects at a wide range of Froude number from 0 to 0.3. When it comes to the heave and pitch motions in Figure 9.1 (c) and (e), we find the discrepancies between the motion responses is not evident at F_n < 0.1. A dramatic increase can be observed at F_n > 0.2. The same conclusion can also be made for the yaw motion of Ship_a, as shown in Figure 9.1 (f). It should also be noticed that the resonant frequencies have been shifted to the lower frequency range as the forward speed increases.

Compared with the motion responses of Ship_a, the motion responses of Ship_b are more sensitive to the forward speed. The resonant frequencies are shifted to the lower frequency range very quickly as the forward speed increases. As a result, at low range of λ/L_b (λ/L_b < 1.5), the response amplitudes of Ship_b with smaller forward speed can be even greater than those with larger forward speed in surge, heave and pitch motions, as shown in Figure 9.2 (a), (c) and (e). But as the Froude number increases, the peak values in heave and pitch motions keep an increase trend, especially when the Froude number is greater than 0.2. This trend can also be observed in Figure 9.2 (b) and (d) in sway and roll motions. The forward speed effects on the surge and yaw motions of Ship_b are more complicated and we find that at F_n = 0.2, the sway and yaw motions become very small. Overall, the forward speed effects can influence the motion responses of both ships significantly and if the other two parameters (*dt* and *dl*) are fixed, we suggest that the travelling speed should be lower than F_n = 0.1.

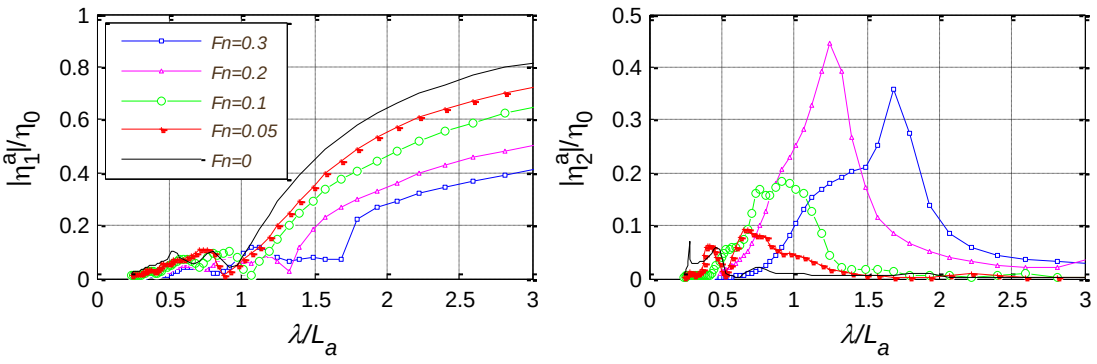

(a) **(b)**

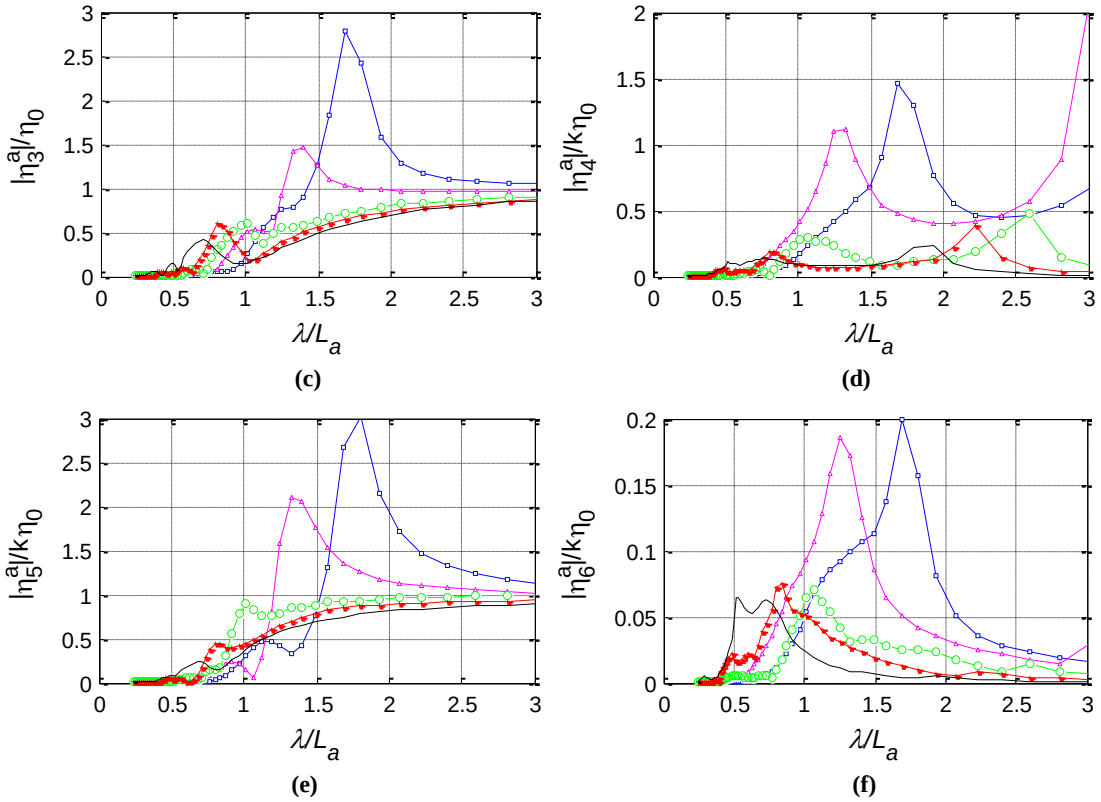

Figure 9.1: Response amplitude operators of Ship_a with different forward speeds in head waves: *dt* = 1.25*m*, *dl* = 0*m*. (a) Surge; (b) Sway; (c) Heave; (d) Roll; (e) Pitch; (f) Yaw.

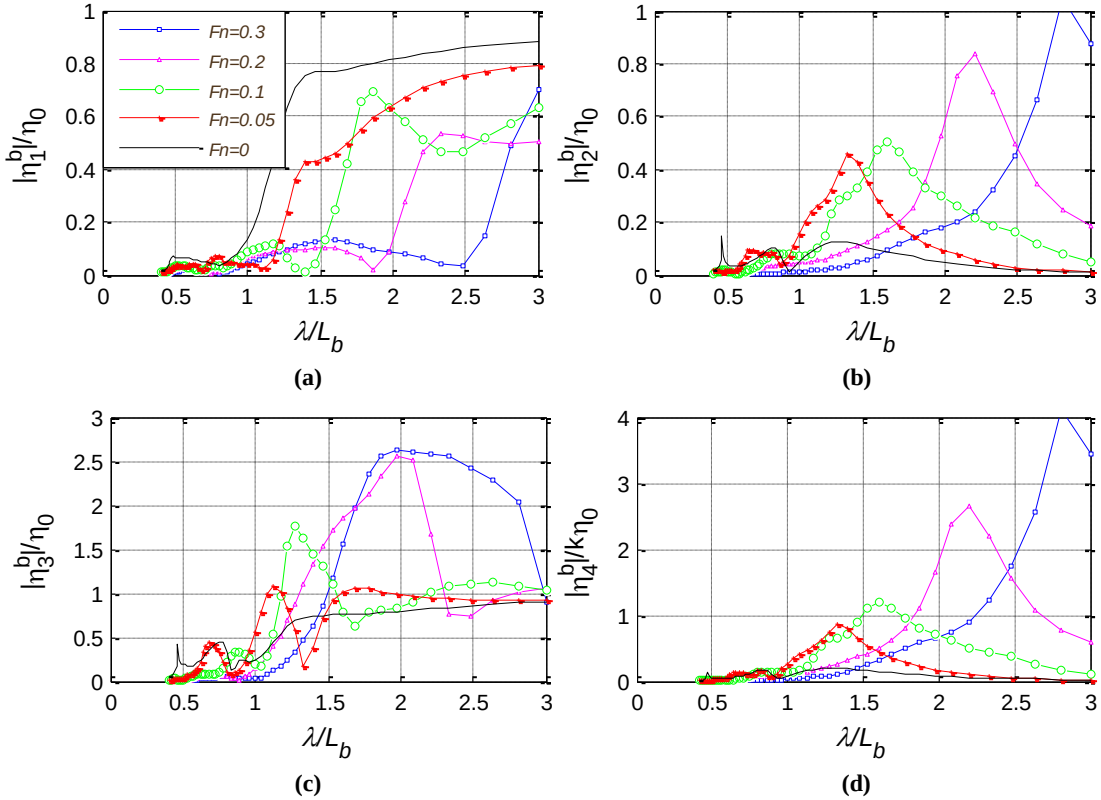

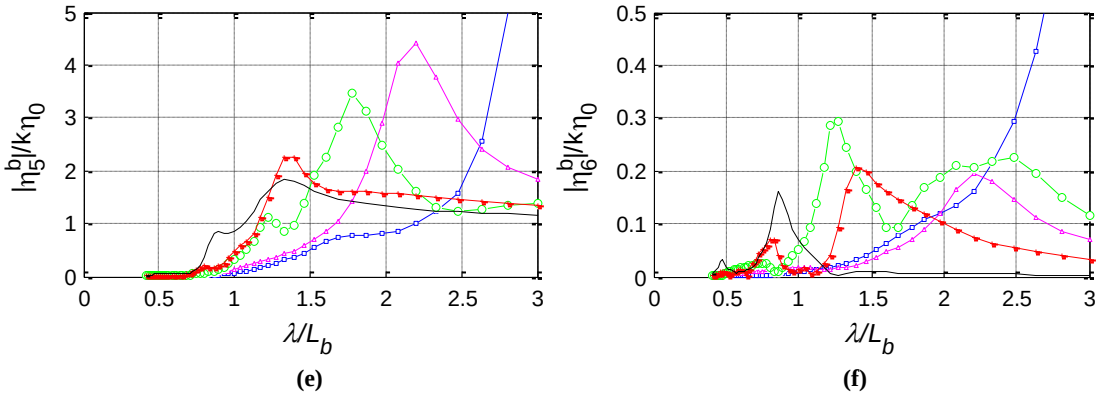

Figure 9.2: Response amplitude operators of Ship_b with different forward speeds in head waves: *dt* = 1.25*m*, *dl* = 0*m*. (a) Surge; (b) Sway; (c) Heave; (d) Roll; (e) Pitch; (f) Yaw.

Figure 9.3 and Figure 9.4 show the wave excitation forces of Ship_a and Ship_b respectively with different forward speeds in head waves. The wave excitation forces are composed of two components: incident wave force (Froude Krylov force) and diffraction force. Incident wave force is determined by the incident wave and it will not be influenced by the existence of the other ship. However, the hydrodynamic interactions could bring a large influence on the diffraction forces since the diffracted waves of Ship_a can act on Ship_b, and vice versa. It can be observed from Figure 9.3 (a), (c) and (e) and Figure 9.4 (a), (c) and (e) that the forward speed effects on surge, heave and pitch forces of both ships are not evident. However, the forces in sway, roll and yaw directions are significantly influenced by the forward speed, as can be seen in Figure 9.3 (b), (d) and (f) and Figure 9.4 (b), (d) and (f). It is very interesting to find that the sway forces decrease rapidly and the spikes at the low range of λ/L_a become very small as the increase of the forward speed. One major reason should be the wave elevations in the gap between two ships. As for the zero speed case, the diffracted waves are trapped in the gap which makes the wave elevations in the gap be much higher than those in the other sides of the ships, as shown in Figure 9.5 (a). The wave elevation difference between the portside and starboard will induce a large sway force as well as a roll moment on both ships, which is shown in Figure 9.3 (b) and (d) and Figure 9.4 (b) and (d). But as the forward speed increases to F_n = 0.3, the energy trapped in the gap could escape downstream, as shown in Figure 9.5 (b). Therefore, the wave elevations in the gap become smaller. As a result, the sway force and roll moment can be reduced accordingly.

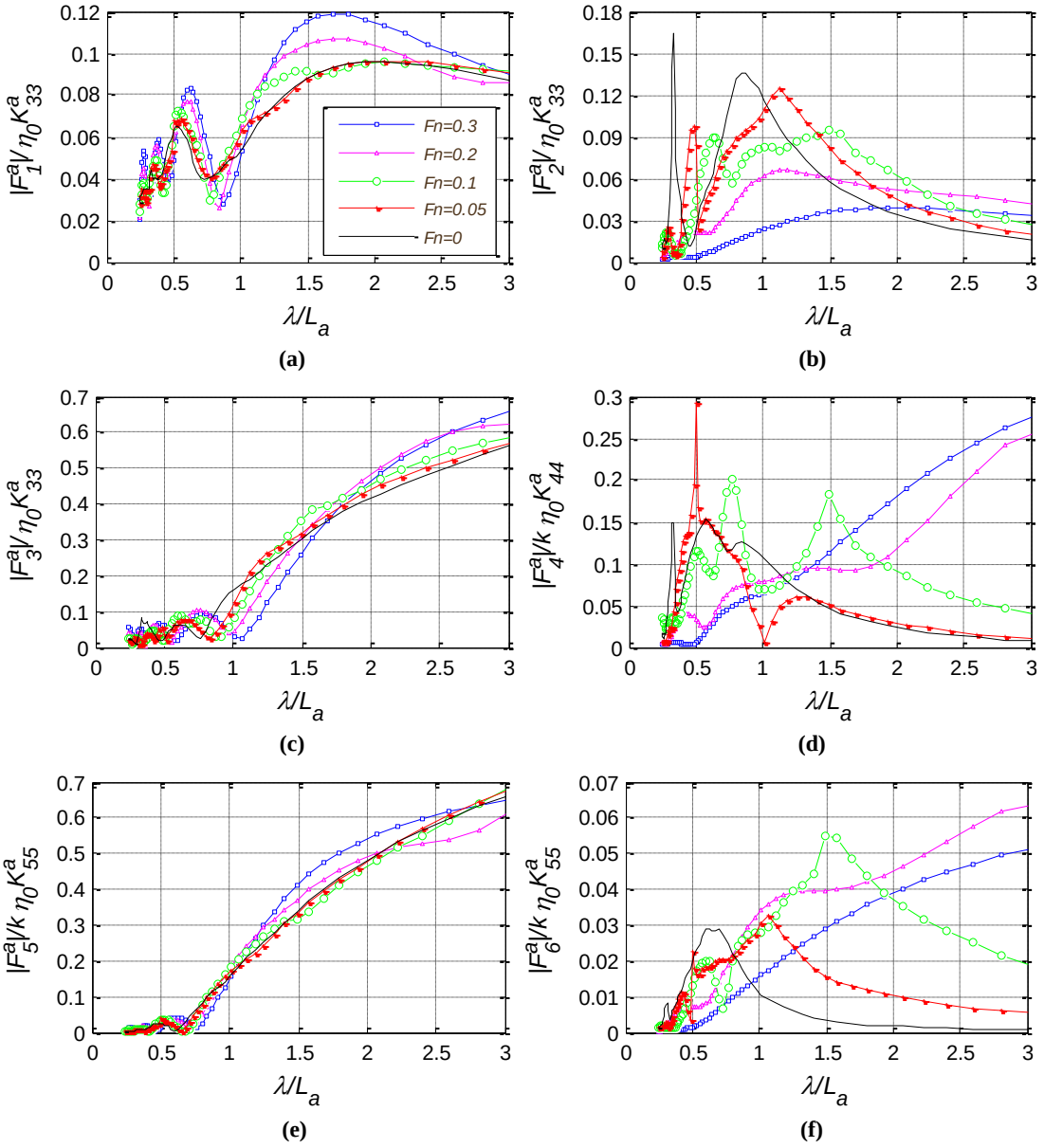

Figure 9.3: Wave excitation forces of Ship_a with different forward speeds in head waves: *dt* = 1.25*m*, *dl* = 0*m*. (a) Surge; (b) Sway; (c) Heave; (d) Roll; (e) Pitch; (f) Yaw.

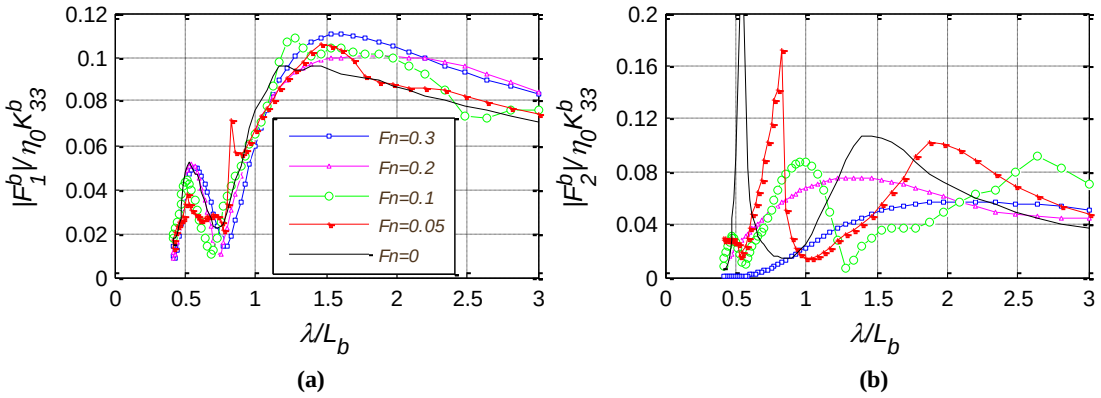

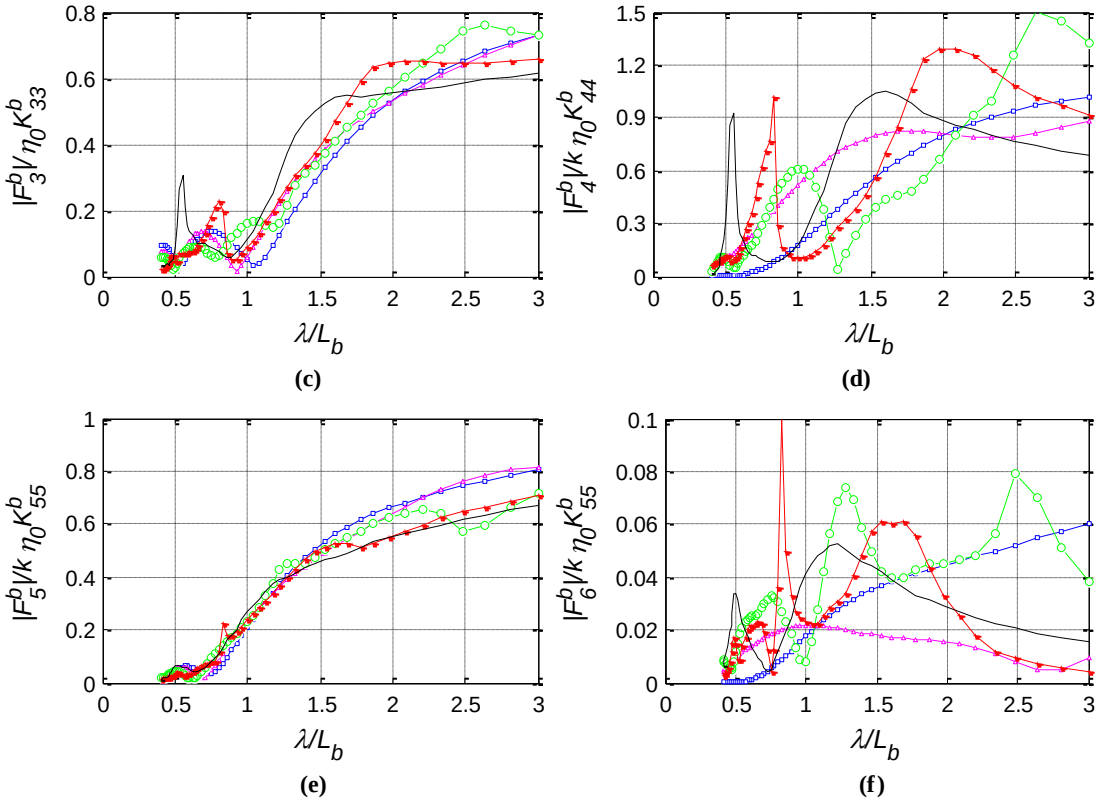

Figure 9.4: Wave excitation forces of Ship_b with different forward speeds in head waves: *dt* = 1.25*m*, *dl* = 0*m*. (a) Surge; (b) Sway; (c) Heave; (d) Roll; (e) Pitch; (f) Yaw.

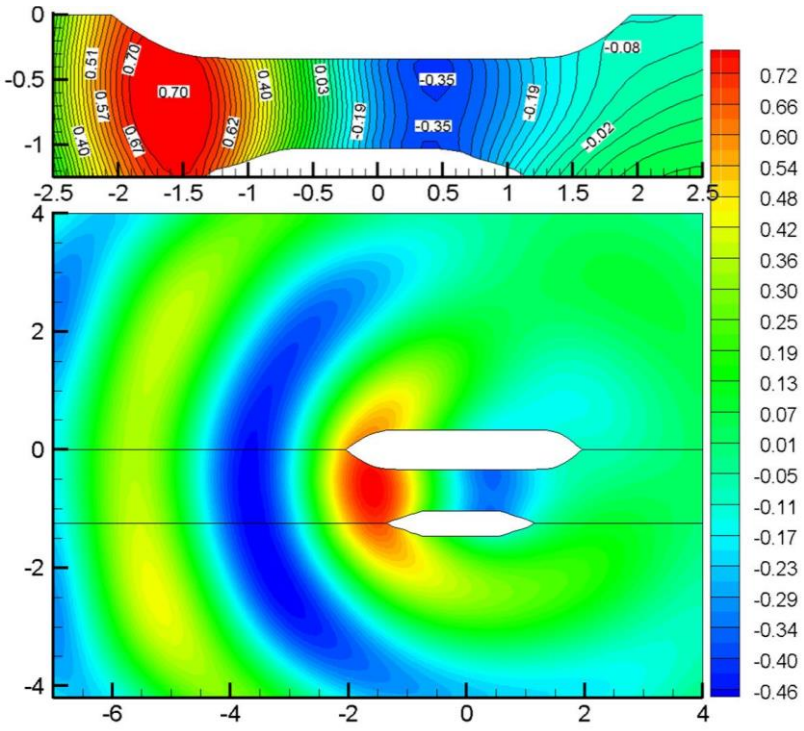

(a)

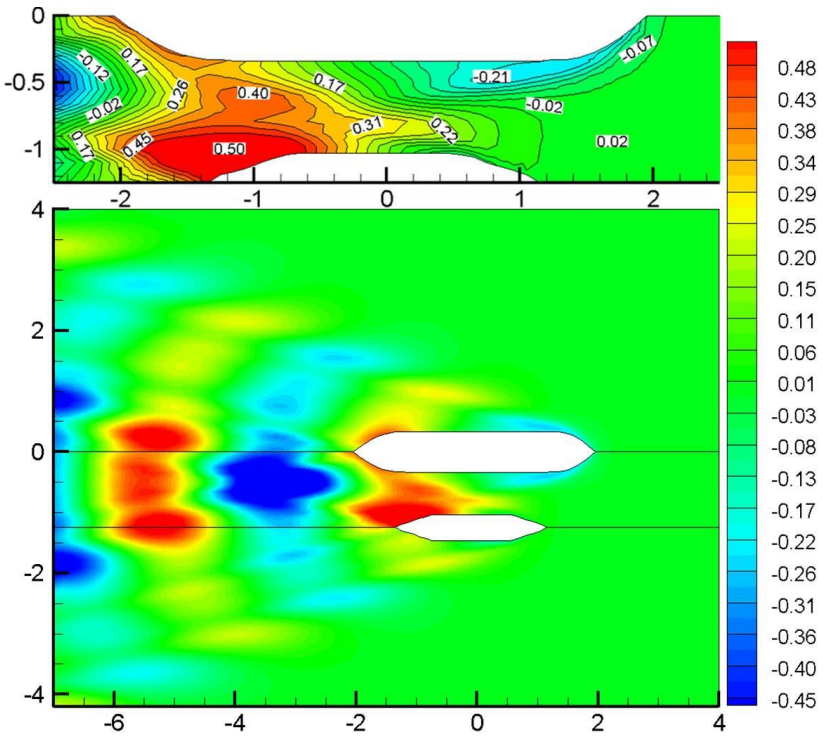

(b)

Figure 9.5: The real part of the diffracted wave patterns of two ships advancing with different forward speeds at $\lambda = L_a$. (a) $F_n = 0$; (b) $F_n = 0.3$.

9.3. Effect of transverse distance

In order to investigate the effect of the transverse distance (*dt*), we fix the forward speed at $F_n = 0.1$ and the longitudinal distance at $dl = 0$ *m*. These two ships travel with the same forward speed in head waves at infinite water depth. As shown in Figure 9.6, we compare the motion responses and wave excitation forces over a wide range of transverse distances ($dt/B_a = 1.25, 2, 3, 5, \infty$, where B_a is the breadth of Ship_a). $dt/B_a = \infty$ denotes the cases without hydrodynamic interactions.

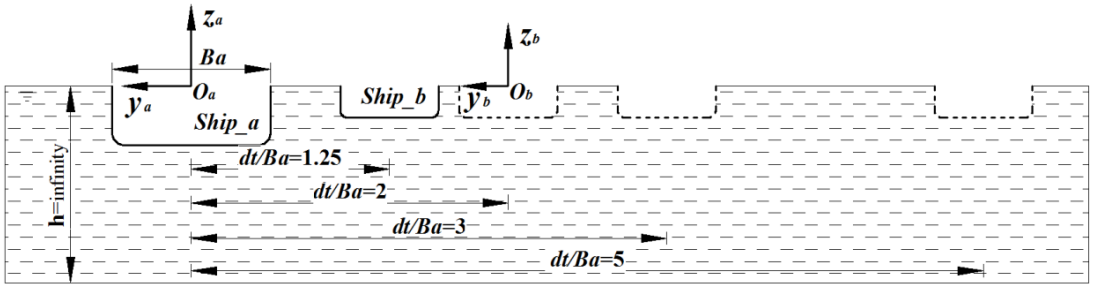

Figure 9.6: Sketch of two ships travelling with different transverse distances.

Figure 9.7 and Figure 9.8 show the response amplitude operators of Ship_a and Ship_b with different transverse distances in head waves. It can be found in Figure 9.7 (a), (c) and (e) that the surge, heave and pitch motions of Ship_a are hardly influenced by the transverse distance. However, the sway, roll and yaw motions are significantly influenced by the transverse distance, as shown in Figure 9.7 (b), (d) and (f). It can be observed that even when the transverse distance becomes very large at dt/B_a = 5, the hydrodynamic interactions are still very important. The peak values of sway and yaw motions (as shown in Figure 9.7 (b) and (f)) at dt/B_a = 3 could even be larger than those at smaller ratios of dt/B_a. When it refers to the roll motion of Ship_a in Figure 9.7 (d), two spikes can be found at $\lambda/L_a \approx 1.1$ and 2.6, which is consistent with Xu and Dong's results (2013). And it can also be found that the second spike drops as the increase of the transverse distance, while the difference of the first spike is not evident.

The influence of the transverse distance on the motion responses of Ship_b is totally different from that on Ship_a. As can be seen from Figure 9.8 (b), (d) and (f), the sway, roll and yaw motions are not sensitive to the transverse distance. It can be observed from Figure 9.8 (d) that the roll motion of Ship_b is unrealistic large. This is due to the inviscid assumption in the potential flow theory, which has been discussed previously in Section 8.2.2. However, the transverse distance can bring an important influence to the surge, heave and pitch motions, which are shown in Figure 9.8 (a), (c) and (e). It is very interesting to find that as the transverse distance increases, the peak values in these three directions will be decreased.

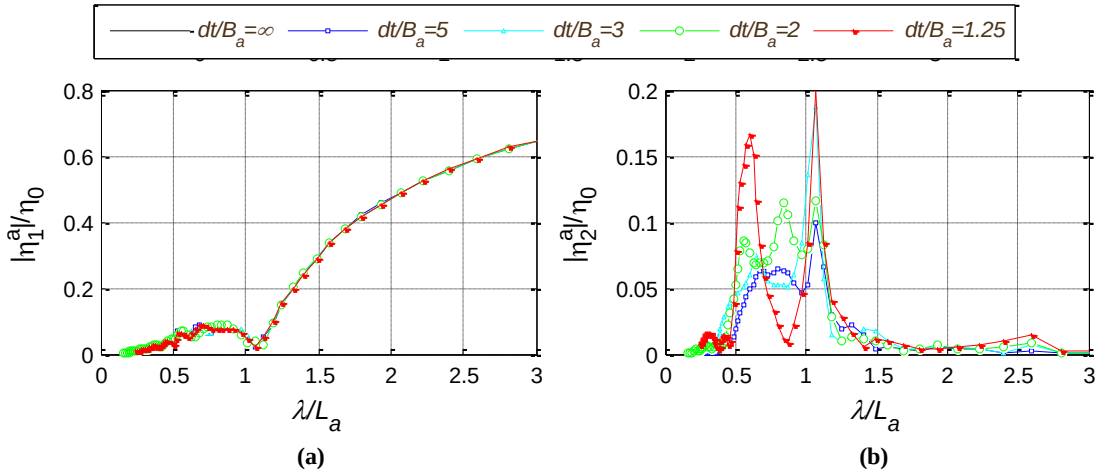

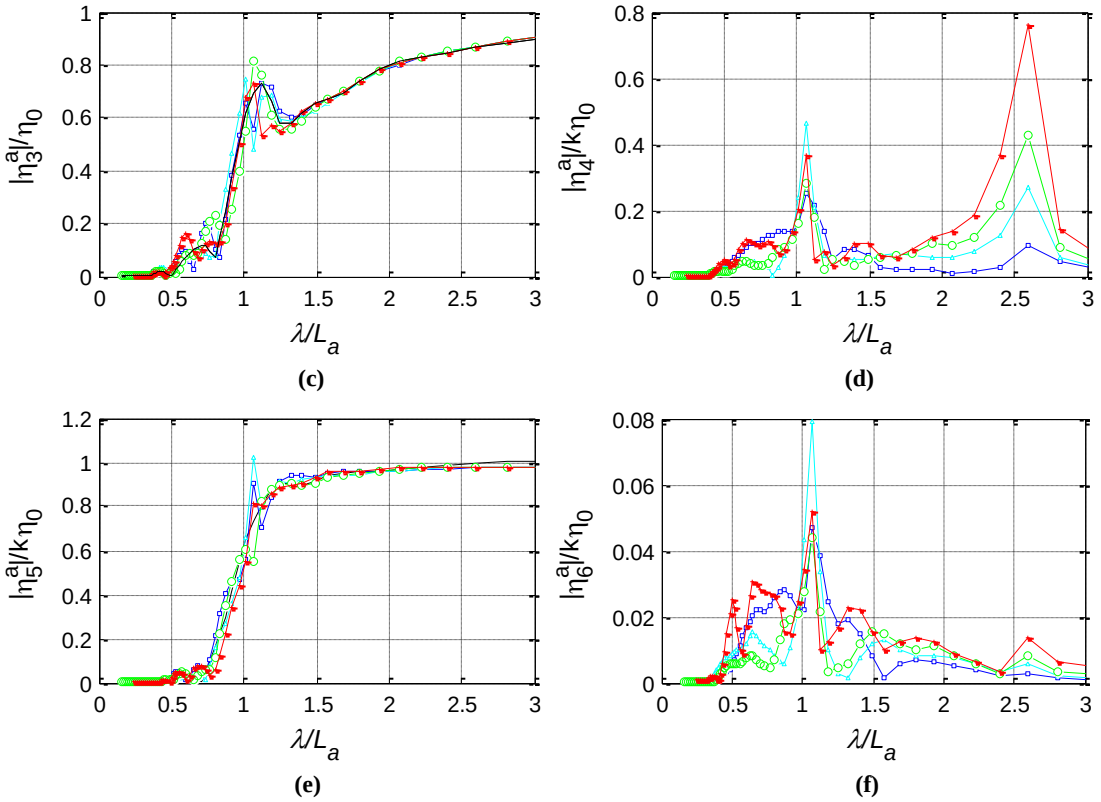

Figure 9.7: Response amplitude operators of Ship_a with different transverse distances in head waves, *Fn* = 0.1, *dl* = 0*m*. (a) Surge; (b) Sway; (c) Heave; (d) Roll; (e) Pitch; (f) Yaw.

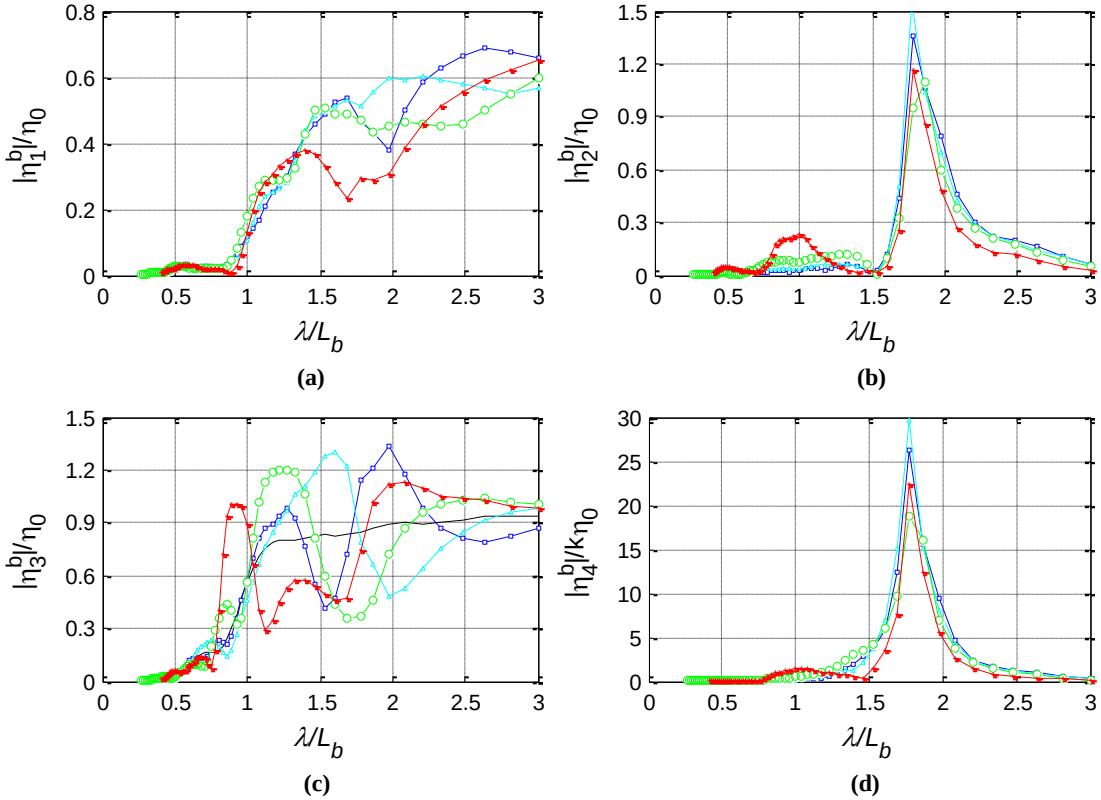

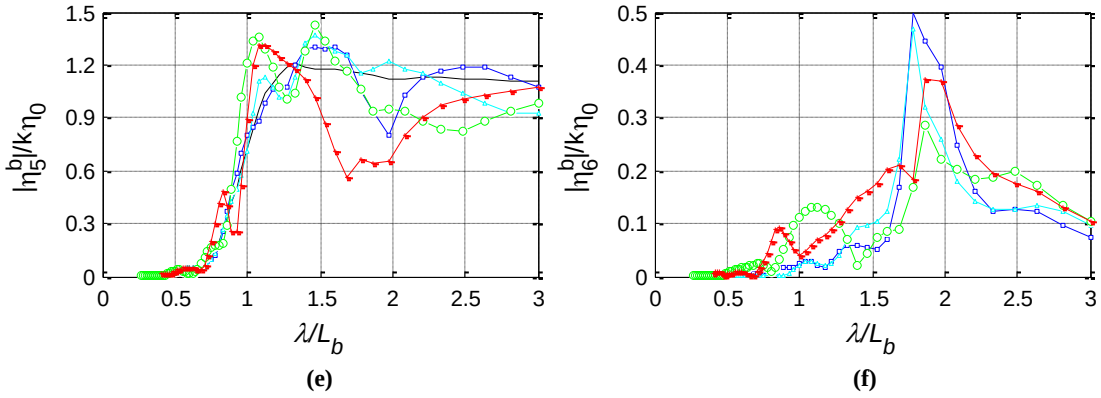

Figure 9.8: Response amplitude operators of Ship_b with different transverse distances in head waves, *Fn* = 0.1, *dl* = 0*m*. (a) Surge; (b) Sway; (c) Heave; (d) Roll; (e) Pitch; (f) Yaw.

Figure 9.9 and Figure 9.10 show the wave excitation forces of Ship_a and Ship_b respectively with different transverse distances in head waves. It can be seen from Figure 9.9 (a), (c) and (e) that the influence of the transverse distance on surge, heave and pitch forces is not evident. But the wave excitation forces in sway, roll and yaw directions are significantly influenced by the transverse distance, which is shown in Figure 9.9 (b), (d) and (f). As the transverse distance increases, the wave excitation forces in these three directions become smaller in the low range of λ/L_a, but in the higher range of λ/L_a, the forces with large *dt* could even be greater (as shown in Figure 9.9 (d) and (f)). The transverse distance effects on the wave excitation forces on Ship_b is similar to that on Ship_a. Overall, the transverse distance effects can influence the hydrodynamic properties of both ships. But there are no fixed rules on how to provide an optimal value. A specific analysis is required for a specific case, since the size of the ships and the working environment could have a great influence on the hydrodynamic interactions between two ships.

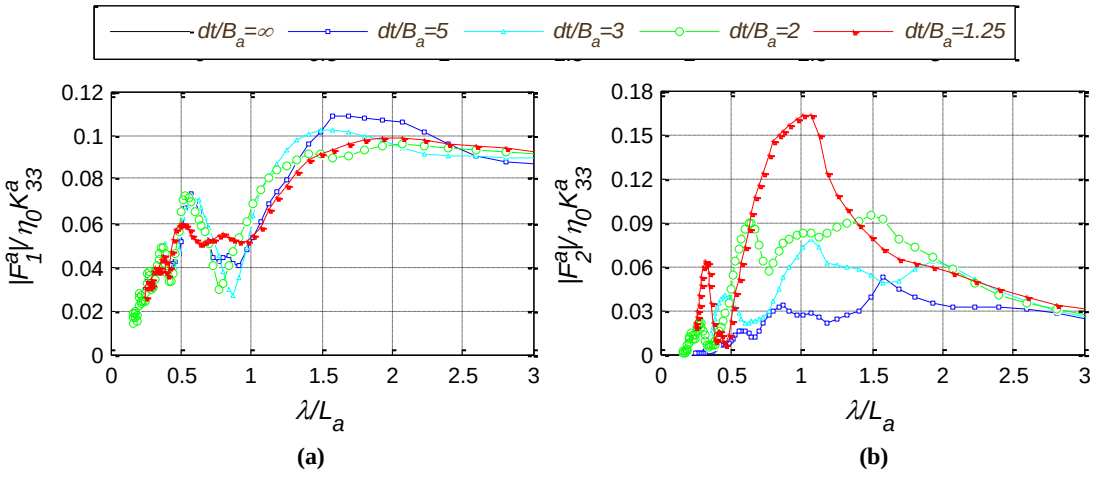

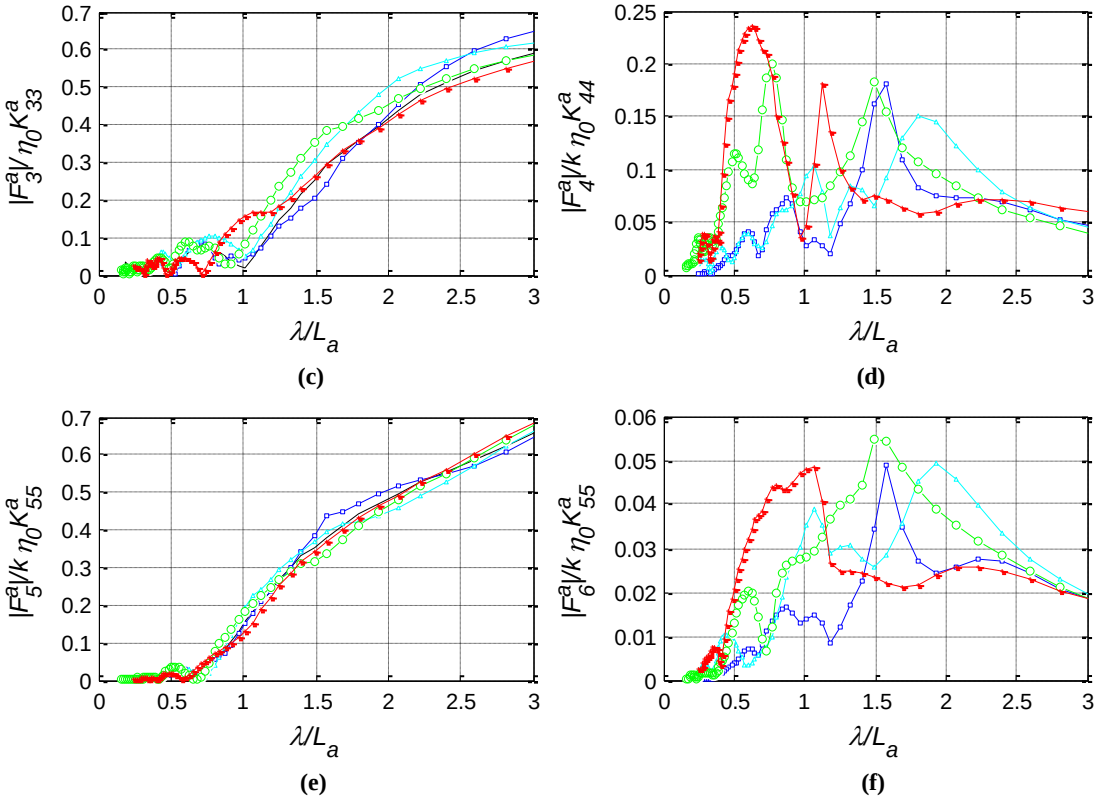

Figure 9.9: Wave excitation forces of Ship_a with different transverse distances in head waves, *Fn* = 0.1, *dl* = 0*m*. (a) Surge; (b) Sway; (c) Heave; (d) Roll; (e) Pitch; (f) Yaw.

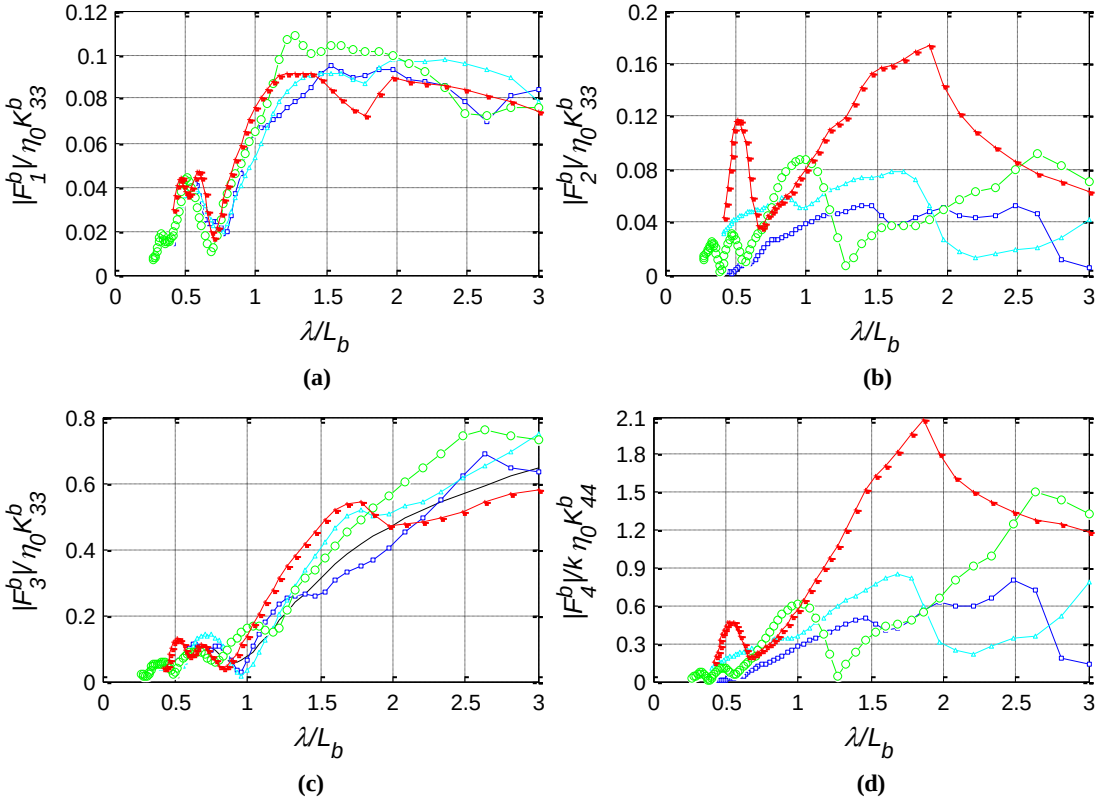

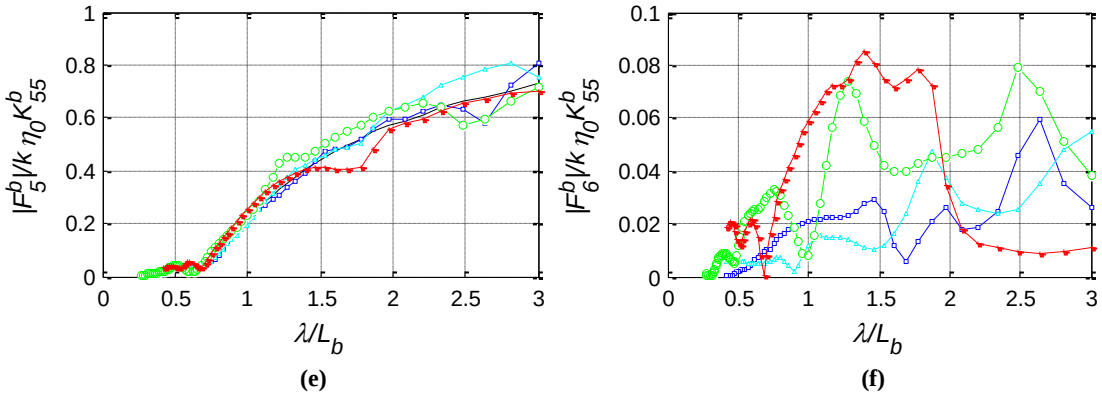

Figure 9.10: Wave excitation forces of Ship_b with different transverse distances in head waves, *Fn* = 0.1, *dl* = 0*m*. (a) Surge; (b) Sway; (c) Heave; (d) Roll; (e) Pitch; (f) Yaw.

9.4. Effect of longitudinal distance

In order to investigate the effect of the longitudinal distance (*dl*), we fix the forward speed at F_n = 0.1 and the transverse distance at *dt/Ba* = 3. These two ships are travelling with the same forward speed in head waves at infinite water depth. As shown in Figure 9.11, we compare the motion responses and wave excitation forces over a wide range of longitudinal distances (*dl* = -3 *m*, -2 *m*, -1 *m*, 0 *m*, 1 *m*, 2 *m*, ∞, where *dl* = ∞ denotes the cases without hydrodynamic interactions).

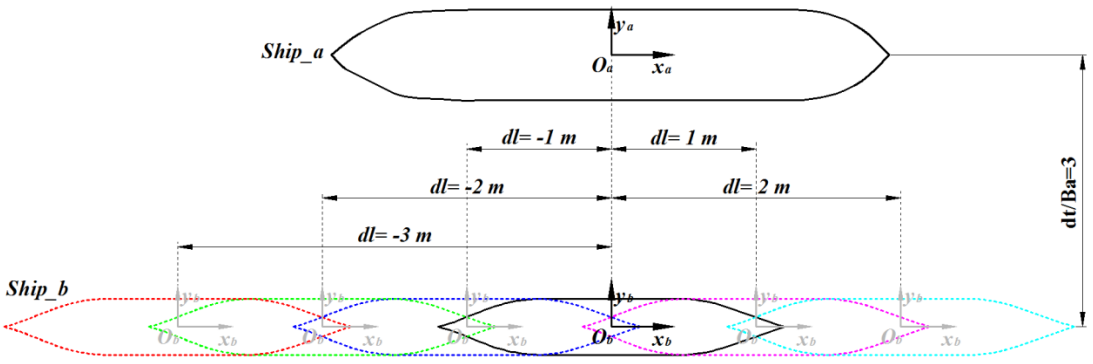

Figure 9.11: Sketch of two ships travelling with different longitudinal distances.

Figure 9.12 and Figure 9.13 show the response amplitude operators of Ship_a and Ship_b with different longitudinal distances in head waves. It can be found in Figure 9.12 (a), (c) and (e) that the surge, heave and pitch motions of Ship_a are hardly influenced by the longitudinal distance. However, the sway, roll and yaw motions are significantly influenced by the longitudinal distance, as shown in Figure 9.12 (b), (d) and (f). At the case of *dl* = 0 *m*, a very large peak values can be observed at $\lambda/L_a \approx 1.1$

in sway, roll and yaw motions. This is a very unfavourable case since $\lambda/L_a \approx 1$ corresponds to the critical incident wave frequency in ship design. Although some spikes emerge at $\lambda/L_a \approx 2.6$ (some of which could even be larger than the spikes at $\lambda/L_a \approx 1.1$), the corresponding incident wave frequency is very low, which is not the typical and critical conditions in the ship design. It could also be observed that as Ship_b shifts from the downstream side to the upstream side of Ship_a, the hydrodynamic interactions on Ship_a generally become more obvious. This is because the scattered waves generated from Ship_b will be convected behind the vessel. When these waves propagate to Ship_a, the pressure distribution around the body surface of Ship_a could be changed. However, if Ship_b is located in the downstream side of Ship_a, only a few amounts of the scattered waves produced by Ship_b can propagate to Ship_a due to the Doppler shift. This explains why the sway, roll and yaw motions of Ship_a at $dl = -3$ *m* and $dl = -2$ *m* are generally very small. But in the low frequency region ($\lambda/L_a \approx 2.6$), even when Ship_b is located in the downstream side of Ship_a, the hydrodynamic interactions on Ship_a are still very important. This is because that at the low frequency range, the Brard number τ ($\tau = u_0\omega_e/g$) is very small, and the scattered waves produced by Ship_b can propagate directly ahead of the vessel. These waves could change the hydrodynamic properties of Ship_a and consequently lead to a large spike in the low frequency responses of sway, roll and yaw directions, as shown in Figure 9.12 (b), (d) and (f).

When it refers to the motion responses of Ship_b, $dl = 0$ *m* and $dl = 1$ *m* becomes the most unfavourable cases since the sway, heave, roll and yaw motions could be very large, as shown in Figure 9.13(b), (c), (d) and (f). The longitudinal distance effects are also important in the surge, heave and pitch motions, as shown in Figure 9.13(a), (c) and (e). It can also be found that the motion responses of Ship_b at $dl = -3$ *m* and $dl = -2$ *m* are relatively small. These two distances are also the preferable cases for Ship_a. It can be concluded that the longitudinal distance has a large influence on the dynamic responses of both ships. If the other two parameters (u_0 and dt) are fixed, we suggest that the smaller ship should be located in the downstream side of the larger ship. The case of $dl = 0$ *m* must be avoided in the ship-to-ship interaction with forward speed problem.

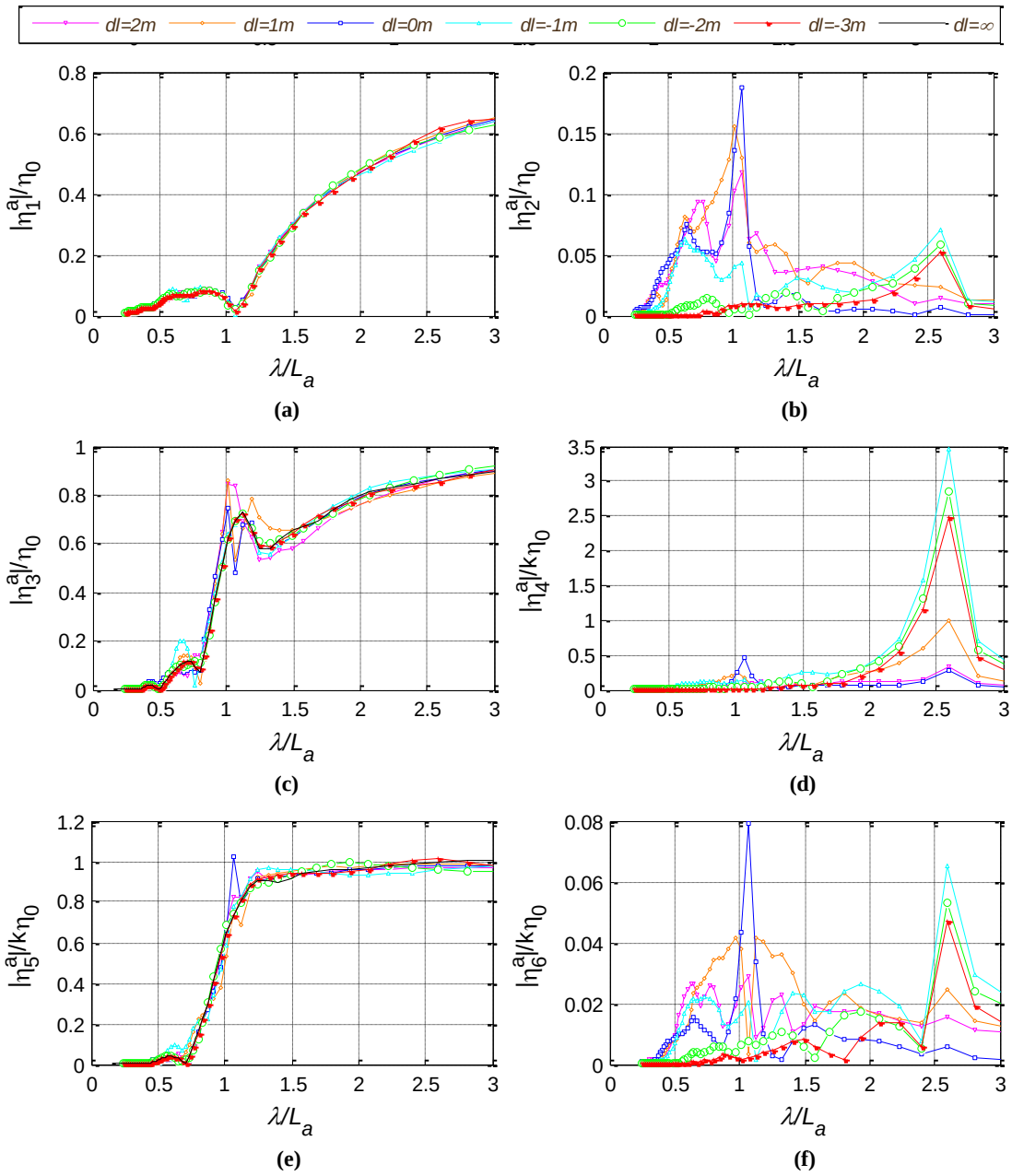

Figure 9.12: Response amplitude operators of Ship_a with different longitudinal distances in head waves, *Fn* = 0.1, *dt* = 1.875*m*. (a) Surge; (b) Sway; (c) Heave; (d) Roll; (e) Pitch; (f) Yaw.

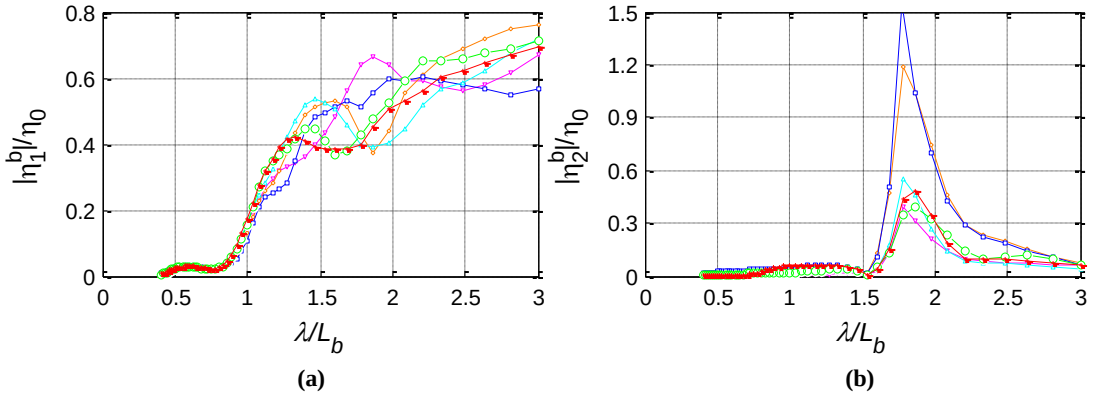

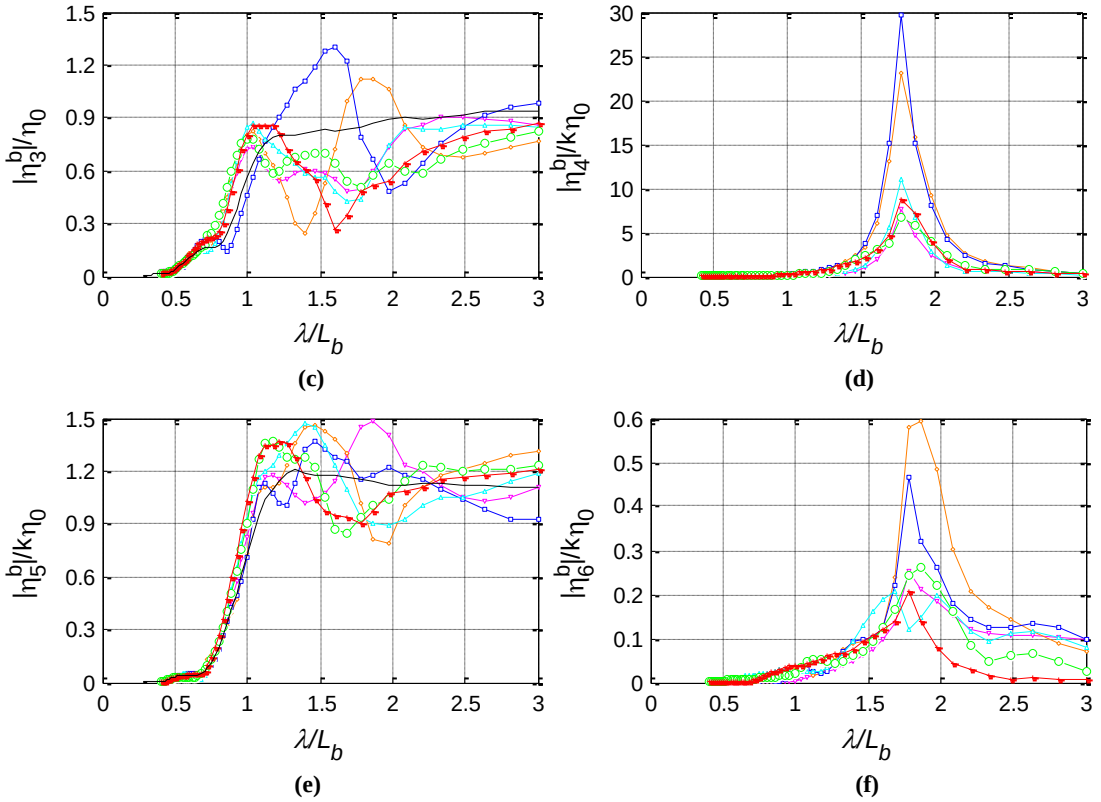

Figure 9.13: Response amplitude operators of Ship_b with different longitudinal distances in head waves, *Fn* = 0.1, *dt* = 1.875*m*. (a) Surge; (b) Sway; (c) Heave; (d) Roll; (e) Pitch; (f) Yaw.

Figure 9.14 and Figure 9.15 show the wave excitation forces of Ship_a and Ship_b respectively with different longitudinal distances in head waves. It can be found that for both Ship_a and Ship_b, the longitudinal distance effects are not important in the surge, heave and pitch forces. But for the rest degrees of freedom, the longitudinal distance has a significant influence. As can be seen from Figure 9.14 (b), (d) and (f), the sway, roll and yaw forces on Ship_a generally keep an increase trend at $\lambda/L_a < 1.2$ as Ship_b shifts from the downstream side to the upstream side. At $\lambda/L_a > 1.2$, the forces in roll and yaw directions become complicated and $dl = 0$ *m* and $dl = -1$ *m* tend to be the most undesirable cases, which is shown in Figure 9.14 (d) and (f). When it refers to the sway, roll and yaw forces on Ship_b, no regular trend can be found, since the influence of the longitudinal distance varies with the incident wave frequency.

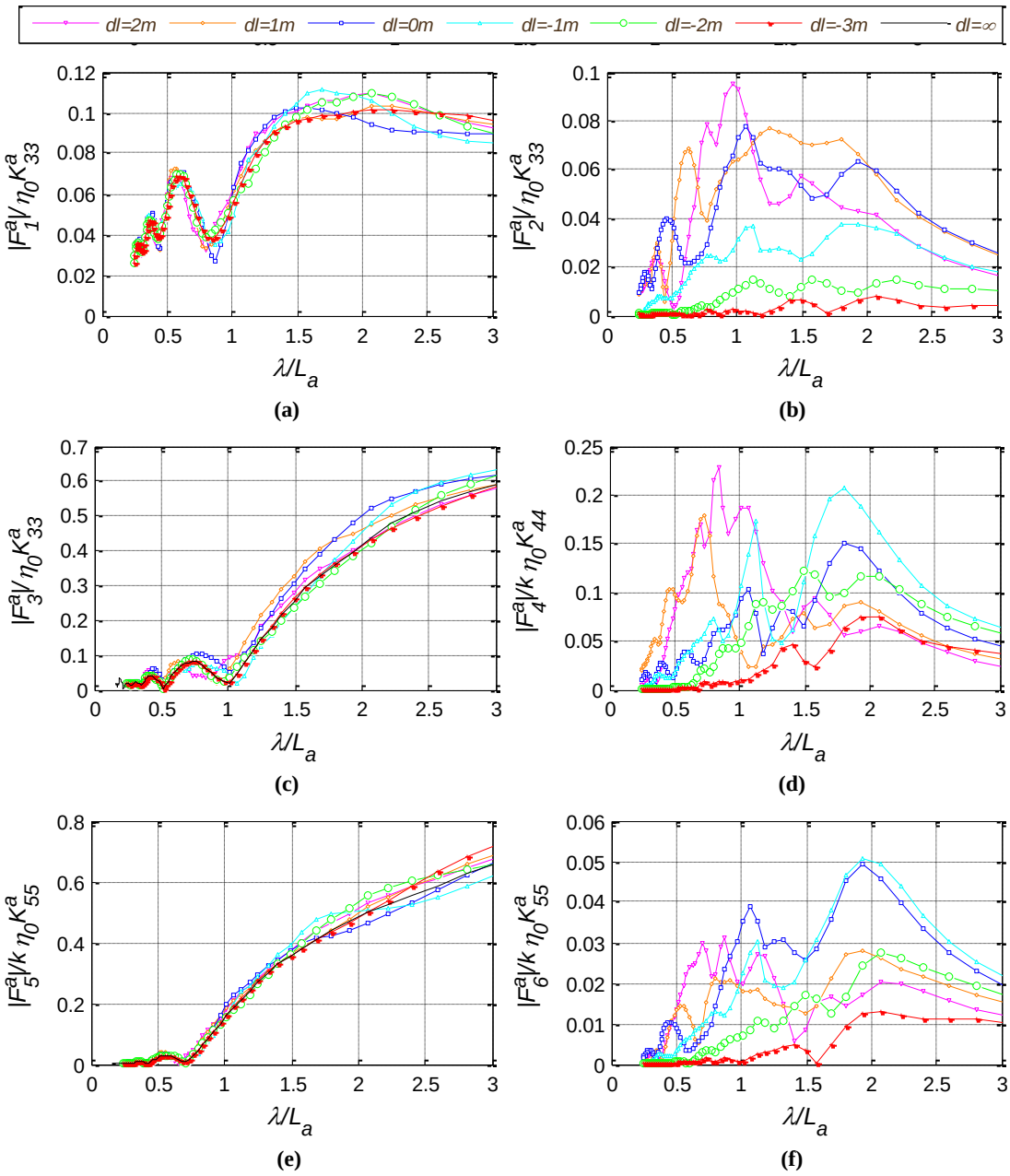

Figure 9.14: Wave excitation forces of Ship_a with different longitudinal distances in head waves, *Fn* = 0.1, *dt* = 1.875*m*. (a) Surge; (b) Sway; (c) Heave; (d) Roll; (e) Pitch; (f) Yaw.

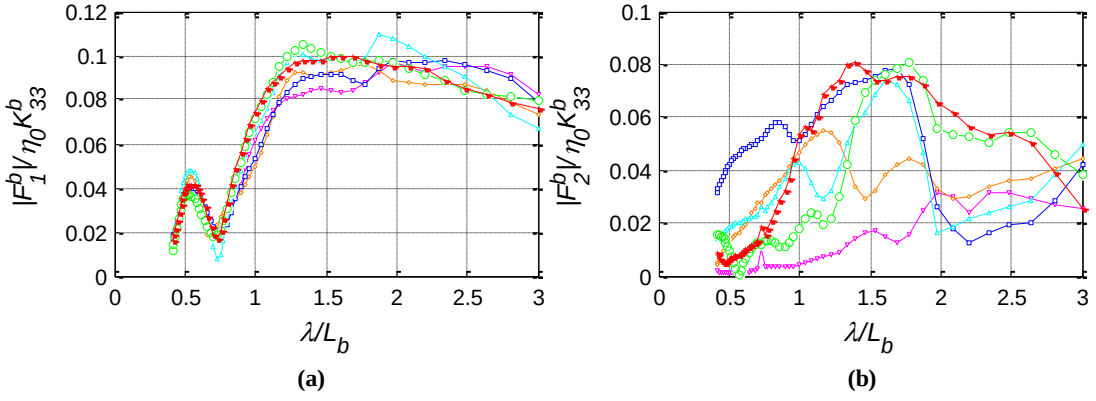

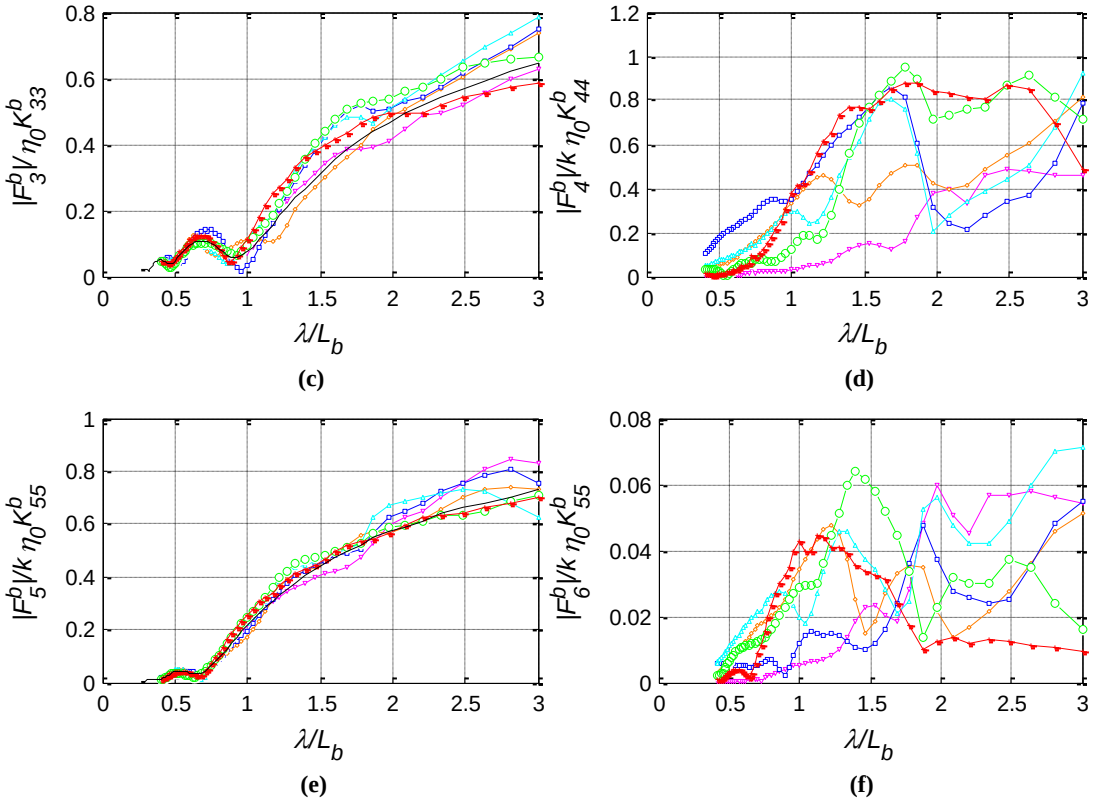

Figure 9.15: Wave excitation forces of Ship_b with different longitudinal distances in head waves, *Fn* = 0.1, *dt* = 1.875*m*. (a) Surge; (b) Sway; (c) Heave; (d) Roll; (e) Pitch; (f) Yaw.

9.5. Optimal design

9.5.1. Validation of double Doppler shift

The hydrodynamic interactions between two ships travelling with forward speed can be mainly influenced by the forward speed (u_0), the transverse distance (dt) and the longitudinal distance (dl). The effect of each individual parameter has been discussed in the previous sections, and in this section we will connect these parameters by the scattered wave patterns. As demonstrated in Section 5.2, the double Doppler shift theory can be used on the control surface to complete the radiation condition. We also find that the double Doppler shift theory can also be applicable on the free surface to determine the propagation of the scattered waves. Applying Eq. (5.5) to the free surface of single Ship_a advancing in head waves at λ/L_a = 1, we can obtain the local wave number ks and the rotated angle θ, which is shown in Figure 9.16. The rotated angle is defined as θ = -1 if there is no solution for Eq. (5.5), and it means there are no scattered waves propagating to these points. The blue region (θ = -1) in Figure 9.16 corresponds to the quiescent free surface. It can be observed that the critical line

between the quiescent and wake region is almost a straight line. The saw teeth on these lines are caused by the discrete meshes in the numerical solution. It can be supposed that if the mesh size on the free surface is very small, the saw teeth will be hardly noticed. It can also be observed that as forward speed increases, the scattered waves will be convected downstream, and the quiescent region becomes larger. It can be supposed that if Ship_b is located in this quiescent region, there should be no hydrodynamic interactions on Ship_b. In order to validate this assumption, we set up two cases at F_n = 0.3, as shown in Figure 9.17. In Case 1, part of Ship_b is in the wake of Ship_a (dl = -1 m). In Case 2, Ship_b is entirely located in the quiescent region (dl = 1 m). In both cases, the transverse distances are fixed at dt/Ba = 3.

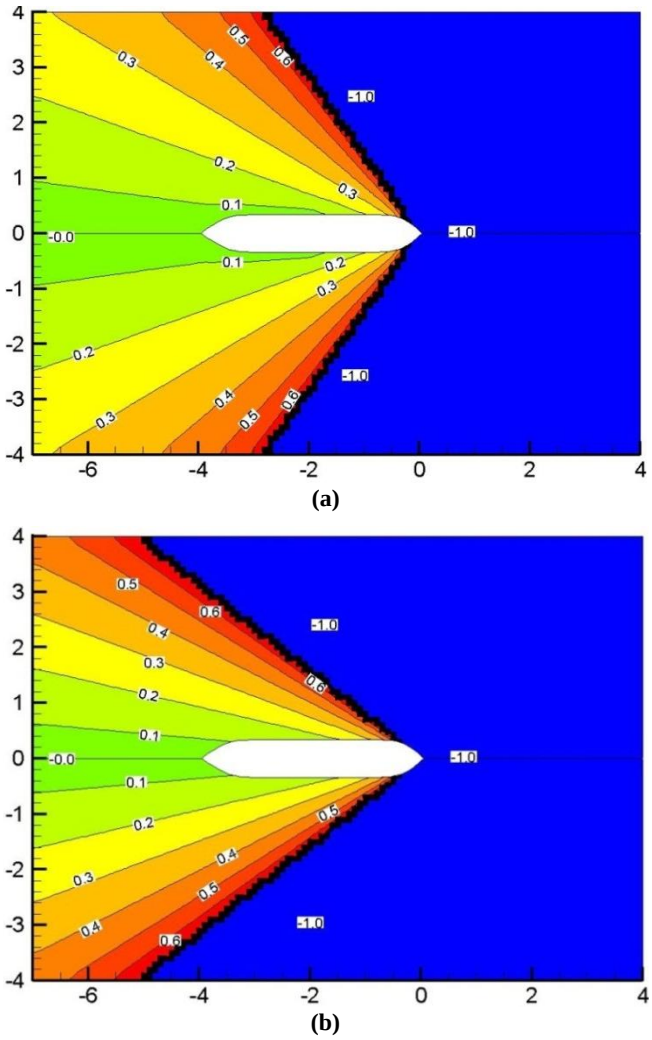

Figure 9.16: The rotated angle θ on the free surface as Ship_a travels with different forward speeds in head waves: λ/L_a = 1. (a) F_n = 0.2; (b) F_n = 0.3.

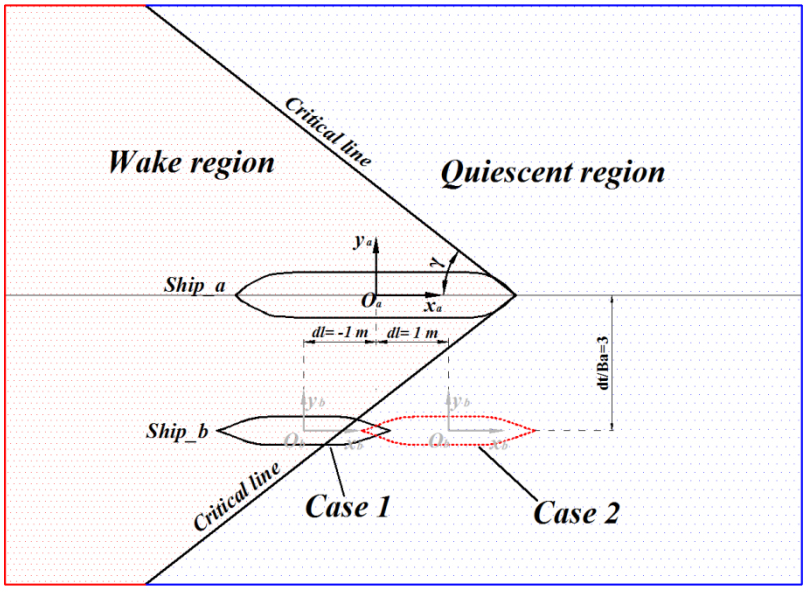

Figure 9.17: Sketch of Case 1 and Case 2.

The hydrodynamic interactions on Ship_b are mainly reflected in two categories: the wave excitation forces on Ship_b ($F_i^{Wb}, i=1,2,...,6$) and the hydrodynamic coefficients of Ship_b due to the motion of Ship_a (μ_{ij}^{ba} and λ_{ij}^{ba} , i = 1,2,…,6, j = 1,2,…,6). Table 9.1 shows the wave excitation forces on Ship_b of both cases. The results of single ship are also included, which represents the case without hydrodynamic interactions. From Table 9.1 we can find that for the single ship case, there are no wave excitation forces in sway, roll and yaw directions in head sea condition. In Case 2, as Ship_b is entirely located in the quiescent region, the wave excitation forces in 6 degrees of freedom are very close to the single ship results. The discrepancies between Case 2 and single ship results are mainly introduced by the numerical models. The computational domain of Case 2 is different from that of single ship case. However, the difference of the wave excitation forces between Case 1 and single ship case is very obvious, especially in sway, roll and yaw directions. It indicates that the hydrodynamic interactions on Ship_b of Case 1 are very important.

Table 9.1: Wave excitation forces on Ship_b in head waves: *dt/Ba* = 3, F_n = 0.3, λ/L_a = 1.

	Surge (N)	Sway (N)	Heave (N)	Roll (N·m)	Pitch (N·m)	Yaw (N·m)
F_i^{Wb} (Single Ship_b)	725.1	0.0	2426.1	0.0	1882.4	0.0
F_i^{Wb} (Case 1)	761.1	189.7	2453.1	16.7	1969.1	86.0

F_i^{Wb} (Case 2)	723.3	17.3	2430.1	1.6	1858.6	2.2

We also compare the hydrodynamic coefficients of Ship_b due to the motion of Ship_a (μ_{ij}^{ba} and λ_{ij}^{ba} , $i = 3, 4, 5,\ j = 1,2,\ldots,6$), as shown in Figure 9.18. The *x*-label in Figure 9.18 indicates the subscript *ij*, which corresponds to the relevant components in Eqs. (3.39)-(3.40). It can be seen that in Case 2, the motions of Ship_a have a very small influence on Ship_b. However, the external-induced hydrodynamic coefficients become much larger in Case 1, which indicates the hydrodynamic interactions are very significant in Case 1.

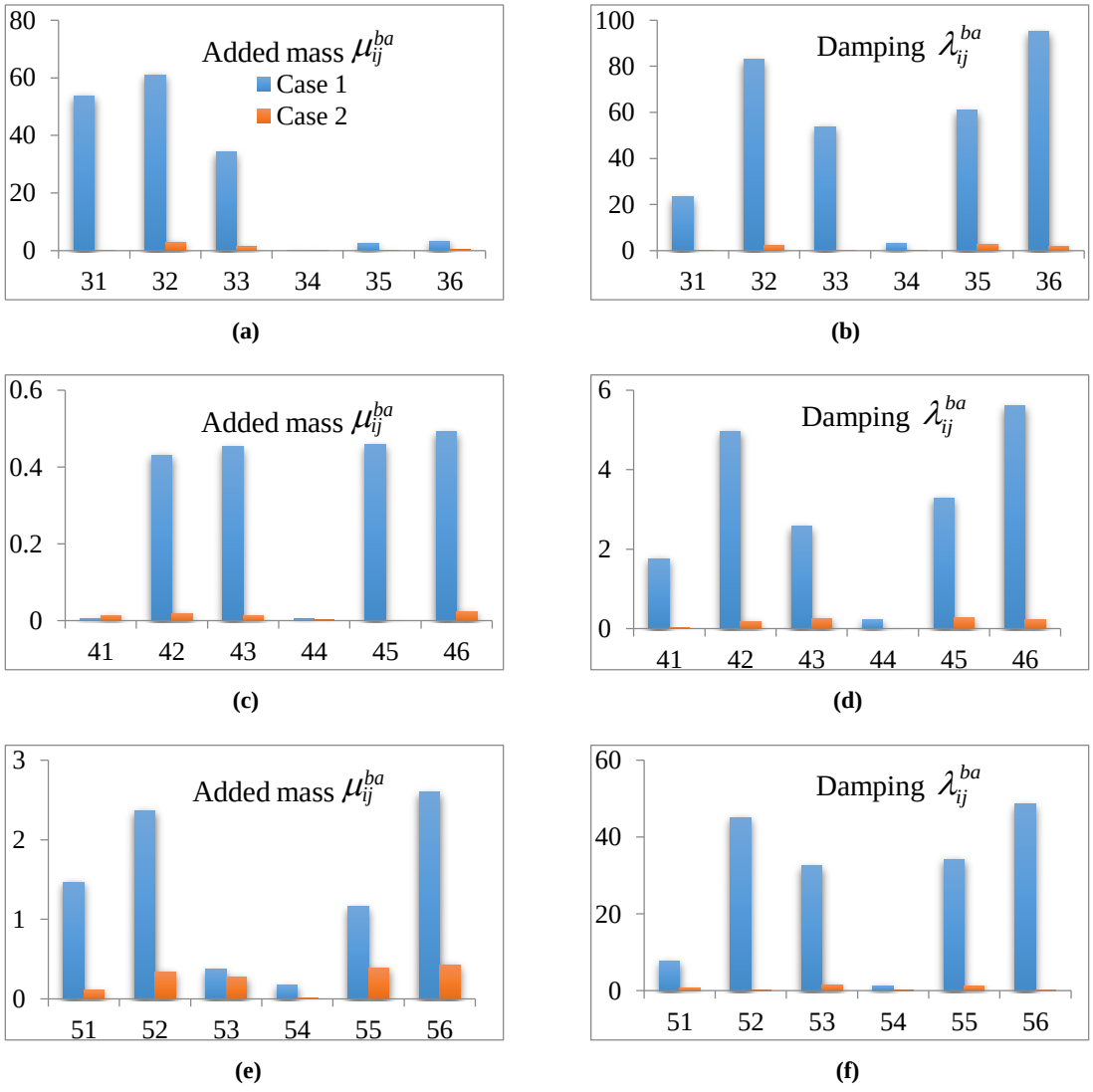

Figure 9.18: The hydrodynamic coefficients of Ship_b due to the motions of Ship_a: *dt/Ba* = 3, F_n = 0.3, λ/L_a = 1. (a) Heave added mass; (b) Heave damping; (c) Roll added mass; (d) Roll damping; (e) Pitch added mass; (f) Pitch damping.

The results of these two cases indicate that the hydrodynamic interactions can be predicted by the propagation of the scattered waves. The double Doppler shift provides an effective and practical method to predict the propagation of the waves. By using this method, we can obtain the critical line between the quiescent and wake region without solving the boundary value problem, which can save a lot of efforts during the modelling and calculations. It was demonstrated in Section 8.3 that the hydrodynamic interactions on the smaller ship are more obvious. Therefore, we suggest that the scattered waves of the larger ship should be calculated firstly. After the critical line between the quiescent and wake region has been determined, the quiescent region could be considered as a safe region for the smaller ship.

9.5.2. Systematic optimization

The method described above provides a simplified approach to obtain the safe region for the smaller ship. Although the hydrodynamic interactions on the larger ship is not as significant as that on the smaller ship, an optimal design is also preferred to provide a best solution, which can guarantee that both ships are located in the quiescent region. Figure 9.19 (a) and (b) shows the rotated angle θ of Ship_a and Ship_b respectively. As can be seen from Figure 9.19 (a), Ship_b (the smaller ship) is located in the wake region of Ship_a (the larger ship). However, when it refers to Figure 9.19 (b), we can observe that Ship_a is entirely located in the quiescent region of Ship_b. As a result, the hydrodynamic interactions can only influence the motions of Ship_b. In order to avoid the hydrodynamic interactions on both ships, the configuration of these two ships should be adjusted. Figure 9.20 shows an example of the optimal configuration. It can be seen that both of the ships are located in the quiescent region. The critical lines pass through the stern of each ship.

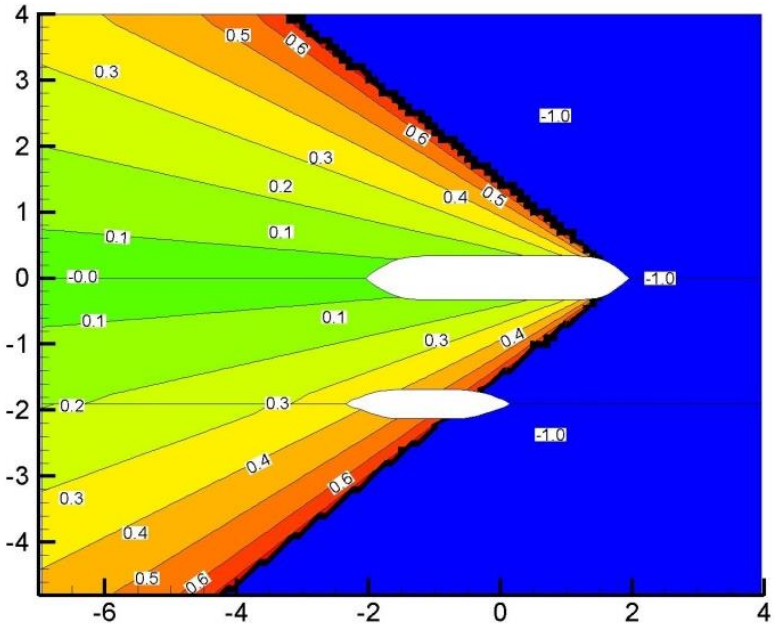

(a)

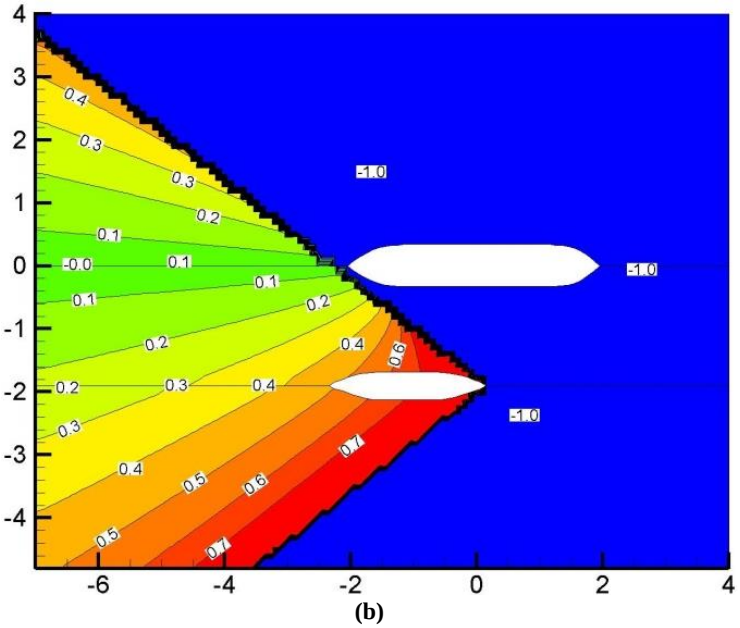

(b)

Figure 9.19: The rotated angle θ on the free surface: dt/Ba = 3, dl = -1 m, F_n = 0.3, λ/L_a = 1. (a) Ship_a; (b) *Ship_b*.

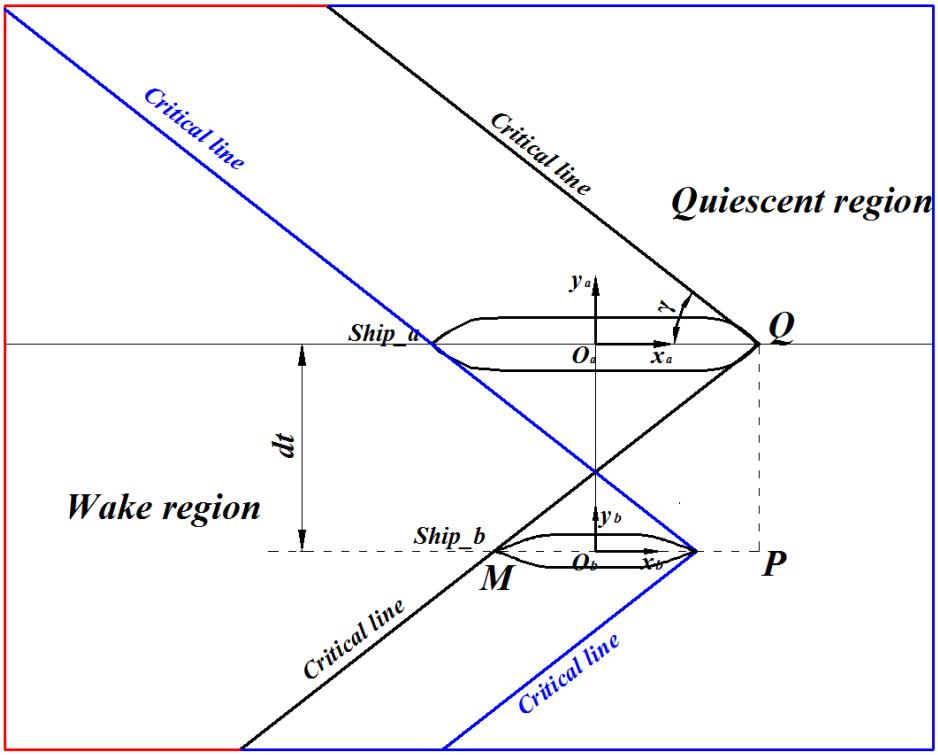

Figure 9.20: An example of the optimal configuration of two ships traveling in head waves: *dl* = 0 *m*, F_n = 0.3, λ/L_a = 1, γ = 38°.

We notice that the critical scattered wave angle (can be called as semi-wedge angle γ, which is the angle between x-axis and the critical line, as shown in Figure 9.20) is a constant when the incident wave frequency and the forward speed are known. In the present case, the critical scattered wave angle of both ship equals to 38° at F_n = 0.3. We assume that the optimal objective is the transverse distance dt. Theoretically, there are mainly seven parameters which can determine the optimal solution of dt. These seven parameters are the water depth (d), the length of Ship_a (L_a), the length of Ship_b (L_b), the longitudinal distance (dl), the incident frequency (ω_0), the forward speed (u_0) and the semi-wedge angle (γ). The transverse distance dt can be expressed in terms of these parameters as

$$dt = f(d, L_a, L_b, dl, \omega_0, u_0, \gamma) \tag{9.1}$$

The effect of the water depth has been discussed in the previous sections and it can change the dispersion relation in Eq. (3.4). As a result, the water depth will influence the semi-wedge angle γ. But, in most of the cases, the water depth to the draft ratio (d/T) is greater than 7, which can be regarded as infinite water depth problem. In the

present study, we assume $d = \infty$. La and L_b are the given parameters. Given that the two ships are travelling with the same forward speed, the optimal longitudinal distance *dl* can be easily determined as zero, as shown in Figure 9.20. It is also assumed that the incident frequency ω_0 and the forward speed u_0 are given before the optimal design. Giving rise to the condition *QP/MP = tan(γ)*, the optimal transverse distance *dt* in Eq.(9.1) can be reduced to

$$dt = \frac{1}{2}(L_a + L_b)\tan(\gamma) \ , \gamma < \pi/2 \tag{9.2}$$

From Eq. (9.2) we can find that the optimal *dt* is only determined by the semi-wedge angle γ. Based on the deep water assumption, Eq. (5.14) provides an analytical solution for the critical rotated angle θ. From Figure 5.1, the relation between θ and γ can be established as

$$\gamma = \pi - 2\theta \tag{9.3}$$

By substituting Eq. (5.14) and Eq. (3.3) into the Eq. (9.3), we can obtain the relation between the semi-wedge angle γ and the incident frequency ω_0 and the forward speed u_0 in head waves as

$$\gamma = \pi - 2\cos^{-1}\left[\frac{g^2}{4u_0\omega_0(g + u_0\omega_0)}\right] \tag{9.4}$$

Figure 9.21 shows some results of the semi-wedge angle γ as a function of ω_0 and u_0.

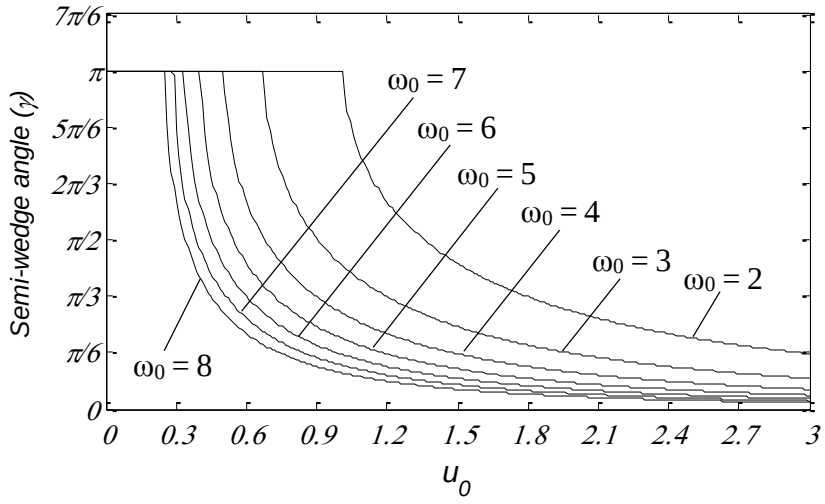

Figure 9.21: The semi-wedge angle γ as a function of ω_0 and u_0. (Unit: γ, rad; u0, m/s; ω_0, rad/s).

It should be noticed that the incident frequency ω_0 and the forward speed u_0 in Eq. (9.4) can be reduced to a single parameter. Let's define the incident Brard number as

$$\tau_0 = \frac{u_0 \omega_0}{g} \tag{9.5}$$

Then the Eq. (9.4) becomes

$$\gamma = \pi - 2\cos^{-1}\left[\frac{1}{4\tau_0(1+\tau_0)}\right] \tag{9.6}$$

From Eq. (9.6), we find that the semi-wedge angle γ is only determined by the incident Brard number τ_0. Figure 9.22 gives the semi-wedge angle γ as a function of τ_0. It should be noticed that only at $\tau_0 > 0.2$, the Eq. (9.6) can be solved. Otherwise, $\gamma = \pi$, which indicates that the scattered waves can directly propagate ahead of the ship. At $\tau_0 < 0.27$, the semi-wedge angle $\gamma > 1/2\pi$ and there is no optimal transverse distance since one of the ship will be inevitably located in the wake region of the other one. As the incident Brard number τ_0 increases from 0.2 to 1, the semi-wedge angle decreases very quickly and the scattered waves are convected downstream. As τ_0 keep increasing, the semi-wedge angle γ will gradually approach 0. However, it will never reach 0.

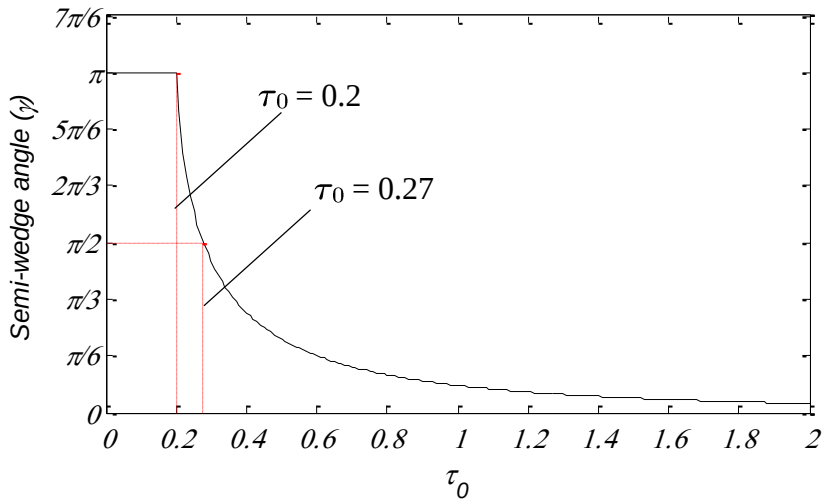

Figure 9.22: The semi-wedge angle γ as a function of τ_0.

Substituting the semi-wedge angle (9.6) into the optimal transverse distance *dt*, Eq. (9.2) becomes

$$dt = \frac{1}{2}(L_a + L_b)\tan\left\{\pi - 2\cos^{-1}\left[\frac{1}{4\tau_0(1+\tau_0)}\right]\right\} \tag{9.7}$$

It is assumed that $L_b/L_a = \upsilon$, the optimal transverse distance dt in Eq. (9.7) can be expressed by its non-dimensional form as

$$dt / L_a = \frac{1}{2}(1+\upsilon)\tan\left\{\pi - 2\cos^{-1}\left[\frac{1}{4\tau_0(1+\tau_0)}\right]\right\} \tag{9.8}$$

The results of the non-dimensional optimal transverse distance are shown in Figure 9.23. It can be found that as the incident Brard number τ_0 increases, the optimal *dt/La* keeps a downward trend. It can also be found that the larger ratio of L_b/L_a corresponds to a smaller optimal *dt/La*.

Eq. (9.8) and Figure 9.23 are applicable to a wide range of engineering practice, as long as the two ships are travelling with the same forward speed in head waves at infinite water depth. As long as the ratio of L_b/L_a is given, we can use Eq. (9.8) to obtain the minimal and optimal transverse distance at different forward speeds and incident waves.

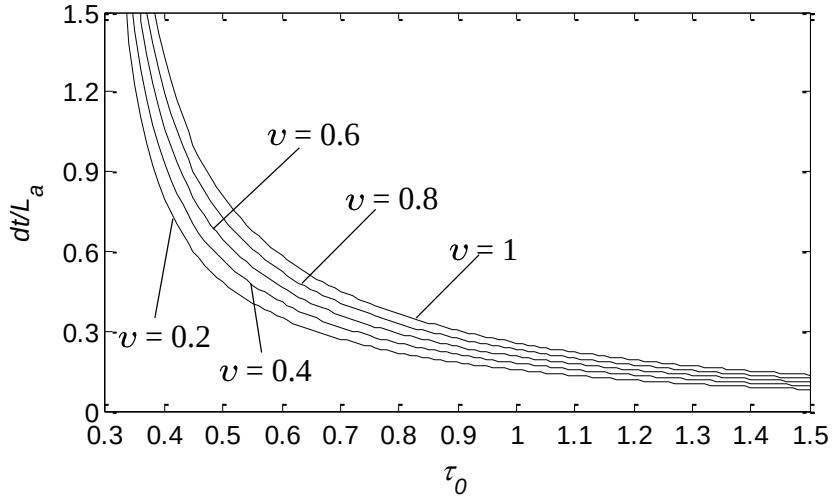

Figure 9.23: The non-dimensional optimal transverse distance.

9.6. Summary

In this chapter, we investigated the main parameters (u_0, *dt* and *dl*) which could influence the hydrodynamic interactions between two travelling ships. It was found that the forward speed effects could influence the motion responses of both ships significantly and if the other two parameters (*dt* and *dl*) are fixed, we suggest that the Froud number should be lower than F_n = 0.1. But the transverse distance effects are complicated and there is no fixed rule on how to provide an optimal value. A specific analysis is required for a specific case, since the size of the ships and the working environment could have a great influence on the hydrodynamic interactions between two ships. We also found that the longitudinal distance had a large influence on the dynamic responses of both ships and the case of *dl* = 0 *m* must be avoided since the hydrodynamic interactions become very violent at this case.

We also carried out the systematic optimization about these three parameters based on the scattered wave patterns. The double Doppler shift was extended to the free surface and the critical line between the wake and quiescent region could be obtained. It was found that if Ship_a was located in the quiescent region of Ship_b, the hydrodynamic interactions on Ship_a could be ignored. Based on this finding, we derive the analytical expression of the so-called semi-wedge angle. This angle is only determined by the incident Brard number. It provides an easy way to obtain the wake and quiescent region without solving the boundary value problem. After the solution of the semi-wedge angle, we established a systematic optimal process. The analytical formulation has been established to obtain the optimal transvers distance between two travelling ships. This method is applicable to a wide range of engineering practice, as long as the two ships are travelling with the same forward speed in head waves at infinite water depth. But, it should be also noticed that the optimal solution can only be found at $\tau_0 >$ 0.27.

10. Conclusions and recommendations

10.1. Achievements against the objectives

The primary objective of the work presented in this thesis is to study the hydrodynamic interactions between two ships travelling or stationary in shallow waters. The main achievements against the objectives are outlined below:

- Develop a numerical program to predict the behaviour of single ships travelling in waves. A 3-D Rankine source panel method has been developed to predict the hydrodynamic properties of marine vessels travelling with a wide range of forward speeds. Double Doppler shift has been taken into consideration in the boundary condition of the control surface. A Wigley III hull travelling with very low or medium forward speed was considered to validate this radiation condition. Comparing with the experimental data, it can be concluded that the present method can provide a satisfactory prediction of the hydrodynamic responses of a single ship travelling with wide range of the forward speeds.
- Develop a numerical program to predict the coupled behaviour of stationary ships moored side-by-side in waves. Based on 3-D Rankine source panel method for single ship, we extended the numerical program to predict the hydrodynamic interactions between two ships stationary in head and beam waves. We examined the hydrodynamic coefficients, wave excitation forces and motion responses and established the comparisons between the present calculations and the commercial software as well as the experimental data. Very good agreement has been achieved which illustrates that the present program is a useful tool to predict the hydrodynamic behaviours of two ships arranged side by side without forward speed. We also calculated the motion responses of both ships at different water depths and separation distance. It was found that the effect of the water depth and separation distance was very important. The discussion was highlighted on the effects of mooring and fender system. We found that the influence of the mooring lines, fenders and hawsers on the motion responses of both ships was not evident.

- Develop a numerical program to predict the coupled behaviour of two travelling ships arranged side-by-side in shallow water. We extended double Doppler shift radiation condition to the ship-to-ship interaction with forward speed problem and developed a numerical program to predict the coupled behaviour of two travelling ships arranged side-by-side in shallow water. The present method was validated through two pairs of models. The computed dynamic responses of both models in heave and pitch motions showed a good agreement with the published experimental results. However, the prediction of the roll motion was full of challenges due to the inviscid assumption in the potential flow theory. It was also found that the hydrodynamic interaction had much greater influence on the motions of the smaller ship. We investigated the hydrodynamic interactions through the hydrodynamic coefficients and wave excitation forces. It was found that the hydrodynamic coefficients of the larger ship were mainly determined by the oscillation of the larger ship itself, while the self-induced and external-induced components of the hydrodynamic coefficients were at the same level for the smaller ship. A very large sway force for zero speed case was predicted when the transverse distance between two ships equalled to the wave length. This extreme force is due to the diffracted wave energy that trapped in the gap and it will bring a great risk to the ship-to-ship offloading operation. We also examined the present radiation condition and the effect of forward speed through a series of numerical experiments involving two ships with a wide range of forward speed in head seas. It was concluded that the present method could provide an effective prediction of the wave patterns for the ships travelling with a wide range of forward speed.
- Validate the numerical programs described above through the commerce software as well as experimental measurements. Our numerical programs have been validated through a series of model tests. For the single ship problem, we used Journee's experimental data (Journee, 1992) to validate our numerical results about a Wigley III hull with different forward speeds. For the ship-to-ship interaction without forward speed problem, we validated our method through two pairs of model. Model 1 was about a modified Wigley hull and a box model at beam sea case and the experimental results as well as Kashiwagi's

(Kashiwagi et al., 2005) numerical results were used for the validation. Model 2 was about two identical Wigley III hulls at head sea condition and the results from the commercial software (Wadam, 2010) are used for the comparison. We also validated our numerical program about two ships travelling in head waves through two pairs of model. Model 1 was about a full scale supply ship and frigate model, and Li's model test results (Li, 2007) were used to validate the present numerical calculation. Model 2 was a tanker and LNG ship model in model scale, and Ronæss' experiments (Ronæss, 2002) provide the motion responses for validation. The corresponding numerical results by using Green function method were also included in our validation. Overall, the agreement between the present calculations and the model test results is satisfactory.

- Carry out parametric studies in order to develop recommendations for ship designers and operators for maximum speed and distance between two ships in given environmental conditions for safe operation. We investigated the main parameters (u_0, *dt* and *dl*) which could influence the hydrodynamic interactions between two travelling ships. It was found that the forward speed effects could influence the motion responses of both ships significantly. If the other two parameters (*dt* and *dl*) are fixed, we suggest that the travelling speed should be lower than F_n = 0.1. But the transverse distance effects are complicated and there is no fixed rule on how to provide an optimal value. We also found that the longitudinal distance had a large influence on the dynamic responses of both ships and the case of *dl* = 0 *m* should be avoided since the hydrodynamic interactions became very violent at this case. We also carried out the systematic optimization about these three parameters based on the scattered wave patterns. The double Doppler shift was extended to the free surface and the critical line between the wake and quiescent region could be obtained. It was found that if Ship_a was located in the quiescent region of Ship_b, the hydrodynamic interactions on Ship_a could be ignored. Based on this finding, we derive the analytical expression of the so-called semi-wedge angle, and the analytical formulation has been established to obtain the optimal transverse distance between two travelling ships. But, it should be also noticed that the optimal solution could only be found at $\tau_0 > 0.27$.

10.2. Contributions of the present study

The contribution of the present study can be summarised as follows:

- Introduce a new radiation condition to solve the hydrodynamic problems and extend it to the ship-to-ship interaction with forward speed problem. This radiation condition takes into account the Doppler shift of the scattered waves. It is applicable to a wide range of forward speeds, including very low forward speed problem where the Brard number is smaller than 0.25. The validation of this new radiation condition was established on both single ship and ship-to-ship cases. The comparison between the present and Sommerfeld radiation condition was made at $\tau < 0.25$, while the comparison between the present and upstream radiation treatment was made at $\tau > 0.25$. Our solution showed a better wave pattern without reflections from the truncated control surface, which confirmed the effectiveness of the present radiation condition as a wave-pattern prediction tool for the ships travelling with a wide range of forward speed.
- Introduce a 3-D Rankine source method to solve the ship-to-ship interaction with or without forward speed problem. Most of the studies on ship-to-ship problem are based on Green function method, which has some limitations, e.g. the so-called irregular frequency problem. However, these limitations can be avoided by using Rankine source method. It takes account of the forward speed into the boundary value problem and the Rankine-type Green function can satisfy the seabed boundary condition through the method of image. We validated the Rankine source method through a number of model tests, as well as the Green function method. It was concluded that the present method could provide a satisfactory prediction of the hydrodynamic properties of ships travelling in waves.
- Derive the analytical expression of the semi-wedge angle based on double Doppler shift theory. This angle is only determined by the incident Brard number. It provides an easy way to obtain the wake and quiescent region without solving the boundary value problem. After the solution of the semi-wedge angle, the analytical formulation has been established to obtain the

optimal transvers distance between two travelling ships. This method is applicable to a wide range of engineering practice, as long as the two ships are travelling with the same forward speed in head waves at infinite water depth. By using this method, we can obtain the critical line between the quiescent and wake region without solving the boundary value problem, which can save a lot of efforts during the modelling and calculations.

10.3. Recommendations for the future work

The present 3-D Rankine source method associated with the double Doppler shift radiation condition can be further improved in several aspects:

- In order to improve the accuracy of the prediction of the hydrodynamic coefficients in radiation problem, the coupled effects between the steady flow and radiation potential should be taken into account in the body surface boundary condition. Meanwhile, the nonlinear free surface boundary condition should also be considered in the future work.
- In order to improve the accuracy of the prediction of roll motion, a roll damping coefficient should be applied in the motion equation to avoid the unrealistic roll motions. Unfortunately, this damping coefficient could not be determined without model test results. A future study based on CFD solutions should be carried out to provide the damping coefficient.
- In order to save the computational time, a high order panel method should be applied to discrete the boundaries. And a self-adaptive mesh refinement technique should be required to provide a more effective boundary element solution of the Laplace equation.
- In order to verify the present radiation condition at very low forward speed, the corresponding model test should be carried out.
- In the present study, our calculations about the mooring and fender systems are based on linear assumption. But the nonlinear effects from these systems are significant during the offloading operation when the two ships are in close proximity. Time domain method should be complemented to account for the nonlinear loads from the fender and mooring line system.

- An extensive study should be carried out on the overtaking and encountering operations.
- The present program for two ships arranged side by side should be expanded to simulate three or more than three bodies travelling or stationary in waves.

References

Andersen, P., 1979. Ship motions and sea loads in restricted water depth. Ocean Engineering 6, 557-569.

Becker, E., 1958. Das Wellenbild einer unter der Oberfläche eines Stromes schwerer Flüssigkeit pulsierenden Quelle. Journal of Applied Mathematics and Mechanics 38 (9-10), 391-399.

Bunnik, T., 1999. Seakeeping calculations for ships, taking into account the non-linear steady waves, PhD thesis. Delft University of Technology, The Netherlands.

Cao, Y., Schultz, W.W., Beck, R.F., 1991. Three-dimensional desingularized boundary integral methods for potential problems. International Journal for Numerical Methods in Fluids 12 (8), 785-803.

Chakrabarti, S., 2001. Empirical calculation of roll damping for ships and barges. Ocean Engineering 28, 915-932.

Chan, H.S., 1992. On the calcualtion of ship motions and wave loads of high speed catamarans. International Shipbuilding Progress 42, 181-195.

Chen, G.R., Fang, M.C., 2001. Hydrodynamic interactions between two ships advancing in waves. Ocean Engineering 28, 1053-1078.

Das, S., Cheung, K.F., 2012a. Hydroelasticity of marine vessels advancing in a seaway. Journal of Fluids and Structures 34, 271-290.

Das, S., Cheung, K.F., 2012b. Scattered waves and motions of marine vessels advancing in a seaway. Wave Motion 49 (1), 181-197.

Endo, H., 1987. Shallow water effect on the motions of three dimensional bodies in waves. Journal of Ship Research 31 (1), 34-40.

Faltinsen, O.M., 1993. Sea loads on ships and offshore structures. Cambridge University Press.

Fang, M.C., Kim, C.H., 1986. Hydrodynamically coupled motions of two ships advancing in oblique waves. Journal of Ship Research 30 (3), 159-171.

Gao, Z., Zou, Z., 2008. A NURBS-based high-order panel method for three-dimensional radiation and diffraction problems with forward speed. Ocean Engineering 35 (11-12), 1271-1282.

Hess, J.L., Smith, A.M.O., 1964. Calculation of nonlifting potential flow about arbitrary three-dimensional bodies. Journal of Ship Research 8 (2), 22-44.

Himeno, Y., 1981. Prediction of ship roll damping-state of the art, Report No.239. Department of Naval Architecture and Marine Engineering, University of Michigan.

Huang, Y.F., 1997. Nonlinear ship motions by a Rankine panel method, PhD Thesis. MIT.

Inoue, Y., Kamruzzaman, M., 2008. Analysis of hydrodynamic characteristics for arbitrary multihull ships advancing in waves. Journal of Marine Science and Technology 13 (3), 231-243.

Iwashita, H., Kataoka, S., 1996. 3-D analysis of the hydrodynamic interaction between steady and unsteady flows for a catamaran, Proceedings of Korea and Japan Joint Workshop, pp. 1-9.

Jensen, G., Mi, Z.X., Söding, H., 1986. Rankine source methods for numerical solutions of steady wave resistance problem, Proceedings of 16th Symposium on Naval Hydrodynamics, Berkeley, pp. 575-582.

Ji, C.-Y., Yuan, Z.M., 2014. Experimental study of a hybrid mooring system Journal of Marine Science and Technology, DOI: 10.1007/s00773-00014-00260-00777.

Journee, J.M.J., 1992. Experiments and calculations on 4 Wigley hull forms in head waves, Report No. 0909. Ship Hydromechanics Laboratory, Delft University of Technology, The Netherlands.

Kashiwagi, M., 1993. Heave and pitch motions of a catamaran advancing in waves, in: Yokohama (Ed.), Proc. of 2nd International Conference on Fast Sea Transportation pp. 643-655.

Kashiwagi, M., Endo, K., Yamaguchi, H., 2005. Wave drift forces and moments on two ships arranged side by side in waves. Ocean Engineering 32 (5-6), 529-555.

Kim, B., Shin, Y., 2007. Steady flow approximations in 3-D ship motion calculation. Journal of Ship Research 51 (3), 229-249.

Kim, C.H., 1969. Hydrodynamic forces and moments for heaving swaying, and rolling cylinders on water of dinite depth. Journal of Ship Research 13 (2), 137-154.

Kim, M.S., Ha, M.K., 2002. Prediction of motion responses between two offshore floating structures in waves. Journal of Ship & Ocean Technology 6 (3), 13-25.

Kim, Y., Yue, D.K.P., Connell, B.S.H., 2005. Numerical dispersion and damping on steady waves with forward speed. Applied Ocean Research 27 (2), 107-125.

Kodan, N., 1984. The motions of adjacent floating structures in oblique waves, Proceedings of the 3rd International Conference on Offshore Mechanics and Arctic Engineering, New Orleans, pp. 206-213.

Kring, D.C., 1994. Time domain ship motions by a three-dimensional Rankine panel method, PhD Thesis. MIT.

Lee, C.H., Sclavounos, P.D., 1989. Removing the irregular frequencies from integral equations in wave-body interactions. Journal of Fluid Mechanics 207, 393-418.

Li, L., 2001. Numerical seakeeping predictions of shallow water effect on two ship interactions in waves, PhD Thesis. Dalhousie University.

Li, L., 2007. Numerical seakeeping simulation of model test condition for two-ship interaction in waves, Proceedings of the 26th International Conference on Offshore Mechanics and Arctic Engineering, San Diego, California, USA, pp. OMAE2007-29328.

Longuet-Higgins, M.S., Cokelet, E.D., 1976. The deformation of steep surface waves on water (I): A numerical method of computation, Proceedings of the Royal Society of London, pp. 1-26.

Maury, C., Delhommeau, G., Ba, M., 2003. Comparison between numerical computations and experiment for seakeeping on ship models with forward speed. Journal of Ship Research 4, 347-364.

McTaggart, K., Cumming, D., Hsiung, C.C., Li, L., 2003. Seakeeping of two ships in close proximity. Ocean Engineering 30 (8), 1051-1063.

Miao, G.-P., Liu, Y.-Z., Yang, Q.-Z., Liu, Z.-Y., 1995. On the 3-D pulsating source of Michell type with forward speed. Journal of Hydrodynamics, Ser. B 2, 84-95.

Nakos, D.E., 1990. Ship wave patterns and motions by a three dimensional Rankine panel method, PhD Thesis. MIT.

Nakos, D.E., Sclavounos, P.D., 1990. Steady and unsteady ship wave patterns. Journal of Fluid Mechanics 215, 263-288.

Nossen, J., Grue, J., Palm, E., 1991. Wave forces on three-dimensional floating bodies with small forward speed. Journal of Fluid Mechanics 227, 135-160.

Ohkusu, M., 1974. Ship motions in vicinity of a structure, Proceeding of International Conference on Behaviour of Offshore Structure, NIT,Trondheim, pp. 284-306.

Ronæss, M., 2002. Wave induced motions of two ships advancing on parallel course, PhD Thesis. NTNU.

Scalvounos, P.D., Nakos, D.E., 1988. Stability analysis of panel methods for free surface flows with forward speed, 17th Symposium on Naval Hydrodynamics, Den Hague, Nederland.

Tarmo, S., 2007. Nonlinear components of ship wake waves. Applied Mechanics Reviews 60, 120-138.

Tuck, E.O., 1970. Ship motions in shallow water. Journal of Ship Research 14, 317-328.

Van Oortmerssen, G., 1976. The motions of a ship in shallow water. Ocean Engineering 3 (4), 221–255.

Wadam, 2010. Wave analysis by diffraction and Morison theory, Version 8.2 ed.

Xu, M., Yue, D.K.P., 1995. Computations of fully-nonlinear three-dimensional water waves, Proceedings of 19th Symposium on Naval Hydrodynamics, Seoul, Korea.

Xiang, X., Faltinsen, O.M., 2011. Time domain simulation of two interacting ships advancing parallel in waves, Proceedings of the 30th International Conference on Offshore Mechanics and Arctic Engineering, Rotterdam, The Netherlands, pp. OMAE2011-49484.

Xu, Y., Dong, W., 2013. Numerical study on wave loads and motions of two ships advancing in waves by using three-dimensional translating-pulsating source. Acta Mechanica Sinica 29 (4), 494-502.

Zou, L., Larsson, L., 2013. Numerical predictions of ship-to-ship interaction in shallow water. Ocean Engineering 72, 386-402.

Publications

The following papers have been published or submitted to publication during the Ph.D. study. Some of the work is not related to this thesis

Journals:

1. **Yuan, Z. M.**, Incecik, A., Jia, L., 2014. A New Radiation Condition for Ships Travelling with Very Low Forward Speed. *Ocean Engineering* 88(2014), 298-309.
2. **Yuan, Z. M.**, Incecik, A., Ji, C. Y., 2014. Coupled analysis of a hybrid mooring system with clump weights and buoys. *Ocean Engineering* 88(2014), 1-11.
3. **Yuan, Z. M.**, Incecik, A., Alexander, D., 2014. Verification of a new radiation condition for two ships advancing in waves. *Applied Ocean Research* 48(2014), 186-201.
4. **Yuan, Z. M.**, Incecik, A., Alexander, D., 2014. Hydrodynamic interactions between two ships travelling or stationary in shallow waters. (Submitted to *Ocean Engineering*).
5. **Yuan, Z. M.**, Incecik, A., Alexander, D., Ji, C.Y., 2014. Optimum spacing of two ships advancing in waves. (Submitted to *Journal of Ship Research*).
6. Ji, C. Y., **Yuan, Z. M.**, 2014. Experimental study of a hybrid mooring system. *Journal of Marine Science and Technology*. (DOI: 10.1007/s00773-014-0260-7).
7. Ji, C. Y., **Yuan, Z. M.**, Chen, M. L., 2011. Study on a new mooring system integrating catenary with taut mooring. *China Ocean Engineering,* 25(3), 427-440.

Conference Proceedings:

1. **Yuan, Z. M.**, Incecik, A., He, S., 2014. Hydrodynamic Interaction between Two Ships Arranged Side by Side in Shallow Water. *33th International Conference on Ocean, Offshore and Arctic Engineering*, OMAE2014-23325, San Francisco, California, USA.
2. **Yuan, Z. M.**, Incecik, A., Alexander, D., 2014. Numerical study on the hydrodynamic interactions between two ships arranged side by side. *2nd International Conference on Maritime Technology*, Glasgow, UK.
3. **Yuan, Z. M.**, Incecik, A., 2013. The radiation problem of vessels advancing in waves by using a new radiation condition. TEAM2013 Conference, Keelung, Taiwan.

4. **Yuan, Z. M.**, Ji, C. Y., Chen, M. L., Zhang, Y., 2011. Coupled analysis of floating structures with a new mooring system. 30th International Conference on Ocean, Offshore and Arctic Engineering, OMAE2011-49597, Rotterdam, TheNetherlands.